UNIVERSITY OF TRENTO - Italy

Department of Physics

Doctoral dissertation

of

Martino Bernard

in partial fulfillment of the requirements for the degree of
Doctor of Philosophy in the subject of Physics

Lightwave circuits for integrated Silicon Photonics

Supervisor: **Mher Ghulinyan**

Cycle XXIX - 2017

Editorial Notes

Lightwave circuits for integrated Silicon photonics,
Martino Bernard - Trento: University of Trento, 27+04+2017.

Contents

Preface 1

Framework and thesis structure 3

Introduction 7
- 0.1 From copper to silicon . . . 7
- 0.2 Photonics building blocks . . . 13
  - 0.2.1 Straight Waveguides . . . 13
  - 0.2.2 Couplers . . . 15
  - 0.2.3 Micro Resonators . . . 17
- 0.3 General methods . . . 21
  - 0.3.1 Fabrication technology . . . 21
  - 0.3.2 Transmission measurement setup . . . 24

1 Heterogeneously integrated laser 27
- 1.1 Introduction . . . 27
  - 1.1.1 Mode Locked Laser . . . 28
- 1.2 Waveguide design and simulation . . . 30
- 1.3 Waveguide Fabrication . . . 37
- 1.4 Propagation Losses . . . 46
- 1.5 Sagnac Loop Mirrors . . . 59
- 1.6 Mach Zehnder Interferometers . . . 66
- 1.7 Wafer Bonding . . . 68
- 1.8 Conclusions . . . 75

2 Strip-loaded UHQ resonators 77
- 2.1 Introduction . . . 77
- 2.2 Strip-loaded guiding . . . 79
- 2.3 Proof of concept . . . 84
- 2.4 Numerical Simulations . . . 86
  - 2.4.1 Losses . . . 90
  - 2.4.2 Layout . . . 93
- 2.5 Fabrication . . . 95
- 2.6 Measurements . . . 97
- 2.7 Conclusions . . . 108

3 Fano resonances in integrated disk resonators 113

3.1 Introduction . . . 113
3.2 Description of the system . . . 114
3.3 Analytical Theory . . . 117
3.3.1 Transmission spectra . . . 120
3.3.2 Experimental Results . . . 122
3.4 Thermo-optic control of Fano-Lamb interaction . . . 124
3.4.1 Analytical Theory . . . 125
3.4.2 Experimental results . . . 130
3.4.3 Numerical Simulations . . . 134
3.5 Conclusions . . . 136

4 $\chi^{(2)}$ non-linearities in silicon **141**
4.1 Introduction . . . 141
4.2 Nonlinear susceptibility . . . 142
4.2.1 Design . . . 144
4.2.2 Fabrication . . . 150
4.2.3 Passive Characterization . . . 153
4.3 Stress measurements . . . 154
4.4 $\chi^{(2)}$ measurements . . . 158
4.5 Conclusions . . . 163

5 Edge profile engineering for photonic applications **165**
5.1 Introduction . . . 165
5.2 Mathematical description of etching profiles . . . 166
5.2.1 Experimental data . . . 170
5.2.2 Surface energy estimation . . . 174
5.3 Possible Applications . . . 177
5.4 Conclusions . . . 182

Conclusions **185**

Acknowledgments **191**

Dissemination activity **193**

Appendices **195**

Appendix A **197**

Appendix B **199**

Appendix C **201**

Symbols and abbreviations **203**

Preface

Dear reader,

here I present you my research work on integrated silicon photonics that I carried out during the three years of my Ph.D. During my Master Degree internship at the Bruno Kessler Foundation I had the opportunity to tap into the world of micro- and nano-fabrication of photonic structures. Then, during my Ph.D. under the guidance of Mher Ghulinyan, and with the aid of Georg Pucker, Lorenzo Pavesi, and the colleagues both in the Centre for Materials and Microsystems (FBK) and in the NanoLab (UniTn), I had the opportunity to experience the whole development process of Photonic Integrated Circuits. From the concept and simulation, to the design and fabrication of photonic structures, to the optical characterization of the resulting chips and the consequent data modeling and analysis I had the possibility to experience both the scientific and the technological challenges of the field.

In addition to the research work, the formation activities in various formats as courses, schools, and workshops gave me the possibility to learn and exchange new ideas, which made this work possible. Regarding this point, a particular mention goes to the week-long workshop Industrial Problem Solving with Physics (IPSP). I had the opportunity to be a participant in the first edition (2014) challenging myself to solve industrial problems with the tools provided by an high-level formation in physics. The effectiveness of the said tools in solving the problems surprised me to the point that in the following year I participated at the event as a member of the Scientific Committee, actively organizing the second edition (2015). At the end of the event the conducted research is summarized in the form of scientific reports as proceedings of the event, reported in the Dissemination Activity section.

Participating at those events made me aware of how effective the "physics tools" are for solving practical problems and developing technology within a limited time. This awareness motivated my work on the All-on-Chip approach: to bring the physics from the optical tables of research laboratories to compact devices in everybody's house.

Martino Bernard
Povo, 27+04+2017

Framework and thesis structure

Since the development of modern electronics the dimensions of electronic devices, their integration density and possible applications have been changed a lot. The reduction in the base element dimension and the development of integrated devices allowed the advent of modern computers. Photonics is following a similar route: starting from the development of optical fibers for long-range signal transmission, nowadays, photonics is rapidly moving to integrated devices with footprints of a few squared micrometers.

The center around which this work revolves is the project SiQuro–"On silicon chip quantum optics for quantum computing and secure communications" [1], financed by the Provincia Autonoma di Trento (PAT). Project SiQuro aims at developing a number of active and passive photonic components for quantum optics integrated on the same chip, in an All-On-Chip (AOC) approach.

The original outline of the project exhibited a series of milestones, the most important of which are the fabrication of a heterogeneously integrated hybrid silicon-III-V pulsed laser, the realization of quantum interference experiments using correlated photons, the development of a novel Mid-Infrared (MIR) single photon detector based on phenomena of photon up-conversion, a Quantum Random Number Generator (QRNG) using silicon as a photon emitter material, and the general advancement in the theory of strongly interacting fluids of light in confined geometry. The frame that links together all of these apparently different scopes is the realization of quantum experiments enabled by non-linear optical processes within a single silicon photonic chip: a "Photonic Lab-On-a-Chip" (PLOC). The concept is to shrink a number of macroscopic tools, normally required to perform the experiment, i.e. the equipment of an optical table with a footprint of m^2, within a single chip of few cm^2. The chosen material platform is silicon which allows to adopt and adapt the worldwide standard of CMOS technology. More in detail, the project is divided into six Work Packages.

WP1 features the realization of an integrated hybrid silicon III-V quantum-dash mode-locked laser that is to be used as the high intensity source of photons necessary for the rest of the WPs. The second worpackage, WP2, aims at the generation of correlated photon pairs in the MIR exploiting non-linear optical effects in silicon. First, a series of experiments designed to measure the non-linearities in silicon need to be realized. At the same time, quantum interference experiments have to be realized on the bench using known (bulk) non-linear materials. Then, integrated structures have to be designed to generate the correlated photons using the pulsed laser of WP1 as the source, which are then manipulated within a silicon Photonic

Integrated Circuit (PIC). WP3 aims at the realization of a single-photon detector for MIR photons, exploiting non-linear up-conversion processes that partially rely on the studies developed in WP2. In parallel, WP4 aims at the realization of an integrated QRNG that features a silicon nanocrystal LED as the source of entropy, which is measured with the same integrated single photon detectors of WP3. In WP5 theoretical works on the interaction of photons are realized, with particular focus on phenomena in strongly correlated photon gases in a waveguide geometry. Last, WP6 addresses the novel field of synthetic gauge fields, with a particular attention to the concept of topologically protected states.

As it can be understood from the outline, the project contemplates the realization of a considerable number of integrated chips, both for testing and device realization. Most of the involved fabrication processes, excluding the single photon detector and the III-V material processing, has been carried on by the FMPS group in the clean rooms of the Center for Materials and Microsystems, FBK, where I developed most of the studies that constitutes this thesis work.

Structure of the thesis

The thesis is structured as follows:

- *Introduction.* In the introduction I give a historical review of the silicon platform, which is the one over which the SiQuro project is developed, exploring the motivations for further research in the field. Then, I give a rapid overview of the basic concepts and building blocks of integrated photonics that will be used along the whole thesis. Finally, I give a general overview of the fabrication process and of the typical experimental setup used to characterize the photonic chips.
- *Chapter One: Heterogeneously integrated laser* - The first building block of a photonic lab-on-a-chip is the light source. A well known problem of silicon photonics is related to the indirect band gap of Silicon, which prevents Silicon based laser sources to be created. In the case of SiQuro, the source of choice is a mode-locked laser, realized by heterogeneous integration of III-V semiconductors, that provide with the gain material, on a Silicon On Insulator (SOI) Photonic Integrated Circuit (PIC). To comply with the requirements of the various working packages of SiQuro, the laser is designed to have a working wavelength around 1490 nm. The chapter begins with an overview of the various components of the laser, the design of which has been realized in collaboration with III-V Lab, (France). The first component that will be addressed in detail is the SOI waveguide. To achieve lasing, indeed, it is necessary to minimize the losses in the complex Si-III-V cavity. Therefore, the design of the waveguide geometry, fabrication process and characterization will be described. Once set the waveguide geometry, fundamental components are designed and tested. The principal components are Sagnac Loop Mirrors, that provide the resonant cavity of the laser, and Mach Zehnder Interferometers, that are used to limit the gain bandwidth. In addition, I will describe some auxiliary structures, such as inverse couplers and racetrack resonators, that I designed, fabricated and measured during the development of the PIC. At the end of the chapter I will describe the development of the bonding technology for the heterogeneous

integration of the III-V material on the SOI wafer.

- *Chapter Two: Strip-loaded UHQ resonators* - In integrated waveguide structures the main source of loss is often the surface scattering. In the first chapter, low-loss SOI waveguides are obtained using the RIB geometry, which consists of a partially etched waveguide with reduced lateral surface. In this chapter, the concept of reducing the sidewall scattering loss in a structure where the light is partially guided in a slab waveguide is pushed to an extreme, realizing etch-less strip-loaded slab waveguides. In the beginning of the chapter I describe the concept of strip-loaded guiding and the demonstration of fully integrated, CMOS-compatible Si_3N_4 strip-loaded waveguiding structures. Then, the design, fabrication and measurement processes are repeated by realizing structures optimized for strip-loaded wave-guiding in the NIR (780 nm) and IR (1550 nm) spectral regions, demonstrating the achievement of integrated devices with Ultra High Quality-factors, that could be employed to enhance non-linear optical phenomena.

- *Chapter Three: Fano resonances in integrated disk resonators* - In this chapter I describe a basic photonic component (a waveguide-coupled microdisk resonator) through the formalism of an open-system model that includes both dissipative and reactive coupling components. The model, based on experimental observations, is then extended to implement an all-optical non-linear experiment which permits to explore various features of the reactive coupling, in particular the complete disappearance of a resonance feature in the transmission spectrum. Furthermore, the optical non-linear tuning developed to explore the reactive coupling is also demonstrated as a possible way to achieve relative frequency detuning between resonances belonging to different radial mode families of the resonator. Finally, the non-linear experiment is matched with the model through numerical solution of the developed non-linear dynamic equation of the system.

- *Chapter Four: $\chi^{(2)}$ non-linearities in silicon* - Within the framework of SiQuro, integrated structures where non-linear interaction of photons may occur are required both for the generation of correlated photon pairs as ell as for the up-conversion of said photons to the detection band of silicon. Both processes may be realized by using a second-order optical $\chi^{(2)}$ non-linearity. While silicon does not natively posses a second order non-linearity, a lot of effort has been put in recent years into measuring the stress-induced $\chi^{(2)}$ non-linearity magnitude in silicon that can be achieved in integrated structures. In literature, the typical configuration for such measurements featured a Mach Zehnder Interferometer, where the measured quantity is the index variation in one of the MZI arms. This variation is induced by the application of a static electric field through the Pockels effect. In this chapter I describe the design, fabrication and passive characterization of racetrack resonators realized with Si_3N_4-stressed SOI waveguides. The resonators have then be used to measure the Pockels effect produced in the waveguides by a low-frequency applied external electric field in a homodyne detection experiment, which exhibits enhanced sensitivity. Our experiment revealed strong free carriers effects which mask any $\chi^{(2)}$ contribution to the refractive index variation in the resonator. The free-carriers induced refractive index variation has been validated by high frequency measurements in the same samples, which demonstrated a vanishing of the modulation effect for frequencies higher than the inverse of the carrier lifetime.

- *Chapter Five: Edge profile engineering for photonic applications* - Wedge angle formation in microfabrication technology is a phenomenon that has been exploited in the past to realize UHQ-resonators exploiting the surface smoothness of chemically etched glasses. In this chapter I investigate the nature of the wedge angle formation, drawing an analogy with the Mach angle formation from aerodynamics. In the first part of the chapter I provide a formal description of etching fronts formation in common silicon-platform materials. The model is validated through measurement of samples etched for different times, reconstructing the etch-fronts characteristic to each material. Then, the nature of the different behaviours found in the realized samples is investigated through contact angle measurement in an attempt to link the photoresist peeling with the free surface energy at the photoresist-material interface in the presence of the BHF etch solution.

- Conclusions and Appendices - The concluding remarks, appendices and list of publication are reported at the end of the thesis.

Introduction

0.1 From copper to silicon

The worldwide internet bandwidth consumption steadily increased in the past years due to the rapid expansion of social media, cloud computing, and big data [2, 3, 4, 5]. To support the extensive use of digital tools in the private, public and business domain data centers have to handle an ever increasing quantity of data, that surpassed the zettabyte/year mark in 2012 suggesting the name of Zettabyte Era [6, 7, 8]. The increasing volume of data that needs to be handled, shown in Fig. 1 poses

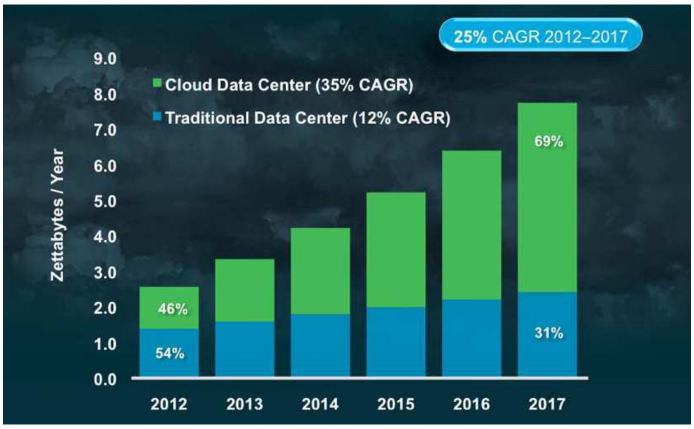

Figure 1: World-wide total data-center traffic growth, from CISCO[6].

issues on many levels, from the bandwidth for the worldwide connection to the data processing capability. Fiber optics have already substituted copper wires in long haul connections from tens to thousands of kilometers. This has been made possible due to the huge improvements that have been achieved in the optical fiber technology over the past forty years. Starting from the single mode fibers of the early 1970 the throughput capacity of a single fiber has increased by a factor of 10^5, as reported in Fig. 2. A huge twist was given by the Wavelength Division Multiplexing (WDM) since the 1990s, thanks to which multiple channels may be encoded in the same fiber at different wavelengths. The development of WDM alone, reported with the red squares in panel a), accounts for a factor of 10^3. In this case, the propagation losses play a crucial role. In contrast to copper wires, that present ohmic losses, optical fibers are affected mostly by scattering and absorption, that follow a Lambert-Beer law. In this field, tremendous improvements have been achieved, spanning several orders of magnitude. The losses, decreased rapidly in the first years of development,

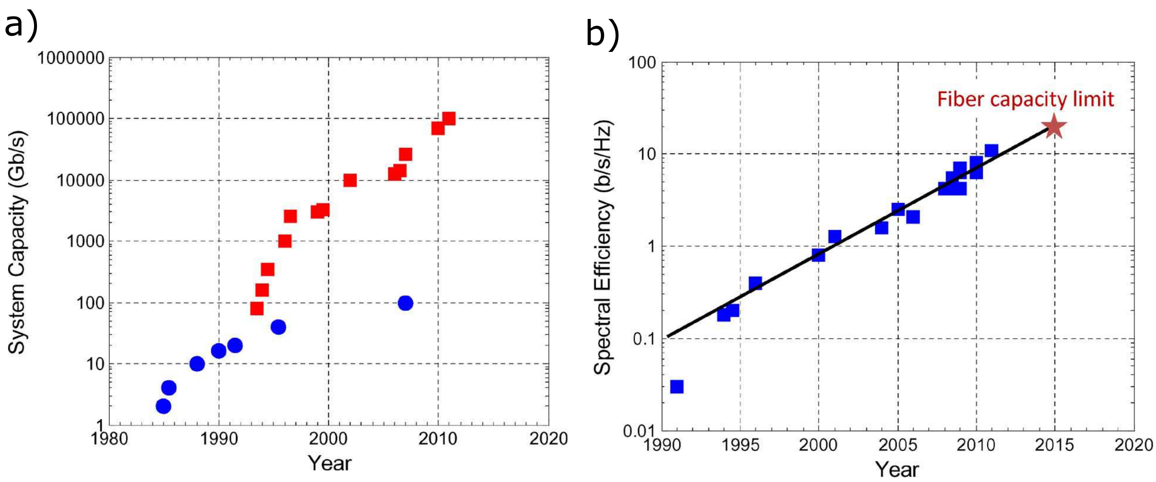

Figure 2: a) fiber system capacity during the years. The blue circles represent single-mode fibers for Time Division Multiplexing, while the red rectangles represent fibers engineered for Wavelength Division Multiplexing applications. b) evolution of the spectral efficiency of single fibers developed during the years. The red star corresponds to the maximum achievable spectral efficiency according to Shannon's limit, set by the non-linear effects in optical fibers. Images from [3]

going from a value that exceeded 1000 dB/km in the beginning of the 1960s to 0.2 dB/km in 1979 in the so called telecom C-band around 1.55 μm [9, 10].

At the same time, the engineering of the fiber wave-guiding properties, such as the chromatic dispersion and the modal birefringence permitted to improve the signal integrity, increasing the distance between signal repeaters.

In the years that followed, the change towards photonics-based communications did not remain confined to the long-haul lines. Soon, the change of paradigm became a reality for the short range as well [11]. While rack-to-rack optical connections are already commercially available, the change of paradigm is propagating further down the ladder, as sketched in Fig. 3, down to the chip-scale.

VLSI

All of this could not have been possible without a corresponding development in the interfaces between the photonic and the microelectronic worlds. Indeed, as shown inf Fig. 4 a), starting from the 1.3 μm wide transistors of the 1970s, the gate width of transistors attained 25 nm in the last few years, with Samsung just recently announcing the commercial development of 10 nm pitch technology. The reduction in the transistor size permitted to integrate a larger number of transistors on the same chip. As stated by the famous Moore's law, formulated 1965, "the number of functions per microelectronic chip will double every two years" [14]. As shown by Fig. 4 b) Moore's vision was proven true, thanks to the enormous investments that semiconductor devices attracted from the industry.

The paradigm of electronics miniaturization, through the Very Large Scale Integration (VLSI), has proven successful up to now steadily increasing the computational power of our devices. Nevertheless, the process of integrated fabrication of miniaturized devices requires a series of different complex operations (deposition, lithography, etching) that may be performed in different ways [15]. The VLSI would hardly have been possible without a coordinated standardization of the semiconductor processes. Since the foundation of the Semiconductor Industry Association in 1977, the need of a common effort into developing semiconductor industry was clear. In 1990 a roadmap

Network type	MAN & WAN	LAN	System	Board	Chip
	Metro & long haul	Campus, Enterprises	Intra-rack Inter-rack	Chip-to-chip	On-chip
				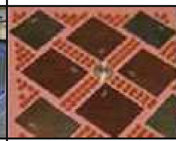	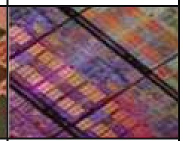
Distance	Multi-km	10 – 300 m	0.3 – 10 m	0.01 – 0.3 m	<2 cm
Adoption of optical	Since 80s	Since 90s	Since late 00s	After 2012	After 2012
Type of Connectivity	All-optical	Point-to-point and All-optical	Point-to-point	Point-to-point	Point-to-point & all-optical

Figure 3: The route of silicon photonics does not stop with optical fibers, but continues down to the integrated scale. Image taken from [5].

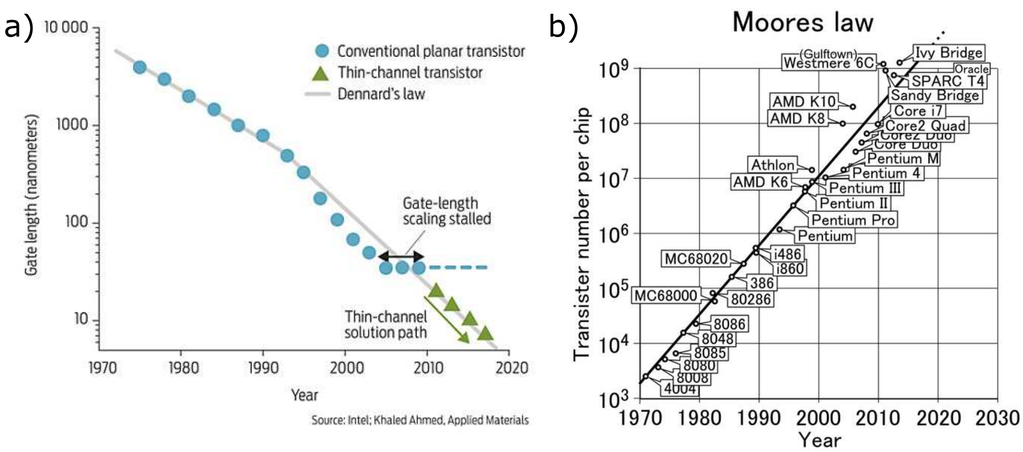

Figure 4: Evolution of the a) gate-length [12] and b) number of transistors per chip (from:[13]). The integration density of the processors realized in the past fifty years is in good agreement with the 1965 Moore's law prediction.

to outline the progress of the semiconductor industry and to match the technology of different companies produced the National Technology Roadmap for Semiconductors. Eight years later the European and Asian companies were also included, creating the International Technology Roadmap for Semiconductors (ITRS) [16].

Power density becomes unbearable

The continuous evolution towards more complex and performant devices, which copes with the increasing demand of bandwidth and data traffic of modern society, is approaching a serious threat in these last years. The wire connections between the chips suffer of Resistor-Capacitance delays and require an activation energy, in the order of 1 pJ, that is dissipated through Joule effect [17]. As the dimension of single transistors is reduced, thus increasing the transistor density, it becomes increasingly difficult to keep up with the required heat dissipation. To make it worse, higher integration means smaller wires with higher resistance. The power density generated in modern CPU is shown in Fig. 5 in comparison with a hot plate and a nuclear reactor. The substrates over which IC are fabricated, thermal silica, has a poor heat conduction setting a threshold to the maximum power density that may be dissipated around 100 W/cm^2. The number is itself impressive, considering that the surface power of a

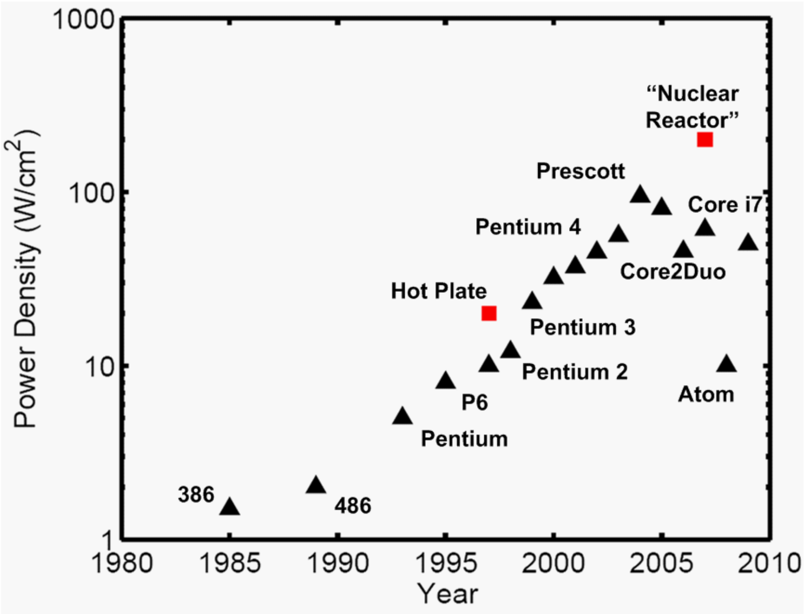

Figure 5: Time evolution of the power density in popular CPUs, compared to the same quantity in a hot plate and a nuclear reactor. Image from [18].

nuclear reactor just around the double. The solution in the past years has been the parallelization of processors into multi-core structures: the computational power of multiple CPUs is combined with a parallelization process, keeping them physically separated to keep up with the generated heat. The communications speed between different cores inside multi-core processors become the limiting factor in the number of units that may be parallelized, fostering the research for low-power optical solutions to this problem. The vision, further down the scale, is the introduction of integrated photonic communication lines , that would allow for a faster and less energy-hungry intra-chip communications [4, 19, 20, 2, 21].

First silicon waveguides

The first waveguides were made of doped silicon and exhibited a very low contrast, on the order of $10^{-3} \sim 10^{-1}$ leading to propagation losses of the order of 15 dB/cm [22]. An example of such a waveguide is shown in Fig.6 a).

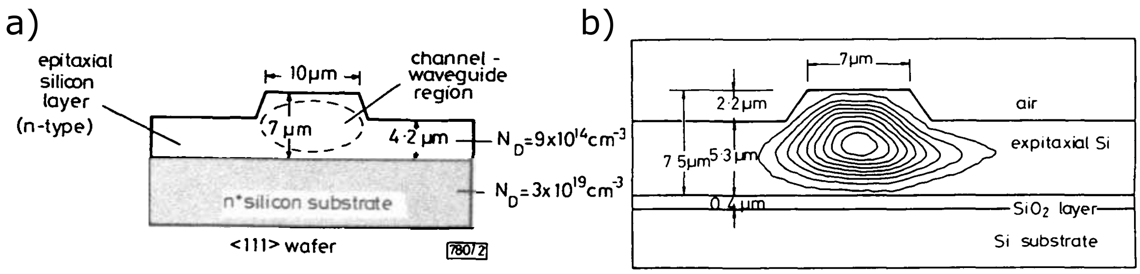

Figure 6: a) a silicon on doped silicon single-crystal waveguide used in Soref's experiments of 1985. The original paper, from which the image is taken, is [22].
b) the introduction of SOI waveguides, with a small silica cladding provided with a large reduction of the propagation losses, from [23].

With the advent of the Silicon On Insulator (SOI) technology, the things changed in the late 1980s. A SOI wafer consists of a crystalline silicon layer separated from the silicon substrate by a silica cladding. Various techniques were developed to obtain this configuration within the IC framework: separation by implanted oxygen (SIMOX), bonded and etch-back SOI (BESOI), and Smart Cut. The SOI platform proved to be ideal for the waveguiding systems: thanks to the low refractive index of silica (~ 1.45), a high core-cladding contrast may be achieved, leading to a better guiding. The first SOI slab waveguides were proposed and analyzed in 1988 [24], soon followed by single-mode waveguides with propagation losses of only 0.5 dB/cm, realized in a rib geometry and with dimensions exceeding 7 μm as shown in Fig.6 b) [23, 25].

Having in mind the paradigms of integration and miniaturization, the problem of propagation losses and bend radius is of paramount importance . While the high index contrast in the vertical dimension introduced by the SOI wafers solved the problem in the vertical direction, different geometries have been adopted over the years to achieve strong horizontal confinement and thus to reduce the bending radius. As early as in 1992, a common route for the worlds of microelectronics and photonics began to emerge in the vision of Abstreiter, that envisaged the OptoElectronic integration of circuits [26]. In the following year Soref proposed the concept of "superchip" [27]: electronics and optical circuits integrated both on the same silicon die. In it's sketch of 1993 (Fig.7) all of the fundamental building block are present: photodiodes, modulators, switches, laser diodes as well as ICs and waveguide-fibers integrated couplers. This shared vision is founded on the milestones of the VLSI standard: a common platform, silicon, and a common technology, the Complementary Metal Oxide Semiconductor technology (CMOS). Two of these two main com-

The Opto-Electronic Integrated Circuit vision

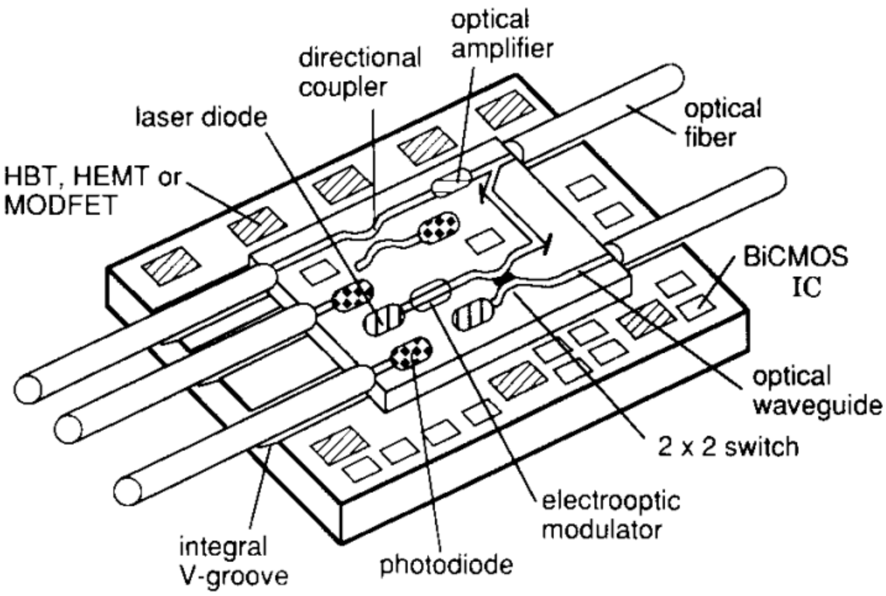

Figure 7: Soref's Opto Electronic Integrated Circuit (OEIC) "superchip" visionary idea, from [27].

ponents, however, were not available directly in the silicon platform at the time. Due to its indirect bandgap, silicon was not suitable to provide efficient light sources and amplifiers [28]. Photodiodes and laser diodes were realized in the already well understood III-V platform, for example with AlGaAs/GaAs and InGaAsP/InP. A third component for which the silicon needed a counterpart was the modulator. Being a centrosymmetric material, crystalline silicon lacks of electro-optic effect, which is the basis for ultra-fast electro optic modulators [29]. In Soref's vision, however, silicon would have been the platform over which the OptoElectronics Integrated Circuits were going to expand: with industrial investments in the silicon technology, it would have surpassed the V-III materials in niche areas, and then get a hold of the market thanks to the well developed low cost processing of silicon circuits, induced by the multi-billion dollar silicon VLSI industry. [27] Ten years later, the vision is mostly fulfilled, with other group-IV elements (mainly Ge and Sn) joining in the picture [28].

Silicon Photonics

The real turning point of Silicon Photonics came in 2004 – the year of the First International Conference on Group VI Photonics. In the previous years, many huge projects started boosting the silicon photonics development. Right after his Terahertz technology program that sponsored two SiGe/Si quantum-cascade laser projects (1999-2003), the Defense Advanced Research Projects Agency (DARPA) opted for a major investment in the 1.55 μm region, launching the four year project EPIC - Electronic and Photonic Integrated Circuits. Meanwhile in Europe, the Silicon Heterostructure Intersubband Emitter (SHINE) was started. The number of articles and citations in the field in Fig. 8 witnesses the huge leap forward that Silicon Photonics had in the last decade [21].

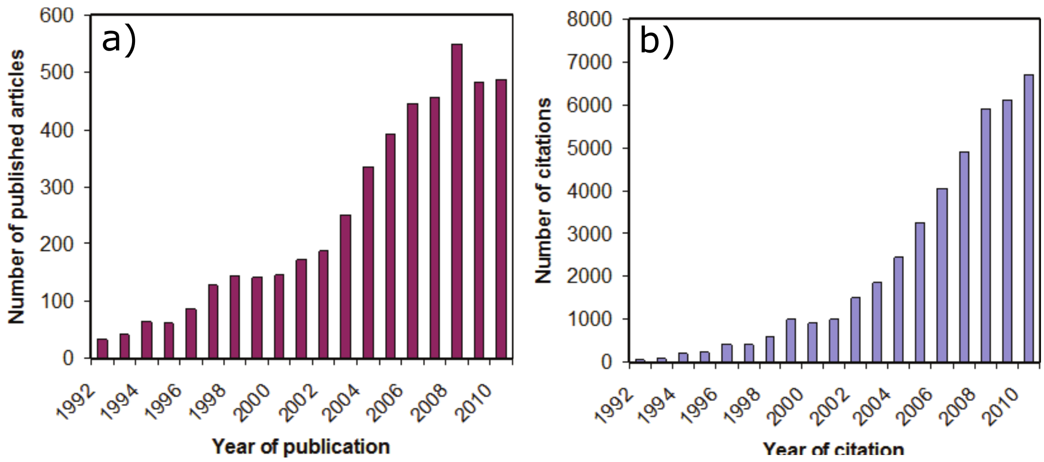

Figure 8: a) publications and b) citations per year with the keywords 'silicon' and 'waveguide', imge from [21].

One of the most important qualities of Silicon Photonics is probably the CMOS analogy and compatibility. As it has happened for electronic circuits, the development of standards and lump elements is of paramount importance to the development of the technology. The route of the IC begun with the development of basic elements, such as resistances, capacitors and transistors. Then, this elements were combined into functional chips that performed simple operations. The chips were then combined to achieve the desired system functionality. With the aid of modern Computer Aided Design (CAD) and Electronics Device Automation (EDA) softwares basics parts and chips may be considered as lumped elements during the design processing, leaving to a later step the optimization, if necessary. Silicon Photonics is following a route much similar to this. First, the building blocks as waveguides, resonators, and directional and grating couplers are build, characterized and optimized so that they may be used as lumped elements at a higher perspective. Then, more complex functionalities may be built at a Photonic Integrated Circuit (PIC) design level, putting together the basic elements into functional chips. This is the case for Mach Zehnder Interferometers, and structures of multiple resonators as well as integrated sources and detectors. This allows for a top-bottom approach in the system design process, by using standardized PIC and basic elements. If needed, other optimization iterations are then performed to address particular functionalities and the yield [30].

Basic PIC components

Within this framework, it becomes apparent that a lot of effort should be put into making the design of the basic elements as much as possible scalable, robust, CMOS compatible and cheap. In order to find the most valuable solutions, many different paths are often explored in terms of materials, geometry, and field of application. For example waveguides of silicon, silicon nitride and silicon oxynitride may be made in channel, rib or loaded geometry depending on the parameter that should be optimized (mode confinement, transparency, scattering losses). Project SiQuro offers us a good example of this approach: the project proposes to realize a chip-scale system which is formed by different functional subsystems (Laser source, photon pair generation, quantum experiments, detection) possibly all within the same platform (silicon) and within the same technology (CMOS plus III-V processing for the source).

0.2 Photonics building blocks

0.2.1 Straight Waveguides

Wave-guiding is one of the most important concepts of a PIC, as it allows control the flow of light around the device. In a ray-optics picture, the light is confined by total internal reflection within a high index material, which is called the core of the waveguide, and can't escape to the surrounding low-index region which is called cladding. Because of the total internal reflection, the light should be trapped within the core for all angles above the critical angle

Total internal reflection

$$\theta_{crit} = arcsin\left(\frac{n_{cladding}}{n_{core}}\right). \tag{0.1}$$

When the wave nature of light is taken into account, however, the angles at which the light is allowed to be reflected become discrete according to the Helmholtz equation. In the case of a straight waveguide, for a monochromatic wave, the equation may be separated taking into account the translational symmetry. The light is confined in the transverse x and y directions while along the propagation direction z the solution becomes a phase term. In this case the Helmholtz equation in paraxial approximation for the field distributions $\mathcal{E}_m$ may be seen as an eigenvalue equation of the form

$$\left(\nabla^2 + \frac{\omega^2 n^2(x,y)}{c^2}\right)\mathcal{E}_m(x,y) = \beta_m^2\mathcal{E}_m(x,y), \tag{0.2}$$

where the solutions, also called modes, are labeled by the m index as m-mode [31].The solution along the factorized dimension is the pure phase $e^{-i\beta_m z}$ The solutions may be labeled with their β_m from which the effective refractive index $n_{eff,m} = \beta_m c/\omega = \beta_m/k$ may be extracted. The effective refractive index indicates that the effective phase velocity of the light within the waveguide is $v_f = \omega/\beta_m$. In general, the waveguide may suffer from lossy channels such as material absorption and surface scattering. In this case the propagation along z ceases to be a pure phase. The losses may be represented as a small imaginary part of β_m (or n_{eff}) that brings in a real part into the exponential, leading to an exponential decay. The losses are usually indicated as

Propagation losses

$$\alpha_m = -2Im(\beta_m) = -\frac{2\omega Im(n_{eff,m})}{c}, \tag{0.3}$$

with the convention that α is positive when the medium is lossy, so that the propagation along the z direction becomes $e^{-i\beta_m z}e^{-\alpha z}$. For a rectangular cross section of

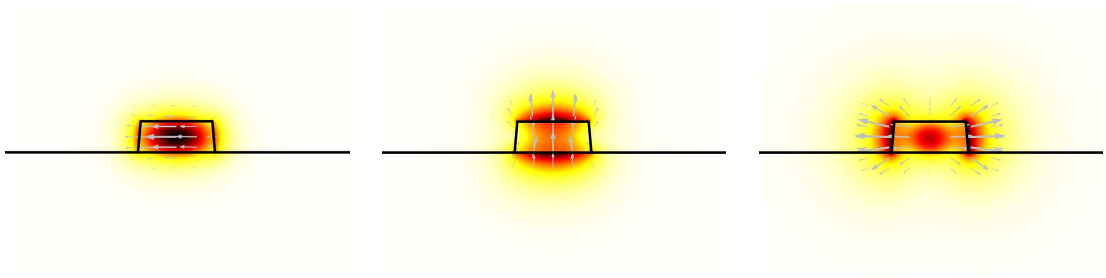

Figure 9: Cross sectional view of TE1, TM1 and TE2 modes in a Si channel waveguide. The color is darker where the field is stronger. The gray arrows represent the direction of the electric field.

the waveguide and a symmetric cladding, the solutions have the shape of sines and cosines inside the waveguide, while the field decays exponentially outside.

m index

In general, the solutions of Eq. 0.2 may have nodes in both x and y directions, but the geometry of the waveguide has usually a width to height ratio larger than one, with the height small enough such that there are no nodes along the y direction. As it is customary the case, the modal number m is used to indicate the number of crests along the in-plane x direction.

Figure 9 show the electric field intensity distribution for the fundamental mode in both Transverse Electric (TE) and Transverse Magnetic (TM) polarizations inside a channel waveguide. The last panel refers to the $m = 2$ mode in transverse polarization, called TE2.

Confinement factor

An important parameter of a waveguide mode is the so called confinement factor

$$\Gamma_m = \frac{\int_{core} \epsilon \mathcal{E}(r)^2}{\int_{all} \epsilon \mathcal{E}(r)^2}, \tag{0.4}$$

that represents the fraction of the field that is confined within the waveguide core. Since the geometry of waveguides may vary, the "core" concept may blur and the domain of integration in the denominator should be specified. In pair with the confinement factor is the mode effective area

Mode effective area

$$A_{\mathrm{eff,m}} = \frac{\left(\int |\mathcal{E}(x,y)|^2 \, dx \, dy\right)^2}{\int |\mathcal{E}(x,y)|^4 \, dx \, dy} \tag{0.5}$$

which is a measure of the mode effective extension in the plane transverse to propagation. The mode effective area is an important parameter when dealing with non-linear effects, where the mode distribution plays a crucial role to determine the local field intensity, and thus the efficiency of non-linear effects. The optical fiber, for example, is a special case of waveguide with cylindrical symmetry, where the high index guiding material is the doped silica core. In graded index fibers the concept of total internal reflection blurs since the interface between a high and a low refractive index media disappears in favor of a gradient of index that gradually bends the light.

Different geometries

Other waveguide geometries are present as well, for example loaded waveguides and rib waveguides. In loaded waveguides a planar waveguide is build first, and then the confinement in one of the planar directions is achieved by locally heightening the effective index with a loading strip of material. The rib waveguide is a special case of strip load waveguide where the load is made of the same material of the slab. In this case, the "core" of the waveguide becomes a blurry concept, so it may be difficult to define a confinement factor.

Dispersions

The solutions of Eq. 0.2 are furthermore dependent from the optical frequency $\nu = \omega/(2\pi)$ (or vacuum wavelength $\lambda = 2\pi c/\omega$), both because of the so called "geometrical dispersion", which takes into account the fact that the waveguide has a finite size compared to the wavelength of the light traveling within, and because of the "chromatic dispersion" which is due to the dependence of the bulk material refractive index on the frequency ($n = n(\lambda)$). This means that the solutions are also a function of the wavelength. An important quantity that emerges from the wavelength dependence of the solutions is the group index, that represents the ratio between the speed of light in vacuum and the group velocity in the waveguide. The group index of mode m is defined as

$$n_{g,m} = n_{eff,m} - \lambda \frac{dn_{eff,m}}{d\lambda}. \tag{0.6}$$

Other interesting quantities are the so called *dispersions*, the derivatives of the propagation constant β_m with respect to the wavelength. The j-th derivative

$$\beta_m^{(j)} = \frac{d^j \beta_m}{d\lambda^2} \tag{0.7}$$

is called j-order dispersion coefficient. Of these, the 0^{th}, 1^{st} and 2^{nd} are the most important. In particular we have that $\beta_m^{(0)} = \beta_m$ is the propagation constant, $\beta_m^{(1)} = n_{g,m}/c$ is directly proportional to the group index, while $\beta_m^{(2)}$ is called Group Velocity Dispersion (GVD).

0.2.2 Couplers

Evanescent coupling

As mentioned before, the waveguide modes decay out of the guiding core with exponential tails. The exponential tails allows us to insulate the waveguide with an appropriately thick cladding. On the other side, however, the evanescent tails may be used to couple different waveguides, making energy flow from one to the other waveguide. A detailed description of the interaction between two waveguides through their exponential tails may be found in [31].

A smart way to obtain the coupling between the two waveguides without having to consider the overlap integrals of the exponential tails is to look at the symmetric and antisymmetric coupled supermodes, shown in Fig. 10. We may consider the two coupled waveguides as a single system with "supermodes" that travel inside both the waveguides instead of two separated systems with proper modes each. In particular, there will be a symmetric and an antisymmetric supermode, the time-evolution of which represents the flow of energy between the waveguides due to the coupling. At a given instant, the sum of the normalized symmetric and antisymmetric modes would have all of the power inside a single waveguide, let's say wg_1 resembling the single-waveguide mode. Due to the energy splitting, the symmetric and antisymmetric super-modes have different n_{eff}, and therefore they travel with different phase velocity, meaning that the power flows from one waveguide to the other periodically. The difference in the effective refractive index of the two modes $\Delta n_{\text{eff}} = n_{\text{eff}}^{sym} - n_{\text{eff}}^{asym}$ allows us to calculate the length over which the power is completely transferred from one waveguide to the other. If we consider all of the light in wg_1 at $z = 0$ the

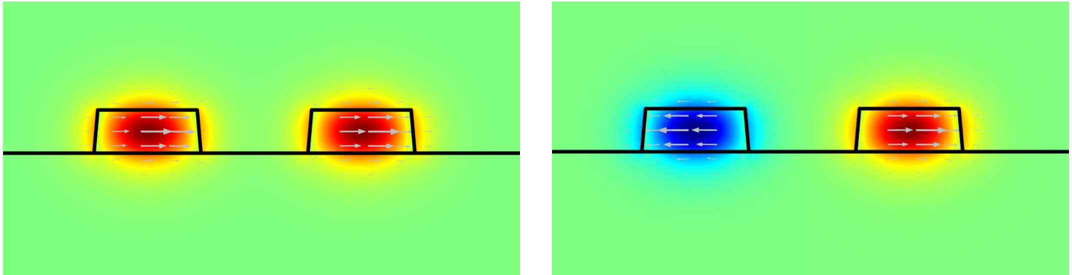

Figure 10: Symmetric and anti-symmetric supermodes of two coupled waveguides. The color represents the intensity of the E_x field component, which is the dominant. The gray arrows are samples of E, showing that E_x is the dominant component, that is opposite in the two waveguides for the asymmetric mode.

equations for the fractional intensities I_1 and I_2 inside the two waveguides are [32]

$$I_1(z) = cos^2\left(\frac{\pi \Delta n_{\text{eff}} z}{\lambda}\right), \tag{0.8a}$$

$$I_2(z) = sin^2\left(\frac{\pi \Delta n_{\text{eff}} z}{\lambda}\right). \tag{0.8b}$$

I/O coupling

Another important issue about coupling is how to transfer the energy in and out of the sample. The light-source, at least during the experimental phase, is a macroscopic object that usually has a free-space or an optical fiber output. There is a huge dimensional mismatch between the free space beam ($\sim 1mm^2$) or the beam traveling inside an optical fiber ($\sim 100\mu m^2$) and the section of a waveguide ($\sim 1\mu m^2$). Because of this dimensional mismatch, simply alignment of a cut fiber with the waveguide (butt coupling) results in a poor matching of the optical profile, which means a lot of insertion losses. A better coupling is achieved making use of a lens. In the fiber case, the fiber is first tapered down to a few microns to further reduce the dimensional mismatch, and then a small lens is fabricated directly at the tip of the core, producing a beam with a waist of only a couple of microns at the focal length. This kind of fibers are called tapered fibers, and represent the external coupling method of choice for this work.

Butt coupling

Other strategies are adopted also on the chip to further reduce the losses.
The waveguide may be tapered at the end to increase the dimension approaching the beam waist of the lensed taper fiber (tapered waveguide). In this case the geometrical mismatch is minimized. However, another problem arises: the effective index for a large silicon waveguide approaches that of bulk silicon, which has a huge contrast with air. This means that a lot of energy is reflected at the air-silicon interface, resulting in additional losses. Furthermore, the facet of the waveguide requires polishing to avoid scattering due to the roughness produced during a regular dicing process. To overcome this problem, an opposite tapering may be realized (inverse tapering) that reduces the width of the waveguide near the coupling region. In this case the effective index of the waveguide changes smoothly from the refractive index of the cladding to that of the proper waveguide, avoiding the interface mismatch that leads to reflection. A huge advantage of this technique is that it avoids completely the problem of facet roughness, having no interface. Despite the problem of geometrical mismatch, this solution proved to be most efficient in terms of coupling losses and

reproducibility, but requires a process capable of realizing very narrow structures. Making use of this technique, insertion losses as low as $0.39dB$ and $0.66dB$ have been reported for TM and TE modes respectively [33] Furthermore, working on the taper-shape optimization may further improve the misalignment tolerance of this technique [34]. In this perspective, leaving the waveguide straight represents an intermediate solution in terms of dimension, sensitivity to the facet roughness and with no further requirement on the resolution of the process, although the requirement of ad-hoc treatment of the facets remains an issue. Another method of coupling makes us of a grating to add the incoming lightbeam a k vector such that it will enter the input waveguide. Such geometries are often realized so that the input beam infringes with an angle close to 90 with respect to the chip's plane on a periodic structure. The periodic structure acts as a grating and adds an in-plane k vector to the beam, so that it couples to a tapered waveguide on the end of the grating. Grating coupler

The huge advantage of such technique is the possibility of in-line probing of the sample during it's fabrication, since no cut is required and the sample is probed out of plane. In principle, the technique could also be used for trimming the optical components. However, this technique comes with three main disadvantages: the grating efficiency is sensible to the polarization, the grating pitch is sensible to thermal fluctuations and the the processing of a grating for $\lambda \sim 1550nm$ requires a resolution at least $\lambda/2/n_{Si} \sim 190nm$. The resolution constrain may be lessened by making use of higher order diffractions, but at the price of higher losses.

0.2.3 Micro Resonators

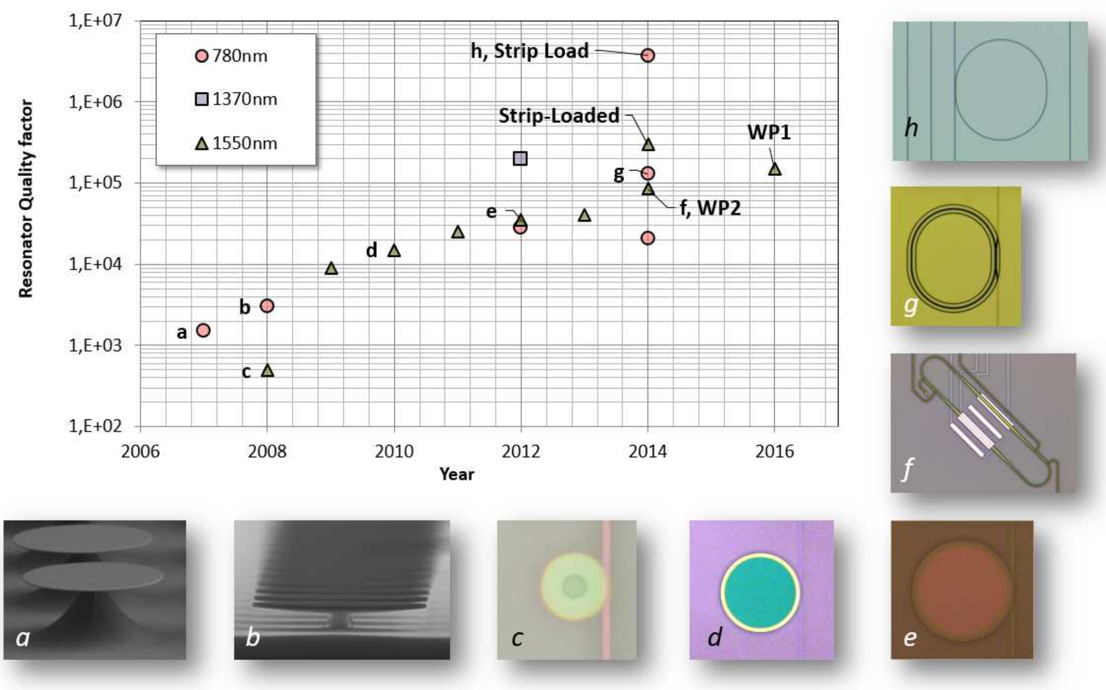

Figure 11: Resonators in various configurations realized at FBK and their Q-factor.
a. Si-NCs μ-disk; b. Si-NCs μ-kylix; c. 1^{st} Si-NCs integrated resonator; d. SiN_x resonator; e. SiN_x wedge resonator; f. SOI racetrack resonator (WP2); g. SiON ring biosensor; h. Si_3N_4 Strip-Loaded ring

Another important basic component for the PICs are the micro resonators, where

the high refractive index contrast offered by silicon poses the premises for a VLSI development [35, 36, 37].
By bending a waveguide in a ring shape we may have a structure in which the light circulates on a closed loop. Figure 11 shows some examples micro-resonators in various configurations. If the losses are low enough such that they are negligible on a round-trip, a light beam inside the resonator would destructively interfere with itself unless its optical path along the ring is an integer multiple of the wavelength. When the optical path traveled by light, which is the geometrical path L times the effective index n_{eff}, equals an integer number M of wavelengths λ_M we have the resonant condition. Namely

Resonant condition

$$\lambda_M = \frac{n_{\text{eff}} L}{M}, M \in \mathbb{N}. \tag{0.9}$$

or

$$\omega_M = \frac{2\pi c m}{n_{\text{eff}}(\omega_M) L} \ , \tag{0.10}$$

At the resonant condition, the light within the ring interferes constructively at each roundtrip, enhancing the field intensity. The distance between adjacent resonances is called Free Spectral Range (FSR) an may be calculated as

Free spectral range

$$\frac{\lambda_M^2}{n_g(\lambda_M) L}. \tag{0.11}$$

In order to excite and probe the resonator, one or more bus waveguides are usually used as shown in Fig. 12. The coupling is very similar to that discussed in 0.2.2. Usually a very low coupling coefficient is implemented, since the enhanced field amplitude inside the resonator is many times the field in the waveguide. When at the resonant frequencies, the resonator ”captures” the light coming from the Input port through the waveguide. On resonance, the phase shift due to the couplings $2Im(\kappa)$ plus the round-trip phase shift $\varphi(\lambda) = 2\pi n_{\text{eff}} L/\lambda$ become $e^{-i(2M+1)\pi} = -1$, with M integer. Therefore, the field of the waveguide and that coupled from the resonator destructively interfere, giving rise to dips in the transmission spectrum of the Throughput port. Out of resonance, the $\varphi(\lambda)$ term changes and the contributions coming from successive roundtrips of the lightbeam inside resonator rapidly average to null. The resonance dips have a finite Full Width at Half Maximum (FWHM) due to the round trip losses $a = e^{-\alpha L}$ with α loss coefficient inside the resonator. A typical transmission spectrum of single waveguide coupled to a resonator, also said All-Pass (AP) configuration, is shown in Fig. 13.

If a second waveguide is coupled to the resonator, as pictured in Fig. 12, dotted lines, the configuration is called Add-Drop (AD).
In this configuration a ”positive” spectrum may be detected on the Drop port, where the waveguide carries the field coupled by the resonator plus an eventual signal coming

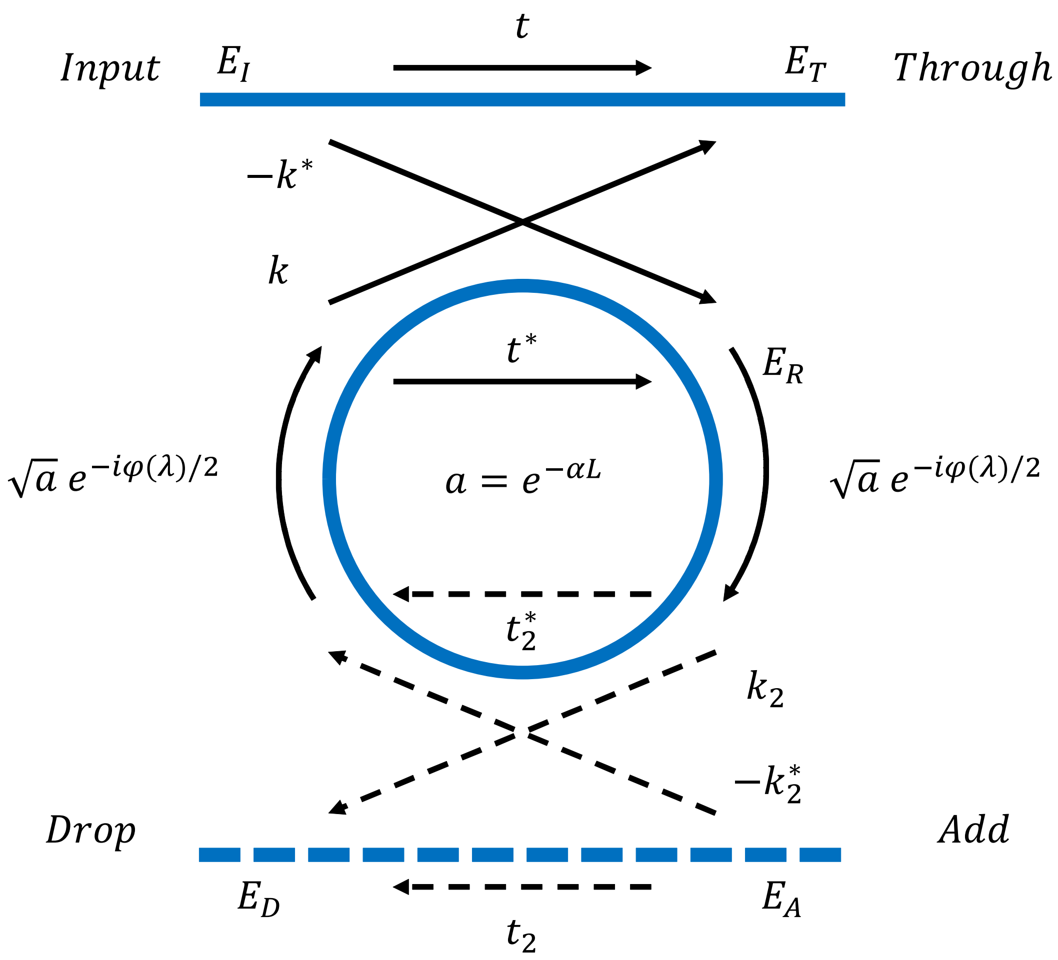

Figure 12: Beam splitter model for the coupling of a resonator to one or two bus waveguides. The single bus waveguide is called All-Pass configuration, the light comes from the Input port, and is partially coupled to the resonator via the κ coefficient. The interference among the transmitted and re-coupled light gives the spectrum at the throughput port. Along the resonator, the waveguide losses attenuate the field by the loss coefficient a at each roundtrip, gaining a phase $e^{-i\varphi}$. Add and Drop ports may be added to the system with a second coupled waveguide (dashed lines).

from the Add port. The transfer function of these systems are

$$E_T^{AP} = R_T^{AP} E_I = \frac{te^{i\varphi(\lambda_m)} - a}{e^{i\varphi(\lambda_m)} - at^*} E_I \tag{0.12a}$$

$$E_T^{AD} = R_T^{AD} E_I = \frac{te^{i\varphi(\lambda_m)} - at_2^*}{e^{i\varphi(\lambda_m)} - at^* t_2^*} E_I, \tag{0.12b}$$

$$E_D^{AD} = R_D^{AD} E_I = \frac{-k^* k_2 \sqrt{a} e^{i\varphi(\lambda_m)/2}}{e^{i\varphi(\lambda_m)} - at^* t_2^*} E_I, \tag{0.12c}$$

obtained using the beam splitter model for the coupler [38, 39]. In the beam splitter formalism, the κ coefficient represents the coupling of the waveguide towards the resonator. As discussed above, the coupling strength depends on many factors, among which the length of the coupling region and the distance among waveguide and resonator. In the resonator's perspective, on the other hand, t represents a loss channel towards the waveguide. When the coupling is made with a proper directional coupler with parallel waveguides the resonator is usually called racetrack resonator.
For circular resonators, the coupling takes the name of point coupling, although the

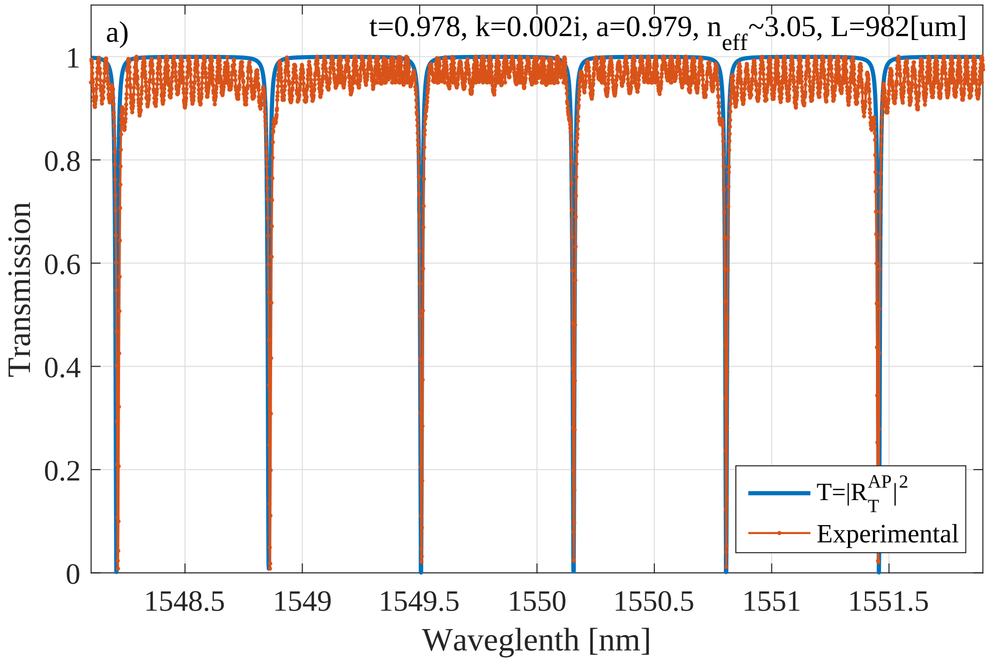

Figure 13: An example of All-Pass Through spectrum from the rib racetrack resonator FIGURE. The experimental points (orange) exhibit sharp quasi-critical resonances. The fast oscillating features near 1 transmission are spurious Fabry-Perot resonances due to the bus waveguide facets. The resonator parameters were then plugged in the All-Pass transfer function, leading to the transmittance (blue) which is $|R_T^{AP}|^2$.

coupling takes place along a finite portion of the resonator circumference. This is particularly important for the resonator with a large radius. The ratio of t and a divides the coupling into three regimes;

- $t/a < 1$ Under Coupling
- $t/a = 1$ Critical Coupling
- $t/a > 1$ Over Coupling

Figure 14 (a) shows the transfer function of the All-Pass configuration in various coupling regimes, using system parameters similar to those of Fig. 13. As shown in the figure, the resulting spectrum resembles a notch filter. The green line shows the critical coupling configuration, where the coupling equals the roundtrip losses. With $a = t$ the light that is transmitted and the light that is re-coupled in the waveguide are equal but opposite, giving complete destructive interference. Indeed, critically coupled resonances reach 0 transmission on resonance. The red line shows the resonator in a typical over-coupled regime, where the excessive coupling spoils the resonator's quality factor, broadening the resonance peak. In the case of under coupling, on the other hand, the quality factor is the resonator is lightly enhanced due to lower coupling losses, but the resonant feature is less incisive on the waveguide transmission, resulting in a less deep resonant peak. Figure 14 (b) shows analogous transmittance spectra for an Add-Drop configuration. The bold and dotted lines represent the transmission spectra of the Trough and Drop port respectively. In faint colors, the transmission of the AP filter is reported for comparison. In this simulation the coupling parameters t_2, k_2 were taken equal to t, k respectively. Is worth note that the condition for critical coupling is different in the AD configuration, being it

	All-pass	Add-drop
FSR	$\lambda_m^2/n_g(\lambda_m)L$	$\lambda_m^2/n_g(\lambda_m)L$
Q	$\frac{\pi n_g(\lambda_m)\sqrt{at}L}{(1-at)\lambda_m}$	$\frac{\pi n_g(\lambda_m)\sqrt{at}L}{(1-at^2)\lambda_m}$
Finesse	$\frac{\pi\sqrt{at}}{(1-at)}$	$\frac{\pi\sqrt{at}}{(1-at^2)}$
FE	$\frac{-k^* e^{i\varphi(\lambda_m)}}{e^{i\varphi(\lambda_m)}-at^*}$	$\frac{-k^* e^{i\varphi(\lambda_m)}}{e^{i\varphi(\lambda_m)}-at^* t_2^*}$
Crit.Cond	$a = \|t\|$	$a = \|t/t_2\|$

Table 1: Relevant resonator quantities FSR, Q and FE. n_g is the group index, L is the geometrical length of the resonator, while the other symbols are as from Fig. 12

$a = |t/t_2|$. Since t and t_2 were taken equal, the AD almost reaches critical coupling for $a = 0.99$.

Micro Resonator relevant quantities

A summary of the relevant quantities for both configurations is reported in Tab: 1 With $\varphi(\lambda) = 2\pi n_{\text{eff}} L/\lambda$.

0.3 General methods

0.3.1 Fabrication technology

During my work I fabricated a lot of different samples in the Clean Rooms (CR) of Fondazione Bruno Kessler (FBK). In order to make the various chapters easier to follow, a short overview of a typical wafer processing is reported here. Each process run, or simply "run" begins with a number of Chemical-Mechanical-Polished (CMP) silicon or SOI 6-inch wafers. Furthermore, in each process a number of silicon wafers are usually included as test wafers. After a standard labeling and initial cleaning step, the wafers are ready for processing. The structures are realized in a top-down approach, where the desired materials are deposited in layers and the excess is removed. SOI wafers already have the guiding material, the crystalline Silicon on Insulator layer, and also the bottom cladding, that consists of a $3\mu m$ thick thermal silicon oxide layer. Silicon wafers are used instead when the guiding material is realized in-house. The layer of guiding material is sometimes also referred to as "device layer". The most used materials for the device layer are silicon nitride (SiN_x), silicon oxynitride (SiO_xN_y), polycrystalline silicon (poly-Si), and Silicon Nano-Crystals (SiNC). The silicon wafers require the realization of a cladding to separate the device layer from the high index silicon substrate. The silicon wafers are therefore covered with a bottom cladding of silicon oxide SiO_2. The first oxide layer is usually realized by oxidizing the silicon. Among the used oxides, this thermally grown silicon oxide is the best in terms of optical properties and impurities. However, the oxidization is realized by diffusion of oxygen, which is via via obstructed by the growth of the oxide, making the oxidization inefficient for large values of thickness. The oxidization

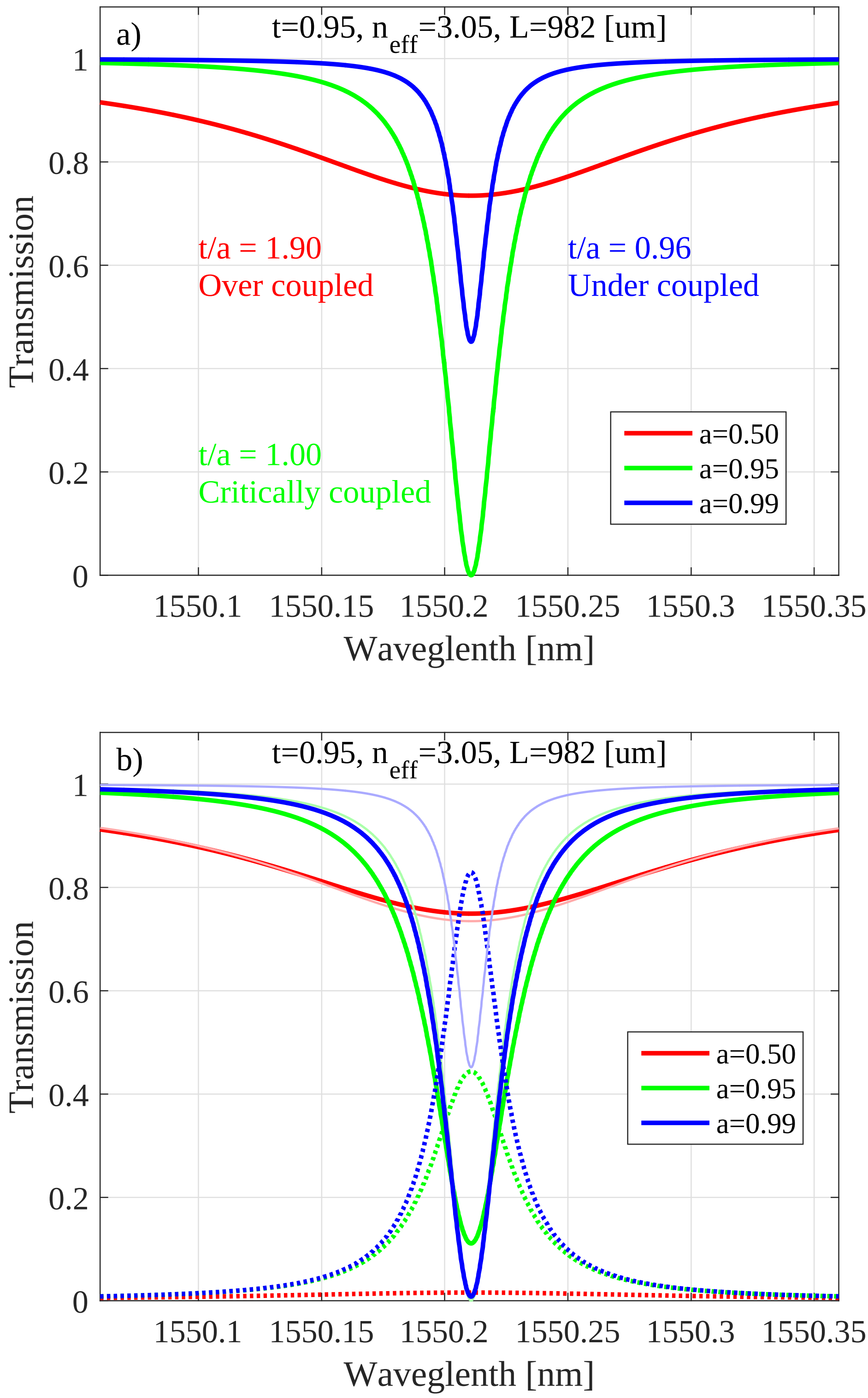

Figure 14: Spectra of AP and AD resonators simulated using the transfer functions of Eq. 0.12c for different values of the loss parameter a. The other parameters were taken similar to Fig. 13. In panel a) spectra for critical- (green), under- (blue) and over-coupling (red) are present. In panel b) the same coupling and loss parameters are used with the Add-Drop transfer functions with $t_2 = t$ and $k_2 = k$. It's woth note that the critical coupling condition is different for an AD filter, namely $a = |t/t_2|$.

is typically realized in furnaces in oxygen of water atmosphere at 975°.The second silicon oxide is realized by Low Pressure Chemical Vapor Deposition (LPCVD) in the furnaces at the temperature of 710°using TetraEthyl OrthoSilicate as a precursor. Upon this cladding layer made of oxide, a layer of higher index material is deposited to form the guiding structures. This step is realized either via LPCVD or via Plasma Enhanced Chemical Vapor Deposition (PECVD). The latter is often followed by a thermal annealing step to reduce the residual hydrogen content. The thickness and the index dispersion of both cladding and guiding layer are verified making use of the Variable Angle Spectroscopic Ellipsometry (VASE) [40]. At this point, both SOI an silicon wafers have the first guiding material layer, usually called "device layer", and proceed with analogous processes. A layer of photo-reactive material is spin-coated on the surface, previously primed with a thin layer of adhesion promoter material. The photoresist is exposed to 365 nm UV light through a chromium mask transferring the layout pattern from the mask to the photoresist, which is then developed and hard-baked. At this point, the layout pattern is on the wafer as structures of photoresist upon the guiding material layer. The undesired material is removed via Reactive Ion Etching (RIE), Deep-RIE (DRIE) or chemical reaction in aqueous solution (wet-etching) and then, the remaining photoresist is removed as well, leaving the patterned guiding layer on top of the wafer. Possibly, other layers are added on the structures, as stressing layers, metalizations or other guiding layers interspersed with cladding layers. A top cladding is usually deposited to protect the structures from the environment. The specific fabrication process that has been developed for each PIC will be discussed in each chapter, along with some considerations on the possibility to implement different components in the same process, and ultimately in the same PIC.

Minimum feature size

One of the most important parameters of the fabrication is the wavelength used for the lithography, which determines the minimum feature size that could be properly resolved. In many state-of-the-art works, Deep Ultra Violet (DUV) at 193 nm or 100 keV electron beam (e-beam) lithography are used to realize the desired pattern. These techniques have the disadvantage to be costly and, in the case of the e-beam, slow. In fact, the Extreme UV (EUV) lithographic technology used for mass production of electronic devices reaches minimum feature size of few tens of nanometers, but the cost of process development is still prohibitive for non-mass production. In the present work, a Nikon NSR-2205i11D using the 365nm i-line was used, for a nominal minimum resolution size of $0.4\mu m$.
The necessity for a small mode volume in non-linear processes together with the single-mode condition operation bring the typical dimensions of the structures at the limit of resolution.
I have put a lot of effort into making the fabrication processes reliable and stable near the resolution limit during this work. Action was taken on many levels: the control of reflections during the lithography, the size-and-shape control during all of the processes, the fine-tuning of the patterned photoresist dimensions and shape and post-etching to further adjust the dimensions. Additional improvements have been carried on also on the simulative front by determining which are the most critical dimension parameters and characterizing the effects of variations in the dimensions.

0.3.2 Transmission measurement setup

A passive characterization setup is required to verify the proper operation of the PICs. Passive characterization is performed on both linear and non-linear devices to measure the low-power response of the devices. In order to achieve this results, there are two frequent configurations: a broad-band source to excite the system in a broad spectrum coupled with a wavelength-selective detecting system, or a tunable laser that sweeps across the desired bandwidth coupled with a broadband detector. In our work, the second configuration is used. Here I present the typical passive characterization experimental setup as it will be used many times through the work with minor variations.

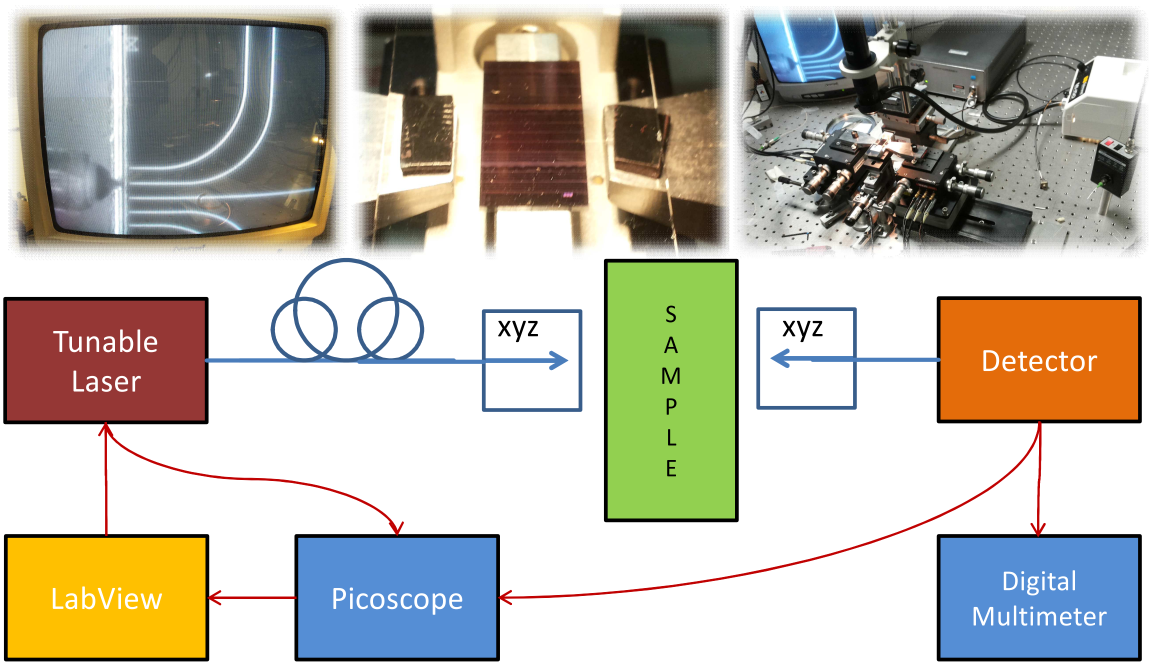

Figure 15: Passive characterization setup. A fiber coupled tunable laser is used as the source. The polarization is controlled by an in-fiber polarization stage. The input fiber terminates with a lensed inverse taper, that is aligned to the sample with a 3-axes piezoelectric stage. At the output, the signal is collected by a similar lensed inverse taper fiber. The optical signal is converted into electrical signal by a broadband germanium detector. The signal on the detector is measured on a digital multimeter for manual alignment and on a Picoscope oscilloscope for the automatic spectrum acquisition.

In most experiments, a *Yenista Tunics T100S* fiber coupled tunable diode laser is used as the source [41]. A polarization control stage, typically in-fiber, is used to set the polarization at the input of the sample. The input fiber is terminated with a lensed taper fiber, which is aligned to the sample with a combination of a 3-axes micro-positioner and a 3-axes piezo-electric nano-positioner. The sample holder has a mechanical micro-positioner with a single axis, that is used to change the coupled device on the chip once the system is aligned. At the output of the sample, a similar lensed taper fiber collects the signal. The alignement of the output taper waveguide is likewise achieved with a combination of micro- and nano-positioners. The collected output signal is converted into voltage signal by a *Large Diameter Ge Photoreceiver, Model 2033*. During the alignment stage, the signal on the detector is continuously measured by a multimeter. The taper fibers coordinates are varied iteratively searching for the maximum of the transmission signal. To facilitate the operation, the laser frequency is swept manually after a first fiber-alignment iteration to identify the local spectral shape, which often features Fabry-Perot resonances, and the alignment is then performed near the (local) maximum with respect to the wavelength closest to the operation wavelength. After the alignment the spectrum of the device is acquired with a triggered continuous sweep of the laser, which is synchronized with a *Pico Technology PicoScope 4424* oscilloscope. At the operative laser intensity of 5mW, the resolution of the continuous sweep measurements is constrained by the slowest sweeping speed of the laser (1 nm/s) and the mid-gain bandwidth of the Ge-detector, which gives a theoretical resolution of 0.03 pm. In most of the measurements, the resolution is set to 1 pm by choosing a sweeping speed of 10 nm/s at a sampling frequency of 10kHz. Since the typical spectrum is acquired over the whole bandwidth of the laser (~ 100 nm) each measurement takes ~ 10 s, over which the thermal conditions of the sample are considered stable. While the laser power output is well stabilized by the internal control feedback over the whole bandwidth for the used output power of 5mW, the spectral response of the whole measurement system, coupled fiber-to-fiber, was acquired daily to obtain a "blank" reference for the transmission data normalization. It's worth to note that the blank reference spectrum is not required for the determination of the propagation losses, but it is needed for an accurate estimation of the fiber-to-chip insertion loss. Furthermore, the "blank" transmission varies slowly with respect to the wavelength, and therefore it is not essential for the measurement of fine spectral features.

The *Tunics T100S* laser wavelength is internally referenced with a (nominal) accuracy of 30 pm, with a repeated precision of 5 pm. In fact, repeated measurements of the same spectra exhibit shifts within the specifications. It is however important to note that this repeated measurement shift affects rigidly a single-sweep data acquisition, meaning that the spectral distances measured within the same spectrum result unaffected, and therefore limited only by the resolution.

This experimental setup will be used, in all of the following chapters to determine the linear response of the system with slight variations specified from time to time, with the notable exception of Chapter 3, where a different setup is used. In the next chapter, this experimental setup will be used at large to measure the propagation loss of light within the circuit and the spectral response of each of the photonic components that constitute the cavity of the laser.

Chapter 1

Heterogeneously integrated laser

1.1 Introduction

While it is not the first step in chronological order, the mode-locked hybrid silicon laser is the first logical step of the SiQuro project. Project SiQuro contemplates a high power pulsed laser operating at a wavelengths near 1490 nm, integrated in the PIC.

An integrated source is indeed the first fundamental building block towards the realization of a Photonic Lab-On-Chip. An integrated and stable laser source is indeed required for most applications, from data-communication to sensing, in particular when non-linear optical processes are involved.

The lack of lasing within silicon itself has fostered the research of other integrable and silicon-compatible materials. Group-IV elements, Ge in particular, has offered promising results, as integrated germanium lasers have been demonstrated. [28, 42, 43]. Another technology that has been propelled by the need of an integrated source is the heterogeneous integration of III-V semiconductors. Hybrid integration of III-V materials has been proven as an alternative solution to group-IV materials, which is still offering cost-effective solutions for on-chip light sources. Indeed, some direct-gap III-V semiconductors, such as GaAs and InP offer highly efficient light emission properties. In this approach, III-V semiconductor dies containing active regions, such as a Multilayer Quantum Well (MQW) or Quantum dots (Qdot), are bonded on the SOI wafers containing the PIC, providing an active material layer on top of the photonic circuit [44, 45, 46, 47, 48, 49, 50]. Then, the III-V substrate is removed and the active layer is processed adding the metal components necessary to inject current in the active region and provide optical gain. Working laser devices exploiting wafer bonding of III-V materials have been demonstrated using two main approaches: (i) the light is mainly guided in the SOI layer and interacts evanescently with the active material [44, 47] or (ii) the light is transferred from the SOI layer to the active layer through some coupler system, achieves gain propagating in the inverted region, and then is coupled back into the SOI layer [45, 48, 49].

III-V active materials

Bonding techniques

The first technique requires a very thin bonding layer (<5 nm) in order to have consistent overlap between the evanescent tails of the mode in the SOI waveguides and the active region. Such a thin bonding layer could be realized by using direct bonding technique, which requires a CMP step to planarize the structured surface of the SOI circuit [51].

The second technique has less stringent requirements on the bonding layer thickness ($\sim 30 \div 150$ nm), as the bonding layer acts as the gap in a directional coupler between the SOI and the III-V waveguide structures. While direct bonding trough silicon oxide is still possible also in the second case, the increased thickness tolerance on the bonding layer enables the possibility to utilize other bonding techniques with less stringent constraints. Polymeric bonding using DiVinyl-tetramethyldiSiloxane BenzoCycloButene (DVS-BCB) has been demonstrated as a valid alternative [52, 53, 48, 50] . In this case, a layer of BCB polymer is spin-coated on top of the SOI surface, acting as a glue between the silicon wafer and the III-V dice. The self-planarizing properties of spinned BCB make further CMP processing of the SOI circuit redundant, lowering the process cost and constraints.

1.1.1 Mode Locked Laser

The realization study of the laser is based on the polymer bonding of the active material over an SOI wafer containing the PIC. The device design was realized in collaboration with III-V Lab (France) [54] where a similar device has already been fabricated [49]. The active region, realized by III-V Lab, consists of InGaAsP MQW epitaxially grown on the InP substrate.

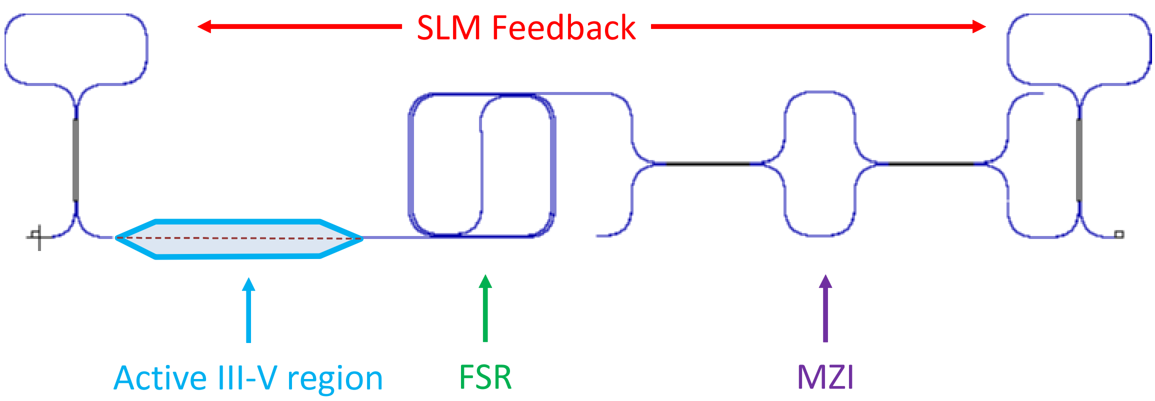

Figure 1.1: Schematic of the laser, under kind permission of III-V labs. The resonant cavity is created by two Sagnac Loop Mirrors (SLM) (red). The active region (cyan), vertically coupled to the underneath silicon waveguide, provides emission and amplification. The allowed bandwidth, tailored by a Mach-Zhender interferometer, is shaped into a comb of peaks through the FP cavity. The optical path (green) determines the Free Spectral Range.

The fabrication of a laser requires a few building blocks: emission, feedback and amplification. In order to achieve pulsed lasing, further steps are required because many phase-locked modes must be present at the same time. Therefore a comb of phase-locked peaks is needed.

Figure 1.1 provides a sketch of the photonic circuit. The emission and amplification are achieved in the III-V material (cyan), while the other components are integrated in the SOI wafer. Under the III-V material region there is a thinner waveguide which is coupled with the III-V material with inverse tapers both in the silicon waveguide and in the III-V material similarly to [53]. The feedback system is provided by (red) two mirrors at the extrema of the PIC. While Distributed Bragg Reflector mirrors may be used, realizing them in silicon would require a low-pitch resolution (∼240 nm) due to the high refractive index. A valid alternative is provided by Sagnac Loop Mirrors (SLM)that allow to obtain precise and tunable reflection coefficients with relaxed constraints on the lithography [55]. The two SLM form a Fabry-Perot (FP) cavity, (green) the path of which is set to have the desired Free Spectral Range (FSR), which determines the repetition rate of the laser emission. The shaped bandwidth is tailored by a Mach-Zehnder interferometer (purple) that permits mode-locking over a restricted number of FP resonances. The test circuit is terminated with inverse tapers. Inverse tapering is important during the testing phase to reduce the spurious FP resonances that are formed by the waveguide facets, and to reduce the insertion losses. Due to the lithography resolution, however, the inverse tapering cannot be realized with the desired shape reducing the waveguide width down to zero. Based on the tests that have been performed during the thesis work, the inverse tapers could be reduced down to a width of 250 nm maintaining a correct shape within our resolution, meaning that the facet reflection is not completely avoided.

While in this simplified scheme the amplification block is summarized in the active III-V region, the reflectance of the SLMs and the propagation losses in all elements need to be considered. Indeed, low propagation losses in the SOI circuitry are of paramount importance in order to achieve overall gain. To achieve lasing, the gain must exceed the total losses. In a FP cavity of length L, with mirror reflectance coefficients R_1 and R_2, loss coefficient α and gain coefficient G over the length L_{gain} the propagation losses condition for laser threshold is

$$\alpha \leq G\frac{L_{\text{gain}}}{L} - \frac{\log(\mathrm{R_1R_2})}{2L}. \tag{1.1}$$

Similar devices in 220mm thick and 500nm wide SOI channel waveguides have been demonstrated recently, exhibiting propagation losses as low as 2 dB/cm by using a 248 nm wavelength lithography [56]. In fact, the main loss channel of an integrated waveguide is the lateral roughness produced by the RIE etching process. The overlap between the optical mode and the rough waveguide sidewalls may be reduced by realizing rib waveguides, as shown in Fig. 1.2.

Rib waveguides are obtained by a partial etch of the guiding material layer, obtaining a structure that may be described as a planar slab waveguide plus a strip of the same material. Depending on the remaining slab thickness, the modes guided inside the rib waveguide have ha significant portion confined in the slab. The confinement within the slab means that the mode has a lower overlap with the shallow sidewalls, resulting in overall lower scattering losses. Additionally, the mode extension in the lateral direction inside the slab allows to realize coupling schemes with larger gaps, which are compatible with a 400 nm lithography.

The used rib geometry, reported in Fig. 1.2, consists in a 500 nm thick SOI layer, partially etched for 200 nm. The result, is a silicon slab waveguide with a thickness of 300 nm that ensures the vertical mode confinement. The remaining strip of silicon, that protrudes for 200 nm on top of the slab, ensures the confinement in the lateral direction. Compared to the channel waveguide case, the optical field shape results stretched inside the silicon slab, reducing the mode overlap with the shallow sidewalls. Furthermore, the lateral extension of the mode inside the slab allows for more relaxed constrains for the gaps between waveguides, permitting the realization of directional

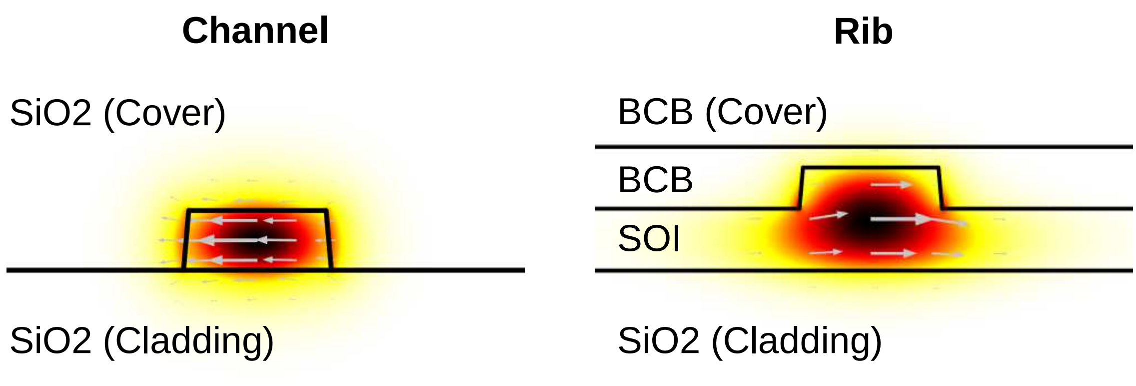

Figure 1.2: Normalized field intensity inside a (left) channel and a (right) rib waveguide for the fundamental TE1 mode. In the channel waveguide the field is strongly confined within a small area, so that the intensity on the lateral surface of the waveguide is strong. In the rib geometry, on the other hand, the light is confined within the much larger silicon slab and only a small fraction of the field touches the shllow waveguide lateral edges.

couplers with coupling length in the order of tens of microns using gaps in the order of 650 nm, well above the critical dimension of the lithography.

The III-V processing is carried on by III-V Lab, with which I collaborated. The photonic circuitry design was carried on in collaboration with III-V labs, while all of the SOI fabrication and the bonding process are realized in FBK. I collaborated with III-V labs in realizing the photonic design, while the fabrication of the SOI circuitry has been carried on entirely by me and my supervisor, Mher Ghulinyan, in the CR of CMM, FBK. I carried on all of the optical passive characterization and analysis of the circuitry in the NL laboratory of UniTN.

1.2 Waveguide design and simulation

The primary tasks for the waveguide design are low propagation losses under the conditions of single mode operation. Once the waveguide typology (RIB) and the substrate (SOI 500 nm) are decided, the waveguide width becomes the setting parameter. To reduce the propagation losses, a large waveguide is desirable, as the mode overlap with the sidewalls is a decreasing function of the waveguide width. On the other side, the single mode operation condition limits the usable width to the value where the second order mode begins to be guided. In the meanwhile, attention should be posed to the mode dispersion, that should be made as flat as possible to permit the phase-locking of the laser modes.

VASE characterization

Computational simulations featuring a full-vectorial Finite Elements Method (FEM) were used to simulate the modal dispersions n_{eff} and n_g of the structure as a function of waveguide width and wavelength. FEM simulations require knowledge of the (complex) bulk refractive indices of the materials in the simulated spectral range. The characterization of each material refractive index was performed with Variable Angle Spectroscopic Ellipsometry (VASE). The working principle of the VASE is much similar to that of a standard interferometer, with the difference laying in the fact that the reflection spectra of the samples are acquired at different angles and

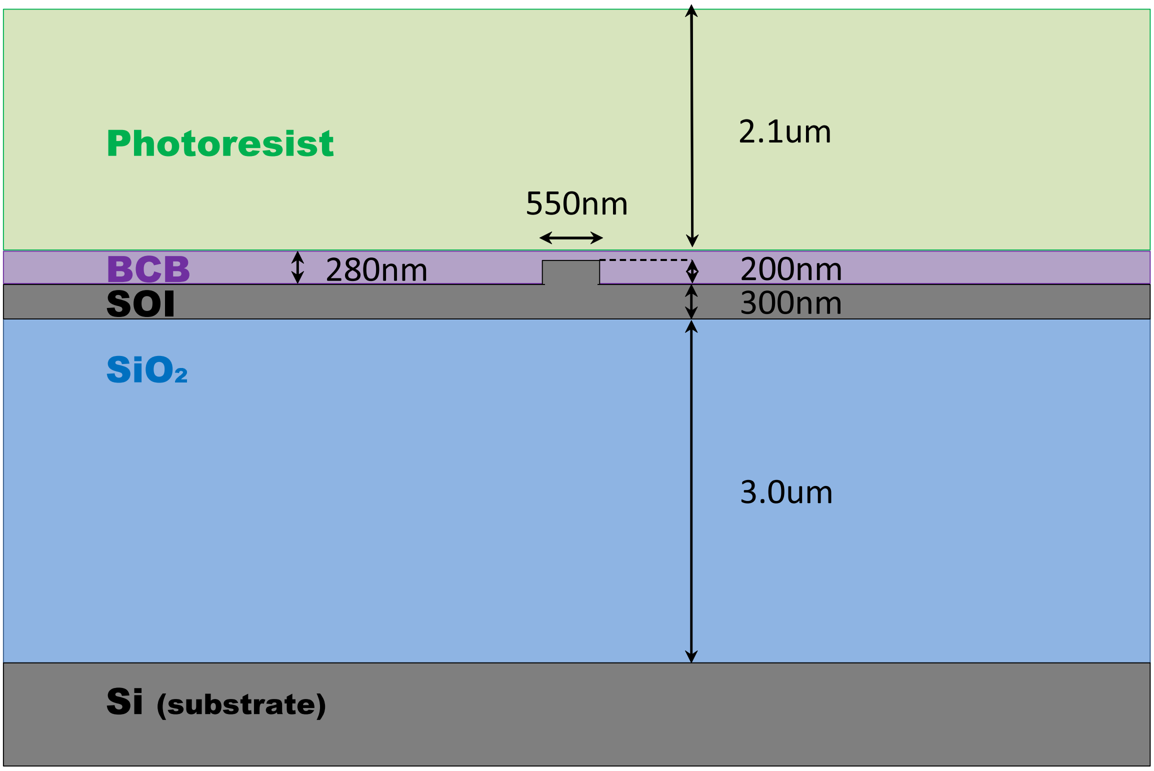

Figure 1.3: Schematic cross section of the used rib geometry (RIB500). The waveguides are obtained with a 200nm RIE on a 500nm SOI with a box of $3\mu m$. The structures are then covered with BCB polymer for bonding, and photoresist polymer for further protection.

with different polarizations. The added degrees of freedom allow to fit both the film thickness and refractive index dispersion at the same time. The reader interested in the details of the VASE technique may refer to [40]. The measured dispersions for the materials of interest are reported in Fig. 1.4.

The computational simulations have been performed with a commercial software [57] using the material dispersions obtained from the VASE measurements. Convergence with respect to mesh finesse and simulative box dimension with scattering boundary conditions was performed to ensure the simulation's reliability on a rib waveguide, as shown in Fig. 1.3. The laser should operate in the fundamental Transverse Electric mode TE1. To determine the geometrical parameters of single-mode operation the effective index of the fundamental and second TE modes TE1 and TE2, and the fundamental TM mode of the waveguides were investigated as a function of both waveguide with wg_w and wavelength λ. The obtained effective refractive indices, reported in Fig. 1.5 a) were then used to compute the group index using Eq. 0.6, reported in Fig. 1.5 b).

Figure 1.6 shows two cross sections of Fig. 1.5 at fixed values of wg_w=390 nm and wg_w=550 nm. The effective refractive index of the modes decreases steadily as a function of the wavelength as expected for fixed slab and rib sizes, which are comparable with the wavelength. The effective index for $wg_w = 550$ nm varies by less than 0.05 along the whole spectral range. The steady derivative compensates the effective index dispersion, flattening the group index, that varies of ≈ 0.025 over the whole investigated spectral range. The TE2 dispersion of n_{eff} and n_g calculated at the two waveguide widths coincide, demonstrating that these are slab modes, not affected by

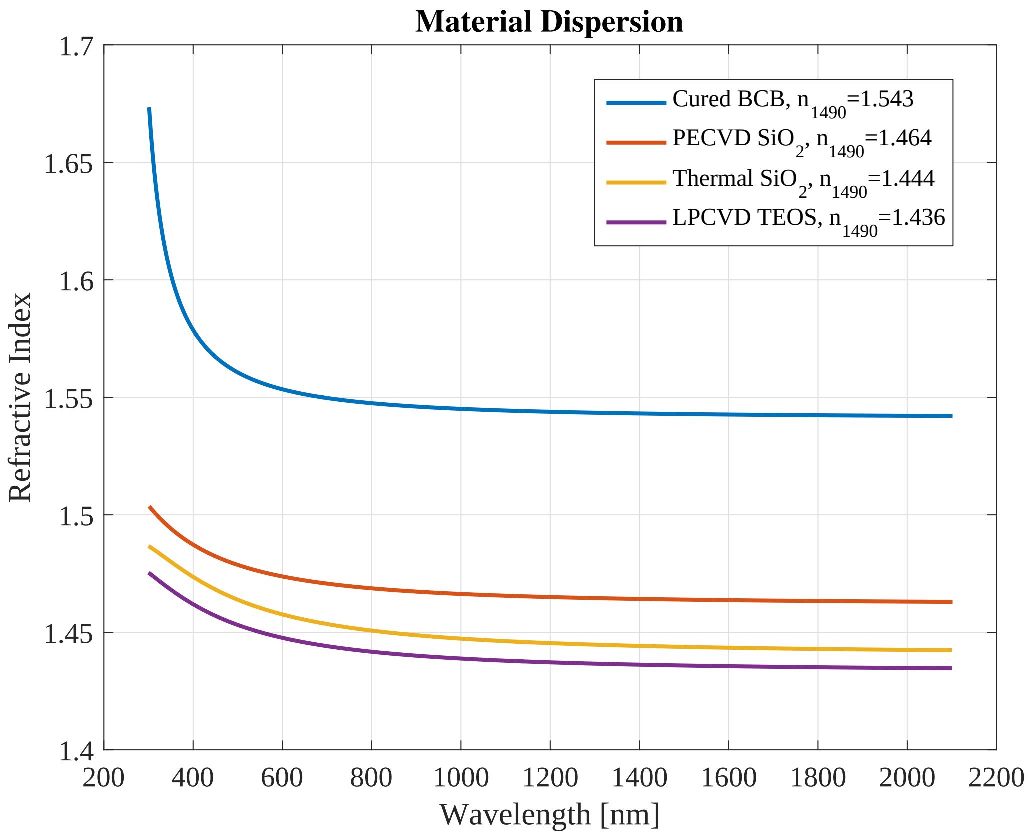

Figure 1.4: Bulk index dispersion of the used materials, fabricated in the FBK facility, measure with VASE.

the rib region. The TM1 modes are similarly not guided in the rib for the selected values of wg_w, and therefore omitted.

Figure 1.7 reports cross sections of Fig. 1.5 for fixed values of wavelength $\lambda_0 = 1490$ nm and $\lambda_0 = 1550$ nm for the TE1, TE2 and TM1 modes. The refractive index of the TE1 mode steadily increases as a function of wg_w, as the mode is more confined inside the silicon rib. The effective refractive indices of the TE mode is substantially constant as a function of the waveguide width, with only a slight increase towards the higher wg_w values. The TM1 modes begin to be guided for wg_w values above 620 nm at $\lambda_0 = 1490$ nm, rapidly growing in n_{eff} value after this point. Notably, the simulated n_{eff} of TE2 has a small artifact discontinuity in correspondence of the wg_w value at which the TM1 mode becomes guided. This effect is due to the fact that the TM1 mode dispersion crosses the one of TE2, causing a jump in the simulated n_g.

The cross sections of the group index of Fig. 1.5 at fixed values of wavelength are reported in Fig. 1.8. The group index of the TE1 mode varies slightly as a function of the wg_w, with a smooth maximum around $wg_w = 550$ nm. The group index of the TE2 mode is substantially flat up to 800 nm, where the mode begins to be confined within the rib rather than diffused in the slab. The bump that is present around 650 nm is an artifact due to the TM1 crossing shown in Fig. 1.7. The TM1 mode, that begins to be confined for $wg_w > 650$ nm, exhibits a higher group index due to the higher derivative with respect to the wavelength.

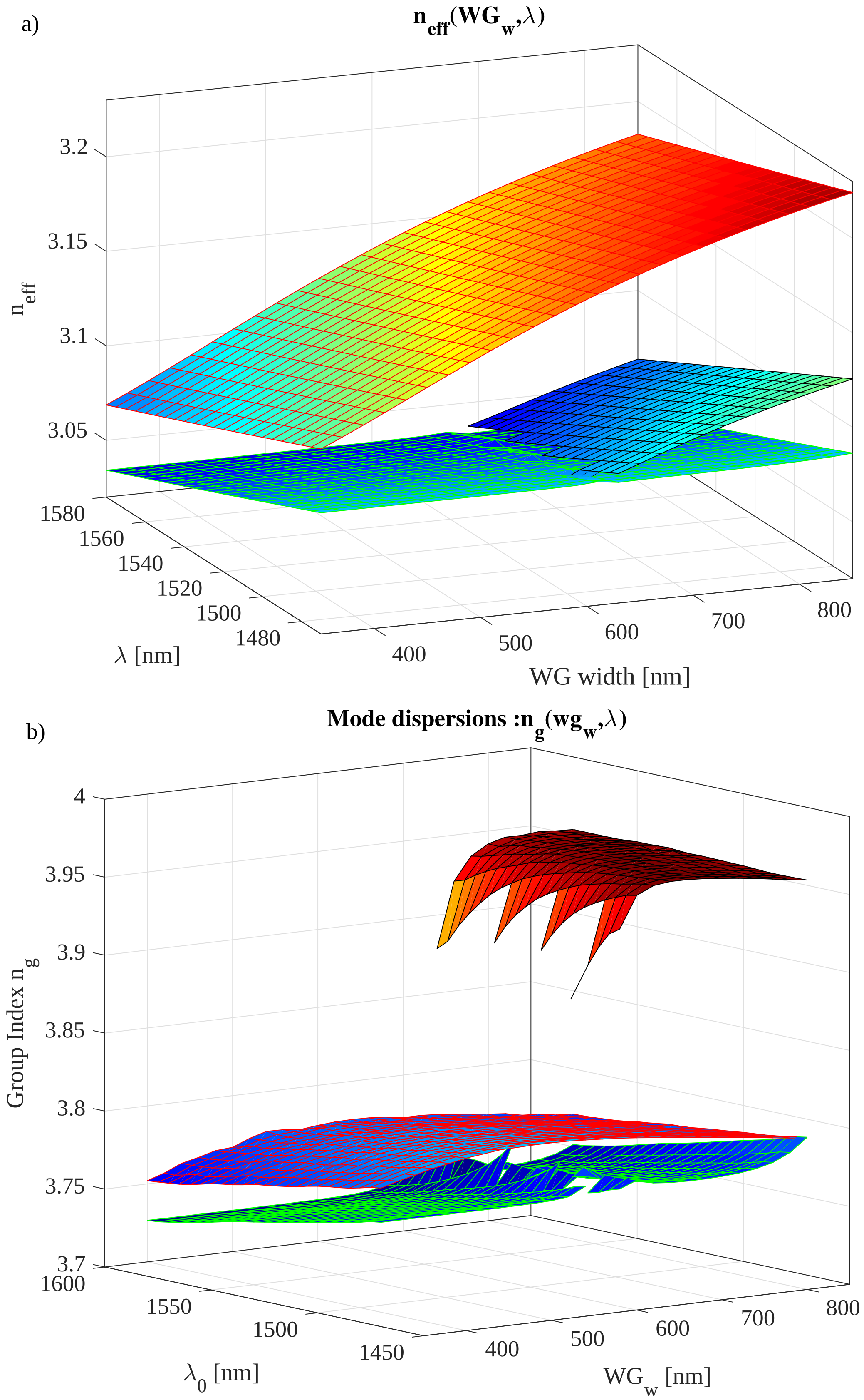

Figure 1.5: 3D plot of the a) n_{eff} and b) n_g dispersions as a function of waveguide width and wavelength, summarizing the results of the simulations. The surface color is proportional to the dispersion, while the grid colors red,black and green are for TE1,TM1 and TE2 modes respectively. The missing points on the TE2 n_g surface were affected from a computational artifact due to the TM1 crossing and removed to avoid confusion.

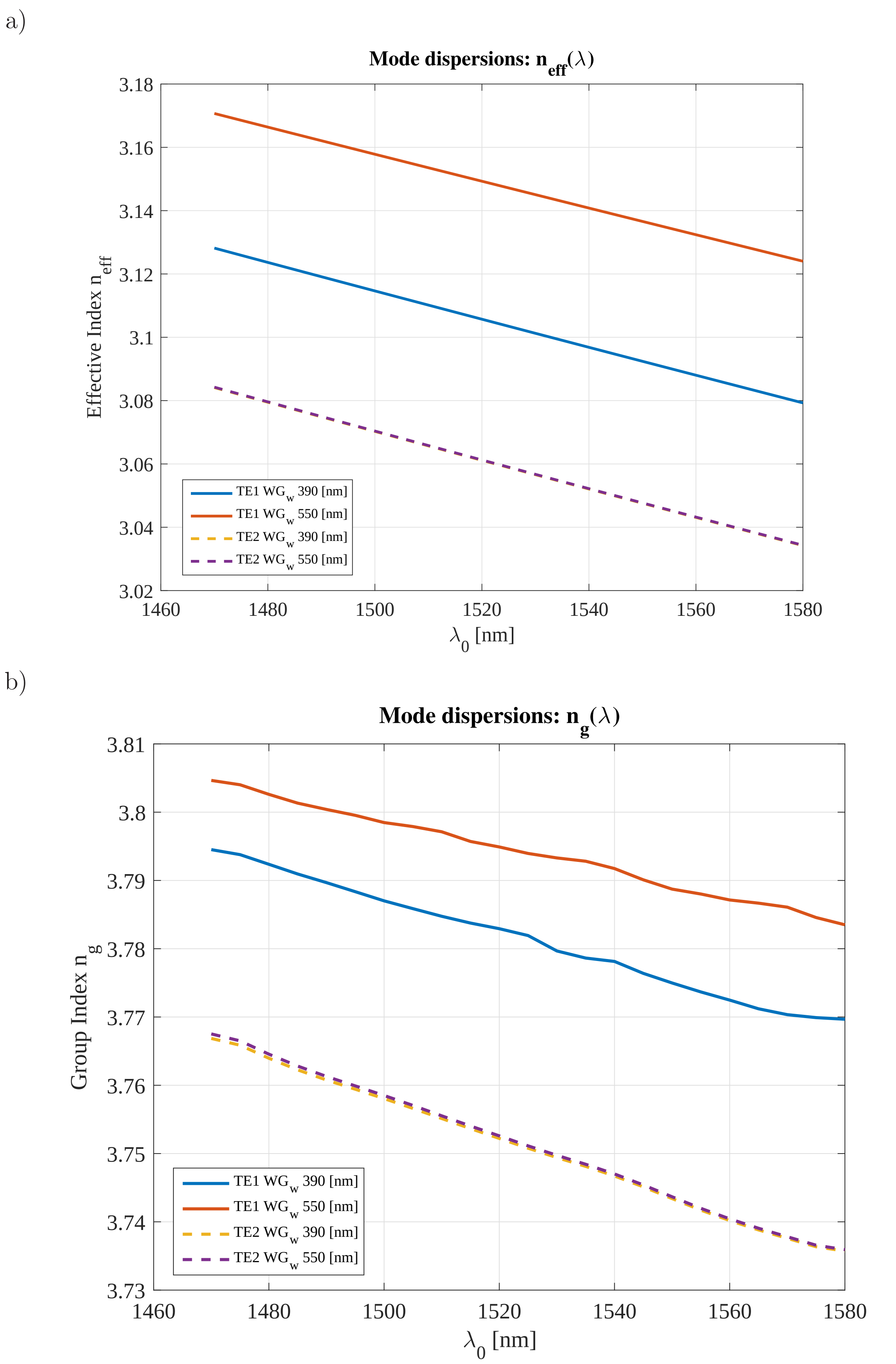

Figure 1.6: Modal dispersions a) n_{eff} and b) n_g as a function of wavelength in the range 1460nm-1580nm for sample widths of 390nm and 550nm. The dispersion of the TE1 mode for the two rib widths coincide, demonstrating that the mode is not confined in the rib and is therefore unaffected by its width. The TM1 are similarly not guided and omitted. The simulations give a value for n_g of 3.8 at 1490 nm for the waveguide width value of 550 nm.

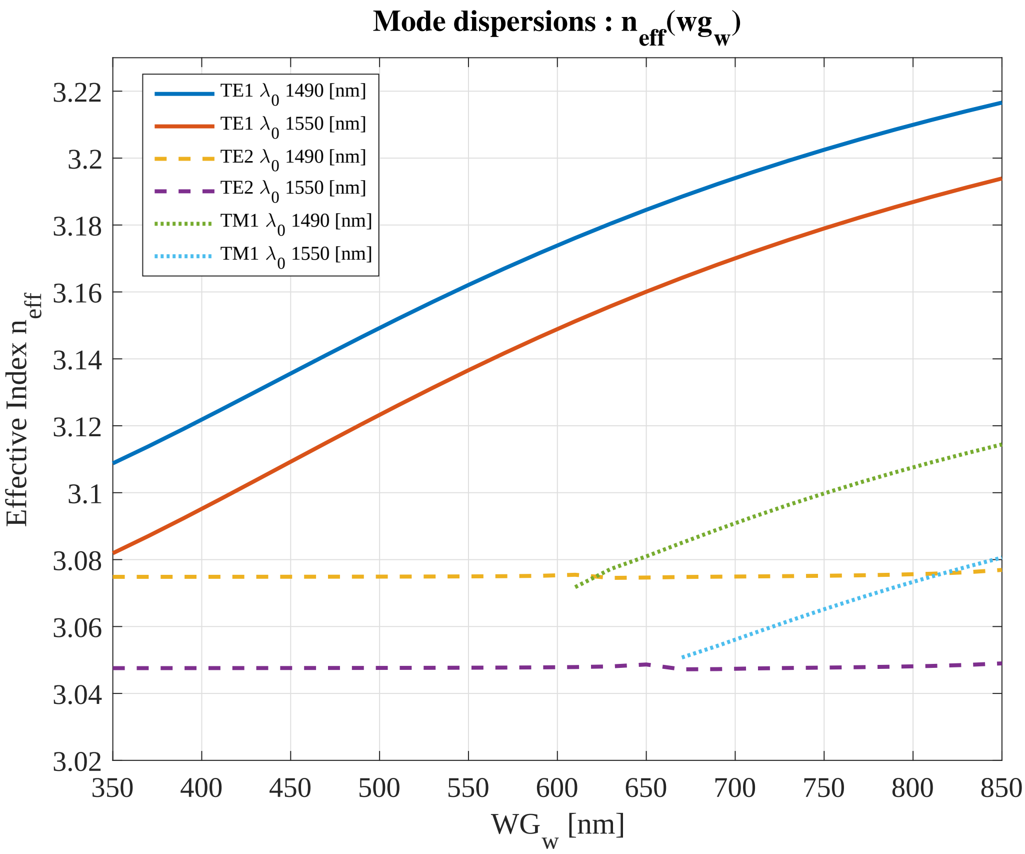

Figure 1.7: Simulated effective refractive indices for TE1, TE2 and TM1 modes in the RIB500 structure as a function of the waveguide width in the range 350-850 nm for the wavelengths of interest 1490nm and 1550nm. For widths below 600nm only the TE1 mode is confined within the rib waveguide, while other TE and TM modes are present as slab modes. For widths above 600nm the TM1 mode begins to be strongly confined, as it can be seen by his rapidly increasing effective refractive index, crossing with the TE2 mode dispersion. The TE2 mode remains as a slab mode with a node in the waveguide center, slightly bending upwards near the edge of the simulation window.

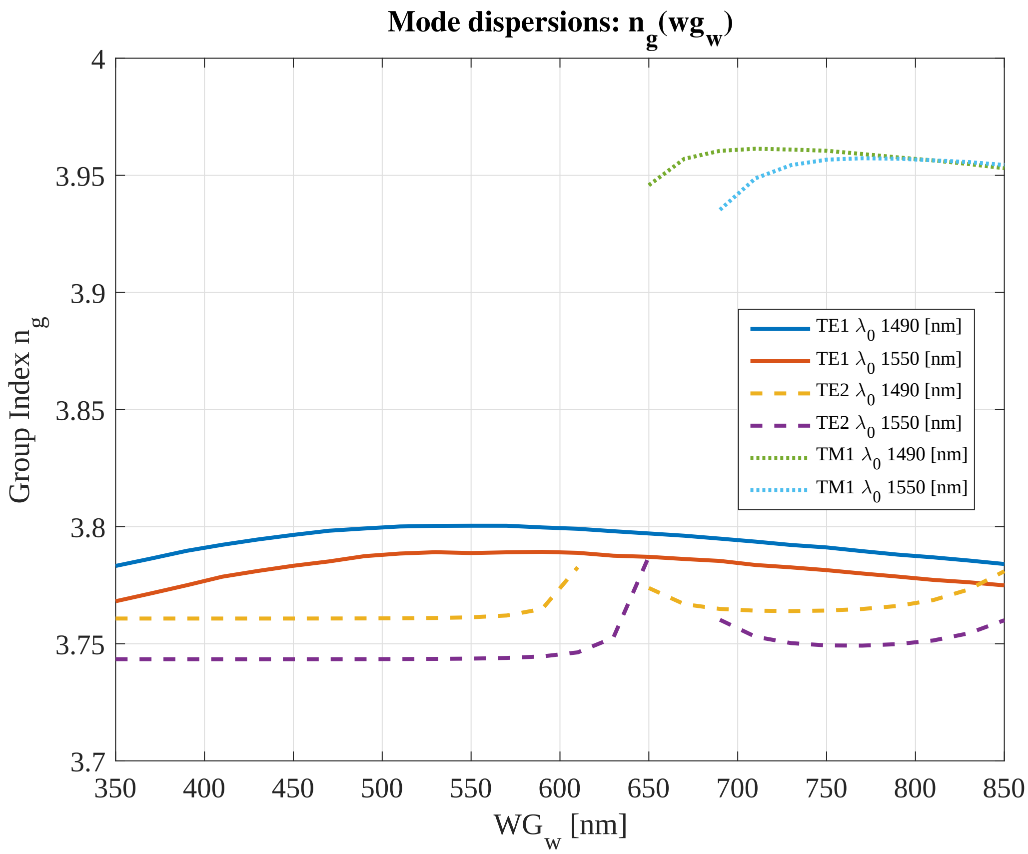

Figure 1.8: Group index dispersions n_g calculated from the simulated n_{eff} show that the TE1 mode has a flat region (with respect to the wg_w) slightly around 550nm, making this value robust against fabrication tolerances. Here the mode crossing among the TE2 and TM1 mode is visible as two bumps in the group index

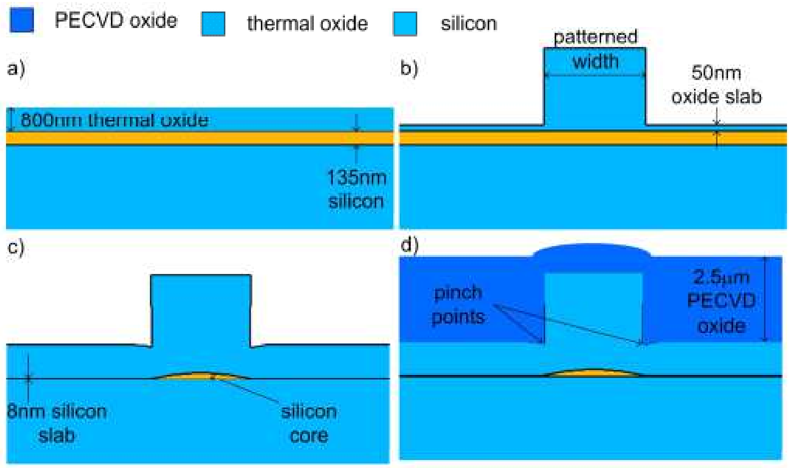

Figure 1.9: Waveguide definition through silicon oxidization results in an exceptionally smooth surface at the cost of a poor control over the waveguide shape. Image taken from [58].

1.3 Waveguide Fabrication

The original surface of the SOI wafer can be exceptionally smooth, with values of roughness as low as $\sigma \sim 0.15\ nm$ for Chemical Mechanical Polished (CMP) wafers. However, the definition of the structures with RIE induces roughness on the sidewalls of the structures, that produce scattering. This brings up a huge issue for SOI waveguides, that present a high refractive index contrast with the typical silica cladding, inducing sensible propagation losses.

To reduce the scattering losses different approaches are possible: the waveguide may be designed to lower the overlap of the optical mode with the waveguide, the index contrast with the surrounding cladding may be reduced and the sidewall roughness may be reduced, for example the waveguide may be realized by oxidizing the silicon instead of etching it [58]. In the last case, various techniques can be used to oxidize the silicon. The most used are dry and wet high temperature oxidization, which exploit the diffusion of oxygen or aqueous vapor. In this case, the silicon surface is oxidized by the high temperature gas, forming a silicon oxide layer with a native interface. The oxidization rate decreases rapidly as the silicon oxide grows thicker and the diffusion of the oxidizing agent is slowed. An example is shown in Fig. 1.9 (from [58]), where the waveguide pattern is transferred to the silicon from a thick oxide layer that acts as a diffusion barrier. While these technique produces waveguides with very low propagation losses (0.5 dB/cm for $wg_w \sim 1.5\mu$m), it features a costly high temperature oxidization process and results in shallow waveguide profiles.

Smoothing the roughness

In 2005 Sparacin & al. [59] proposed a new approach: the waveguide is realized with standard techniques, and then smoothed in a second moment via wet-etching in aqueous solution. The proposed technique exploits the different surface curvature of defects on the waveguide surface to oxidize the defects faster than the flat surface, thus achieving smoothing. This smoothing phase, driven by the chemical potential, is limited to an oxidization of few nanometers. As the silicon is oxidized the oxide grows on the surface acting as a barrier for the reaction. The oxide growth slows down the oxidization process into a diffusion-limited stage, which is no more roughness-selective. A big advantage of this technique is that it may be performed using the common RCA cleaning, always available in all CMOS fab.

RCA cleaning

RCA cleaning is a standard procedure in silicon manufacturing that is used to clean the surface of silicon during the processing [60]. The procedure is performed in three steps, interspersed by DI water rinses to remove the residual chemicals. The first step, called Standard Cleaning 1 (SC1), consists of a wet chemical etching in a bath composed of DI H_2O, H_2O_2 and NH_4OH in a $5:1:1$ ratio at 70°C for ten minutes. SC1 aims at removing organic contaminations and small particles. After RC1 a thin layer of silicon oxide is formed on top of the silicon. After the rinse, the oxide layer may be removed with a HF dip in diluted and/or buffered hydrofluoric acid at room temperature, that constitutes the second step. The third step, called Standard Cleaning 2 (SC2), consists of a wet chemical etching in a bath composed of DI H_2O, H_2O_2 and HCl in a $6:1:1$ ratio at 70°C for ten minutes. This step aims at removing residual metals from the surface and at creating a protective layer of hydrous oxide at the surface.

Using the standard times (ten minutes for both SC1 and SC2) about ~ 5 nm of silicon is consumed during the RCA cleaning. In principle the time of each step could be increased, but in order to maximize the etching in the dynamic-driven regime it is better to repeat the cycle a number of times, so that at no time the oxide is thick enough to achieve diffusion-driven oxidization.

In the present work, the waveguides are fabricated using the process shown in Fig. 1.10. The device pattern is transferred to the SOI layer using a lithographic process and then RIE is used to remove the excess material. Then, the RCA smoothing technique is used to smooth the waveguides, repeating the process 3 to 5 times. Furthermore, due to its well-determined silicon consumption, the process is also used to fine-tune the lateral dimension of the waveguides by adding further cycles to slightly etch the sidewalls if necessary.

Hard Masks

While the smoothing process improves the lateral surfaces of the waveguide, the top surface of the waveguide, smoothed with CMP, has already a very low roughness of the order of $\sigma \sim 0.15\ nm$. The smoothing process has a lower limit of roughness, which varies between $\sigma = 0.2 \div 0.8$ nm, depending on the actual concentration of NH_4OH in the SC1 bath [59]. This kind of roughness is greater than the native one, and therefore unnecessary RCA treatments of the top surface should be avoided. Furthermore, it is often desirable to maintain the initial SOI thickness, whilst the smoothing process etches out $15 \div 25\ nm$ depending on the number of cycles.

In order to protect the top surface, a Hard Mask (HM) is commonly used. The HM is a layer upon the SOI that protects it during the processing. A process involving a HM is characterized by a selectivity parameter. The selectivity of the process is the ratio between the etching rates of the protected material and that of the HM. More formally, for a HM of material m_1 protecting a layer of material m_2, the selectivity of the process A for the material m_2 with respect to the material m_1 is the ratio of the etch rates (ER) $s_A(m_2, m_1) = ER(m_2)/ER(m_1)$. The photoresist itself, in a broad sense, is a HM. The photoresist, indeed, has an extremely high etching rate in the development process (the reacted photoresist is rapidly dissolved) and a relatively low etching rate during RIE attacks, thus offering protection to the underneath silicon.

The primary objective of the HM is to protect the underneath material during all the etching process. Therefore, the HM should be thick enough so that it survives to the end of the etching. The minimum HM thickness HM_h required to realize the etching can be calculated as a function of the etch rates ER(HM) and ER(l) of the HM and

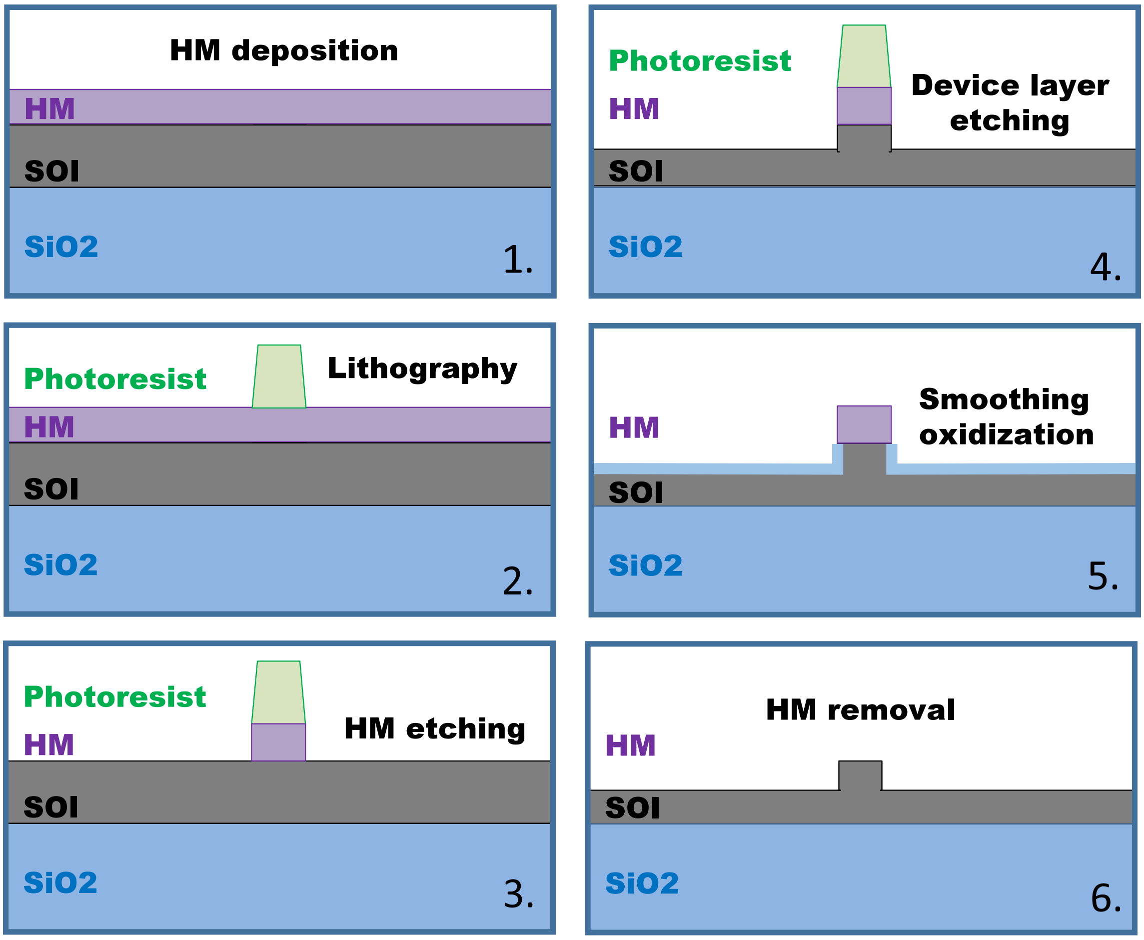

Figure 1.10: Process flow for the realization of the devices. The SOI layer is covered with a HM layer and then with photoresist, that is patterned using stepper lithography. The pattern is transferred from the photoresist to the HM using RIE, and then again from the HM to the SOI using RIE. After the pattern definition, the photoresist is removed and the structures are smoothed using wet chemical oxidization. The oxide layer and the HM are then removed, leaving bare the smoothed structures.

the layer respectively, and the etched layer thickness l_h as

$$HM_h = ER(HM)l_h/ER(l). \tag{1.2}$$

In principle, following Eq. 1.2, any HM is viable for direct silicon etching, provided a sufficient HM thickness. This is true even in processes where the selectivity coefficient is smaller than one, that is, even when the photoresist is etched faster than silicon, as long as the HM is made sufficiently thick. In this case of poor selectivity, however, another problem will arise: the etching will produce very angled edges, as shown in Fig. 1.11 a) where the selectivity is $s_A = 0.4$. The photoresist walls, indeed, are slightly angled, as shown in Fig. 1.11 a-d). Due to the photoresist sidewalls angle $\alpha_1 \sim 80°$ the photoresist edge will retract during the etching process, as the foot of the photoresist is etched. This retraction progressively uncovers the underneath layer, resulting in an angled surface as well. The angle α_2 that is transferred in the etched material may be calculated by geometrical considerations as

Etching angle

$$\alpha_2 = \text{atan}\left(\frac{ER_2}{ER_1}\tan(\alpha_1)\right) = \text{atan}\left(s_A \tan(\alpha_1)\right). \tag{1.3}$$

In standard processes the selectivity of silicon with respect to the photoresist is $s_A > 1$, and therefore the sidewall angle is brought closer to 90°passing from the photoresist to the silicon following Eq. 1.3 as shown in Fig. 1.11 b). The sidewall angle may be further increased by inserting an intermediate layer, usually of glass material, that constitutes a proper HM with a more favorable selectivity. An example, featuring TEOS as the HM material, is shown in Fig. 1.11 c) where the final sidewall angle of the silicon structure is increased to 89°. In this case two etching processes are needed: one on the HM and another on the device layer. The different etching rates in the two processes is be exploited to bring the silicon walls angle closer to 90°. The material should be chosen with a high selectivity with respect to the photoresist during the HM etching process, as well as a high selectivity of the silicon with respect to the HM material during the device layer etching process. The thickness should be chosen such that none of the HM layers (the photoresist and the glass material, in this case) is consumed completely during the device layer etching, to avoid the propagation of secondary angle fronts in the HM layers.

WP1_P1

A fist preliminary process, named WP1_P1, was realized with a HM of 150 nm thick LPCVD TEOS oxide, which was deposited on the 500 nm SOI wafer. The mask layout of the process, shown in Fig. 1.12, contains test structures and folded waveguides of different length. The thickness of the deposited materials was verified with interferometric or VASE technique at each step. A test layout was transferred to the spin coated OIR photoresist with stepper lithography. After the developing and hard baking of the patterned photoresist the quality of the lithography was assessed by systematic SEM analysis on the waveguides widths. These were adjusted with a soft oxygen plasma etching, that also has the effect of trimming the residues of photoresist near the foot of the patterned structures.

The standard deviation of the waveguide width values was very high during the first tests ($\sim$ 30 nm), and has been improved in the following processes. Then, the HM was etched down to the silicon layer using a DRIE process.The c-Silicon was etched with RIE for 185 nm in order to achieve the desired depth of 200 nm once three cycles of RCA smoothing were applied. A sketch of the cross section is reported in Fig. 1.11 c).

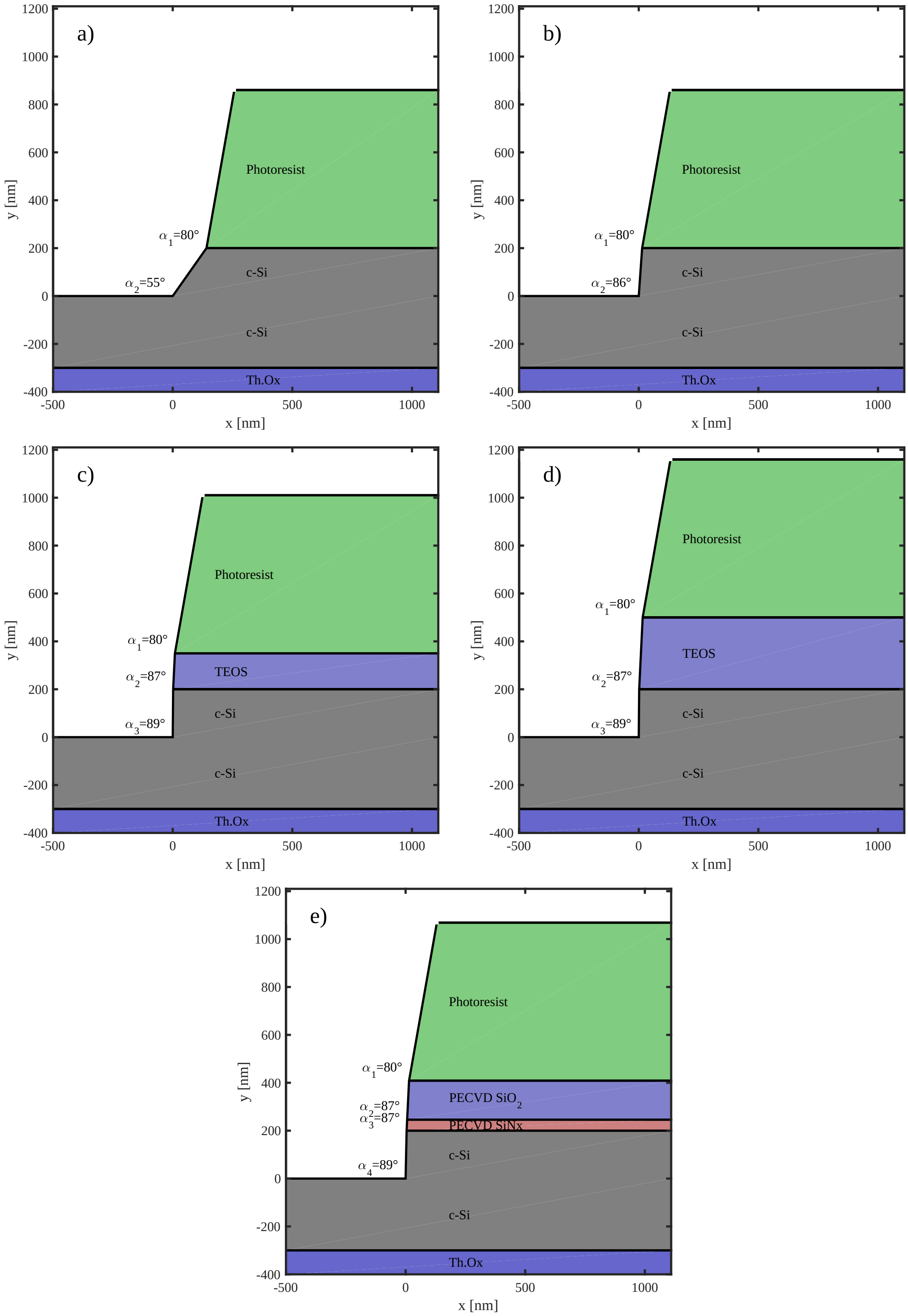

Figure 1.11: Etch profiles of various HMs, simulated using Eq. 1.3. The axes have been kept in scale to maintain the proportions. (a) processes with a poor selectivity result in shallow sidewalls. (b) in standard processes, the bare photoresist may be used directly to pattern the device layer. (c) using a mask of a hard material, as PECVD silicon oxide, the sidewall angle of the device layer may be brought closer to 90°. (d) a thicker HM does not change the final angle, but is expected to improve the waveguide smoothness. (e) the HM may be realized by different materials, realizing an anti-reflection coating.

a)

b)

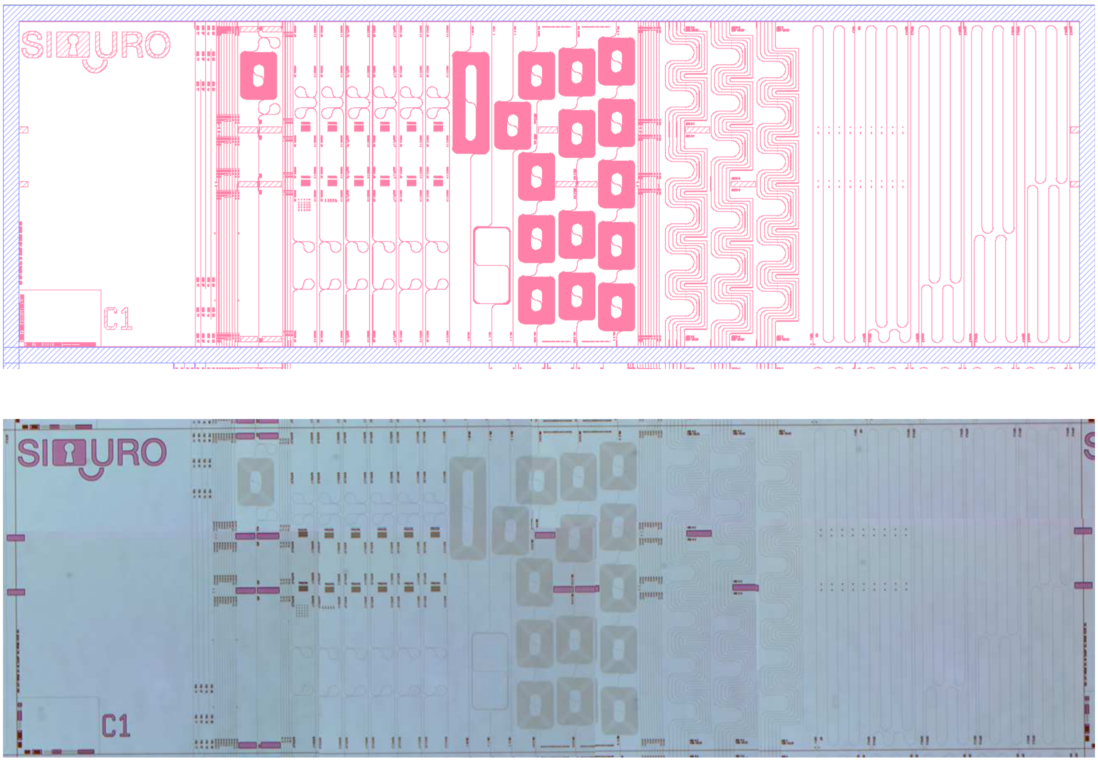

Figure 1.12: a) layout of the first test mask with b) an optical imaging of a realized device. The structures realized to measure the propagation losses are on the far right.

Dimension control

Dimension control on the structures is realized by statistical analysis on SEM images at different stages of the processing. The dimension of the structures is acquired after the photoresist pattern definition, then pattern transfer to the HM, and finally at the device layer stage before and after the RCA smoothing cycles. For each stage, SEM images of the critical structures are acquired on a grid on each wafer, resulting in a number of images in the order of $\sim 10^2$ per stage, in each process. During the thesis work I developed a dedicated software routine to systematically extract the dimensions of waveguides and directional couplers from the SEM images. An example of the waveguide dimension mapping is shown in Fig. 1.13.

In a typical SOI process, a test lithography is realized on a blank silicon wafer first. The width of the structures patterned in the photoresist is then measured with SEM imaging, and adjusted as needed by trimming in oxygen plasma or soft baking. There are many critical parameters in the lithography resolution. The flatness of the surface, in particular, is important to obtain homogeneity of focus. Indeed, the wafers may be not completely flat for a number of reasons: inhomogeneous layer deposition, stress layers that cause the wafer to bow, and the presence of particles, that hinder the correct positioning of the mask. Sometimes, due to the presence of different multiple patterns laying on different layers on single device, the planarizing photoresist lies with different thicknesses, making it impossible to achieve simultaneous focus of the lithographic process over all of the device. Finally, both the photoresist and the etched materials may have a reflection coefficient that varies from process to process, changing the effective dose absorbed by the photoresist. Therefore, if the SEM measurements waveguide width values of the patterned photoresist are not within a range of ± 40 nm, which is adjustable after the lithography, the source of the anomaly

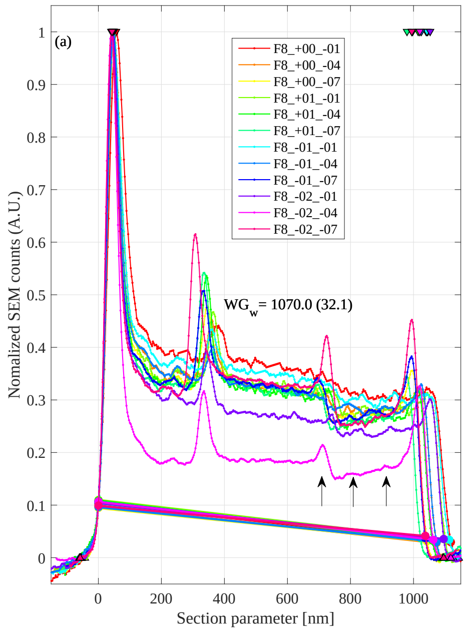

	-3	-2	-1	0	1	2	
4	b)		x	x			4
3		x	x	x	x		3
2	x	x	x	x	x	x	2
1	x	x	x	x	x	x	1
0	x	x	x	x	x	x	0
-1	x	1096.10	1114.30	1119.50	1100.80	x	-1
-2	x	x	x	x	x	x	-2
-3	x	x	x	x	x	x	-3
-4	x	1062.40	1072.90	1073.30	1059.40	x	-4
-5	x	x	x	x	x	x	-5
-6	x	x	x	x	x	x	-6
-7	x	1038.10	1037.30	1043.50	1022.10	x	-7
-8		x	x	x	x		-8
-9		x	x	x	x		-9
-10		x	x	x	x		-10
-11			x	x			-11
			— FLAT —				
	-3	-2	-1	0	1	2	

Figure 1.13: a) Waveguide section profiles extracted from the SEM images of structures from the WP1_P2. Different colors refer to measurements of the same structures in different positions over the wafer, shown in panel b). The 2D intensity profile measured by the SEM image is integrated along the waveguide direction to obtain the average sections. The routine then recognizes the background (upward triangles) and the waveguide top edges (downward triangles) so that the waveguide width may be identified and the waveguide profile normalized (colorlines). Other than the waveguide edges, other bright structures are visible on the top surface of the waveguide, as pointed by the black arrows. The most intense peak near the center of the waveguide is the edge of the oxide HM which has shrank during the BHF dips. The smaller bumps are the trace of the previous HM etching positions during the cycles, that leaved stairs in the silicon waveguide.

is investigated and action is taken, before repeating the lithography. For example, the bow of the wafers has been corrected by adding stress compensating layers on the back of the wafer. The focus issues have been addressed by realizing multiple markers to ensure correct focusing of the stepper. Some of these problems, as the simultaneous focus over structures laying on different planes could not be resolved within the CR, and an optimization at the structure design level has been realized instead. The solution to the problem of the layers reflectivity is of particular interest for this process, and will be addressed later in this section.

Once the dimensions on the silicon wafer are satisfying, the lithography is realized on the SOI process wafers. The effective dimension of the photoresist structures is again acquired with SEM imaging and adjusted if needed. DRIE is used to define the HM under the photoresist. Further SEM imaging on the HM determines the final dimension of the structures that will be transferred on the device layer. Since SOI devices will be subject to the smoothing process that consumes silicon, the structures must be adequately larger than the target dimension at this stage. Fine tuning of the lateral dimension is possible thanks to the smoothing process, that is precisely controllable thanks to its stable and slow etching rate. It's worth to note that as the multiple RCA smoothing consumes $15-25$ nm from each lateral side of the waveguide, and that the same quantity is removed from the silicon slab as well. The smoothing-associated etching is therefore considered and subtracted from the RIE process that transfers the pattern from the HM to the silicon. The etch rate is estimated on the test silicon wafer, by measuring the depth with an optical profilometer.

After the RIE process that defines the device layer, the residual photoresist is removed using oxygen plasma, as it can not be present on the wafer during the RCA cycles of the smoothing process. The dimensions of the structures transferred to the silicon layer are once again verified via SEM imaging.

The wafer are then cycled through the RCA process, eliminating the grown silicon oxide with BHF dips of 6 s. The surface roughness reduction of each RCA cleaning is limited by the NH_4OH-induced roughness . After 3-5 smoothing cycles, any further RCA cycles are used mainly to exploit the etch-rate reliability of the process as a fine tuning technique for the dimension of the structures.

Inverse taper waveguides

During the fiber-waveguide coupling, the waveguide and the fiber modes usually have a large spatial mismatch. While the waveguide has a typical dimension of 500 nm, or less in the case of channel waveguides, the minimum beam waist is 2.5μm for the lensed taper fibers used in this work. A common approach to solve this problem is to taper the end of the waveguide up to the beam waist. The tapering should be designed sufficiently long so that the mode shape inside the waveguide changes adiabatically and the losses towards scattering and higher order modes are negligible.

When the light is coupled to the waveguides it is partially reflected due to the high index mismatch between the air and the waveguide. This reflection occurs both while coupling the light from the fiber to the waveguide and vice-versa. The waveguide therefore acts as a Fabry-Perot cavity between the two facets, that form partially reflecting mirrors. While the tapered termination aids the mode-matching with the external beam, it also provides with a larger effective mode index at the interface. Due to this, the reflection at the faced is enhanced, which results in a stronger FP modulation of the waveguide spectrum.

An alternative method to reduce both the insertion losses and the facet reflection is

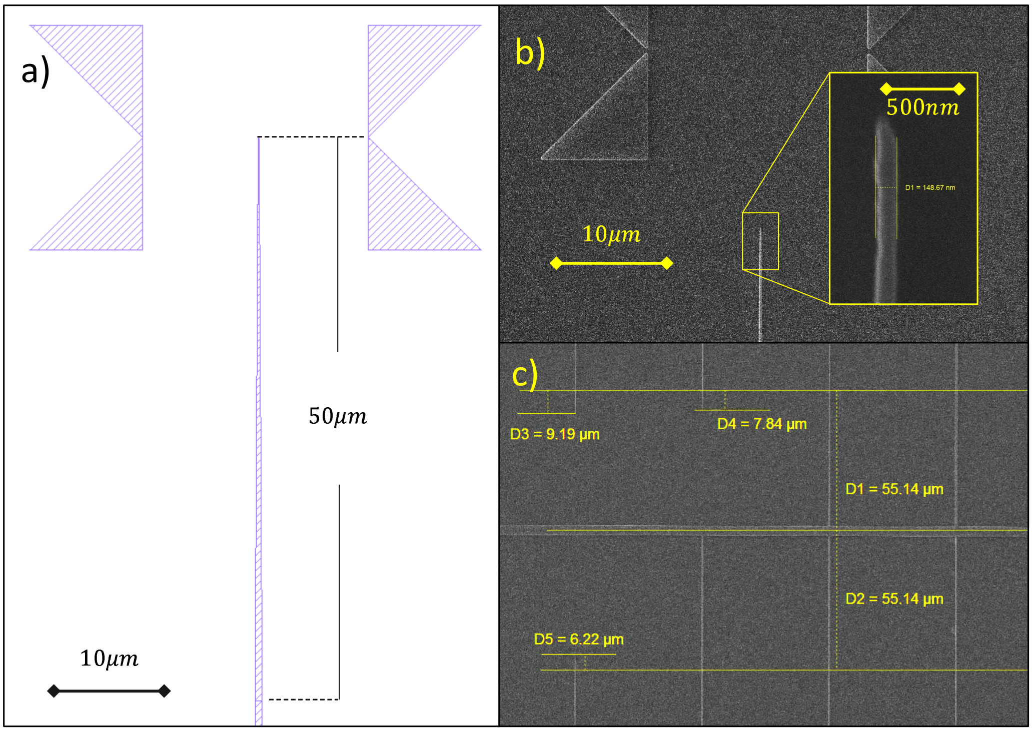

Figure 1.14: Design and SEM imaging of the inverse taper couplers. a) in the design the inverse taper width goes to zero at the tip over a length of 50 μm. b) due to the resolution of the lithography, however, the tip of the waveguide is formed at the limit finite width of $\approx$ 150 nm, resulting shorter with respect to the designed 50 μm length. c) the remaining length is however enough to extend the inverse taper in the cut-line of the polishing saw (long yellow lines) permitting to obtain a final inverse tapering from 550 nm to $\approx$ 200 nm over 25 μm.

to realize an inverse tapered waveguide, where the waveguide width is progressively towards the coupling interface. The most efficient inverse tapers are realized by reducing the waveguide width as close as possible to zero, engineering the tapering shape, and changing the environment refractive index [33, 34].

On the mask, I designed test structures for complete inverse tapers, that shrink the waveguide width from 550 nm to 0 nm over a length of 50 μm. Fig. 1.14 Shows SEM images of the test inverse tapers after the smoothing. In the design the inverse taper width goes to zero at the tip, as shown in the layout (Fig. 1.14 a)). Due to the resolution of the lithography, however, the tip of the waveguide is formed with a finite width of $\approx$ 150 nm at a shorter length, as shown in Fig. 1.14 b). The remaining length is however enough to extend the inverse taper in the cut-line of the polishing saw (Fig. 1.14 c)) permitting to obtain a final inverse tapering from 550 nm to $\approx$ 200 nm over 25 μm.

Dicing

The wafer was then covered by the BCB bonding polymer, backed to simulate the bonding process and then covered again with a thick photoresist to protect the samples for environmental dirt during the dicing step. The dicing is carried on in two phases: first, the facets of the waveguides are defined by a polishing-millstone-saw that abrades a 100 μm deep groove along the chip border, as shown in Fig. 1.15. The sides of the polishing millstone are designed to polish the formed walls, where the newly formed waveguide facets are located. Then, a thinner and coarser millstone saw is used to saw through the whole wafer and separate the dices.

1.4 Propagation Losses

The propagation losses are estimated by measuring the transmission of waveguides with different lengths. In fact, the attenuation of light in the waveguides follows the Labert-Beer's law:

$$\frac{I_{out}(L)}{I_0} = Ae^{-\alpha L} \tag{1.4}$$

where L is the sample length, α is the coefficient of propagation losses and A is a constant that takes into account for the insertion losses. Often, the transmission intensities are recast in logarithmic units:

Lambert - Beer Losses

$$10\log_{10}\left(\frac{I_{out}(L)}{I_0}\right) = -\alpha^{prop}_{dB/cm}L - \alpha^{ins}_{dB}. \tag{1.5}$$

In this way the logarithmic transmission ratio becomes a linear law from which the propagation losses $\alpha^{prop}_{dB/cm}$ and the insertion losses α^{ins}_{dB} are readily extrapolated by linear regression in the usual units of dB/cm and dB respectively. In the WP1_P1 device serpentine structures which have variable length but with the same number of bends are present (Fig. 1.16) The measurements were carried on with the setup described in 0.3.2, by taking a single manual transmission measurement for each length. Since the transmission spectrum of the waveguides is modulated by the FP that is formed between the waveguide facets at the chip extrema, each measurement was made at the FP resonance crest nearest to 1500 nm. The layout of the used

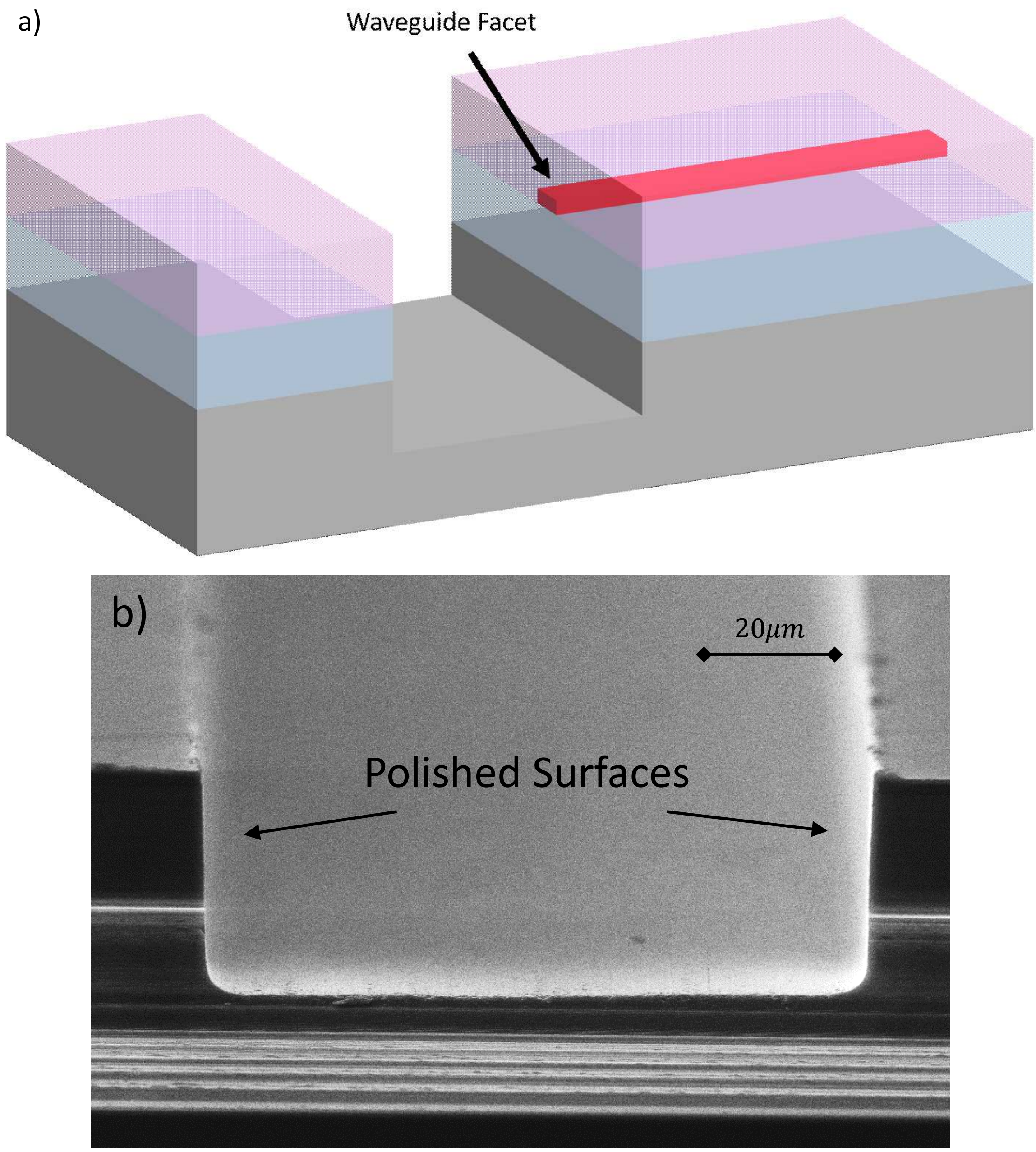

Figure 1.15: a) facet definition during the dicing process is achieved with a polishing-millstone-saw that abrades a 100 nm deep groove in the wafer, while polishing the sidewalls where the waveguide is present at the same time (image is not in scale). Proper dicing through the whole substrate is realized in a second step, with a thinner millstone that does not touch the polished walls. b) SEM image of a test groove before complete dicing.

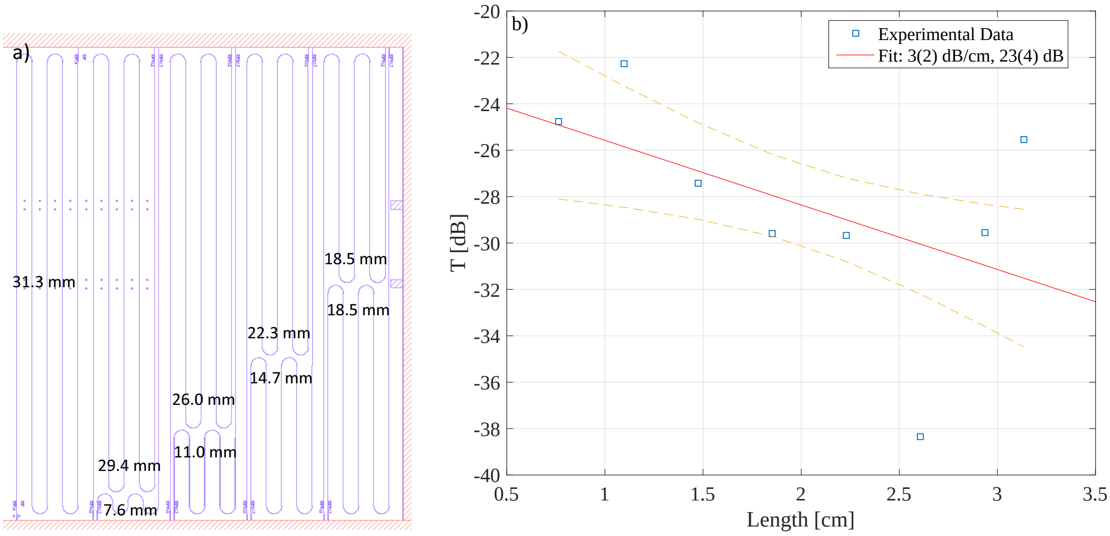

Figure 1.16: a) folded structures dedicated to the propagation loss measurements. b) Transmission measurements (blue squares) of the variable length serpentine structures of layout C2 from the test sample WP1_P1. The measurements were taken using the passive characterization setup described in Sec. 0.3.2, acquiring a single transmission measure for each structure, near wavelength 1500 nm. The linear regression (red line) of the data estimates the propagation losses as 3 ± 2 dB/cm. The rather large uncertainty reflects the ample confidence interval (dashed orange curves), which is due to the data scatter. Data scatter is believed to be caused by insertion losses variations, and will be countered with multiple measurements in the following experiments.

structures and the results of the transmission measurements are reported in Fig. 1.16 a) and b) respectively.For this preliminary study a single chip was measured, which led to estimated propagation losses of 3 ± 2 dB/cm.

WP1_P2 Thicker HM

A first trial of improvement was attempted by increasing the HM thickness [61] in process WP1_P2. Therefore, a second run with 300 nm of TEOS HM was realized. The wafer processing is the same as for WP1_P1 with the exception of the HM thickness (Fig. 1.11 d)). The mask layout (Fig. 1.17 a)), features bunches of straight waveguides to obtain proper propagation losses measurements with statistical significance.

Figure 1.17 reports the propagation losses measurements for the WP1_P2 run. This time, for each waveguide length multiple measurements (blue squares) were taken to estimate the transmission variance of nominally identical waveguides. For each length, the mean value (orange stars) and standard deviation (orange bars) of the data are reported. The standard deviation does not seem to depend strongly on the sample length, with an average value of $\sigma_T = 2.9$ dB, leading to the conclusion that its variance is attributable to the insertion losses. To verify this hypothesis, repeated measurements were realized mis-aligning and re-aligning the setup on the very same waveguide, giving identical results within the sensibility of the setup, suggesting the inhomogeneous waveguide facets as the cause of the data spread.

The linear regression of the data (red line) gave $\alpha^{prop}_{dB/cm} = 5.5 \pm 0.5$ dB/cm and $\alpha^{ins}_{dB} = 14.3 \pm 0.4$ dB. While the insertion losses dropped by 8 dB, the propagation losses seem to be higher in the new sample. Even if the two measures are not incompatible, an increase in propagation losses seemed inconsistent. The bizarre fact was explained

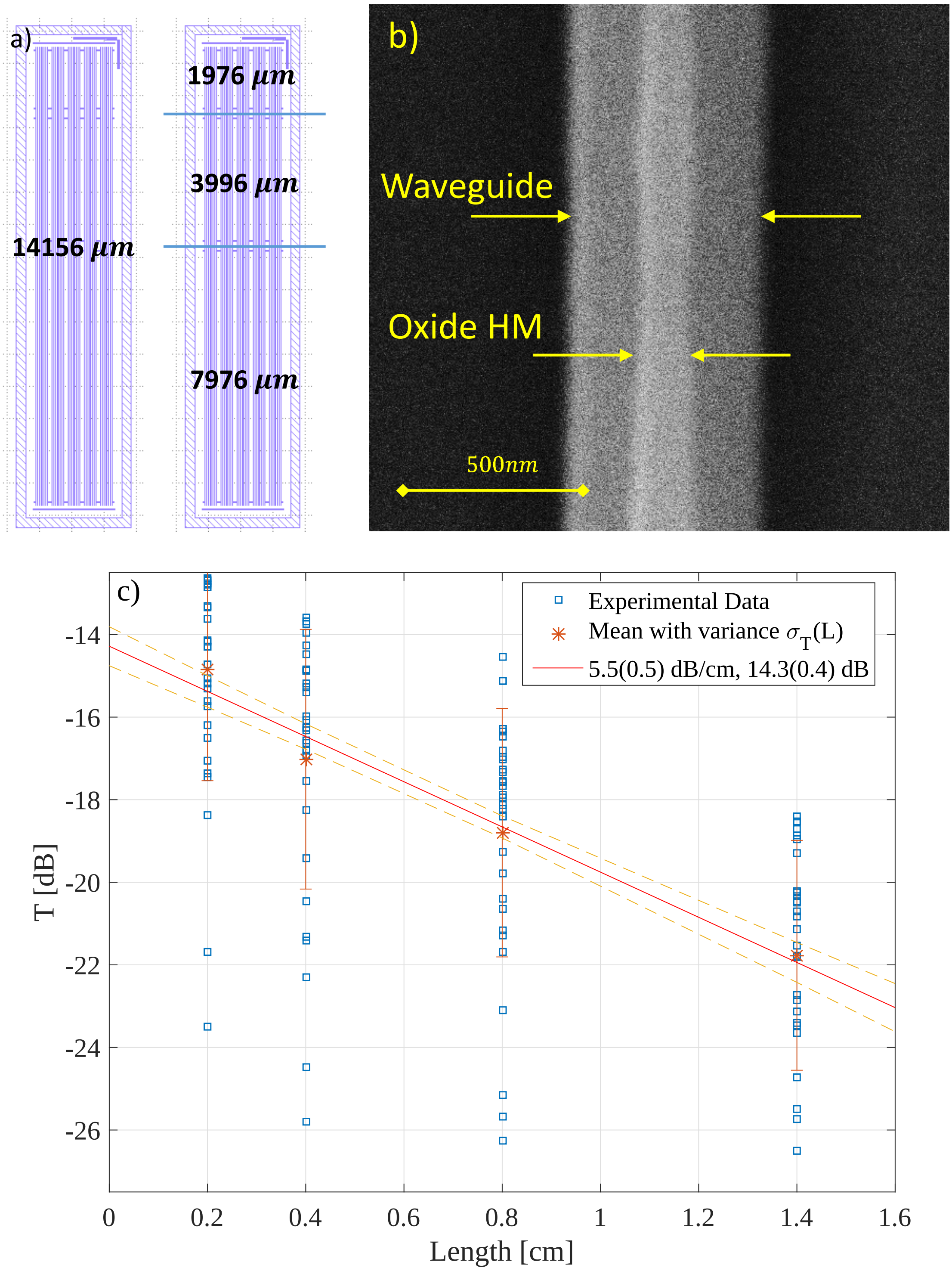

Figure 1.17: a) test layout with bunches of straight waveguides that are cut at different lengths. b)SEM image of the HM over the waveguide after the smoothing. The BHF dips during the RCA cleaning progressively consume the TEOS of the HM, leaving the top side of the waveguide unprotected. c)(blue squares) Transmission measurement of the variable length waveguides of layout AUS on the test sample WP1_P2. The measurements were taken using the passive characterization setup described in Sec. 0.3.2, acquiring a single transmission measure per waveguide at the FP crest nearest to 1500 nm. For each value of waveguide length, multiple waveguides were measured (~ 30) in order to estimate the (orange stars and bars) mean value and standard deviation at each length. The standard deviation seems to be constant over the sample length, and therefore it is interpreted as an insertion losses noise, that is estimated as $\sigma_T(L) = 2.9\ dB$ Linear regression (red line) of the data estimates the propagation losses as 5.5 ± 0.5 dB/cm. The (dashed orange lines) 1σ confidence interval is also shown.

by taking into account the efficiency of the lithographic process. In fact, during the lithography, the UV light that patterns the photoresist layer is very sensitive to both the horizontal dimensions of the structures and to the thicknesses of the layers. Especially if the layers have thickness values comparable with the UV wavelength, interference paths may spoil the resolution.

To verify this hypothesis, an auxiliary Si wafer was covered with a 350 nm thick oxide layer that was gradient-etched in BHF by immersing the wafer in the etchant and pulling it out slowly. This resulted in a spatial gradient of the oxide HM thickness on the wafer, as shown in Fig. 1.18. The thickness of the HM was then characterized along the wafer's diameter with interferometric measurements. The wafer was then covered with photoresist and patterned with a test mask along the measured diameter using the same lithography process as in WP1_P2. The features near the critical dimension were then inspected with an optical microscope, revealing a periodic spoiling of the lithography quality, as it can be seen from the Directional Couplers (DCs) in the insets of Fig. 1.18. The effect is due to the photoresist and oxide layers that, acting as a dielectric mirror, reflect the UV light resulting in unwanted interference patterns that cause the gaps to close. Indeed, at the interface between two bulk materials with refractive index n_1 and n_2, light impinging at normal incidence is subject to a reflection coefficient $R = (n_1 - n_2)^2/(n_1 + n_2)^2$. When dealing with thin films however, the light is reflected at each interface and a complex interference pattern, that depends on the thicknesses and refractive indices of the materials, is formed. Moreover, as the light travels inside the media, absorption may occur as it is the case for the 365 nm UV light in the SOI layer.

The transmission and reflection of the multilayered structure may be calculated, known the thicknesses and the (complex) refractive index of each layer, using a transfer matrix approach. The simulated reflection of the photoresist-HM dielectric mirror is shown in Fig. 1.18 as a function of the HM thickness on the test wafer.

The simulated reflectance and the optical images at the measured thicknesses are in qualitative accordance, demonstrating that the lithography patterning is not resolved for a reflecting stack, as sketched in Fig. 1.19 (a). This results are in accordance with the previous results. Indeed, the WP1_P1 run was made with a 150 nm thick HM, which is near the minimum of reflection, while at the new HM thickness of 300 nm the reflection for the 365 nm wavelength of the lithography i-line grows over 40%. It's worth note that the reflection of the photoresist-SiO_2-SOI stack reaches 7% at the minimum. The minimum reflectance of the stack could be further reduced by adding dielectric layers or by choosing materials with a different refractive index, realizing thus an anti-reflection coating.

Furthermore, during the RCA cycles of the smoothing process, the BHF dip consumes the SiO_2 of the HM, leaving the top edges of the structures unprotected from the next-step oxidization. As it was previously discussed, this may worsen the waveguide top surface and generate stairs as the oxide is removed, as it shown in Fig. 1.13. Therefore, a third run was realized with a new HM specifically designed to address these problems.

Anti reflection coating HM

Both problems were solved by adding a second HM layer of a material that is resistant to HF, Si-etching, compatible with the process and with an intermediate refractive index between SiO_x and Si. Therefore, the HM of the WP1_L1 run was changed from

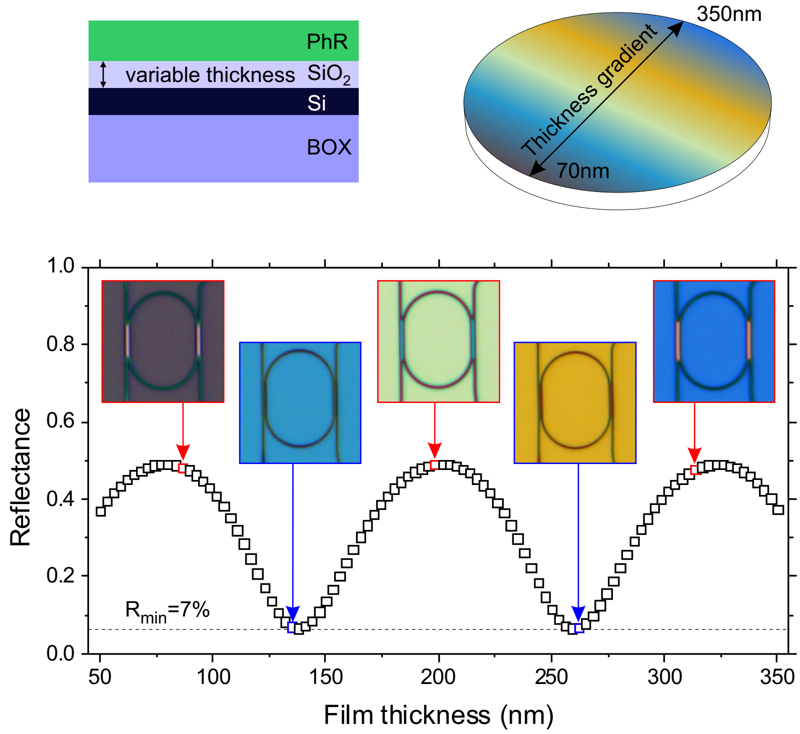

Figure 1.18: A variable-thickness photoresist-SiO_2 HM-SOI stack may be realized by gradient BHF etching of the SiO_2 prior to photoresist deposition. The insets show optical images of a structure with couplers featuring gaps near the limit of resolution (400 nm) taken at various positions on the wafer that correspond to the film thicknesses pointed by the arrows. The reflectance of the stack as a function of the SiO_2 thickness for UV light with wavelength 365 nm at normal incidence is calculated with the transfer matrix approach to determine the local reflectance coefficient near the inspected positions. The images show how the gaps are visually resolved near the minimum reflectance, while they are completely unresolved when the reflectance is near the maxima.

TEOS to a double layer PECVD SiNx and PECVD SiO_x HM. The SiN_x indeed is left untouched by the BHF dip, offering protection to the edges of the waveguide during the smoothing process. Furthermore, thanks to the higher index of the PECVD SiN_x (2.26 at 365 nm), a proper anti-reflection coating may be designed. The layers thicknesses were designed by minimizing the reflection using again the transfer matrix approach as a simulative tool. Figure 1.19 (b,c) show the designed anti-reflection HM with the simulated reflectance near the i-line wavelength. By using a two-layer HM, the reflectance may be brought down to 0 at the wavelength used in the lithography. The expected sidewall angle with the new HM, sketched in Fig. 1.11 e) is substantially unvaried with respect to the TEOS case.

For this run, another two masks layout were realized. One layout contains test structures with various length, replicated with both direct and inverse coupling, to reduce the insertion losses and, in particular, the insertion loss fluctuations due to imperfections of the waveguide facets. The inverse couplers are realized with adiabatic linear tapering from the waveguide with of 550 nm to 0 nm over 25 μm. The facets are cut at halfway, leading to an expected inverse taper width at the tip near 270 nm. It's worth to note that the inverse tapering involves features which are under the resolution of the 365 nm lithography, and therefore requires dedicated process testing. Another set of test structures features bunches of straight waveguides with inverse-, no- and normal-tapering, to evaluate the differences in the coupling losses. Further-

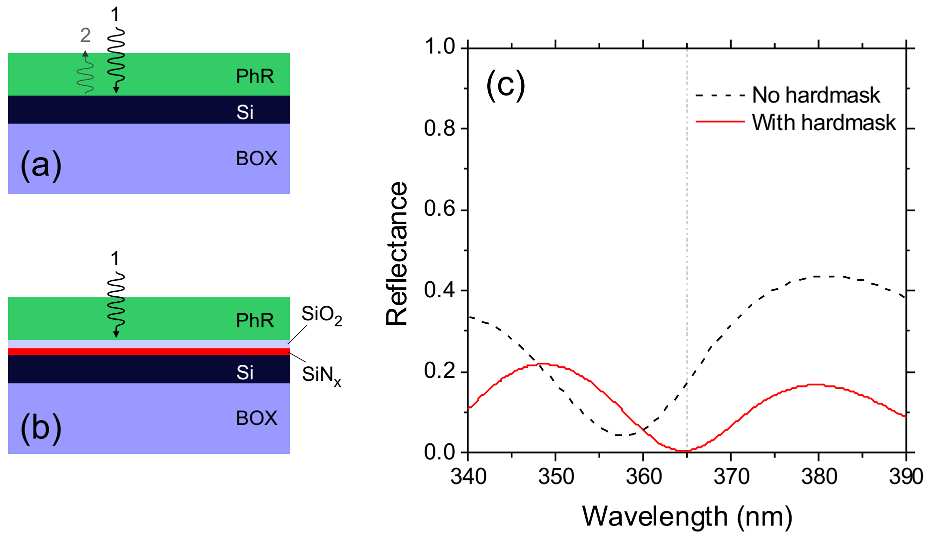

Figure 1.19: (a) the UV light of the lithography patterning is partially reflected at the material interfaces between the layers, modifying the light pattern inside the photoresist. (b) a HM with a sufficient number of layers may be used to realize an anti-reflection coating. (c) making use of transfer-matrix simulations, the reflectance of the anti-reflection HM may be brought to 0.

more, I designed a set of racetrack ring resonators in All-Pass configuration with various coupling lengths that were included in the mask. Finally, a second layout contains the laser structures designed in collaboration with III-V labs, that will be analyzed later.

Final losses: 1.7 ± 0.3 dB/cm

To asses the propagation losses, I performed optical transmission measurements were on four test chips in both tapered and inverse tapered configurations to estimate the insertion losses difference between the two coupling schemes. The results of the measurements are reported in Fig. 1.22. By fitting the experimental data, I demonstrate propagation losses of only 1.7±0.3 dB/cm, consistently for both tapered and inverse-tapered waveguides. The two kinds of waveguides have indeed the same measured propagation losses, while the insertion losses are different. The untapered waveguides have in average 17.9±1.0 dB of insertion losses, while the inverse tapered waveguides have 3.5 dB lower insertion losses . The average of the standard deviation of the measurements calculated at each length is also reduced from the $\sigma_S = 2.14$ of the straight waveguides down to $\sigma_I = 1.58$ for the inverse tapered case, showing how the inverse-tapering reduces the facet variations issue.

In Fig. 1.23 propagation losses values for SOI waveguides are reported. The geometry, as well as the source of each point are reported in Tab. 5 in the appendix. From Fig. 1.23 a) it can be seen that propagation losses values below 1 dB/cm have been achieved in the past in SOI waveguides, in particular with a geometry similar to the RIB500 reported in the present work [62]. Most of the results reported in panel a), however, have been achieved using Deep Ultra Violet (DUV) or e-beam lithography, which feature an intrinsically smoother sidewall profile at the photoresist patterning stage. The difference in the resulting sidewall roughness produces a huge gap in the propagation losses that can be achieved with such techniques in contrast with standard UV lithography. A clear example is provided by **??** which features a comparative study between the propagation losses of waveguides realized with the same geometry using e-beam and i-line (365 nm) UV lithography, exposing a propagation loss difference as high as 12 dB/cm. It is therefore useful to compare

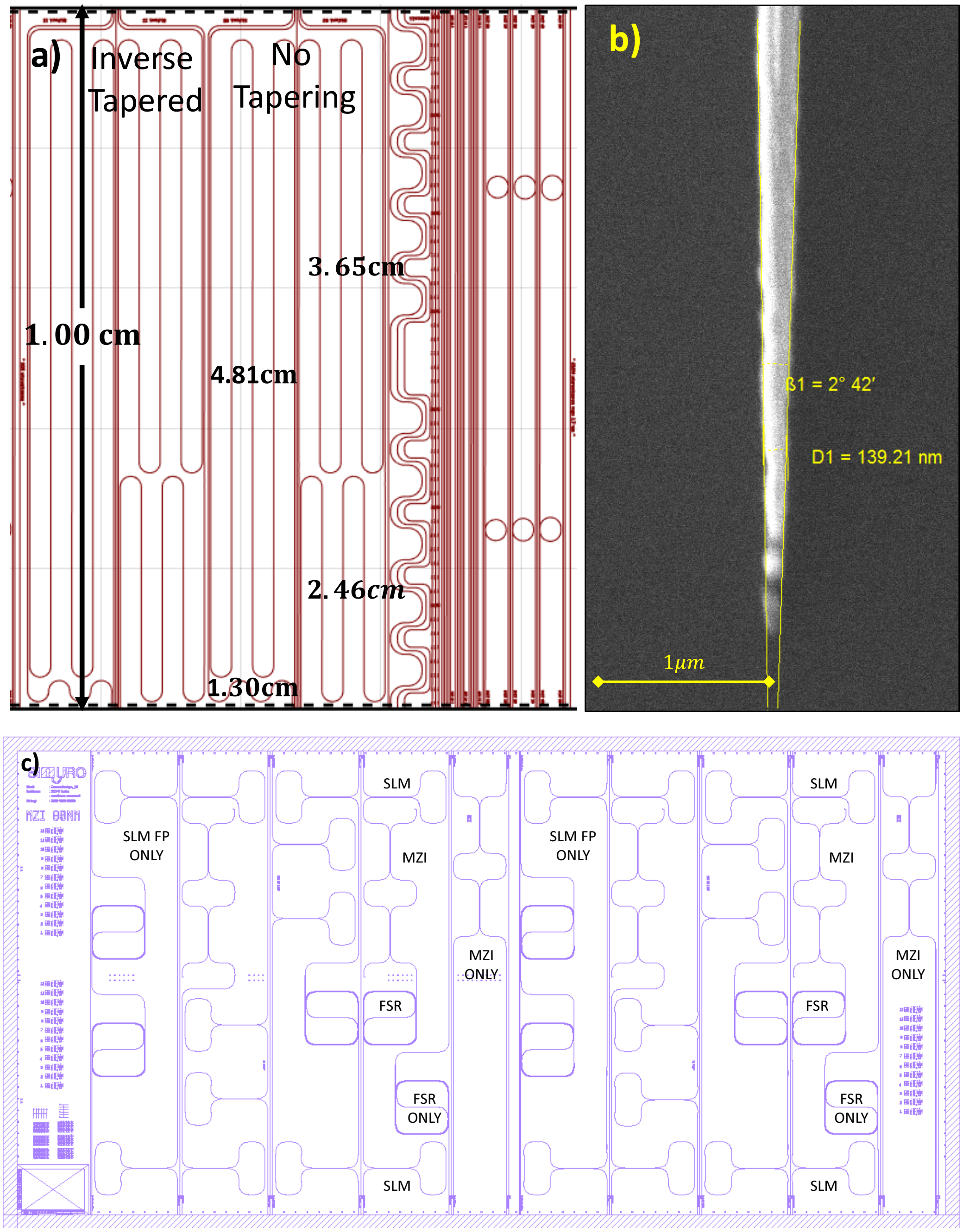

Figure 1.20: a) test layout of the WP1_L1 process. (left) folded waveguides of different length are present in both inverse-tapered and straight termination configurations. Among the other test structures, All-Pass racetrack ring resonators with different coupling length are present on the layout.
b) SEM image of the tip of an inverse-taper structure. The quality and dimensions of the tip are improved with respect to that of WP1_P1 (Fig.1.14). (c) layout of the device, containing, other than the final device, separated structures for each component of the design. Each structure is again repeated both in inverse-tapered and un-tapered configurations.

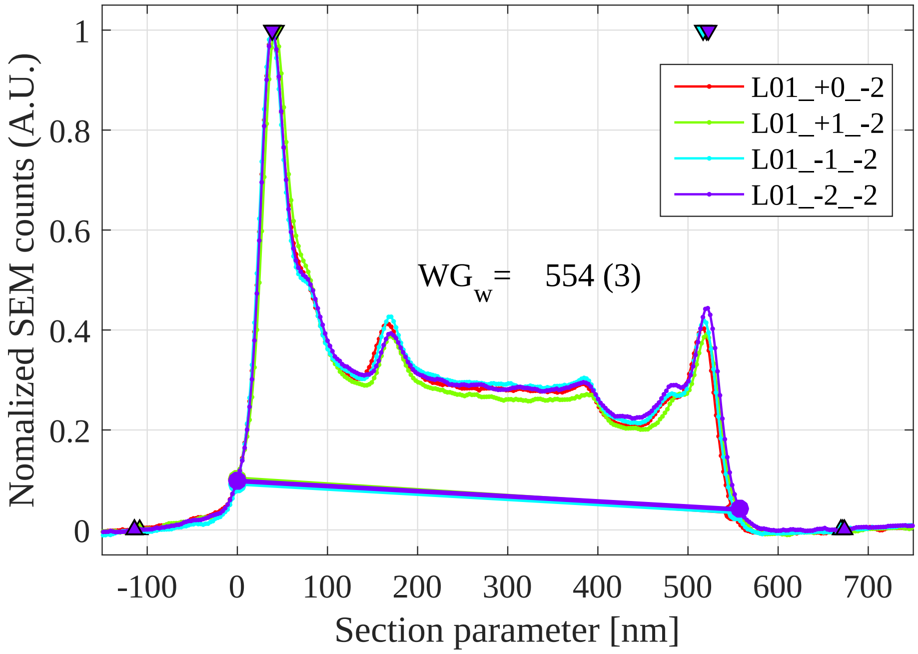

Figure 1.21: Waveguide width analysis obtained through SEM image data elaboration on the straight waveguides in the WP1_L1 run. The measurements on four different chips exhibit a standard deviation of only 3 nm, demonstrating the improvements achieved in the lithography process with respect to Fig. 1.13. Here, the bumps in the SEM counts on top of the waveguide signal are again due to the oxide edges, but the underneath silicon top surface is protected by the un-etched silicon nitride layer.

the results obtained in the present work with others using a similar UV technology. Figure. 1.23 b) shows how the propagation losses in SOI waveguides achieved in the SiQuro project are in line with the state of the art for the UV lithography.

Coupling losses

During the various design layouts realized for WP1, I have included many test structures to realize efficient inverse tapers. The main difficulty lies in the lithography resolution, which being of the order of 400 nm gives little margin to taper down the 550 nm waveguides. During the test processes I realized sub-resolution inverse taper structures down to 140 nm, although with irregular walls near the tip, as I shown in Figs 1.14 and 1.20. In the WP1_L1 test layout the inverse tapered waveguides have been realized and tested by dicing the taper at c.a. 270 nm width, creating partial inverse tapered waveguides.

Figure 1.24 compares three typical spectra of (red) inverse-, (green) no- and (blue) direct-tapered waveguides realized during the process. In Fig. 1.24 (top left) the three spectra over the wavelength range 1490 nm-1550 nm are shown. Figure. 1.24 (top right) shows a smaller portion of the spectra, where the FP crests are well visible. While the inverse-tapering did not drastically reduce the FP amplitude, the couped intensity has been increased, as already demonstrated during the losses analysis.

The presence of the FP crests, however, may be exploited to measure the group index of the waveguide, by measuring the FSR of the crests. The group index in the FP cavity is related to the FSR by

$$n_g(\lambda) = \frac{\lambda^2}{2\ L\ \mathrm{FSR}(\lambda)} \tag{1.6}$$

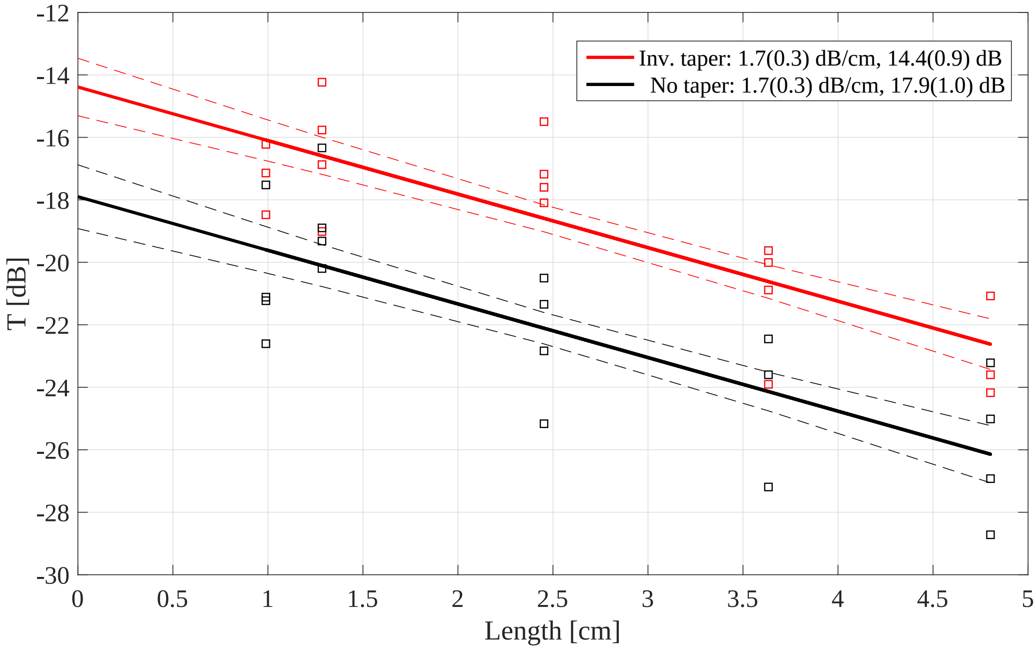

Figure 1.22: Inverse-tapered (red) and untapered (black) waveguide transmission measurements from test devices of run WP1_L1. The waveguide transmission was acquired over four samples in both untapered and inverse-tapered waveguides configurations using the setup described in Sec. 0.3.2 (square points). The propagation losses of the waveguides are calculated by linear regression on the data (solid lines). The dashed lines represent the $1-\sigma$ confidence interval. The propagation losses resulted of only 1.7 ± 0.3 dB/cm consistently in both coupling configurations. The insertion losses in untapered configuration exhibited total insertion losses of 17.9 ± 1.0 dB, while the inverse-tapered configuration gave 14.4 ± 0.9 dB of insertion losses, demonstrating a 3.5 dB improvement in the coupling efficiency.

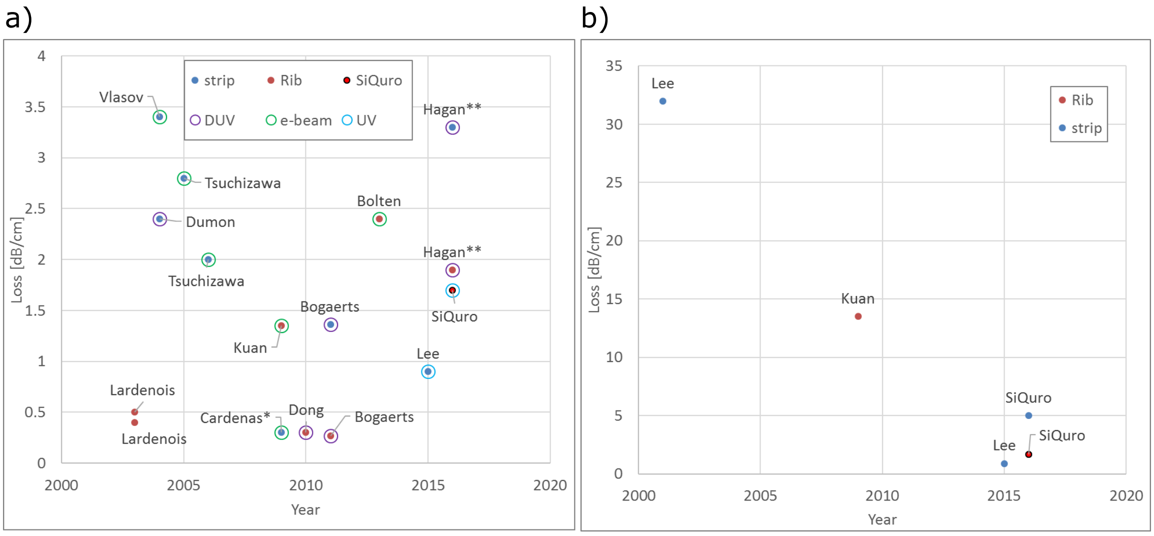

Figure 1.23: Propagation losses of various waveguide structures over the years. a) using electron-beam or Deep Ultra Violet (DUV) lithography, losses below 1 dB/cm in sub-micrometer SOI waveguides have been reported already in the first years of the 2000. b) in the case of SiQuro, however, the structures are realized with UV lithography (i-line), which produces waveguides with higher losses compared to the e-beam for the same geometry. It's important to note that the reported works span a wide range of waveguide dimensions (from 350 nm to 5000 nm) and different processes, as reported in Tab. 5. A faithful comparison between waveguides realized through e-beam and UV lithography has been realized by Kuan&al. [63] where the same structures were realized by using the two approaches.

where L s the length of the waveguide. Therefore, I developed a software to measure the position of the FP maxima, marked by the starred points in Fig. 1.24 (top right). The FP resonances spectra position is used to estimate the FSR over the whole spectrum, as it is reported in Fig. 1.24 (bottom left), where the bold lines represent polynomial fits of the data. The FSR is then used to estimate the group index of the waveguide by using Eq. 1.6, as shown in Fig. 1.24 (bottom right).

Rib racetrack resonators

On the WP1_L1 layout racetrack AP resonators are also present to demonstrate the high quality factor that are achievable with such small losses. Figure 1.25 shows the transmission spectrum of a racetrack resonator of length 1002.5 μm with a straight coupling region of 30 μm. The spectrum shows the comb of resonances from 1490 nm to 1640 nm, which reaches a critical coupling regime near 1533 nm, as highlighted in the zoomed spectrum. At the critical coupling the round-trip losses equal the coupling losses, and the transmission drops to zero, maximizing the resonance signal with respect to the FP that is generated among the waveguide facets. I developed a dedicated software routine to analyze the spectrum of resonators and automatically compute relevant parameters, such as the quality factor, by fitting the resonances, as shown in Fig. 1.25 (bottom). The intrinsic quality factor of this resonator is above 1.5×10^5. Figure 1.26 shows my result in comparison to other state of the art similar structures. The blue diamonds represent channel resonators, which usually have lower quality factors but do not need long bending radii. The green triangles represent other rib resonators, while the two red squares represent the results that I achieved within the SiQuro project regarding channel and rib resonators.

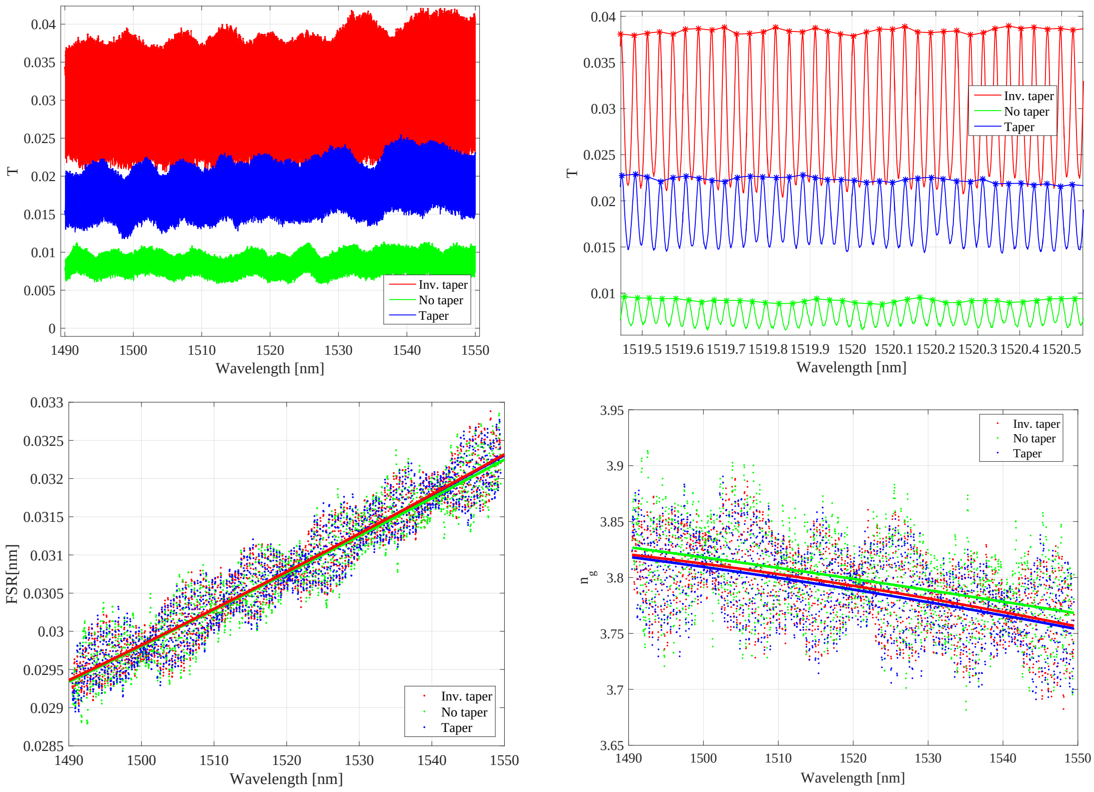

Figure 1.24: (top left) typical transmission spectra of three sample waveguides in (red) inverse-, (green) no-, and (blue) direct-taper configurations. (top right) the software I developed identifies the FabryPerot crests and measures (bottom left) the distance among the crests, which is the Free Spectral Range. The solid lines are quadratic polynomial fits of the data. (bottom right) the FSR values are used to estimate the group index of the waveguide. The solid lines are $n_g(\lambda)$ estimations using the fit lines of the previous figure.

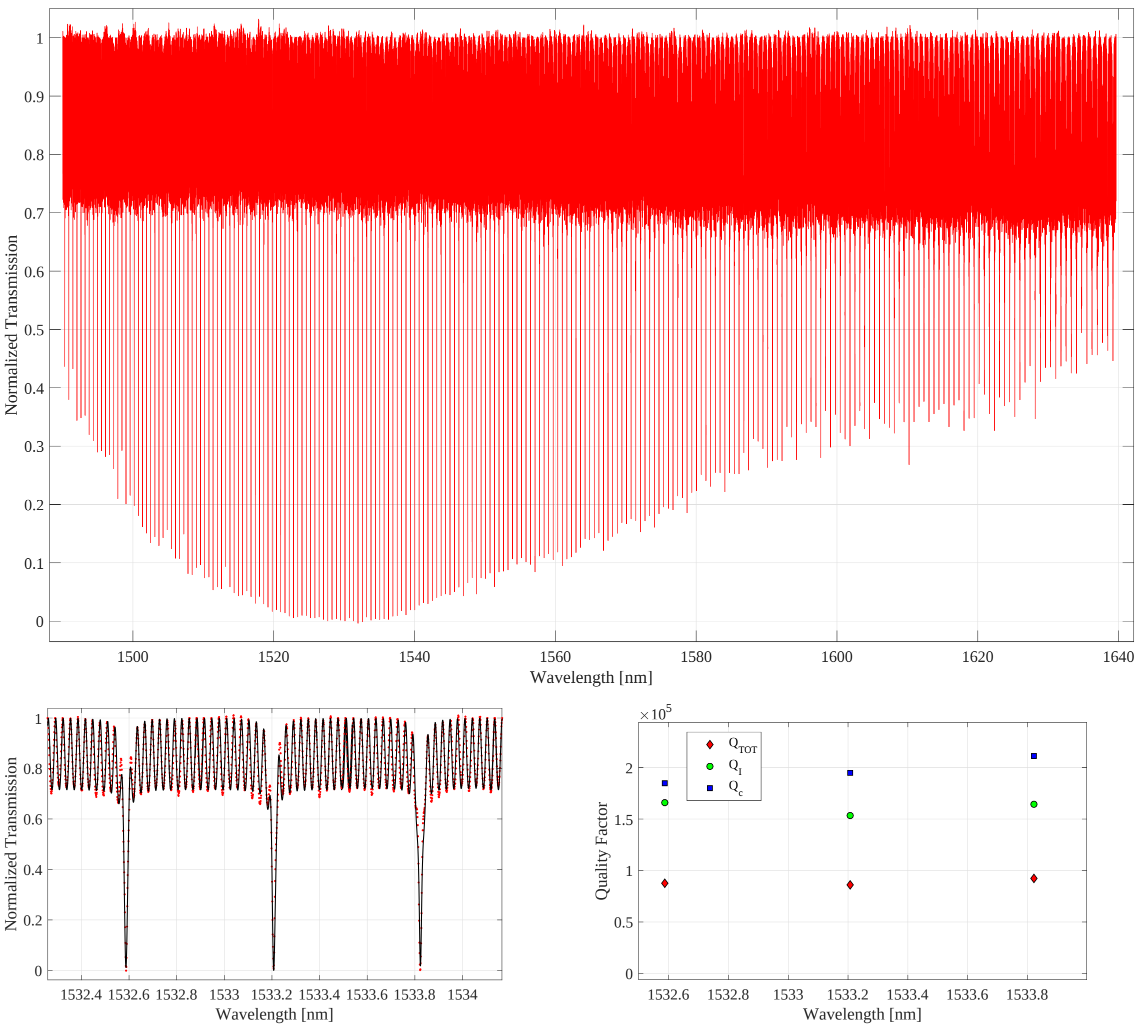

Figure 1.25: (top) Transmission spectrum of rib racetrack resonator on the range from 1490-1640 nm. The resonator length is 1002.5 μm, the coupling region is 30 μm with a 600 nm gap. The spectrum, on the range from 1490 nm to 1640 nm, exhibits a comb of resonances that reach critical couping near 1533 nm. (bottom left) near the critically coupled condition the ratio between the racetrack resonances and the FP crests due to the waveguide facets is maximum, and the resonances can be fitted to extract (bottom right) the quality factor of the resonator. The intrinsic quality factor of this resonator is above 1.5×10^5.

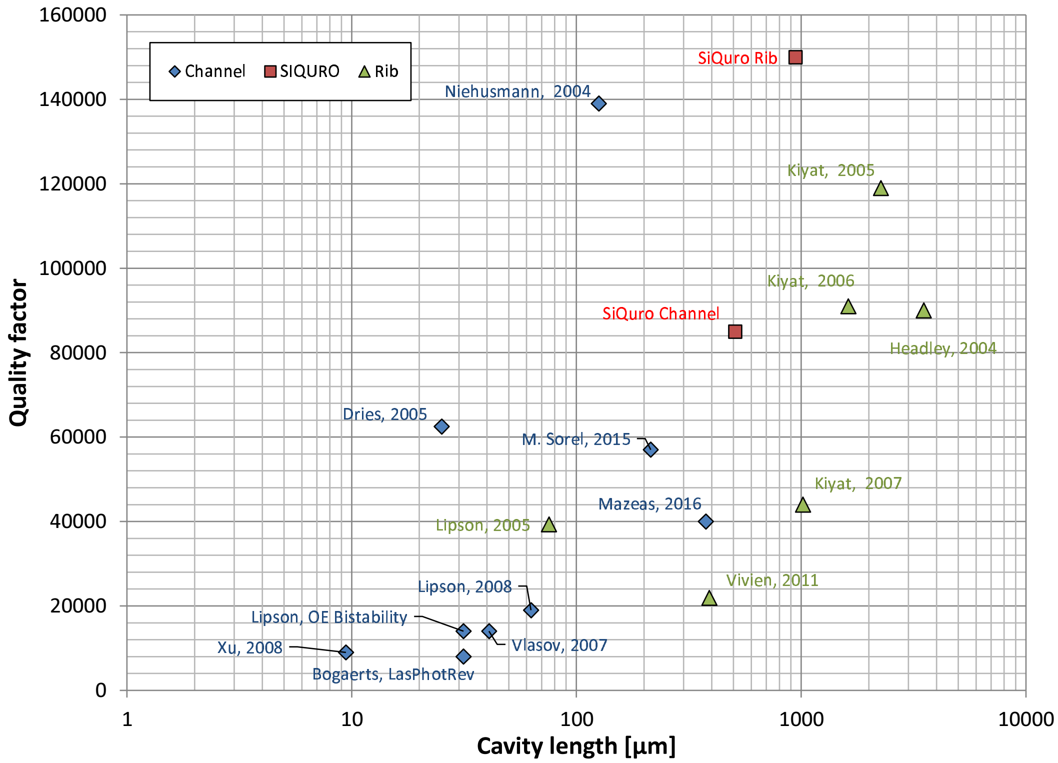

Figure 1.26: State of the art of the Q-factors for similar integrated devices as a function of the cavity length. The graph shows both (blue diamonds) channel and (green triangles) rib structures. The structures I developed during project SiQuro (red dots) fit in the frame.

1.5 Sagnac Loop Mirrors

The laser cavity is realized with two Sagnac Loop Mirrors (SLM). In Fig. 1.27 the functionality scheme of a SLM is shown. The light coming from the input port is coupled with itself in a open-loop configuration. Using the notation of Figure 1.27 for the round-trip losses a, the transmission coefficient t, and the coupling coefficient κ of the coupler region, the transfer functions for the reflected and transmitted field amplitudes are

$$E_T = S_T E_I = ae^{-i\varphi(\lambda)}(|t|^2 - |\kappa|^2)E_I, \tag{1.7a}$$
$$E_R = S_R E_I = ae^{-i\varphi(\lambda)}(-2\kappa^* t)E_I. \tag{1.7b}$$

The transmission and reflection coefficients thus become

SLM transmission and reflection

$$T = |S_T|^2 = (2|t|^2 - 1)^2 a^2, \tag{1.8a}$$
$$R = |S_R|^2 = 4|t|^2(1 - |t|^2)a^2. \tag{1.8b}$$

In the above equations, the parameter $|t|^2$ may be set by using Eq. 0.8b and considering that $|t|^2$ is the transmission of the directional coupler, namely $I_1(z)$ [56]. The reflectivity of the Sagnac Loop Mirror may thus be controlled acting on the length of the coupler and/or the coupling strength between the two waveguides.

In our case 100% and 20% reflectors are realized forming FP laser cavity, as well as 50%-50% couplers for the Mach-Zehnder interferometer are present, according to

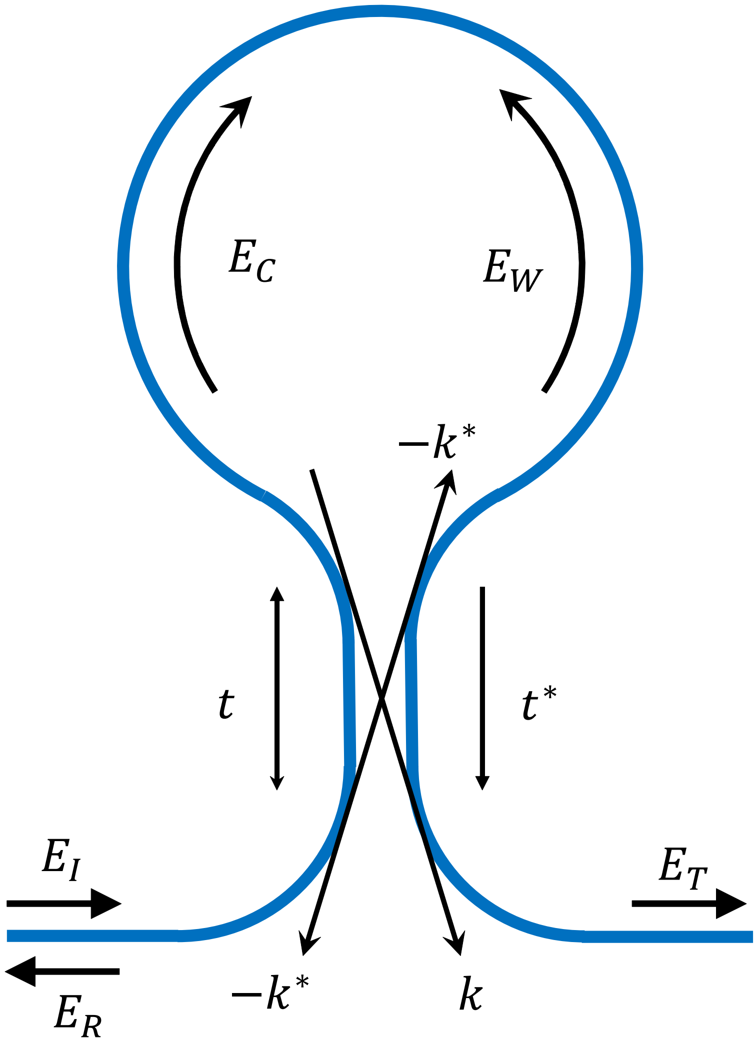

Figure 1.27: Coupling scheme of a Sagnac Loop Mirror. The notation used for the coupler is similar to that of Fig. 12. The input field E_I enters from the left. The couplers splits the amplitude into the clockwise and anticlockwise components E_c and E_w, which are in turn split again at the coupler. The interference between the split E_c and E_w gives rise to the transmission and reflection spectrum.

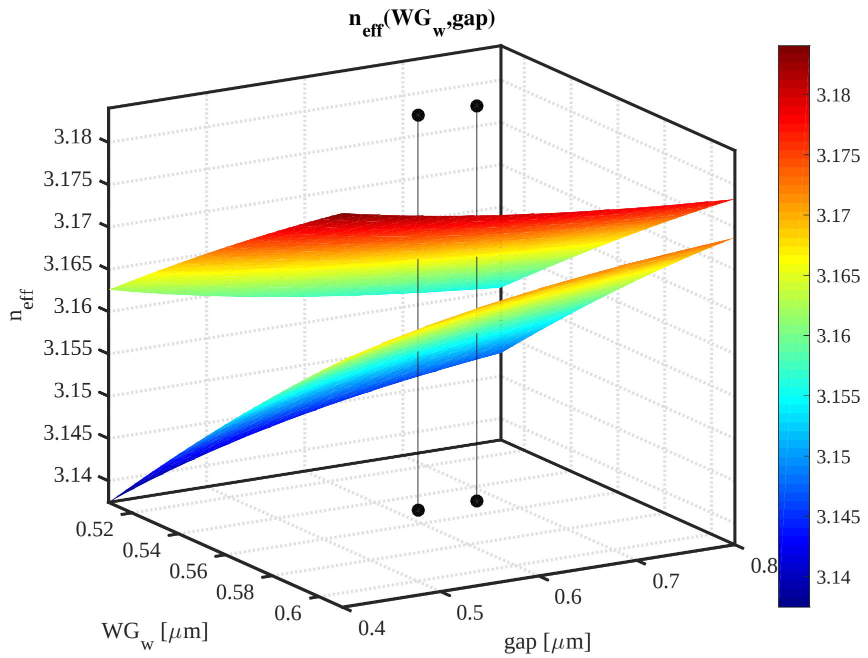

Figure 1.28: Effective refractive indices of the symmetric and anti-symmetric supermodes as a function of wg_w and gap for the designed directional coupler.

the design of III-V labs. When actual couplers are designed, the coupling region is not sharp. The waveguides are gradually brought to the gap distance using smooth curves to avoid bending losses. The coupling of the modes occurs also along these smooth connections, although the coupling coefficient varies continuously with the gap. The overall coupling that occurs out of the designed coupling region may be described with a phase term ϕ as

Real DCs have a bend phase

$$I_1(z) = cos^2\left(\frac{\pi \Delta n_{eff} z}{\lambda} + \phi\right), \tag{1.9a}$$

$$I_2(z) = sin^2\left(\frac{\pi \Delta n_{eff} z}{\lambda} + \phi\right), \tag{1.9b}$$

where the value of ϕ may be extracted empirically or numerically. If the bends are adiabatic, i.e. if they may be locally approximated as a series of shifted parallel waveguides, ϕ may be numerically computed making use of the step approximation described in [31]. Using this approach, the bent region is approximated as a series of parallel regions with different gaps. By performing supermode-simulations while varying the gap, the symmetric-antisymmetric index difference $\Delta n(gap)$ may be estimated. The function $\Delta n(gap)$ is well represented by an exponential decay for values of the gap $\gtrsim \lambda$, as the refractive index difference is caused by the interaction of the degenerate modes, that is mediated by the evanescent tails. The function $\Delta n(gap)$ is therefore simulated for small values of the gap, and then extended by fitting the simulations with an exponential decay. At this point, the global phase of the transfer function may be estimated as a function of z by integrating $\Delta n(gap(z))$. The

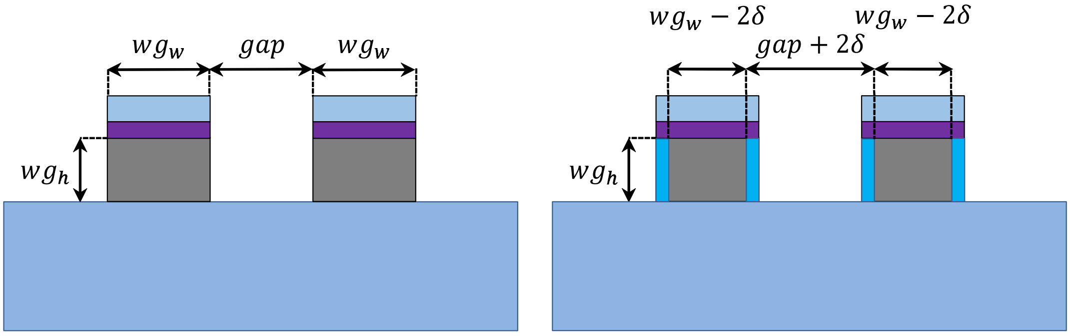

Figure 1.29: Waveguides in a DC(left) prior and (right) after a smoothing cycle. Each RCA cycle of the smoothing process consumes $\delta = 5$ nm of silicon. The waveguides are therefore reduced by an amount 2δ and the gap in the DCs is increased accordingly. The image is not in scale.

equations for the intensity in the two branches of the coupler therefore become:

$$I_1(z) = cos^2\left(\frac{\pi \int_{\text{coupler}} \Delta n_{eff}(gap(z))dz}{\lambda}\right), \tag{1.10a}$$

$$I_2(z) = sin^2\left(\frac{\pi \int_{\text{coupler}} \Delta n_{eff}(gap(z))dz}{\lambda}\right), \tag{1.10b}$$

where the integration should be taken over all the coupler region, adiabatic curves included. These calculations become very valuable especially during the fabrication process, where in addition to the gap of the waveguides, the waveguides widths and the remaining SOI slab thickness is also considered.

DC fine tuning

During the fabrication process, a fine tuning of the waveguide widths and gap is performed in order to obtain performances as close as possible to the target. At the photoresist level, slight underexposure of the photoresist and long hard baking allow to obtain slightly wider structures with respect to the mask layout. On the other side, a soft oxygen plasma etching may be used to reduce the dimension of the structures. Final dimensions of the photoresist levels are then transferred to the HM. At this stage, the widths of the structures should be larger than those of the design, so that they may reach the target width after the smoothing process. If needed, additional RCA cycles may be performed to further reduce the waveguide width.

In all of the mentioned actions, however, the waveguide width and gap are linked by the mask layout as shown in Fig. 1.29: each variation on the waveguide width is reported with opposite sign on the gap. Due to this constrain, depending on initial values of the waveguide width and gap, it may be not possible to reach the target geometry. However, rather than getting as close as possible to the design geometrical parameters, it is possible to find other couples in the (wg_w, gap) parameter space that realize the same coupling. By extending the FEM simulations of the symmetric/anti-symmetric supermodes used to calculate the coupling coefficient to an extended area in the (wg_w, gap) parameter space, it is possible to find the locus of points that permit to reach the target transmission coefficient. When a certain point (wg_w, gap) is measured by SEM imaging during the fabrication process, it determines the slope $wg_w + gap = \text{const}$ along which it is possible to adjust the dimensions (Fig. 1.29) aiming directly at the optimum transfer value rather than at the geometrical design values. From Eq. 1.10b, the coupled intensity dependence on the (wg_w, gap) parameters comes from refractive index asymmetry $\Delta n_{\text{eff}}((wg_w, gap))$, that determines the locus of points where $I_2(wg_w, gap)$ assumes the same values. The curves along which $\Delta n_{\text{eff}}((wg_w, gap))$, and therefore I_2, are not far from the adjustable slopes. This is due to the fact that enlarging the gap and shrinking the waveguide have two opposite trends: when the gap gets larger the coupling decreases exponentially due to the reduced overlap of the evanescent tails of the stand-alone waveguides. On the other side, shrinking the waveguide width to values below the wavelength pushes more and more of the mode volume outside, into the evanescent tails.

The device performance may therefore be optimized by adjusting the geometry to the intersection of the two curves. Figure 1.30 a) reports a color-map of the simulated intensity transfer $I_2(wg_w, gap)$ of a directional coupler of fixed length as a function of the waveguide width wg_w and the gap for the RIB500 geometry. The target coupling values are reached at the design geometry for the 100%(20%) reflectance SLM respectively, represented with full black(green) circles . The solid black(green) lines represent the locus of points where the same target coupling values are achieved. The empty black(green) squares represent the waveguide geometry before the RCA smoothing cycles, which can be moved towards the left along the dashed black(green) lines that represent the $wg_w + gap = \text{const}$ geometrical constrain of the smoothing. The best reachable target point therefore lies at the intersection of the solid and dashed curves.

Analogous considerations are valid for Fig. 1.30 b), where the coupled intensity map $I_2(wg_w, gap)$ is used to estimate the actual SLM reflection coefficients.

It is important to note that moving along the RCA smoothing slopes to adjust the directional couplers also modifies the waveguide width in the rest of the chip. However, around $wg_w = 550$ nm the group index is almost flat, as it was shown in Fig. 1.8, permitting to have small wg_w variations without modifying the group index. Furthermore, the RCA smoothing process also consumes the SOI slab, meaning that the RIE etching that defines the SOI layer must be adjusted accordingly.

SLM FP characterization

The realized SLM Fabry-Perot interferometers were then tested with the passive characterization setup described in Sec. 0.3.2. On the devices, two kinds of SLM-FP interferometers are present with different cavity length, as shown in Fig. 1.31 a,b). The length of the cavity is used to change the FSR, which determines the repetition frequency of the mode-lock-laser. The two SLM resonators spectra are reported in Fig. 1.31 c-f). Panels c) and e) show broadband measured spectra of the short and long cavities of panel a) and b), respectively. The broadband spectral shape is essentially the same for the two cavities, while the fine FP modulation varies both in shape and intensity due to the different cavity lengths. Panels d) and f) show an extract of the spectra around 1500 nm. The fine structure of the spectra exhibits two main spectral contributions. The shortest modulation, with a period of 21 pm and 12 pm for the short and the long cavities, respectively, is the desired SLM-FP modulation. The broader modulation, with a period of 87 pm, corresponds to a cavity of 3.45 mm length. As described before, the input and output of the device is realized with inverse taper waveguides, which terminate with a width of about 275 nm. The facets of the waveguides, that are formed by the remaining 275 nm strip and the silicon slab, provide the system with additional mirrors. Another cavity, highlighted in red in Fig. 1.31, is therefore formed in the waveguide between the input/output facets and the SLM. The parasitic cavity does not depend on the spacing between a)

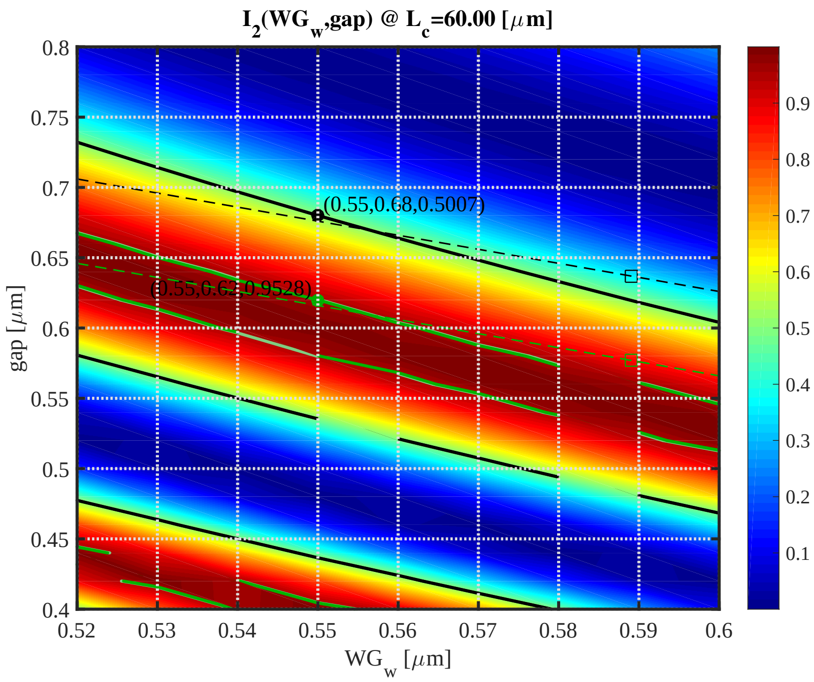

b)

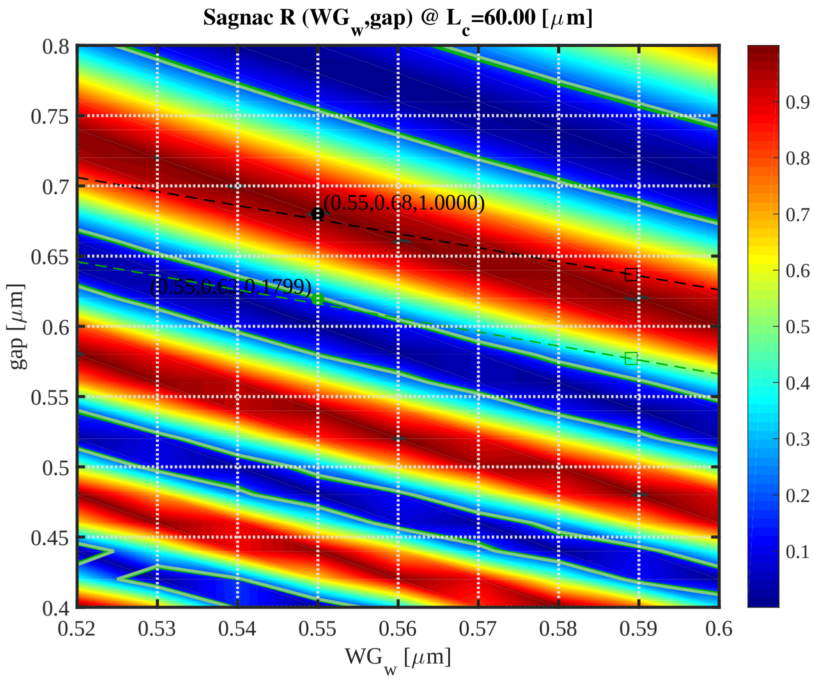

Figure 1.30: a) simulated coupled intensity $I_2(wg_w, gap)$ that is transferred through the coupler. The green(black) dot correspond to the realized couplers with $wg_w = 550$ nm and a gap of 620 nm(680 nm). The combinations of wg_w and gap that lead to the same energy transfer are highlighted with a green(black) line. The green(black) square corresponds to the measured dimensions of the coupler before the smoothing. The dashed green (black) line shows the configurations that are accessible through smoothing. b) correspondent reflectance of the SLM. Analogous iso-curves are traced in the graph for the simulated reflectance values.

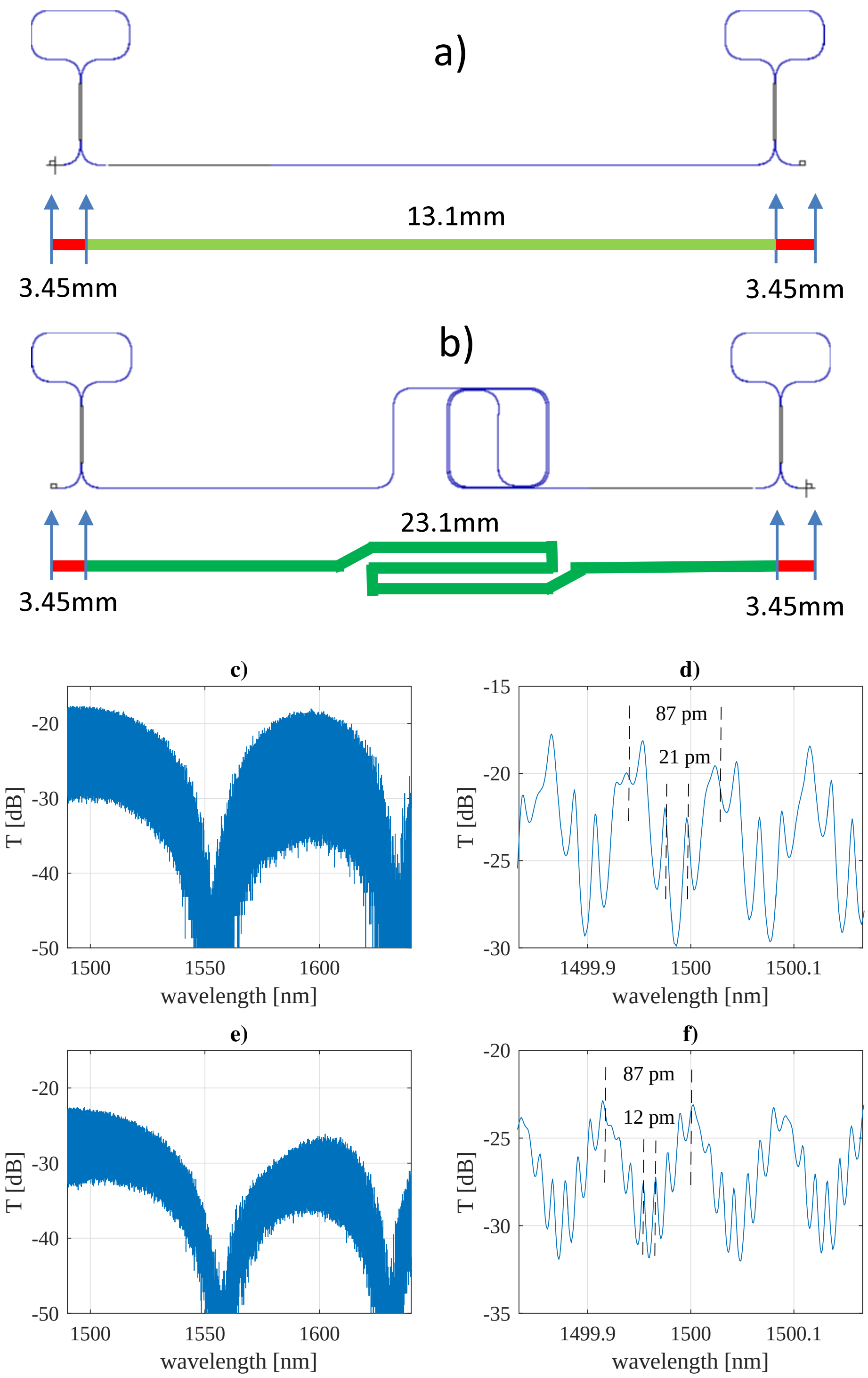

Figure 1.31: a-b) SLM-FP cavities of length 13.1mm and 23.1mm were realized on the chip. c,e) the broadband spectra of both short and long cavity respectively. d,f) the fine structure of the spectra is modulated by two FP. The short-FSR modulation is the desired cavity formed by the SLM, and exhibits the desired FSR of 21 pm and 12 pm for the short and long cavity respectively. The broader modulation is due to the FP formed between the SLM and the spurious facet reflection and is indeed constant in the two cases. However, in the final device, the spurious facets are not present as the cavity will be directly connected with the circuit.

the two SLM, and is indeed the same for the two devices. In any case, in the final device, where the laser is directly connected to the PIC, the facets will not be present and the spurious modulation should be eliminated.

1.6 Mach Zehnder Interferometers

The other important building block of the design is the Mach Zehnder Interferometer (MZI). Mach Zehnder interferometers divide a lightbeam in two by using a beam splitter. The two resulting lightbeams are driven in arms of different length and then recombined with a second beam splitter. Since the two portions of the original light travel a different length in the respective arm of the interferometer, interference will occur after the second beam splitter. Figure 1.32 shows a scheme of the used integrated MZI. The MZI is formed by two waveguides that are bent to form two directional couplers, that act as beam splitters, and the two different-length arms in between. The modulation due to the interference of the MZI is complete when the light is equally distributed in the two arms. This balanced coupling condition is achieved by realizing two 3 dB directional couplers. In a MZI with arm length difference ΔL the interference fringes are separated by a FSR which is

$$FSR = \frac{\lambda^2}{n_g \Delta L}. \tag{1.11}$$

The mask layout contains identical devices that differ only for the MZI arm length. Series of devices with $\Delta L = 10.8$ μm and 8.10 μm are both present, corresponding to FSR of 80nm and 60nm respectively.

The passive characterization of the MZIs is slightly different from that described in 0.3.2 since an MZI is a two inputs - two outputs system, as shown in Fig. 1.32 (top). Figure 1.32 (bottom) reports the transmission spectra of all single-input configurations for a device with a FSR of 80nm. The first panel shows the In-1 Out-1 configuration, which is the transmission of the continuous waveguide that forms the longer arm of the MZI. The spectrum exhibits a shallow and deep interference fringe, implying that the directional couplers are well-balanced. The second panel, In-1 Out-2, shows the reciprocal spectrum, with the interference fringe of In-1 Out-1 now appearing as a peak. This is the configuration that is used as a bandwidth filter in the laser photonic circuit. The 80 nm FSR is pointed by the black arrow near the interference fringes around the central peak. The bottom spectra show how the DC symmetry is reflected in the transmission spectrum: since the used DC are 50%-50% beam splitters, the In-1 Out-2 configuration is equivalent to the In-2 Out-1, while the configuration In-1 Out-1 is equivalent to In-2 Out-2.

It's worth to note that in all the graphs the transmitted intensity is modulated by the FP cavity that is formed between the facets of the waveguides, producing a dense comb of fringes over the MZI spectral response. The modulation intensity, depending on the reflectance of the In and Out facets and on the overall losses, varies slightly among the four measurements. In the MZI case, it is important to consider that because of the directional couplers light is present in both waveguides, so that all four facets play a role in the FP fringes. The effect is apparent by comparing In-1 Out-1 with In-2 Out-2, which exhibit the same MZI spectral response, but with a very different FP modulation.

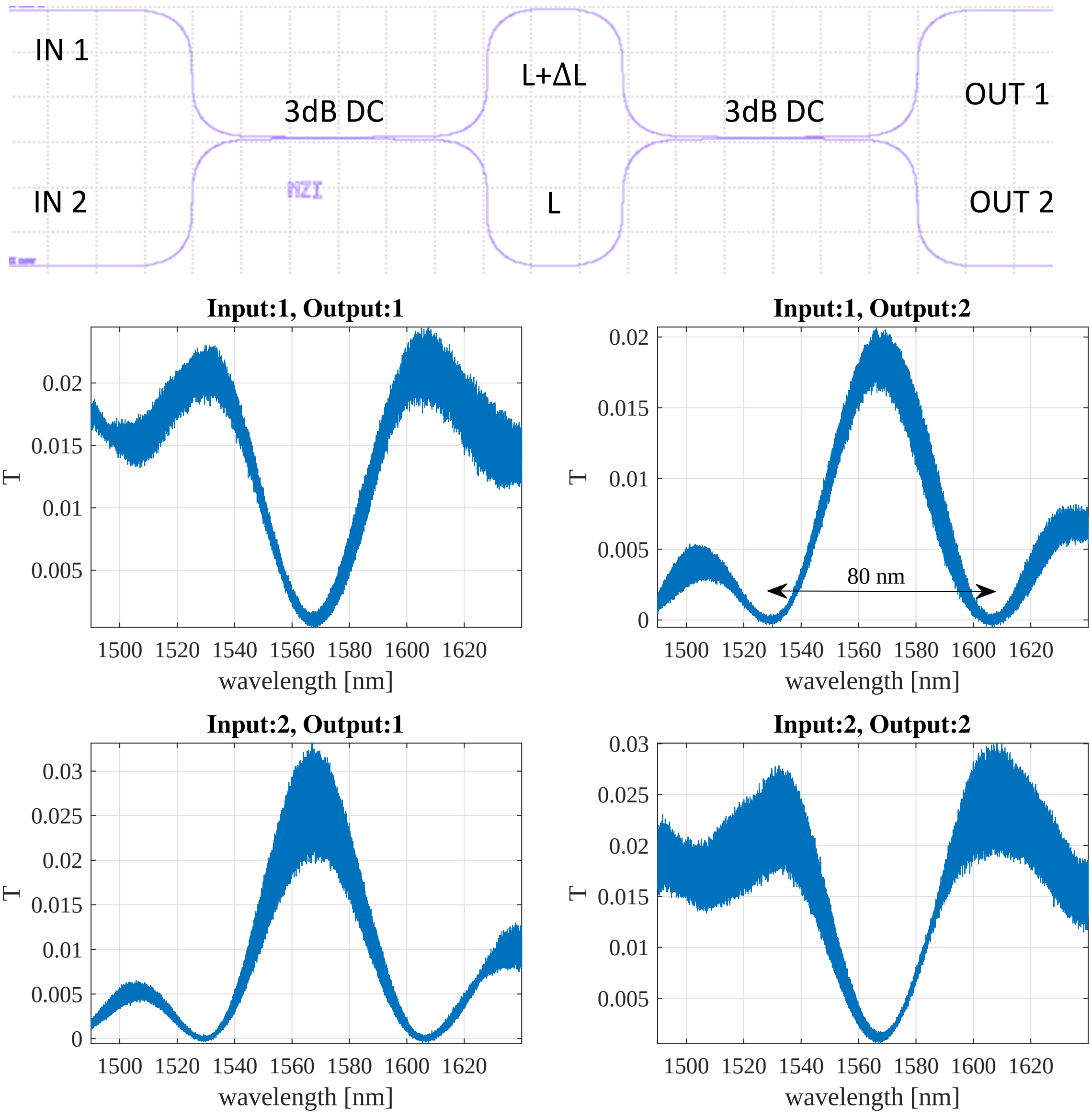

Figure 1.32: Experimental spectra of the MZI. The four panels report the four single-input I/O combinations of the MZI. Since the MZI is realized in order to isolate a band for mode-locking, the DC of the MZI are designed for balanced interferometry, that gives the maximum modulation. The symmetric behaviour is clearly visible by comparing the In:1 Out:1 and In:2, Out:2 panels, which exhibit the same spectral shape. The measured Transmission is slightly different due to the fluctuations in the insertion losses of the four facets. This is also confirmed by the different amplitude of the FP fringes in the four spectra.

The passive characterization of WP1_L1 required the dicing of the wafer, that is therefore no more processable for the III-V integration. A further run WP1_L2 was then realized following the WP1_L1 processing.

1.7 Wafer Bonding

Bonding process

Once the SOI PIC is ready, the III-V material has to be bonded to the wafer to realize the active region. The bonding is realized trough a thin DVS-BCB layer that glues together the SOI wafer and the III-V chip.

The bonding process requires ultra-flat and clean surfaces, as any particle or imperfection larger than the bonding layer thickness ($\sim$ 250 nm) would prevent, at least locally, the contact of the two surfaces. The bonding process relies on the adhesion of BCB on both substrates, that need to be functionalized in order to maximize the adhesion. The functionalization may be realized either by chemical reaction at the surface, or by a thin layer of priming material. In our case, a sub-nanometric thin layer of AP-3000 adhesion promoter is spin-coated on the surfaces at 1500 rpm, and then backed at 125°C for 90 s to promote the adhesion. Then, the BCB solution is spin-coated on the SOI wafer and backed to eliminate the solvent. The BCB thickness value and homogeneity is verified with interferometric measurements.

Then, the InP wafer is manually aligned with the SOI wafers using the flat of the wafer, that mark the crystalline direction, as a reference. To ensure that the angular mismatch among the two crystals is less than 5°, lines parallel to the SOI wafer flat are present on the device. Once aligned, the InP wafer is laid on the BCB by using a sucker. The two wafers are brought on the hot plate of the bonding chamber where they are pressed together and heated in low-pressure N_2 environment to avoid oxidization of the BCB and formation of bubbles. After the bonding, the wafers are gradually brought back to room temperature and removed from the bonding-press, ready for further processing. During the thesis work, we developed the bonding technology step by step by making Si-Si bonding first, then passing to bonding structured wafers, to bonding blank InP wafers to structured Si and finally the III-V wafers to the patterned SOI PIC. In order to couple the light efficiently from the SOI PIC to the III-V gain material and vice-versa the thickness of the BCB layer above the waveguides should be no more than 200 nm, preferably much lower. While there is no commercially available BCB solution for sub micrometer thicknesses, adding a solvent reduces the viscosity of the BCB, permitting to create thinner layers. The BCB thickness is therefore tuned acting on the spin-coater's rotating speed and by diluting the DVS-BCB [64]. Figure 1.33 a) shows the measured thicknesses of BCB as a function of dilution at the speed of 2000rpm. The BCB thickness is approximatively linear with respect to the BCB volume fraction in the BCB-Mesitylene solution. Figure 1.33 b) shows the BCB thickness as a function of the spin-coater speed for a 1:6 BCB-Metisylene solution.

BCB characterization

Si-Si bonding

The bonding technique was tested on Si wafers, structured with 200 nm deep waveguides to simulate the device. A 1:2.5 BCB-mesitylene solution was spin coated on the structured Si wafer at 2000 rpm. After a rapid bake at 135°C for 150 s the BCB thickness resulted 249.0 nm as the mean of five points on a cross over the wafer, with a standard deviation of only 0.5 nm. The low variance reflects the excellent degree

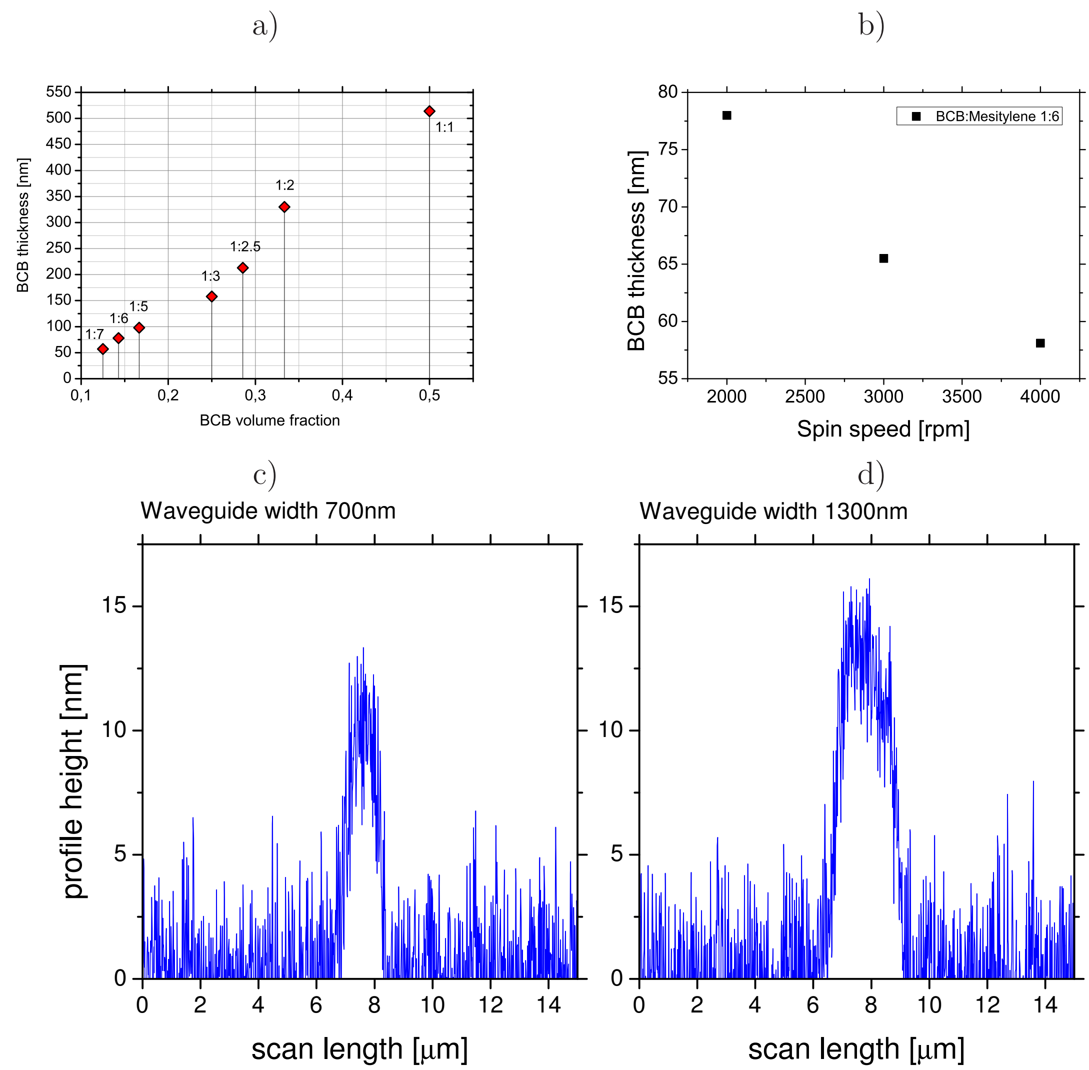

Figure 1.33: BCB thickness as a function of a) the dilution in mesitylene and b) the spinning speed. b,c) profile height measurements of the BCB above the waveguides demonstrates the achieved degree of planarization.

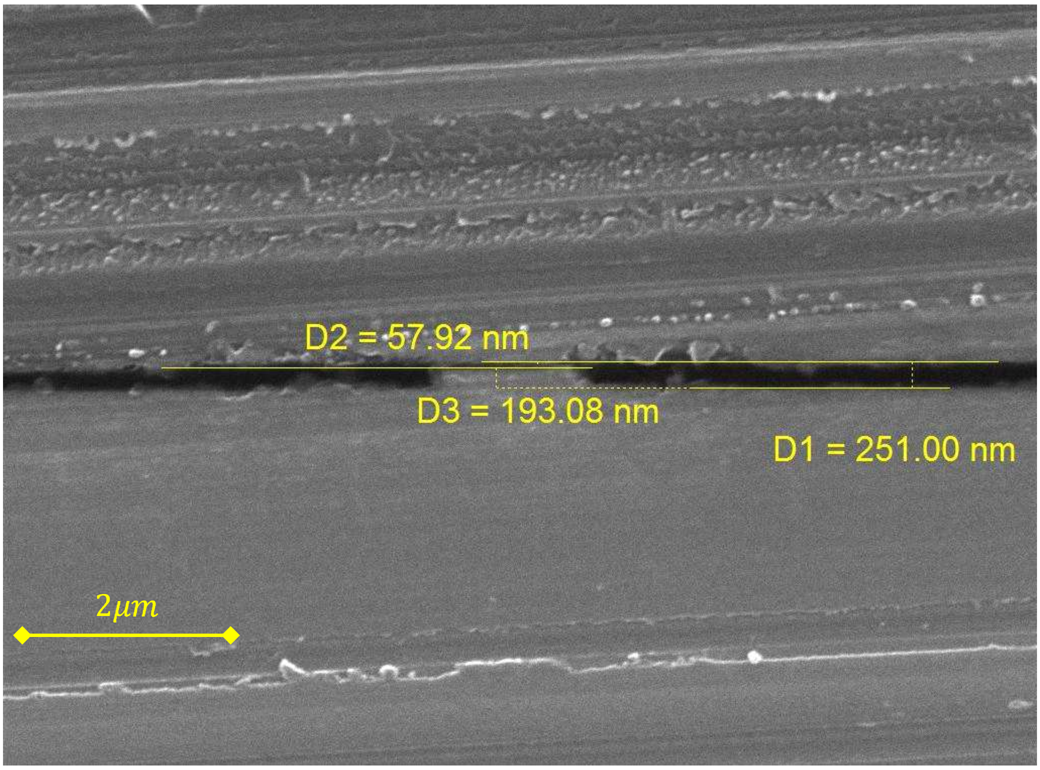

Figure 1.34: Cross section SEM image of a Si die bonded on a structured Si wafer. The image shows how the bonding may be realized with a residual BCB layer on top of the waveguides as thin as 60 nm.

of planarization achieved. Figure 1.33 c,d) shows the profile of the BCB near the waveguides, acquired with a mechanical profilometer with tip radius of 2μm. The BCB forms a smooth bump of only 15 nm over the waveguides, leaving them covered with c.a. 60 nm of BCB.

A 3 cm$\times$3 cm Si die, previously cleaned in BHF and with oxygen plasma, was then positioned and manually aligned at the center of the Si wafer using a dedicated sucker. The wafer was then placed in the bonder chamber, and the die was pressed at 300kPa on the BCB in vacuum environment. The wafer was heated at 150°C for 20 minutes in N_2 atmosphere to pre-bake the BCB. After the pre-bake the pressure was decreased down to 300kPa while the temperature was increased to 250°C for one hour to bake the BCB. During the backing process, the chamber is filled with N_2 to prevent the BCB oxidization.

The bonding resulted successful, as the bonded Si dice remained bonded after a further dicing step to expose the bonded region. Figure 1.34 shows a SEM cross-section image of the bonded structured Si wafer. The image demonstrates the quality of the bonding and the possibility to form a BCB layer that is as thin as 60 nm on top of the waveguides.

Si-InP bonding

The InP wafer is thoroughly cleaned in deionized water with ultra-sound for 10 minutes to remove particles, while organic contaminations are removed by an oxygen plasma at 80°C for 4'20". The 1:2.5 BCB-mesitylene solution was spin coated on the Si wafer at 1500 rpm to obtain a slightly thicker layer. The wafer was then soft baked at 135°C for 150 seconds to let most of the mesitylene to evaporate. The layer thickness, averaged over five points on the wafer, resulted 268.1 nm with a standard

a) b)

Figure 1.35: a) III-V wafer bonded on Si. b) III-V layer after the substrate removal. A small portion of the borders resulted ill-bonded and detached during the substrate etching. Over all, $> 80\%$ of the MQW surface remained after the substrate removal, although deformations of the layer are present on the edges, as shown in Fig.1.36.

deviation of 1.2 nm.

The InP wafer is then positioned and aligned at the center of the Si wafer and placed in the bonding chamber. The wafers are then pressed together in the bonder chamber under vacuum with a pressure of 550kPa. Then the wafers were heated at 150°C for 20 minutes in N_2 atmosphere to pre-bake the BCB. After the pre-bake the pressure was decreased down to 300kPa while the temperature was increased to 250°C for one hour to bake the BCB. Figure 1.35 shows the 2-inch InP wafer bonded on the Si wafer after the cooling.

InP substrate etch

After the bonding, the InP substrate needs to be removed to leave the 3μm thick layer that contains the MQW on the surface. The substrate is etched by immersing the wafer into a ETCH35 ($HCl{:}H_3PO_4{:}H_2O$ 50%:35%:15%) solution at room temperature. Prior to the substrate removal, the etch rate of BCB in the ETCH35 solution was tested by measuring the thickness of cured BCB on a test wafer before and after a 2 hours bath. The measurements were identical within the variance over the wafer, indicating that the cured BCB is not etched by the solution.

The InP wafer was therefore etched in the ETCH35 bath while steering to facilitate the detachment of the hydrogen bubbles that form at the surface. The wafer after substrate removal is shown in Fig. 1.35. An optical inspection of the bonded substrate revealed that imperfections are present, as shown in Figs. 1.36 a-d) and Fig. 1.37 a-b). In panels a) and c) of Fig1.36 it is possible to see that a portion of the InP substrate was completely removed, leaving a mark in the BCB. Panels b) show that the III-V multilayer tends to detach, in most cases starting from the border. d) in some areas the III-V layer detached completely near the border and fragmented during the steering. Figure 1.37 shows particulars of the underneath Si layer with a higher magnification.

Two BCB layers

The wafers were then sent to III-V labs for further processing. However, probably due to residues of mesitylene, the BCB released gas bubbles during the low-power O_2 plasma clean that is performed in the first stages of the III-V material processing. In order to avoid the formation of said bubbles, another approach was attempted

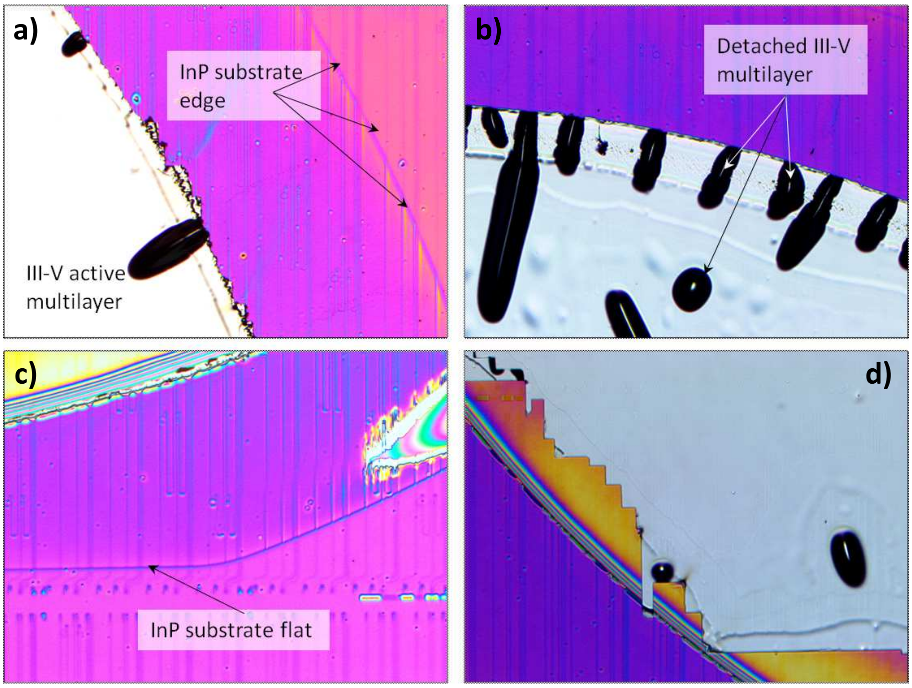

Figure 1.36: Optical images of the bonded III-V substrate. Panel a) show footprint of the substrate ind the BCB. The same footprint is also present in panel c) where the flat of the III-V wafer is aligned to the structures of the SOI wafer. b) the active layer is partially detached near the borders or c) partially etched.

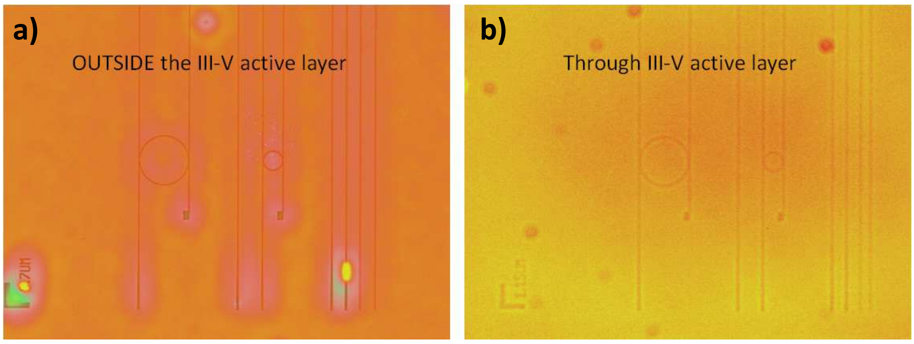

Figure 1.37: Optical images of the SOI PIC a) under the BCB layer and b) through the III-V active layer.

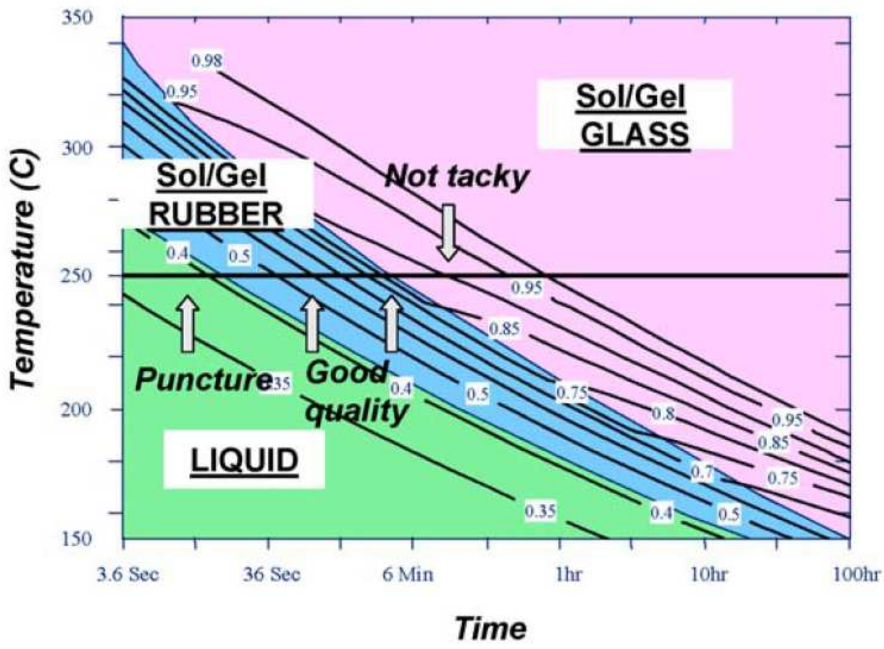

Figure 1.38: Time-Temperature transformation diagram of DVS-BCB. Image from [64]

considering two BCB depositions [64, 65], and compared to the previous approach.

First, a 250 nm 1:2.5 BCB-mesitylene solution is spin coated on three test wafers, previously covered with AP-3000 primer. The first wafer, A, undergoes soft-backing for 150s at 135°C reducing the BCB layer thickness from 245 nm to 228 nm as in the previous trial. The second and third wafers (B and C) are instead hard baked at 210°C for 40 minutes in N_2 environment to remove all the mesitylene. This way, BCB is also partially cured into the Sol/Gel regime as shown in Fig.1.38. In this case, the thickness reduction is much more apparent, bringing the two wafers from 248 nm and 243 nm to 204 nm and 201 nm respectively.

Then, a second 63 nm thick layer of 1:6 BCB-mesitylene solution is spinned on top of the hard backed BCB. Hard backing of the previous layer is necessary to deposit a second layer, otherwise the BCB would just be spin away. The two wafers then undergo a brief thermal annealing at 250°C for 2 minutes in N_2 flux to let the mesitylene evaporate. After the brief thermal annealing the wafers have a total BCB thickness, measured far from the waveguides, of 258 nm and 254 nm respectively.

In order to analyze the bubbles formation on the wafer A and the possible improvements on wafers B and C, a 500 nm thick layer of aluminum is deposited at room temperature on wafers A and B to simulate the RF absorption of the upper semiconductor layer.

Wafers A and B were undergone a series of oxygen plasma etchings with increasing power of plasma to test the bubble formation in the BCB under the metal. The first step consisted in an oxygen plasma with 75W of power for 260s at 82°C. Optical inspection revealed conic structures on wafer A in the aluminum layer, whilst wafer B remained unchanged. The same procedure was repeated two more times with plasma power of 100W and 120W respectively. The conic structures on wafer A progressively grew, while no reaction was observed on wafer B. Since during the III-V processing the plasma RF power is $\leq$ 75W, the test indicates that the double-

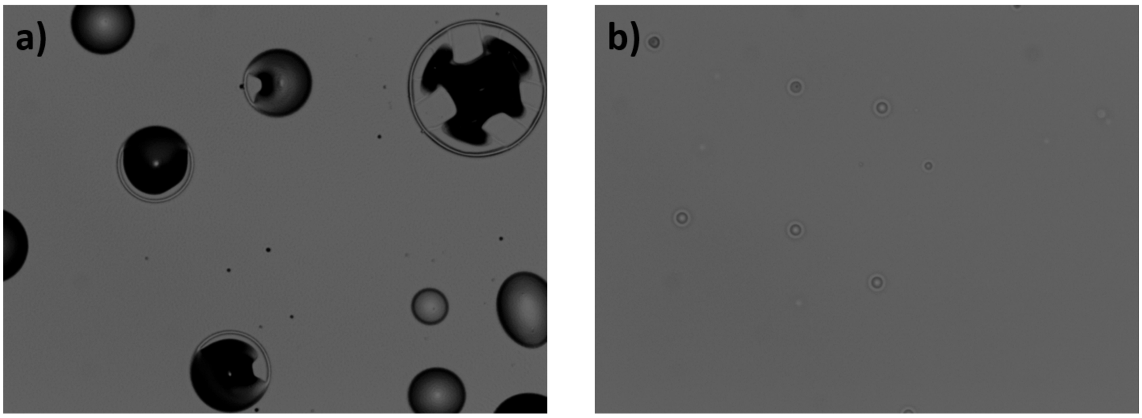

Figure 1.39: Optical image of the effect of bubble formation on the test aluminum layer on wafers A and B after several low-power O_2 plasma cleanings and 1 minute of stronger 450W oxygen plasma at 200°C. a) the aluminum layer on wafer A, which undergone only a soft-baking at 135°C for 150s exhibits severe damage with big bubbles forming conic structures and even burst bubbles. b) the aluminum over wafer B, which has a thick layer pre-cured at 210°C for 40 minutes and a thin layer rapidly annealed at 250°for 2 minutes shows minor defect formations on the surface.

layer BCB spinning should be applicable with no bubble formation. As a further qualitative test, the wafers were subjected to a high power oxygen plasma (Organic strip: 450W at 200°C) for one minute. In this case the substrate temperature is higher, and under the effect of the plasma could possibly reach temperatures that damage the BCB. Indeed, with the high power plasma the bubbles on the wafer A began to explode, as shown in Fig.1.39 a), while small formations began to appear also in wafer B (Fig.1.39 b)).

The last wafer, C, was used for a test bonding with four blank Si dices of 3 cm × 3 cm. The wafers were bonded following the usual procedure: after the manual alignment of the dices on the wafer, the bonder machine was put under vacuum and the Si pieces pressed at 300kPa. Then, the bonding chamber is filled with N_2 to avoid oxidization of the BCB while the bonding stage is heated to 250°C. The BCB is cured for one hour at 250°C maintaining the pressure of 300kPa. After the bonding, the silicon dices resulted well attached.

As the next step, the two-layers bonding was tested on a blank InP wafer, without the MQW layer. The test was realized bonding the blank InP on a structured Si wafer (200 nm etching) using the same procedure as described above. The final double-layer BCB thickness after the second layer brief annealing resulted in 288.5 ± 1.5 nm far from the waveguides. The InP wafer was cleaned in BHF solution, rinsed, and then cleaned in oxygen plasma at 80°C with 200W of plasma power for 3 minutes. Then, the InP wafer was covered with AP-3000 adhesion promoter and soft baked at 125°C for 100 s. The bonding was realized following the procedure described above for the Si-Si bonding, with the exception of the pressure on the InP wafer that was set to 500kPa. The InP wafer resulted bonded.

The substrate was then etched in the ETCH35 solution while steering at 35 rpm. Since the blank InP wafer does not have the III-V device layer protected by an etch stop, the etching had to be repeatedly manually stopped to verify the remaining substrate thickness. After 1.5 hours the bonded wafer was extracted from the etching bath, rinsed, and measured with the mechanical profilometer to measure the remain-

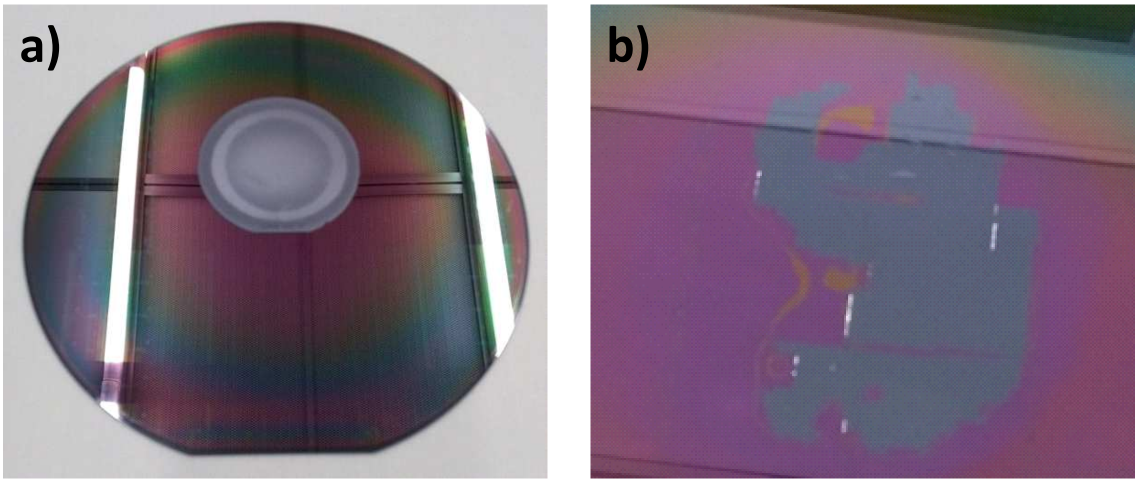

Figure 1.40: a) InP wafer bonded on the patterned SOI wafer and b) III-V layer after the substrate removal. The III-V device layer was partially detached during the substrate etching, but leaved large intact areas.

ing substrate thickness. This procedure was repeated until the remaining substrate was 55 μm thick on average. The etching did not induce InP detaching. The wafer was then tested under oxygen plasma at various RF power to verify the adhesion of the InP and the absence of bubble formation. After two cycles of 75W oxygen plasma at 82°C of 3 minutes each the InP wafer resulted well bonded. The procedure was repeated increasing the RF power to 100W with the same result. The four oxygen plasma etchings consumed the BCB, leaving a BCB thickness out of the bonded region of 138 nm.

The double-layer BCB bonding was finally applied to bond the manufactured InP wafers with the III-V MQW on a structured SOI wafer, using the same procedure as described above. Using the two-layers bonding the SOI wafer, realized following the WP1_L1 process described in Sec. 1.4, was successfully bonded to the InP wafer, as shown in Fig. 1.40.

After the substrate removal in the ETCH35 solution a consistent portion of the MQW layer remained successfully bonded, and therefore the wafer was sent to III-V lab for further processing.

1.8 Conclusions

In this work I designed, fabricated, and characterized a PIC for the realization of a hybrid III-V laser in collaboration with III-V Lab.

In order to achieve a positive overall gain in the cavity I developed and characterized low-loss silicon structures with propagation losses of only 1.7 ± 0.3 dB/cm. The result is up to the state of the art for the used technology and was obtained with a careful iterative design and testing of the fabrication process, where I exploited the HM design to obtain three main advantages:

- **Top surface protection** from the wet-etching of the smoothing process. This was achieved by using silicon nitride as the HM material, that has a very low etching rate compared to silicon in the smoothing process.

- **Enhanced verticality** of the lateral waveguide walls. This is achieved realizing a HM that has a very low etching rate compared to silicon during the etching process.
- **Improved lithography**. By making an anti-reflection coating out of the HM, the quality of the lithography is improved bringing both higher fidelity to the design and smoother photoresist pattern that ultimately resulted into lower propagation losses.

The high quality of the waveguides has been also tested by realizing racetrack ring resonators, that proved to have quality factors comparable with the state of the art of the technology.

Computational simulations were used to analyze and adapt the design of III-V Lab, that was rearranged in various test masks plus the device mask, developing dedicated analysis software where needed.

During the process, I introduced and developed inverse tapers to mitigate the problem of the waveguide facets irregularity induced by the dicing, that causes high insertion losses. With my design, I obtained an average signal increase by 3.5 dB with respect to straight polished waveguides.

Each run of fabrication was undergone rigorous testing, mostly via VASE and SEM imaging to verify and adjust *in-process* the dimensions of the structures. In the trimming process, the computational tools were used to find the optimal geometrical configuration to match the design functionalities. Passive optical characterization of the structures was carried on at each step, making statistical analysis wherever possible and improving the structures with the feedback of III-V labs.

In the meanwhile, the adhesive bonding technique has been developed for Si-Si and InP-Si wafers to join the active III-V material with the PIC. The MWQ layers were successfully bonded to the SOI wafer with the PIC, reaching values of the BCB layer thicknesses as low as 57 nm on top of the SOI waveguides.

Chapter 2

Strip-loaded UHQ resonators

2.1 Introduction

The confinement of electromagnetic radiation in small mode-volumes for long times that is obtainable in Whispering Gallery Mode Resonators (WGMR) enhances the light-matter interaction permitting to explore a variety of phenomena.
The figure of merit characterizing the resonant modes of a WGMR is the Quality factor Q. The quality factor represents the capability of the optical cavity to store the light for a time much longer than the lightwave period. The classical definition of Q-factor for an optical cavity is

$$Q = \frac{\omega_m U_c}{P_{\text{loss}}} \tag{2.1}$$

where U_c is the energy stored inside the cavity, ω_m is the optical frequency of the resonant mode, and P_{loss} is the power dissipated by the resonator. In practice, the quality factor of a cavity is usually expressed in terms of the central wavelength (frequency) $\lambda_0(\omega_0)$, and the resonance width $\Delta\lambda(\Delta\omega)$ as:

$$Q = \frac{\lambda_0}{\Delta\lambda} = \frac{\omega_0}{\Delta\omega} \tag{2.2}$$

In general, when dealing with quality factors exceeding the million, it is said that the resonators exhibits a Ultra High Quality (UHQ) factor [66].

From Eq. 2.1, the Q-factor of a cavity is inversely proportional to the loss of the resonator. The loss may come from various sources and sum directly. This means that the quality factor of an optical cavity is proportional to the inverse of the sum of all of the loss contributions

$$Q \propto \frac{1}{\Sigma\alpha_i}. \tag{2.3}$$

The most important loss terms in practical applications are usually four:

1. Material losses, given by material absorption;
2. Scattering losses, caused by the surface roughness of the resonator.
3. Bending losses, due to the finite size of the cavity;
4. Coupling losses, which are necessary to drive the cavity;

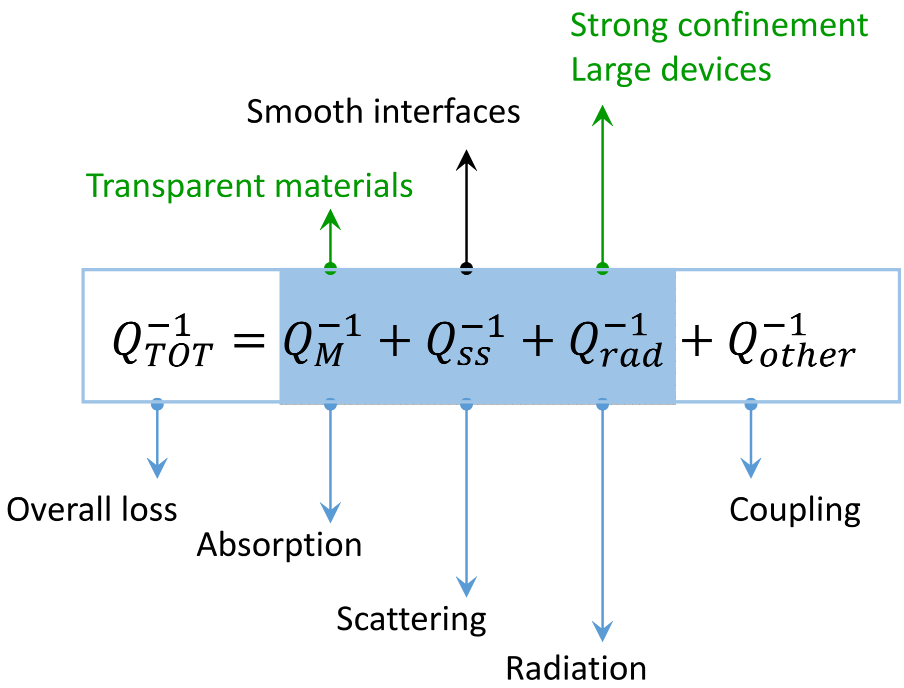

Figure 2.1: The total quality factor of a cavity may be expressed as an inverse sum of various contributions: material absorption, surface scattering, radiative losses, mainly due to bending and coupling losses. The first three terms, highlighted by the box, constitute the intrinsic quality factor, while the last contribution, Q_{other}, is controlled by the coupling design.

Equation 2.3 may also be expressed in therms of an inverse sum of the various contributions to the quality factor, as shown in Fig. 2.1. Apart from the coupling losses, which are usually under control as explained in Sec.0.2.3, the other kind of losses are intrinsic, and need to be addressed while designing an optical cavity. Material losses are countered by making use of very transparent materials. In the case of high fields inside the resonator, the material is also required to have a bandgap larger than twice the photon energy to avoid Two Photon Absorption losses. Bending losses may be addressed either by realizing structures with a large curvature radius, or with a large confinement factor. The remaining contribution, the scattering losses, is often the dominant term in integrated devices, where the surface patterning through Reactive Ion Etching (RIE) generates rough surfaces. Surface scattering is countered in a number of modes, the most important being mode confinement, sidewall-smoothing and low index-contrast.

Indeed, UHQ cavities are typical in microspheres [67, 68] and microtoroids [69], where the sidewall roughness can be very small due to the absence of etching processes. In addition, the mode confinement is high due to the dimension of the cavity and the index contrast between a low-index glass and air. On the other side, realizing integrated cavities with comparable performances is a challenge of significant importance for various fields of application, such as sensing [70, 71], space [72, 73], communication networks [74, 75] and quantum optics [76, 77].
In the past, different approaches have been investigated to reach UHQs in integrated structures, as wet etching on suspended oxide structures [78] and thick silicon nitride [79, 80, 81] resonators. Etchless silicon waveguides and resonators have also been

investigated [58, 82, 83], where the high confinement and index contrast offered by silicon can be retained.
In this work I present the design, fabrication and characterization of fully integrated resonators based on silicon nitride in strip-loaded (SL) configuration [84] reaching Q-factors exceeding 10^6.The great advantage of the strip-loaded waveguides is that light travels mostly within the etch-less slab layer, sensibly reducing the scattering losses.
After a coarse simulation, fabrication and measurement of test structures to demonstrate the wave-guiding in the NIR (780 nm), the strip-loaded structures are studied with FEM simulations to optimize the geometrical parameters in both NIR and third-telecom window (1550 nm). The samples are fabricated using a slab of LPCVD Si_3N_4 as main guiding material, and silicon oxide, deposited with various techniques, as the index-loading material. The samples transmission is then measured to characterize the propagation and bending losses in dedicated structures. Furthermore, series of racetrack resonators have been designed and measured in the SL configuration, that exhibited UHQ-factors.

2.2 Strip-loaded guiding

In Strip-Loaded (SL) configuration the guiding material is a slab of high refractive index material, that ensures light confinement in the plane. Lateral confinement within the plane is achieved with a strip of a "load" material, situated above the slab, that locally increases the effective index. Figure 2.2 shows an example of SL waveguide. In this case, the slab is realized in LPCVD silicon nitride (Si_3N_4), on top of a 4μm thick silicon oxide cladding, while the load is realized in silicon oxide, with no other upper cladding.

Since the light is mostly guided in the slab, which is a planar structure, the concept of waveguide core becomes blurred in the SL configuration. While the contrast between the bulk refractive indices of the used materials is important to determine the scattering losses, it is useful to define some quantities that mimic the standard waveguide parameters. In the case of SL-waveguides, indeed, the typical definition of refractive index contrast [85], Effective contrast

$$\Delta n = \frac{n_{\text{core}}^2 - n_{\text{clad}}^2}{2n_{\text{core}}^2} \tag{2.4}$$

suffers from the ambiguous definition of the waveguide core and cladding. Indeed, if the silicon nitride slab is considered as the core, the modes guided by the SL configuration and the slab modes would have the same contrast. While the usual definition of index contrast is to be used locally to evaluate the scattering losses at the interfaces, it is useful to define another quantity to describe the in-plane confining properties of the SL waveguide.

It is useful to define the effective index contrast of a strip-loaded waveguide Δ_{eff} in terms of the strip-loaded waveguide mode n_{eff} and the slab-guided mode n_{slab}, defined as

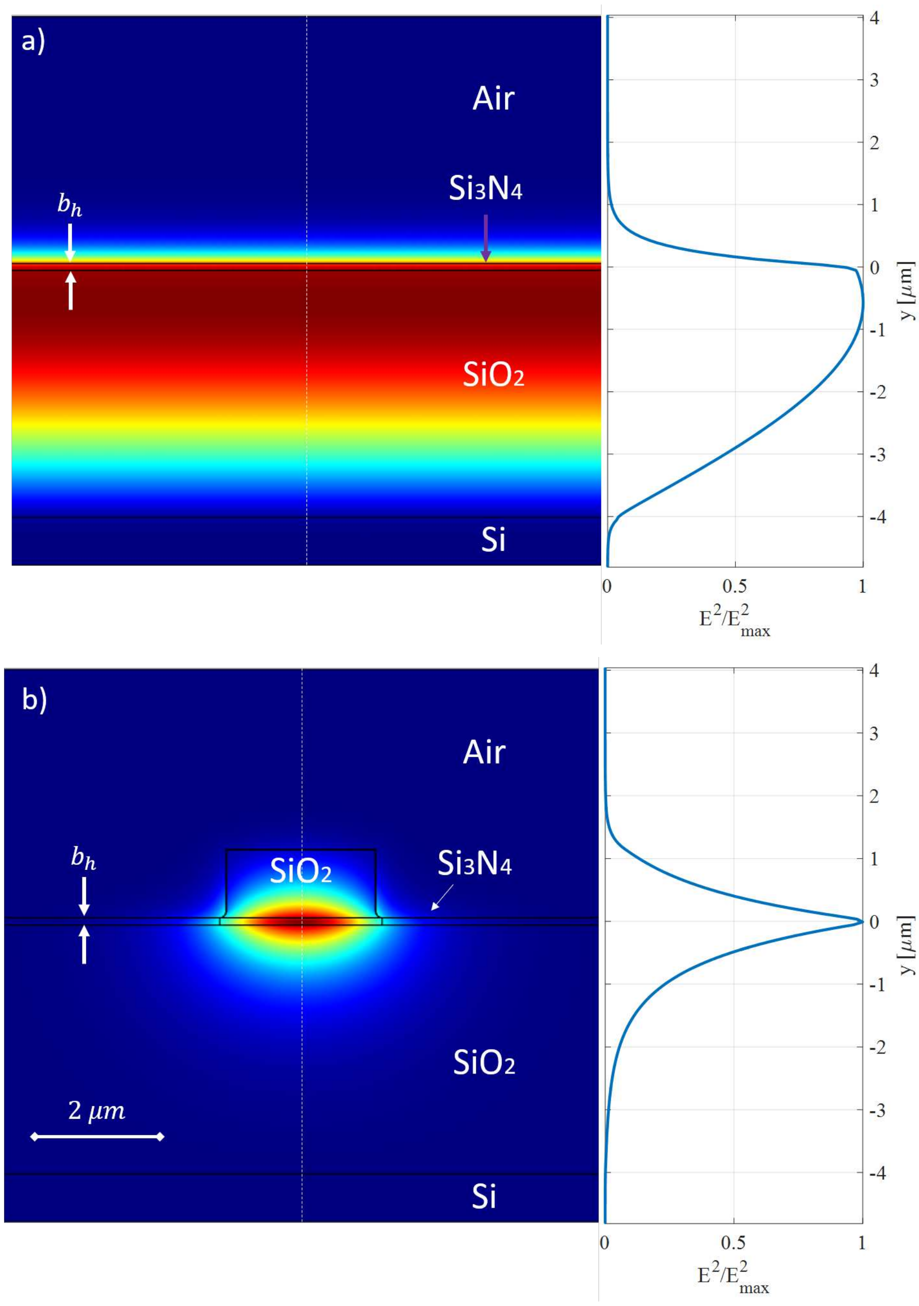

Figure 2.2: 2D FEM simulation of a SL waveguide mode profile. a) the mode is confined in the vertical direction by a thin Si_3N_4 slab, with long tails extending in the high index bottom cladding. b) when the loading strip is present the effective refractive index of the slab is locally changed, and the mode is localized under the strip, sensibly reducing the mode extension towards the substrate. On the right, the section (dashed white line) of the respective electric field intensity is reported in the two cases.

$$\Delta n_{\text{eff}} = \frac{n_{\text{eff}} - n_{\text{slab}}}{n_{\text{eff}}} \tag{2.5}$$

The effective index contrast represents the capability of the SL-waveguide to confine the light within the plane under the loading strip. For thin Si_3N_4 layers loaded with a SiO_2 strip the effective contrast is very low (<0.03) in a wide wavelength range for single-mode waveguides. A low Δ_{eff} implies in general high bending losses, meaning that large radii are needed to realize efficient structures. A high value of Δ_{eff} means that the mode is well confined by the loading strip. This definition of Δ_{eff} is therefore useful in our contest to understand the best geometrical configuration in order to avoid scattering losses towards the slab channel.

The principal degrees of freedom in designing the waveguide are the slab thickness b_h, the load strip width l_w and the load strip height l_h. To individuate the geometry which provides with the better waveguiding it is useful to discuss through FEM simulations the behavior of the effective index contrast as a function of these three parameters and of the wavelength.

As a first step, during the realization of the proof-of-concept devices, an existent layout was used, fixing the loading strip width parameter $l_w = 1100\ nm$. The oxide thickness was also fixed to a value of 1 μm. During this first phase, I will therefore focus on the slab thickness, b_h, as the only free parameter and will consider the others fixed.

From general considerations, the effective index of both the slab and the SL-waveguide should increase when increasing the slab thickness, and should decrease with increasing wavelength, as the ratio b_h/λ_0 becomes smaller.

This general behavior is indeed reflected in the FEM simulations of Fig. 2.3, where the behavior of the effective refractive index contrast is reported as a function of wavelength and slab thickness.

For each slab thickness, the effective index contrast exhibits a maximum, which shifts towards longer wavelengths as the slab thickness is increased, forming a crest. These maxima have higher values at short-wavelengths and thin slab, that decrease gradually when the slab thickness is increased, as the mode results more confined in the slab the evanescent field penetrates less into the loading strip.

It is therefore apparent from Fig. 2.3 that the configuration that maximizes the contrast features a thin Si_3N_4 slab that guides the better at short wavelengths. The slab thickness was therefore optimized for the study with a NIR laser operating between 770 nm and 790 nm, leading to an optimum slab thickness of 77 nm.

As a further note, the realization of a prototype guiding in the third-telecom band was also considered in this stage. However, using the fixed $l_w = 1100$ nm the maximum contrast is achieved at a thick (>160 nm) Si_3N_4 slab. The LPCVD silicon nitride layer produces a high stress on the wafers, which had proven to lead to film cracking for film thicknesses above 130 nm, preventing the realization of thick Si_3N_4 layers.

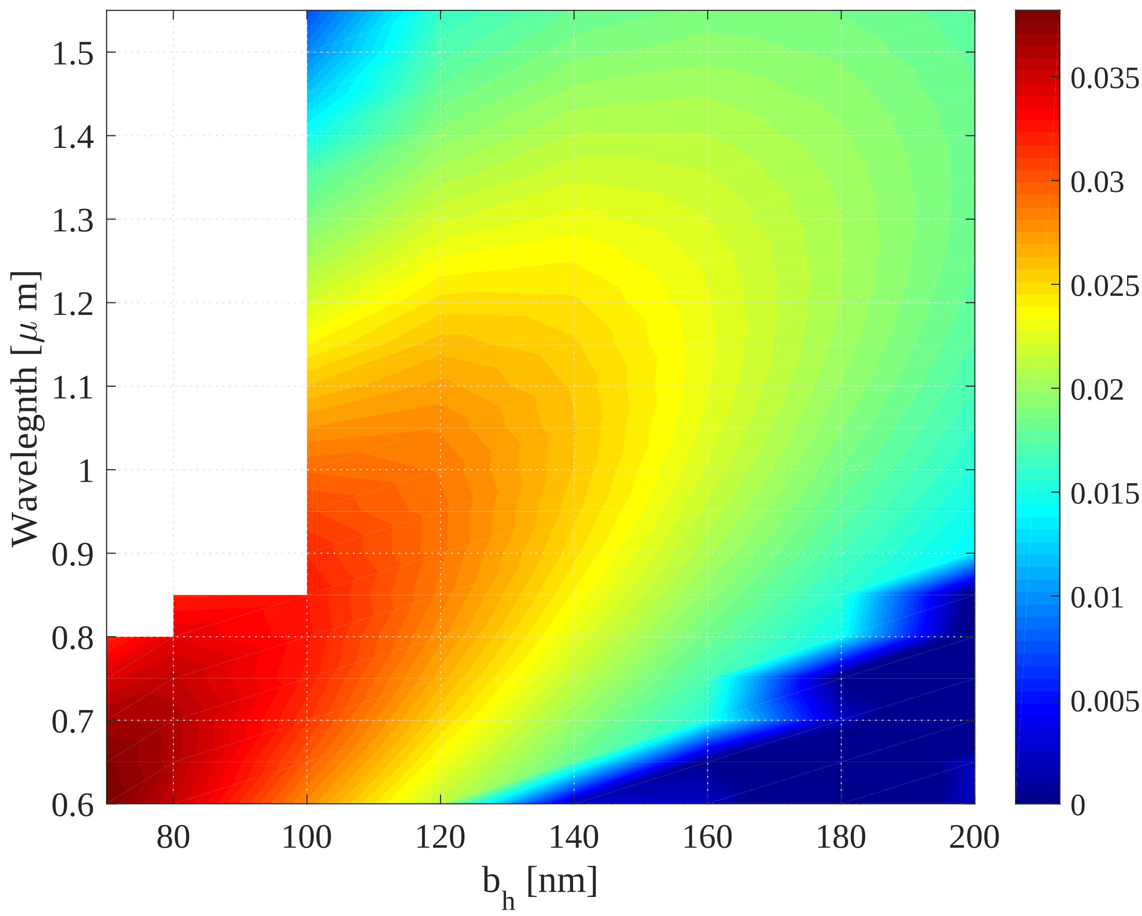

Figure 2.3: Effective index contrast Δ_{eff} between the slab-guided and the strip-loaded guided modes as a function of the slab thickness b_h and the probe wavelength obtained from 2D FEM simulations.

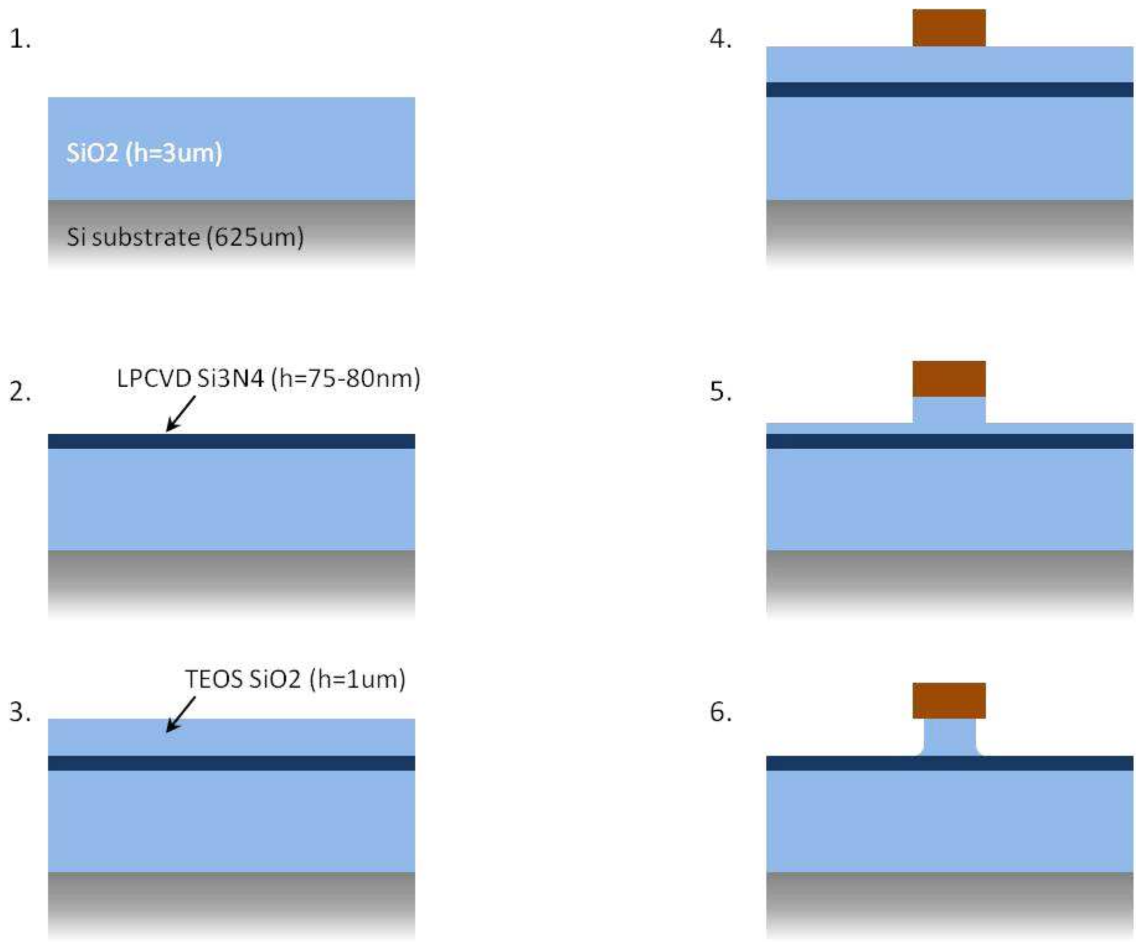

Figure 2.4: The process flow used to realize the SL waveguide. (1) Growth of a 3um-thick thermal oxide cladding on top of a silicon substrate. (2) The deposition of LPCVD Silicon Nitride of 77nm (planar waveguide) is followed by (3)a deposition of TEOS oxide of 1.0 μm. (4) A lithographic step is used to pattern waveguide structures on top of TEOS, which is (5) first dry-etched for 0.9 μm. (6) and wet-etched for the last 100 nm in a BHF solution. This last wet etching step is highly selective, etching the TEOS oxide at a fast rate and leaving the Si_3N_4 layer unaltered. Finally, the remaining photoresist is removed and device chips are diced.

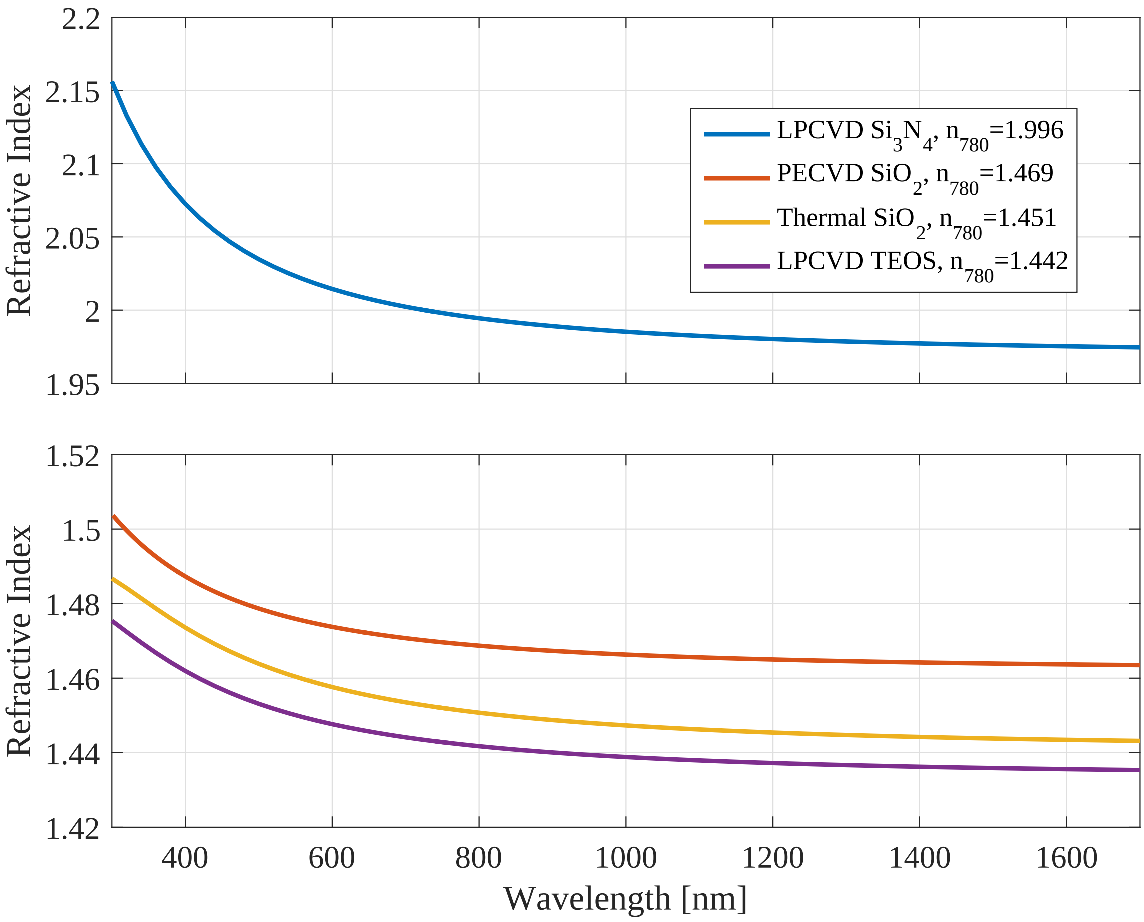

Figure 2.5: Bulk refractive index dispersion for the materials used for the bottom cladding (Thermal oxide), the guiding slab (LPCVD Si_3N_4), and loading rib (TEOS / PECVD SiO_x).

2.3 Proof of concept

The strip loaded prototypes were then realized following the fabrication process flow sketched in Fig. 2.4. The process began with growing a 3000 nm thick thermal oxide on top of crystalline silicon wafers. Afterwards, LPCVD was used to deposit a 77 nm thick layer of silicon nitride Si_3N_4 followed by 1000 nm of TEOS. All the various materials refractive index dispersions and layer thicknesses were carefully controlled by Ellipsometric measurements (VASE). The measured dispersions of the used materials are reported in Fig. 2.5.

Next, the wafers were coated with photoresist (Fujifilm OIR 674-9, 760 nm thick) and the waveguide structures were patterned using the stepper-lithography. The exposed photoresist was developed and hard baked at 120°C for 1h. Then, the TEOS was etched for 900 nm using RIE, leaving a 100 nm layer still covering the slab. The remaining 100 nm of TEOS was wet-etched in a BHF 7:1 solution. The combined dry and wet etchings have a double effect:
(i), the high etch rate for the TEOS, about 375 nm/min, produces a smooth circular foot at the base of the oxide loading strip, where the evanescent tails of the mode are stronger;
(ii), in contrast with RIE, the etching rate of Si_3N_4 in BHF is null. Therefore, it acts as an etch-stop layer, leaving the guiding slab layer untouched.

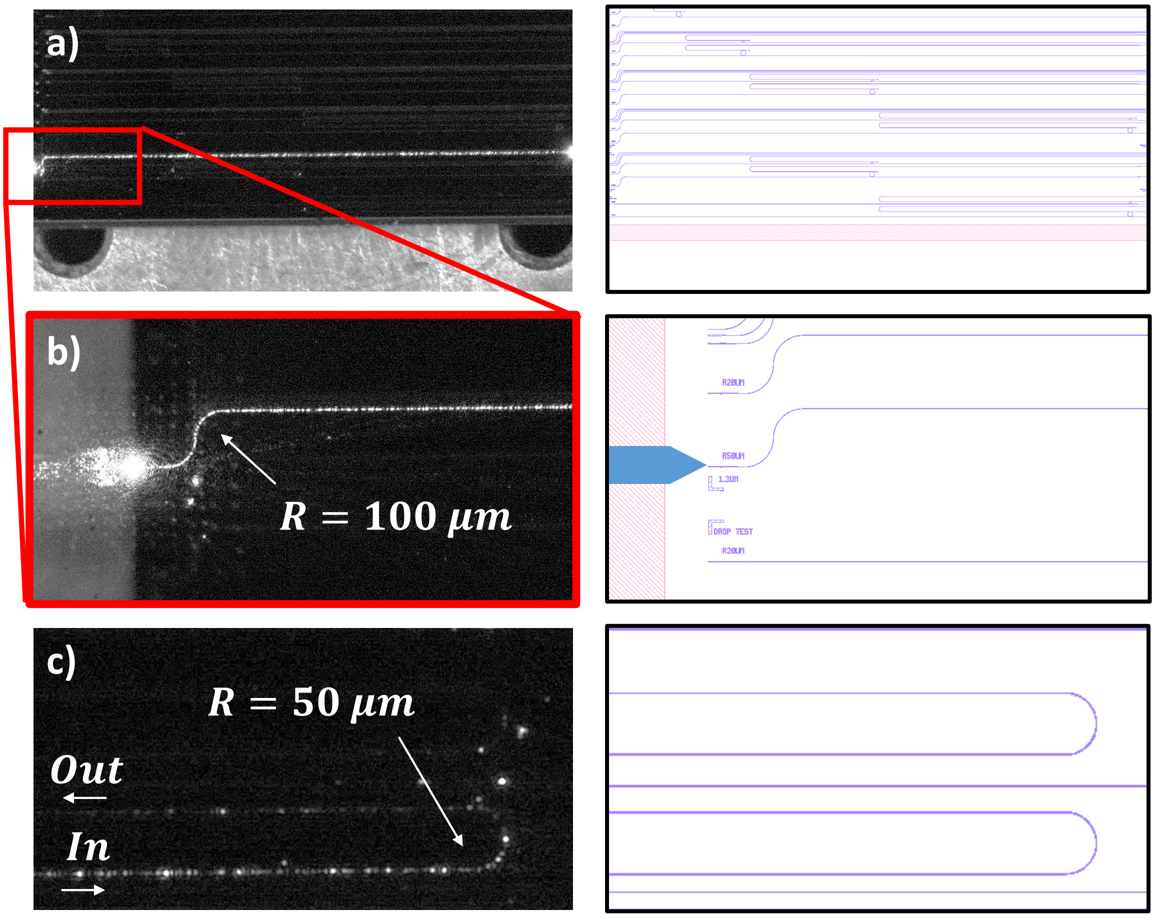

Figure 2.6: The waveguiding properties of the strip-loaded prototype are assessed by top-view image acquired with a camera over the sample. On the right is shown the respective device layout of the field view. (a) the light is coupled inside the sample on the left, and produces a bright spot on the right at the output. The scattered intensity does not visually decrease over the waveguide length (1 cm). (b) the light travels through the waveguide bends that are present at the input, which have a curvature radius of 100 μm, (c) but is strongly attenuated by the 50 μm bends, present on other regions of the chip, due to radiative bending losses.

After this, the remaining photoresist was removed in a Piranha solution (85% H_2SO_4 and 3.5% H_2O_2 at 95°C for 40 min). At this point the waveguides are ready for the facet definition. In this case, the facets were defined using RIE, followed by a Deep Reactive Ion Etching (DRIE) to form a groove larger than the dicing saw, thus avoiding that the saw comes in contact with the facets.

Therefore, the wafers were prepared for a second lithographic step with a dedicated mask that leaves all of the chip protected but for the waveguide edges. During this step, a thick photoresist (AZ, 6 μm thick) is used to protect the PIC from the aggressive DRIE, leaving only a few microns of waveguide extremities uncovered. The waveguide facets are defined with RIE by etching the layers down to the Si substrate. Then DRIE is used to etch the Si substrate for 35 μm realizing a deep groove. Finally, the wafers were diced and prepared for optical characterization.

The samples were characterized using a passive characterization setup similar to that described in Sec. 0.3.2, but using components for the NIR. The source is a tunable NIR laser diode (770 nm-790 nm) that passes through a polarization control stage and is injected into the sample using a lensed fiber. At the other side of the sample, the light is collected with another lensed fiber and sent to the detector.

Proper measure of the propagation losses inside the substrate had not been possible due to the lack of structures with different length and the impossibility to efficiently cleave the sample at different lengths. The waveguiding of the structure was therefore assessed qualitatively by acquiring the light scattering from the top of the sample with a camera, as shown in Fig. 2.6.

Figure 2.6(a) demonstrates that the light is coupled in the waveguide and passes through the whole chip, which is 1 cm long. The scattered intensity does not visually decrease over the waveguide length, indicating low scattering losses. Panel (b) shows that the light is transmitted through the waveguide bends that are present at the input, which have a curvature radius of 100 μm. Since the bending losses depend strongly on the curvature radius of the bend, further tests were performed in other structures with a shorter bending radius of 50 μm, shown in panel (c). Here, the light is visibly attenuated by the 180°bend, suggesting strong bending losses for such curvature radius.

The strip-load guiding in Si_3N_4 was therefore successfully demonstrated by the proof-of-concept devices.

2.4 Numerical Simulations

Next, we realized a optimized layout design for SL-waveguides and resonators in both the NIR and IR bands. FEM simulations were used to optimize the SL waveguides with respect to the parameters l_w, and b_h and to analyze the guiding behavior with respect to l_h. The optimization was realized around the target wavelengths of 780 nm in the NIR and 1550 nm in the IR. For clarity, the names of the target spectral regions, NIR and IR, will be used to identify the respective simulations and realized chips.

NIR and IR target wavelengths

The FEM simulations were performed following the same approach for both spectral regions. First, the effective refractive index contrast Δ_{eff} is mapped as a function of b_h and l_w, leaving momentarily l_h fixed at the maximum height of 1100 nm. In order to calculate Δ_{eff}, the effective index of the fundamental modes of the slab are obtained as a function of the slab height, $n_{\text{slab}}(b_h)$, while the effective refractive index of the SL-guided mode is simulated as a function of both the slab width and the loading strip width, $n_{\text{eff}}(b_h, l_w)$. The best parameters for SL-guiding may then be obtained by finding the maximum of Δ_{eff}. However, while the effective index contrast increases for the fundamental mode, higher order modes may reach $\Delta_{\text{eff}} > 0$ and be guided.

Single Mode Operation

Therefore, in order to achieve single mode operation of the waveguides, it is necessary to simulate at least the effective index of the higher order SL-guided mode TE2 in order to evaluate the region where $\Delta_{\text{eff}}^{\text{TE2}} > 0$.

Figure 2.7 shows the resulting $\Delta_{\text{eff}}(b_h, l_w)$ map for the a) TE1 and b) TE2 modes at wavelength 780 nm. The effective contrast of the fundamental mode TE1 increases monotonically as a function of l_w, asymptotically approaching the contrast of a slab embedded in two claddings of thermal oxide and TEOS. As the loading strip is made larger, however, higher modes begin to be guided, as it is shown in Fig. 2.7 b). The bold green line marks the region where the effective contrast of the TE2 mode achieves $\Delta_{\text{eff}}^{\text{TE2}} > 0$, becoming guided, and is reported in both panels a) and b) for clarity. The working point for the realization of the SL-waveguides (black dot) has been chosen

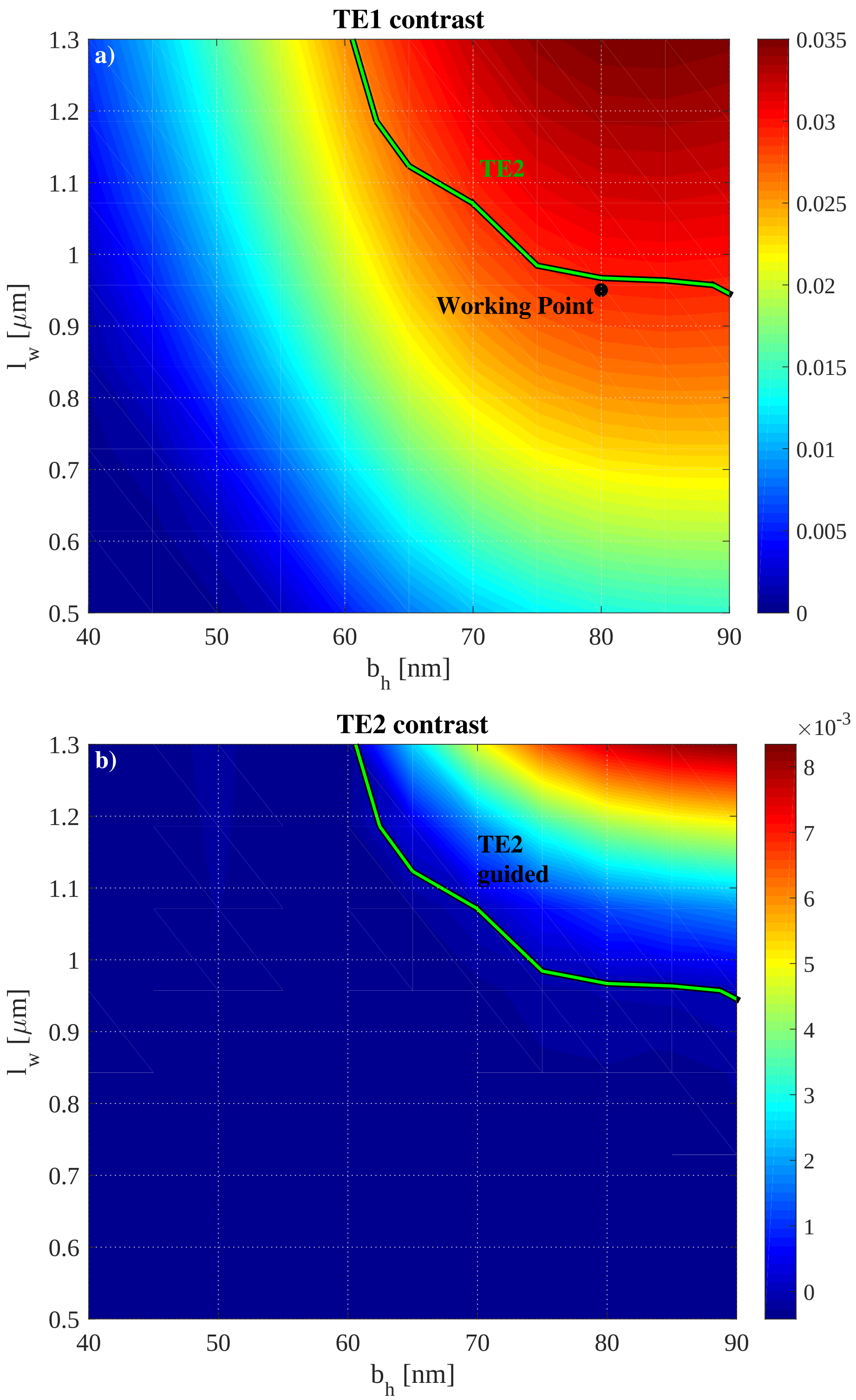

Figure 2.7: Refractive index contrast as a function of the slab thickness b_h and loading strip width l_w for a) the TE1, b) TE2 modes in the SL configuration at wavelength 780 nm. The maximum contrast for the TE1 steadily increases with the l_w, asymptotically approaching a Si_3N_4 slab embedded between two SiO_2 claddings. The green bold line represent the point of zero effective contrast for the TE2 mode, determining the single mode condition. Therefore, the working point, marked with the black dot, has been chosen at a safe distance from the multi mode condition for TE polarization.

maximizing the effective index contrast of the TE1 mode out of the $\Delta_{\text{eff}}^{\text{TE2}} > 0$ region in the (b_h, l_w) parameter space.

An analogous procedure was repeated for the IR region, as it is shown in Fig. 2.8. In this case, the b_h domain has been upper-bounded to 130 nm in the FEM simulations because of the risk of wafer cracking due to the high stress induced by thick layers of Si_3N_4 during the fabrication process. Panel a) shows $\Delta_{\text{eff}}(b_h, l_w)$ for the fundamental TE1 mode. The purple and green lines represent the boundary over which the TM1 and the TE2 modes are SL-guided respectively. It's worth to note that the TM1 contrast has to be calculated with respect to the TM fundamental mode of the slab, and does not interfere with the waveguide geometry optimization in our experiments, where the polarization is selected by external mean. The working point, marked with a black dot, has been selected again maximizing the TE1 contrast near the edge of the TE2-guided region, and has coordinates $b_h = 120$ nm and $l_w = 2.4$ μm.

Figure 2.8 panels b) and c) show the effective contrast for the TM1 and TE2 mode respectively. Due to the rather large waveguide widths (4.5μm) explored in the simulation, an ample region where the TE2 mode is well SL-guided ($\Delta_{\text{eff}}^{\text{TE2}} > 0.02$) is present. Figure 2.9 shows the normalized intensity profile of the a) TE1, b) TM1 and c) TE2 optical modes inside the SL-waveguide.

As a further study, the FEM simulations for the IR band were extended to the unaccessible b_h region from 130 nm to 190 nm, restricting the l_w below 2.1 μm due to the presence of the TE2 mode. The results of this simulations, IR*, are shown in Fig. 2.10. Panel a) shows the $\Delta_{\text{eff}}(b_h, l_w)$ map in the extended region. The TM1 mode, shown in panel b), has crossed the TE2 mode in the (b_h, l_w) parameter space, including more than half of the simulation domain. Not considering the TM polarized mode, that would be excluded in our case by injecting polarized light, the best single mode condition point is identified by the gray dot.

During the numerical simulations, the height of the loading strip has been kept fixed at $l_h = 1.1$ μm. This limit was imposed by the maximum TEOS thickness that can be safely deposited on the wafer.

The behavior of the effective index contrast was further studied, through numerical simulations, near the working points found during the $\Delta_{\text{eff}}(b_h, l_w)$ maximization. $\Delta_{\text{eff}}(l_h)$ is expected to monotonically increase with l_h, as the increased quantity of higher-than-air index material increases the loading capacity of the strip. On the other end, the exponential shape of the evanescent tails of the mode are reflected in $\Delta_{\text{eff}}(l_h)$ that rapidly converges to its asymptotic value over a length $l_h \approx \lambda$. This behaviour is observed in the numerical simulation results, shown in Fig. 2.11. In the (blue) NIR waveguides case , $\Delta_{\text{eff}}(l_h)$ saturates very fast. In the (orange) IR case, due to the limited thickness of the slab, the evanescent tails are pushed further into the loading strip, slowing down the saturation of $\Delta_{\text{eff}}(l_h)$. The effect is well evidenced by (yellow) the faster convergence for the IR* case, obtained with the optimized geometry for the IR without the slab thickness restriction. In all cases, the starred dots represent the design values for l_w, which is restricted to 1100 nm in the IR case due to the fabrication constraints.

Finally, Tab. 2.1 summarizes the final values for the optimized parameters in the NIR, IR and IR* cases.

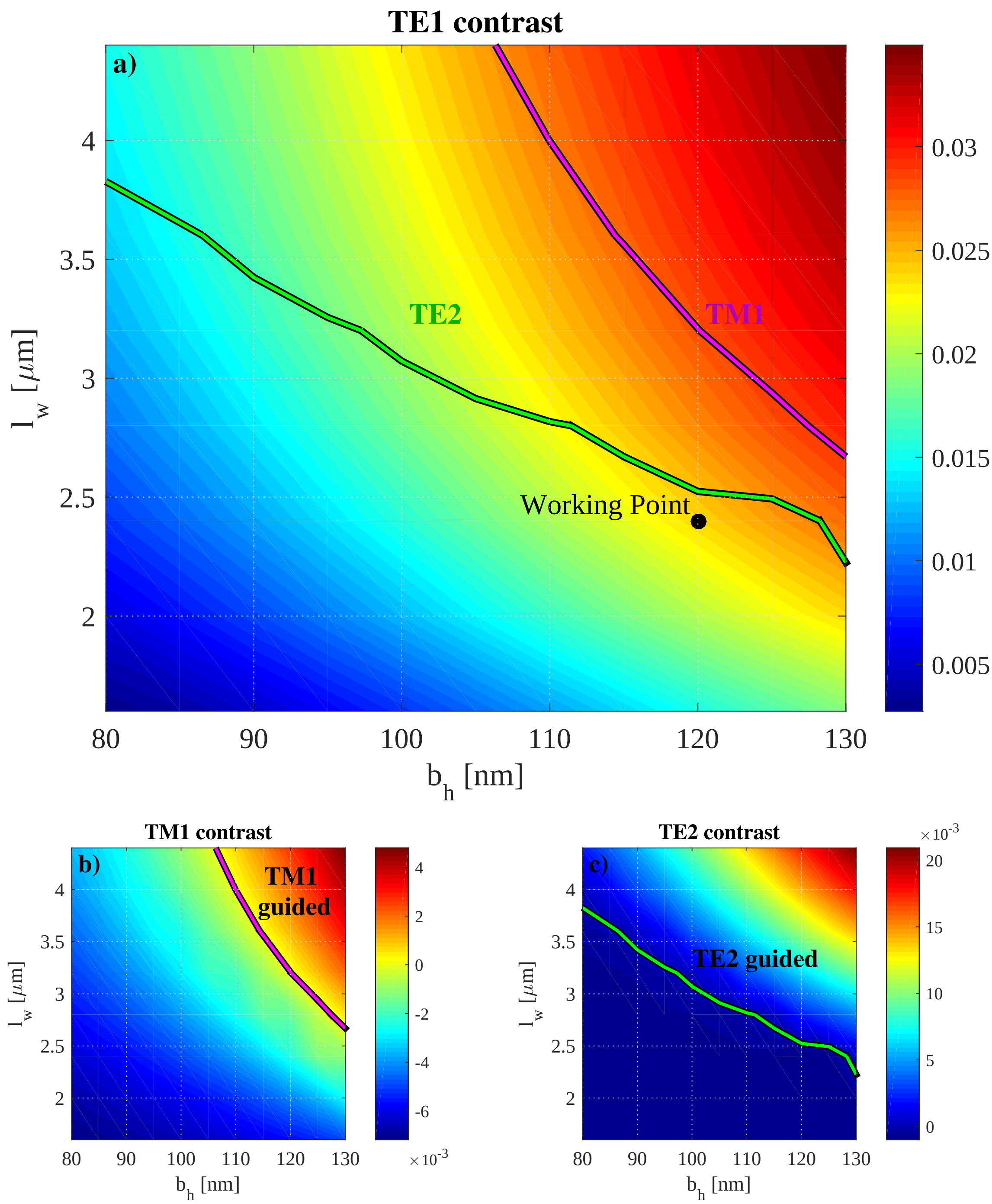

Figure 2.8: Refractive index contrast as a function of the slab thickness b_h and loading strip width l_w for a) the TE1, b) TM1 and c) TE2 modes in the SL configuration at wavelength 1550 nm. The b_h values are restricted below 130 nm, over which film cracking occurs. The maximum contrast for the TE1 steadily increases with the l_w, asymptotically approaching a Si_3N_4 slab embedded between two SiO_2 claddings. The green(purple) bold lines represent the point of zero effective contrast for the TE2(TM1) mode, over which these additional modes are guided. Therefore, the working point, marked with the black dot, has been chosen at a safe distance from the multi mode condition for TE polarization.

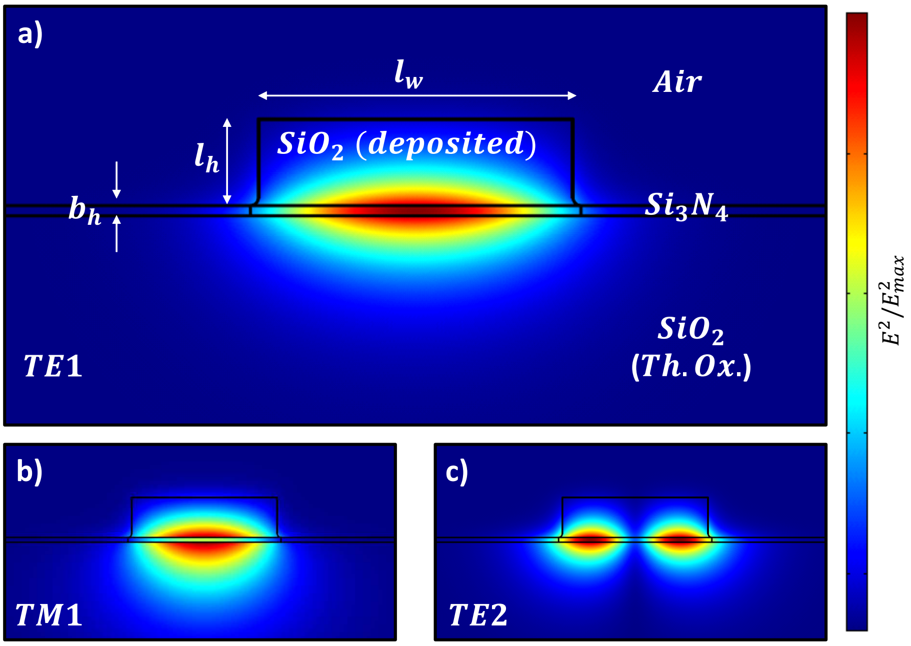

Figure 2.9: a) TE1 b) TM1 and c) TE2 SL-guided modes simulations. The images refer to the top-right point of Fig. 2.8 with waveguide parameters l_w = 4 μm, b_h = 130 nm, and l_h = 1.1 μm at a wavelength value of 1550 nm.

Wavelength		b_h	l_w	l_h
780 nm	NIR	80 nm	950 nm	650 nm
1550 nm	IR	120 nm	2400 nm	1100 nm
1550 nm *	IR*	165 nm	1950 nm	1100 nm

Table 2.1: Parameters for the simulated SL-waveguides, optimized for guiding at 780 nm and 1550 nm. The starred series (*) corresponds to the optimal condition for guiding at 1550 nm, which are not achievable within our current technology.

2.4.1 Losses

As it was stated before, the confinement along the vertical direction in SL-waveguides is ensured by the high-index Si_3N_4 slab. The mode is insulated from the high-index silicon substrate by the 4μm thermal oxide cladding, where the mode extends with exponentially decreasing evanescent tails. However, as the slab thickness is reduced, the mode is squeezed, penetrating further inside the cladding, giving an increasing contribution to the evanescent tails.

The amount of evanescent tails that reach the silicon substrate may be calculated from the FEM simulations, as shown in Fig. 2.12. The figure reports the mode intensity profile, normalized to the maximum, in logarithmic scale. The figure refers to an IR waveguide, where the mode is even more pushed out of the slab due to the sub-optimal slab thickness, providing with long evanescent tails that extend down to the silicon, even though with an intensity in the order of 10^{-9} with respect to the mode maximum. This value is well above the computational noise limit, visible in the upper angles of the simulation, which is in the order of 10^{-17} with respect to the maximum.

The losses due to substrate leakage are therefore calculated for all of the simulated configurations, as it is shown in Fig. 2.13. In the NIR case, the substrate leakage is

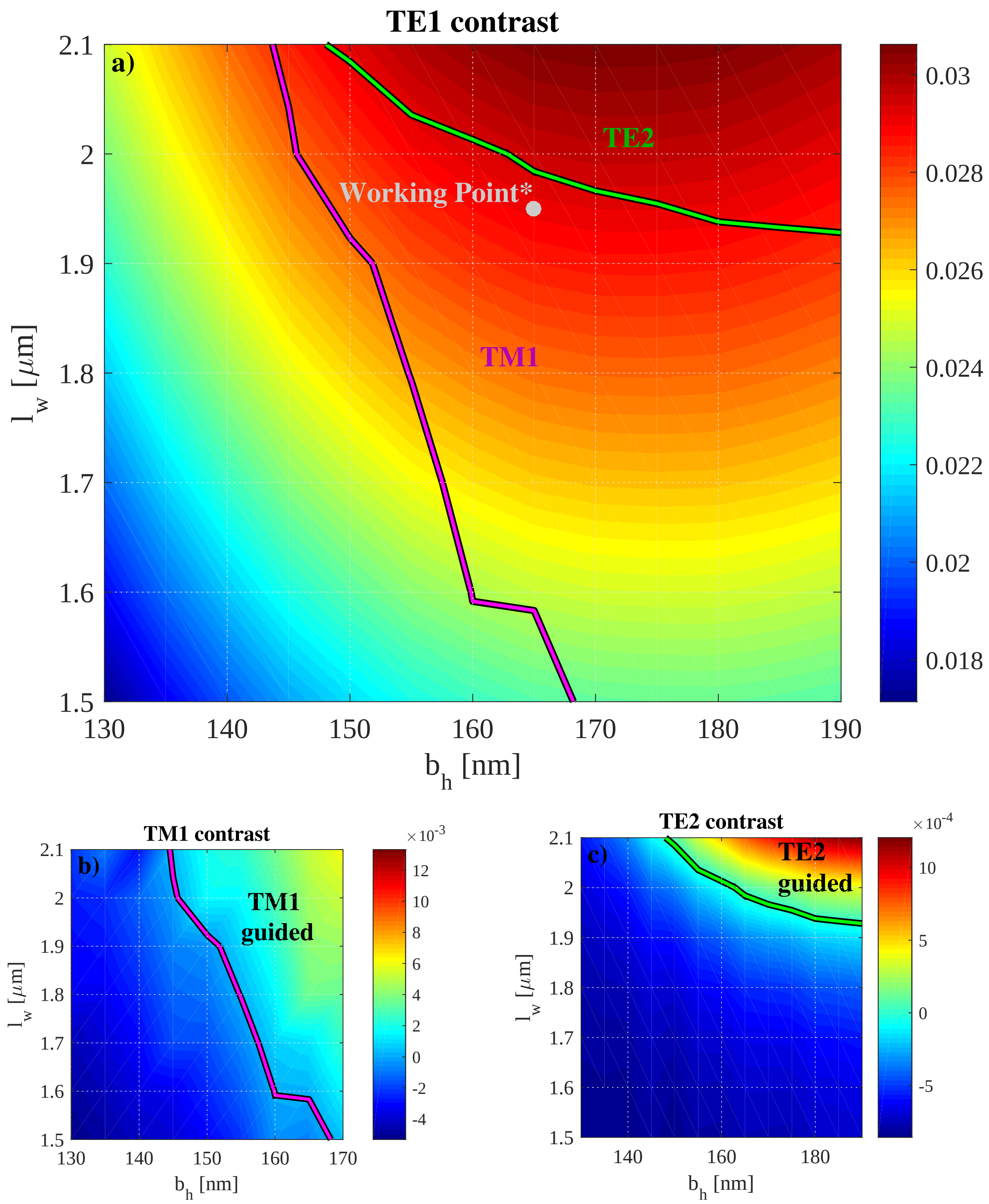

Figure 2.10: Refractive index contrast as a function of the slab thickness b_h and loading strip width l_w for a) the TE1, b) TM1 and c) TE2 modes in the SL configuration at wavelength 1550 nm. The b_h values are extended over 130 nm. The green(purple) bold lines represent the point of zero effective contrast for the TE2(TM1) mode, over which these additional modes are guided. Assuming TE operation, the working point, marked with the gray dot, if found maximizing the contrast out of the TE2-guided region.

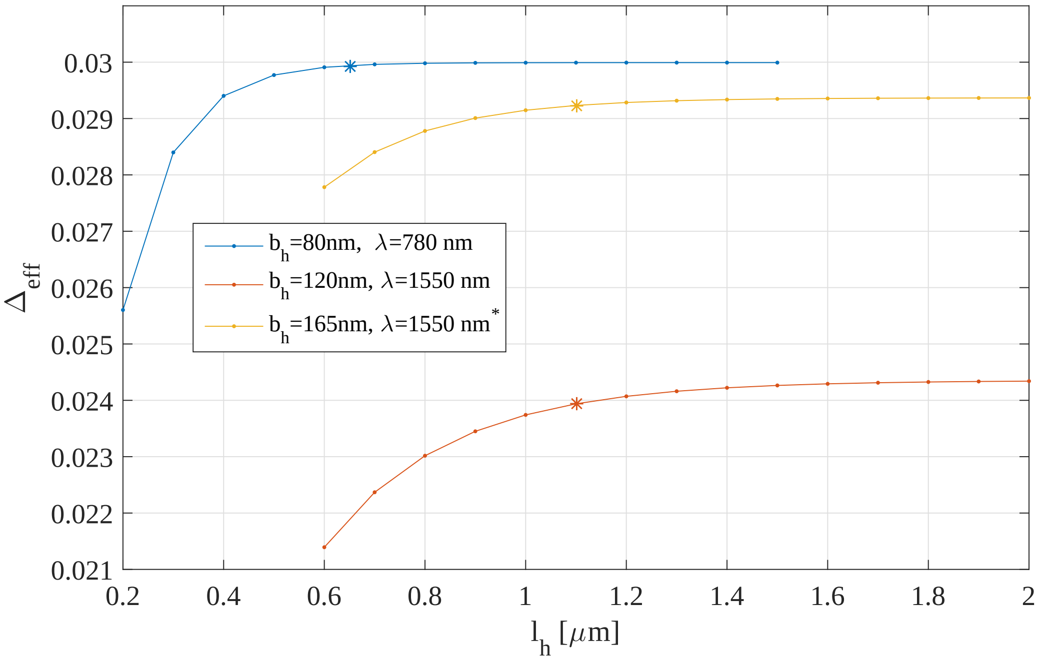

Figure 2.11: (blue) NIR, (orange) IR and (yellow) IR* $\Delta_{\mathrm{eff}}(l_h)$ curves for the designed working points.

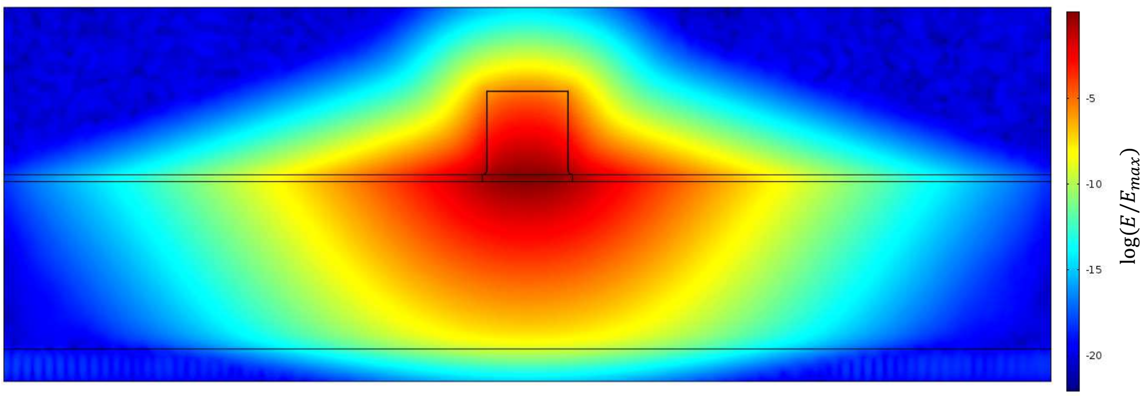

Figure 2.12: Mode intensity profile, normalized to the maximum, in logarithmic scale. The figure refers to an IR waveguide, where the mode is pushed out of the slab due to the sub-optimal slab thickness, providing with long evanescent tails that extend down in the cladding to the silicon.

very low due to the shorter wavelength and good confinement that is achieved with the optimized configuration. The IR case shows rather high losses, due to the longer wavelength and the sub-optimal guiding layer thickness, that provides with longer evanescent tails that extend toward the substrate. Indeed, in the IR* case, where the slab thickness is increased to reach optimized contrast, the losses (in units of dB/cm) decrease by two orders of magnitude.

Another source of loss that may be estimated through numerical simulations is the bending loss. When a waveguide is bent the mode is pushed towards the outer wall of the waveguide. In the SL configuration the effect is marked, since the mode is guided inside the slab, that does not bend, and is weakly confined by the local index variation Δ_{eff} due to the strip. The portion of the field that is pushed towards the outside increases as the waveguide is bent more, i.e. when the bending radius is reduced.

In order to design structures with appropriate bending radii, the bending losses are estimated through numerical simulations. In this case, it is convenient to realize a 2D axisymmetric simulation, where the simulated structure is a ring resonator of a set radius. Simulations are performed by realizing a simulative box that is stretched by values of the radial coordinate tens of microns larger than the curvature radius. The losses are simulated by the absorption properties of a Perfect Match Layer (PML) on the extreme of the simulative box. The PML absorbs the light that reaches the far end of the simulative box, which is identified as light scattered in the slab. The simulations are realized by varying the radius of the ring resonators between 50 μm and 800 μm, using the parameters obtained by the optimization process for the waveguide cross section.

The quality factor as a function of the bend radius is reported in Fig. 2.14 for the NIR and IR resonators. In both cases,the Q-factor reaches saturation near $R =$ 300 μm. Over this value the other contributions of the losses, mainly the substrate leakage, dominate, with the bend loss asymptotically approaching that of the straight waveguide.

In the NIR case the simulated Q-factor reaches values above 10^{14}. However, as it was stated in the introduction, the dominant term for the propagation losses is expected to be the surface scattering. The bend radii to be used in the layout design are therefore obtained hypothesizing an upper bound to the scattering losses of the order of 10^8. Considering this, the bend radii for negligible-loss have been set to 125 μm for the NIR structures and to 350 μm for the IR structures.

2.4.2 Layout

In order to measure the bending and propagation losses of the strip loaded devices two dedicated mask layouts have been realized, as shown in Fig. 2.11. In the first layout, racetrack resonators with different radii and coupling lengths are realized for both the NIR and IR bands. The resonators are designed to achieve critical coupling condition by designing directional couplers whose transmittance equals the internal round-trip losses of the resonator $a = e^{-\alpha L}$, as already discussed in Sec. 0.2.3. A summary of the designed resonators parameters is reported in Tab. 2.2. Each resonator design is repeated five times, adding and subtracting two incremental 2 μm variations to the coupling length to secure the realization of a resonator in critical coupling condition.

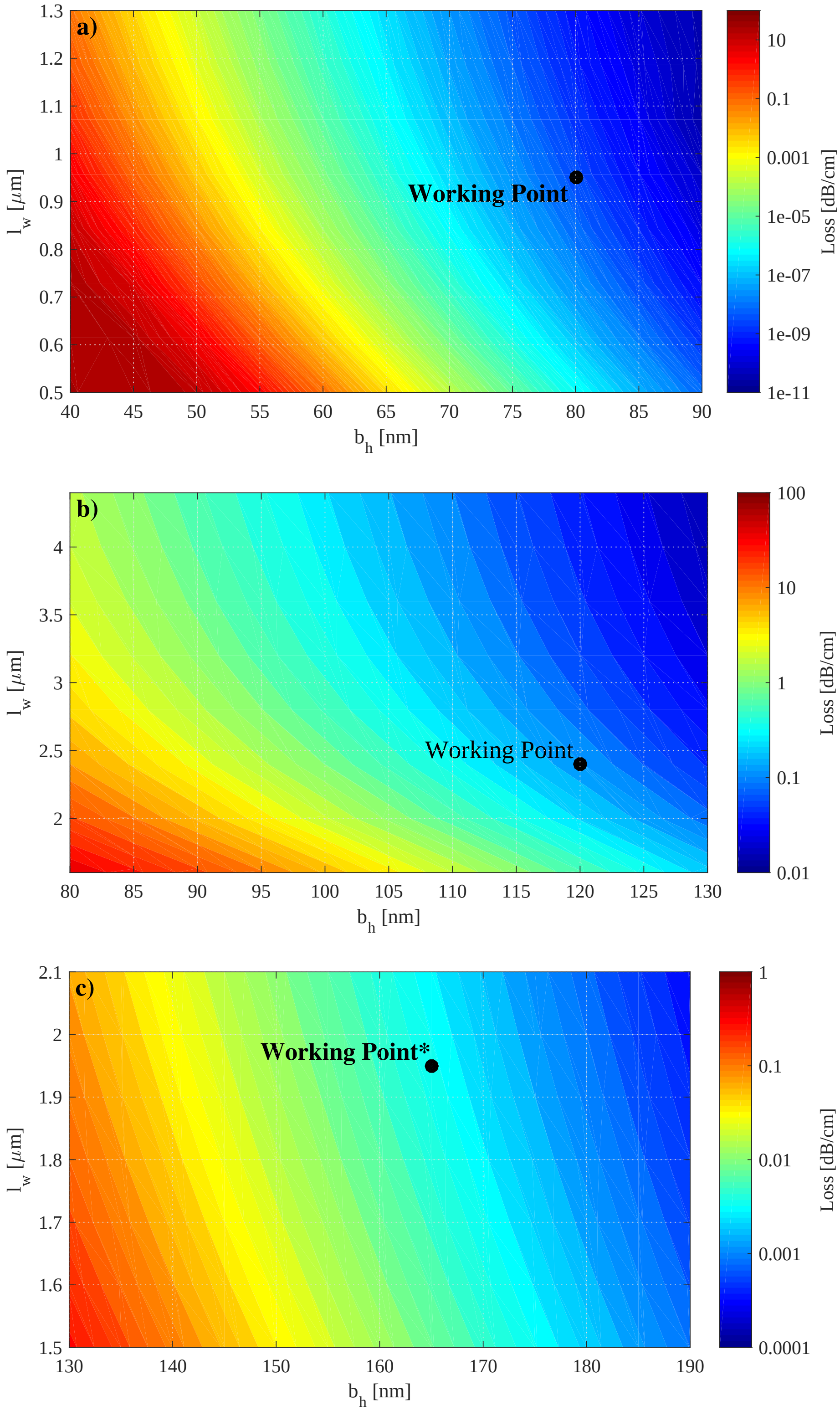

Figure 2.13: Simulated substrate leakage losses due to the finite bottom cladding for the a) NIR, b) IR and c) IR* configurations. The losses, in units of dB/cm, are represented in logarithmic scale.

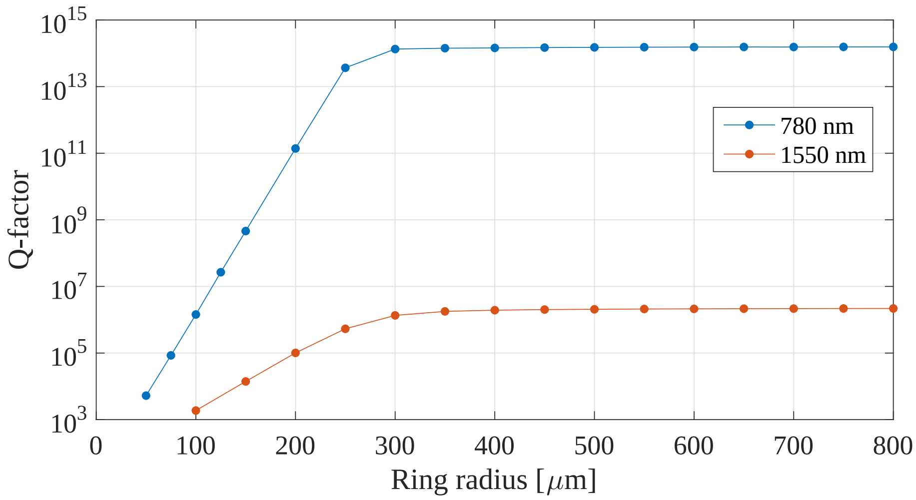

Figure 2.14: Simulated quality factors of SL-resonators for the (blue) NIR and (orange) IR SL-resonators as a function of the curvature radius. The resonators are simulated using an axisymmetric 2D scheme, where the losses that determine the Q-factor are simulated by a Perfect Match Layer absorber situated far from the SL structure.

	780 nm			1550 nm		
Radius [μm]	75	100	125	150	25	350
Expected Q	8.5×10^4	1.4×10^6	2.6×10^7	1.4×10^4	5.2×10^5	1.8×10^6
Estimated FSR [pm]	850	640	510	102	1030	740

Table 2.2: Expected quality factors and FSRs for the designed racetrack resonators.

Furthermore, copies of the large radii resonator structures with $\pm 0.4\mu$m variations in l_w are also included in the layout.

The second layout features series of waveguides with progressively increasing radius of curvature and with increasing length to measure the bending and propagation losses of the structures simultaneously. This approach will be detailed in Sec. 2.6.

2.5 Fabrication

The devices were fabricated on four blank Si wafers over which a 4 μm thick cladding of thermal SiO_2 was grown. In addition to the four device wafers, other four test wafers are used during the process to measure the actual deposition rate, etch rate, and total thickness of deposited material during the various steps. Indeed, blank wafers are required as reliable references for the VASE thickness measurements, as the 4μm thick cladding on the device wafers makes the fitting of VASE measurement very difficult.

The device wafers are divided in two couples, one couple for the NIR and one for the IR wavelength operation. The Si_3N_4 slab-waveguide layer was deposited on the wafers using LPCVD at 770°C. VASE measurement on two of the test wafers gave thickness values of 80 nm and 115 nm for the NIR and IR wafers respectively.

Then, the oxide layer of the loading strip was deposited. For each couple of wafers, one of the wafers was covered with PECVD SiO_x deposited at 300°C while the other was

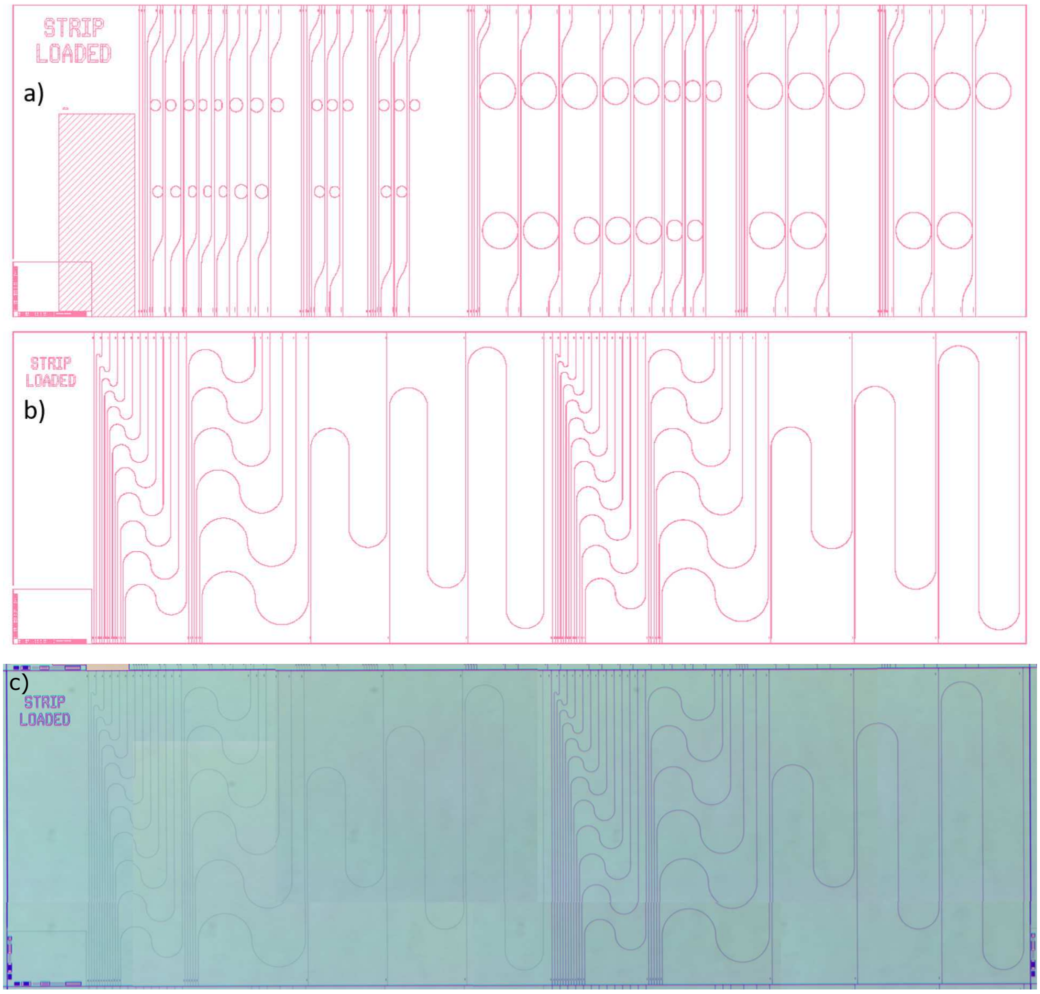

Figure 2.15: Mask layouts for the measurement of the waveguiding properties of the optimized SL-waveguides. a) the losses of the waveguides may be measured by evaluating the quality factor of racetrack resonators. Racetrack resonators of different radii and coupling with the waveguide are present in the layout for both NIR and IR bands. In the IR case, the bending losses are expected to be much greater than the NIR case, and therefore larger resonators are realized. b) the propagation losses may be assessed by measuring the transmission of waveguides with different length, realized with the same number of bends and a large bending radius to reduce the bending losses contribution. The bending losses of the waveguides may be analogously evaluated comparing the transmission of waveguides bent with different curvature radii. c) Optical image of a realized chip.

Wafer	SL1	SL2	SL3	SL4
Design wavelength	780 nm	780 nm	1550 nm	1550 nm
Si_3N_4 height	80 nm	80 nm	120 nm	120 nm
TEOS height	650 nm	-	1100 nm	-
SiO_x(PECVD) height	-	650 nm	-	1100 nm

Table 2.3: Design values of the four kinds of SL waveguide structures implemented on the wafers.

covered with TEOS using LPCVD at 710°C. The layers thicknesses were of 650 nm and 1100 nm for the NIR and the IR wafer couples, respectively.

The wafers were then covered with photoresist, and patterned with both layouts on each wafer using the standard lithography procedure. The pattern was transferred to the oxide using RIE down to 100 nm, forming the loading strips. The remaining 100 nm were etched in BHF solution to maintain the original surface quality of the LPCVD Si_3N_4. The BHF etching, being isotropic, consumes also 100 nm of material on each sidewall of the strip, leaving a smooth round foot at the bottom of the structures.

After the definition of the loading strip, the wafers are ready for dicing. In this case, both DRIE and polishing-millstone approaches to the facet definition were used, on different regions of the wafers.

The wafers were covered once again with thick photoresist and patterned on two chip rows in the central region for DRIE etching, leaving the waveguides terminations uncovered. The waveguide facets are then defined on the central rows using RIE and protected from the dicing saw by a 100 μm wide DRIE groove. The waveguide facets on the remaining chips are defined using the polishing-millstone, as described in Sec.1.3. Then all of the chips are diced, with the dicing saw in the center of the formed grooves without harming the waveguide facets.

The actual cross section of the realized structures is measured on sacrificial chips, that are covered with a thin gold layer to avoid charging during the SEM imaging. In Fig. 2.17 the SEM images of the waveguide facets are reported.

A new set of simulations for the effective contrast was run, as a function of the wavelength, taking into account also the slightly different dispersion of the PECVD oxide. In this series of simulations, we used the geometrical parameters of the structures as measured from the SEM imaging. The results of the simulations, reported in Fig. 2.18, show that the higher index of PECVD oxide can play a crucial role in confining the mode.

2.6 Measurements

The samples were then measured with the experimental setup for passive characterization described in Sec. 0.3.2, with slight variations for the NIR measurements as described in Sec. 2.3. More in detail, the NIR source was a *Sacher Lasertechnik LiON TEC-500* stabilized with an external Littman-Metcalf cavity as shown in Fig. 2.19. The external cavity could be operated in two ways: (i) with a motor, for a broad wavelength range scan, and (ii) with a piezoelectric actuator for more

NIR laser

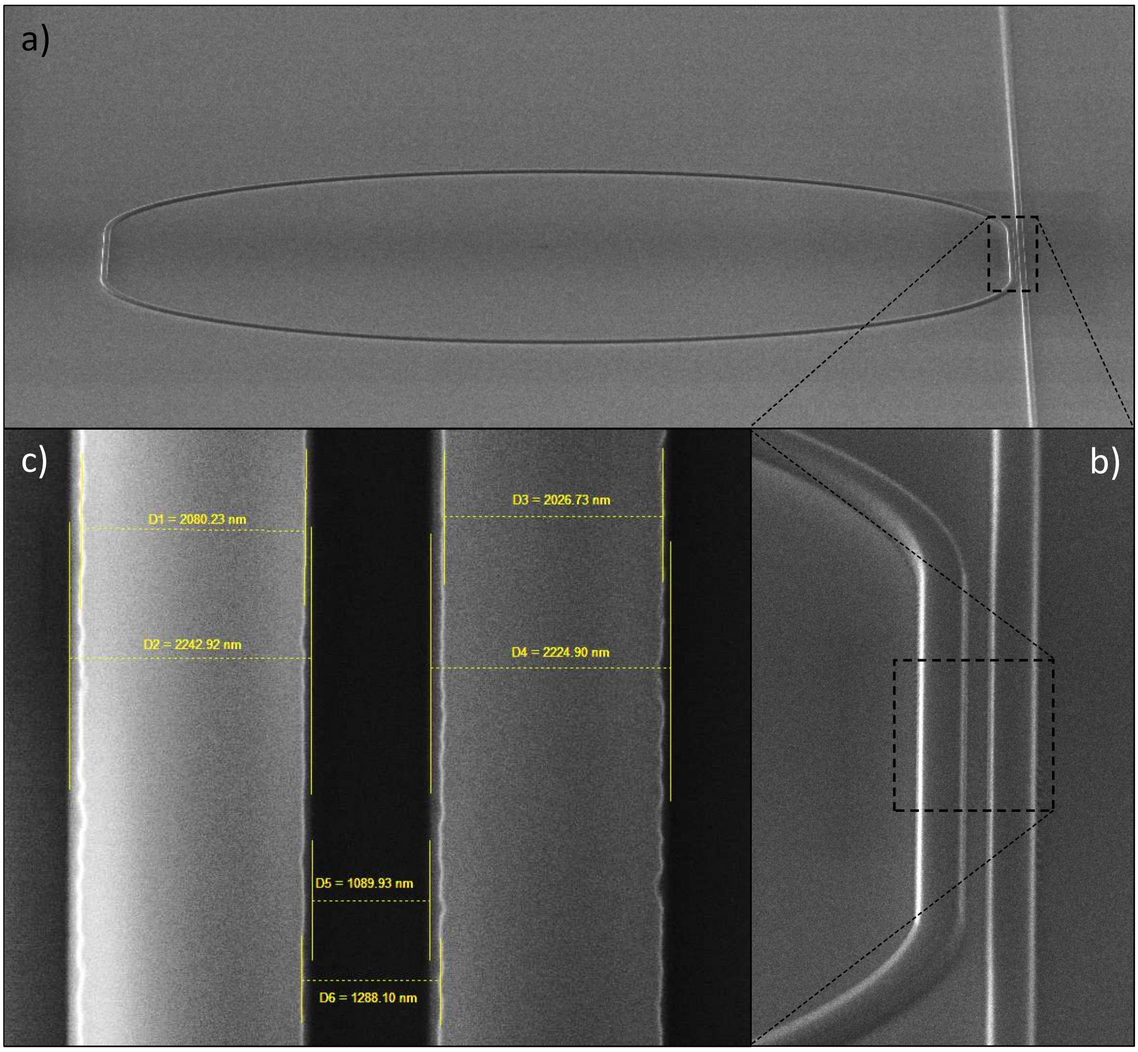

Figure 2.16: SEM images of the samples during the fabrication permitted to measure the actual dimensions of the structures. a) Fish-eye image of a strip-loaded racetrack resonator. The b) coupling region dimensions are crucial to obtain critically-coupled resonances, and are therefore c) verified through SEM imaging.

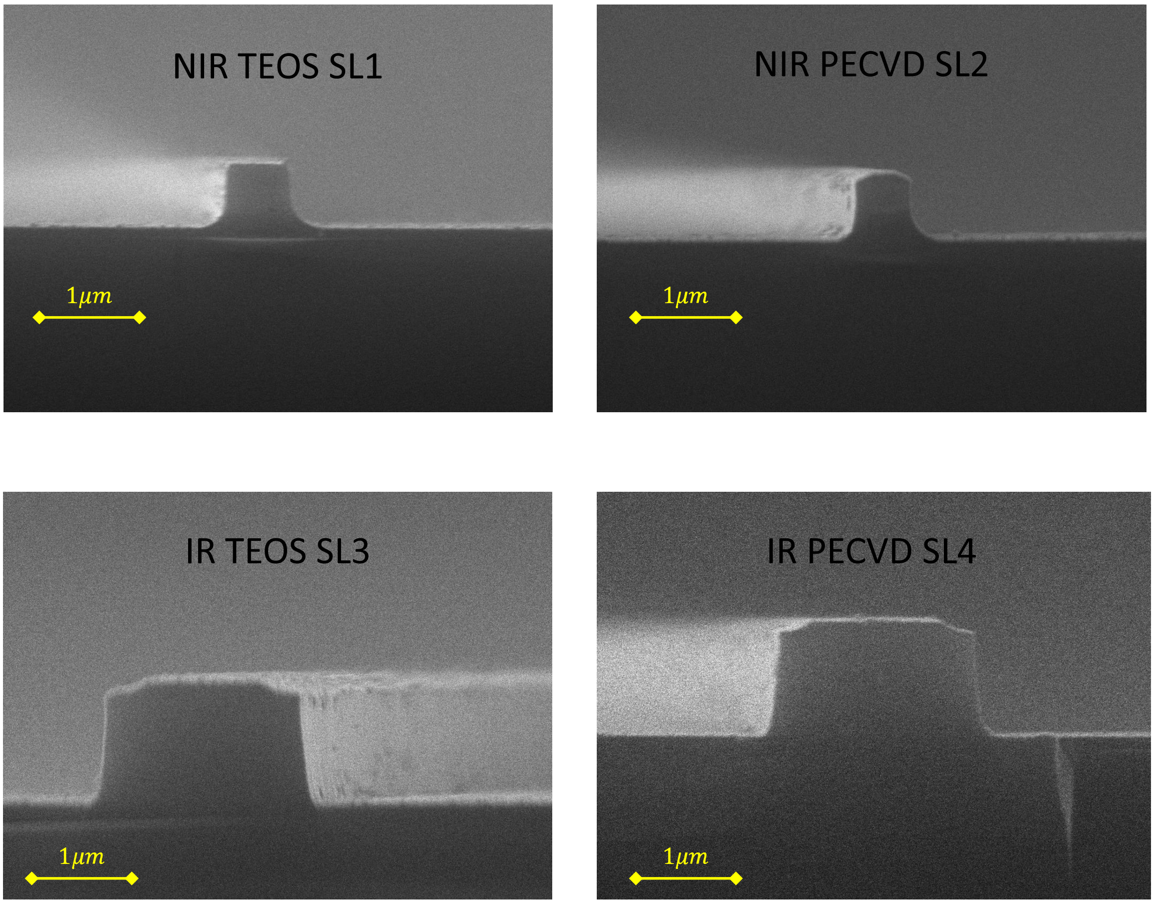

Figure 2.17: SEM images waveguides facets from the different realizations. In all samples the round foot at the base of the strip due to the wet-etching of the final 100 nm is visible. The waveguides are covered with a thin gold layer to avoid the accumulation of charges during SEM imaging, which is responsible for the visible roughness.

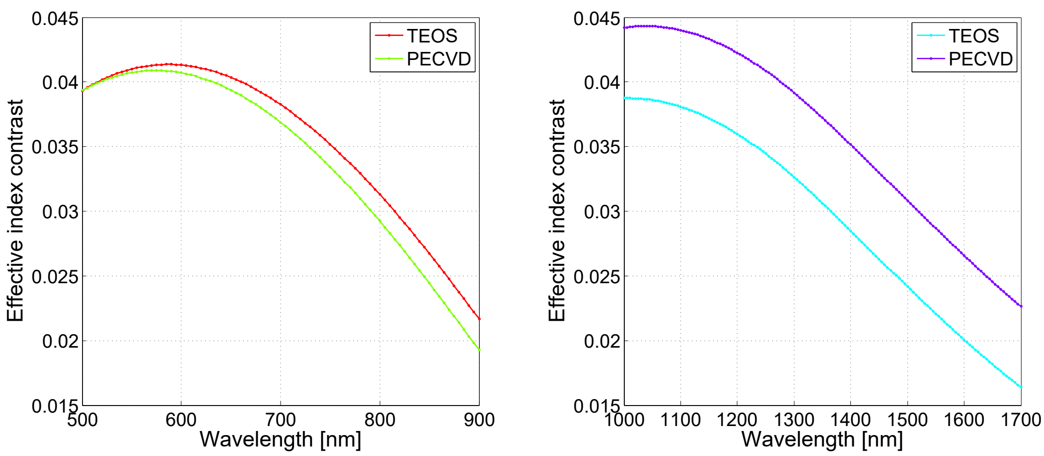

Figure 2.18: FEM simulations of $\Delta_{\text{eff}}(\lambda)$ calculated using the geometrical parameters obtained from SEM imaging and considering both TEOS and PECVD dispersions.

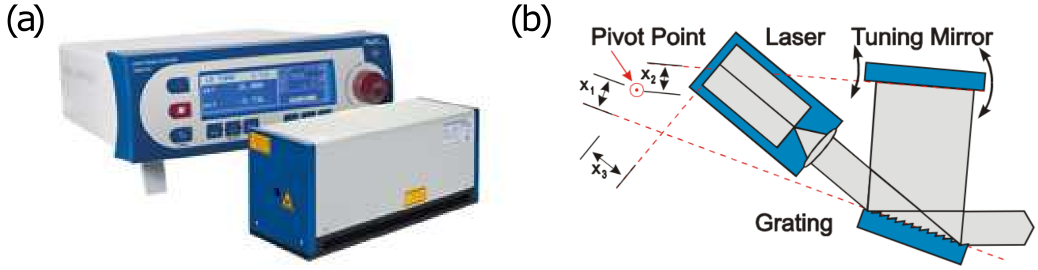

Figure 2.19: *Sacher Lasertechnik LiON TEC-500* NIR laser source with external cavity. The cavity is controlled via a motor for long wavelength scans and via a piezoelectric actuator for accurate analysis in a small wavelength region.

accurate measurements over a small range. The output intensity of the laser results strongly modulated as a function of the wavelength. In order to obtain a proper normalization of the spectra, the intensity modulation is measured by dividing the light with a 90/10 fiber splitter before the sample, and measuring the 10% fraction with a photodetector. Then, both the signal out of the sample and the reference are synchronously measured by the *Picoscope* oscilloscope together with the driving signal of the motor/piezo to recover the spectral information. Another issue of this laser source is the presence of mode hopping, especially during the motor-driven scans, which prevents the proper measurement of long-range spectra. This issue resulted somehow mitigated in the short-range spectra acquired with the piezoelectric, making it possible to perform measurements near the WGMR resonances. Indeed, the experimental setup was originally realized to perform on-resonance measurements for biosensing. A more detailed analysis of the setup may be found in the thesis work of Davide Gandolfi [86].

Bending and propagation losses

Figure 2.20 reports on the results of the measurements on the S-bends with different radii of curvature and with large curvature but increasing length. The propagation losses may be estimated from the waveguides with different lengths and large radius of curvature, which are hypothesized to give negligible bending loss contribution, using the usual Labert-Beer's law (Eq. 1.5) as discussed in Sec. 1.4. The bending losses may instead be estimated according to [87] as

$$\alpha_b(R) = c_1 e^{-c_2 R} \tag{2.6}$$

With c_1 and c_2 constants to be determined from the fit.

In the case of the S-bends, the increasing curvature radius causes the overall length of the waveguide to increase. Given L_0 the length of a straight waveguide, the length of an S-bent waveguide is correlated by $L = L_0 + 2\pi R$. In this case, both bending and propagation losses contribute to the total loss of each waveguide, that results in a combination of the two, plus the constant term due to L_0 that should be subtracted. The length of the coiled structures with fixed radius of curvature is instead $L_0 + 2\pi R_{\text{max}} + 2L_{\text{coil}}$. By considering the bending loss contribution thanks to the large radius, these structures may be used to obtain a better estimation of the propagation losses.

The fit of the propagation losses is therefore realized considering a combination of bend and propagation losses. The experimental data for the TEOS-loaded samples and the PECVD-loaded samples, measured in the IR at $\lambda = 1550$ nm is reported in

Load	α_p[dB/cm]	c_1[dB/cm]	c_2[cm$^-1$]
TEOS	2.3 ± 0.2	$2 \pm 1 \times 10^3$	$3.8 \pm 0.4 \times 10^2$
SiO_x(PECVD)	2.8 ± 0.4	$1.2 \pm 0.5 \times 10^3$	$3.9 \pm 0.3 \times 10^2$

Table 2.4: Propagation and bending losses results, obtained by fitting the transmission values of the S-bend structures at 1550 nm.

Figs. 2.20 and 2.21 respectively, exhibiting similar behaviour. In each figure, the data are expressed both in terms of the ring radius and the total sample length. In the first panel, expressed in terms of the radius of curvature, the bending losses dominate at short bending radius and the transmission rapidly increases, reaching a plateau around a radius of curvature of 250 μm. Above this value, the transmission decreases as a function of the curvature radius due to the contribution of the propagation losses, that become dominant. This second contribution becomes apparent in the second panel, where the data are represented as a function of the total length of the structure, after subtracting the contribution of L_0. In this case, the propagation losses contribution is clearly dominant for large values of the length, determining the asymptotic behaviour. The results of the used fit functions, are reported in Tab. 2.4.

In the NIR region, on the other side, mode hopping in the laser source made the measurements very difficult. Due to instability of the laser intensity, the transmission measurements in the NIR produced scattered data, as reported in Fig. 2.22. The data is too much noisy to be fitted, and features even unphysical values of transmission $T > 1$. The total losses $\alpha_T = \alpha_p + \alpha_b(R)$, however, may still be evaluated from an analysis of the racetrack resonators, by using

$$\alpha_{\mathrm{tot}}(R) = \frac{2\pi\lambda_0}{\mathrm{FSR}(\lambda_0)\ \mathrm{Q}(\lambda)\ \mathrm{L}} \tag{2.7}$$

where L is the physical length of the racetrack resonator.

NIR Resonators measurements

The laser mode hopping made also the measurement of the NIR resonators spectra rather difficult. In some cases, the mode hopping made the measurement skip the resonator resonances, that in combination with the short tunability range, made the FSR impossible to estimate with sufficient accuracy.

Nevertheless, measurements in the range 770 nm-790 nm were carried on on all of the NIR designed resonators, and even on the IR-designed resonators. Figure 2.23 reports the measurement and fit of a TEOS-loaded resonator designed for IR with l_w of 2400 nm and $R = 350\mu$m. The resonance features a FWHM of only 0.2 pm, leading to a total Q-factor of $Q_{\mathrm{tot}} = 3.6 \times 10^6$. In this case, the resonator is not specifically designed to guide in the NIR, with an undercoupled transmission dip barely reaching a 0.9 value. The high quality factor in conjunction with the shallow resonance dip suggests that the resonator is in highly under-coupled regime. Lorentzian fitting of the resonance leads indeed to an intrinsic Q-factor of $Q_i = 3.7 \times 10^6 \approx Q_{\mathrm{tot}}$.

Table 2.5 summarizes the results of the resonators measurements in the NIR. The measurements on the three optimized dimensions for single mode operation, show that saturation of the Q-factor is still not achieved. The Q-factor was measured also on structures with larger l_w, which are in principle multi-modal. However, probably due to the much higher losses of the TE2 mode, a single comb of resonances appeared in the spectra. The Q-factor measurements on the larger structures provided with

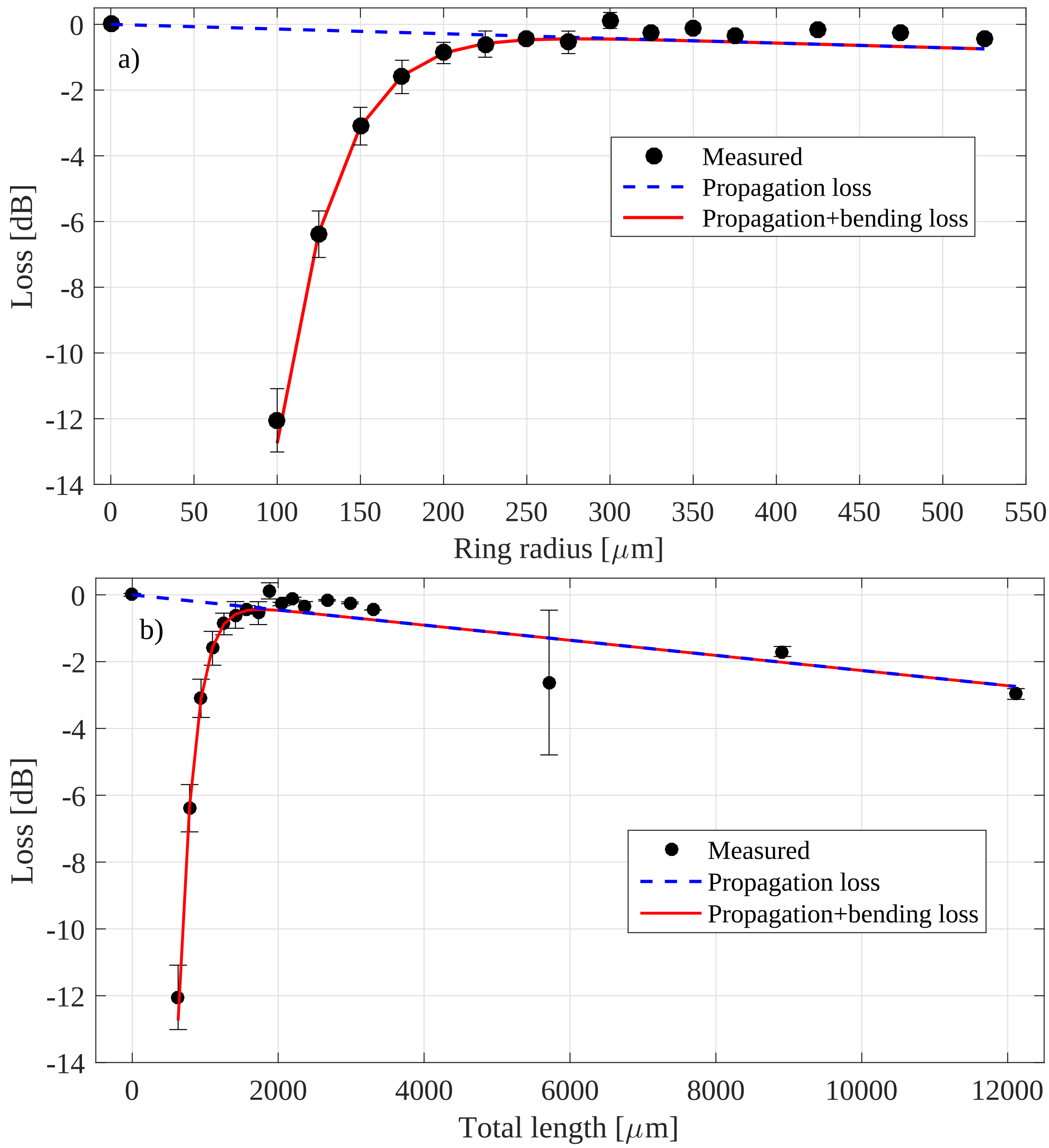

Figure 2.20: Transmission measurement of the S-bend waveguides samples for the TEOS-loaded samples in the IR region reported as a function of (top) curvature radius and (bottom) total waveguide length. The errorbars on the data represent the standard deviation over three samples. The red line represents the fit of the data using Eqs. 1.5 and 2.6. The result of the fit is reported in Tab. 2.4.

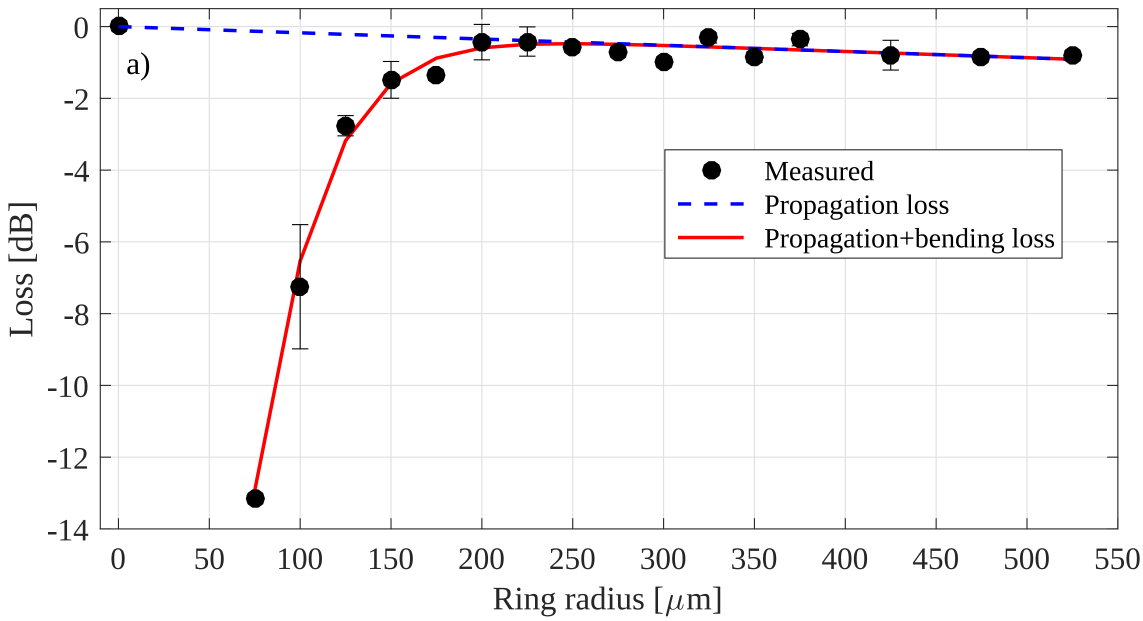

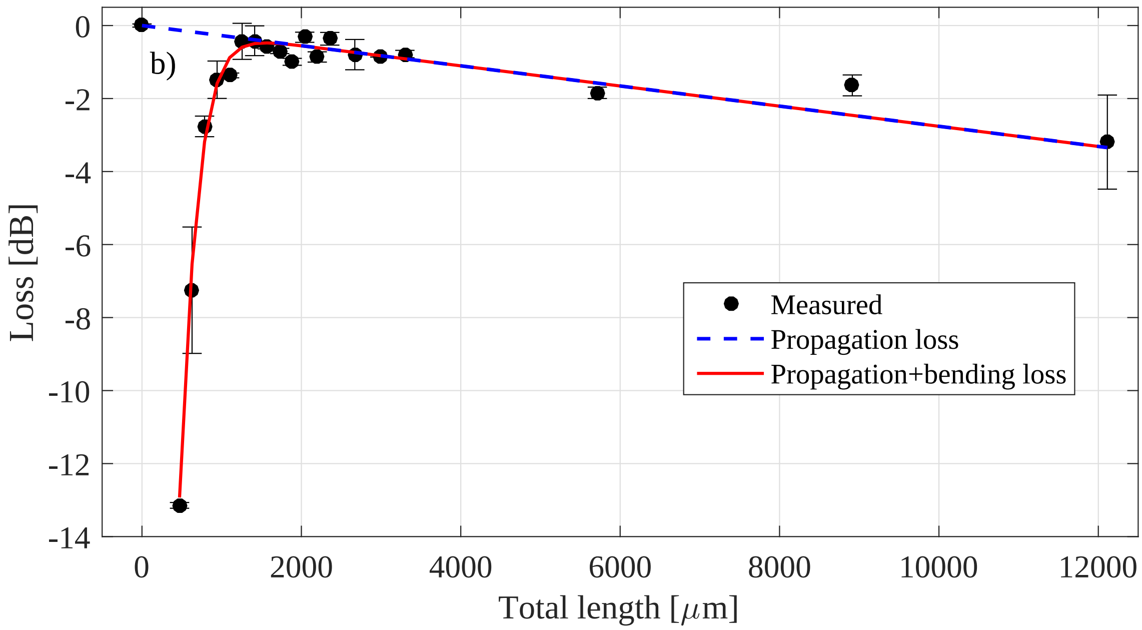

Figure 2.21: Transmission measurement of the S-bend waveguides samples for the PECVD oxide samples in the IR region reported as a function of (top) curvature radius and (bottom) total waveguide length. The errorbars on the data represent the standard deviation over three samples. The red line represents the fit of the data using Eqs. 1.5 and 2.6. The result of the fit is reported in Tab. 2.4.

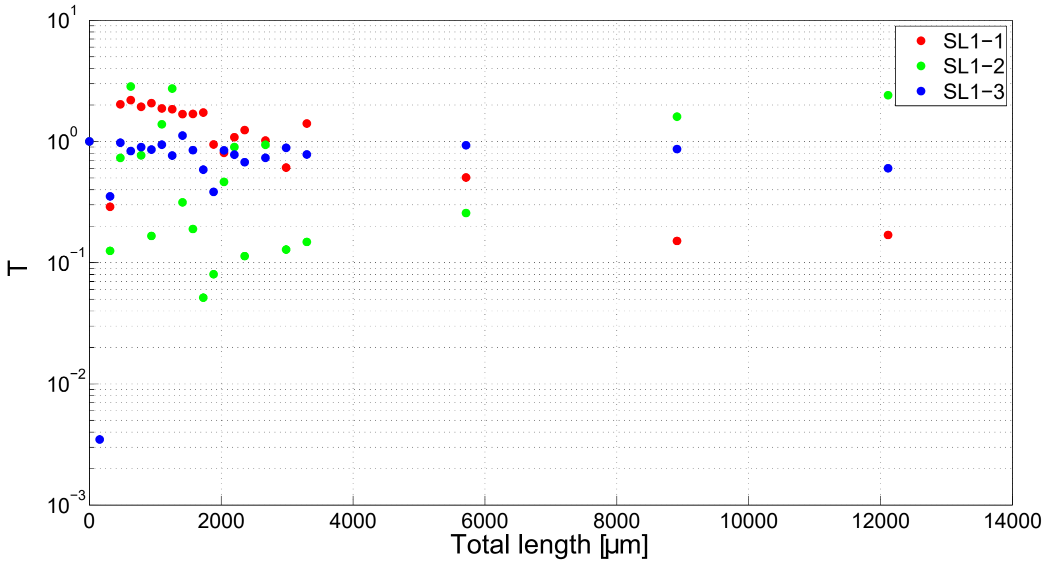

Figure 2.22: Transmission measurements on the S-bend waveguide structures in the NIR region. Due to mode hopping in the laser source the data is scattered, even reaching unphysical results of $T > 1$.

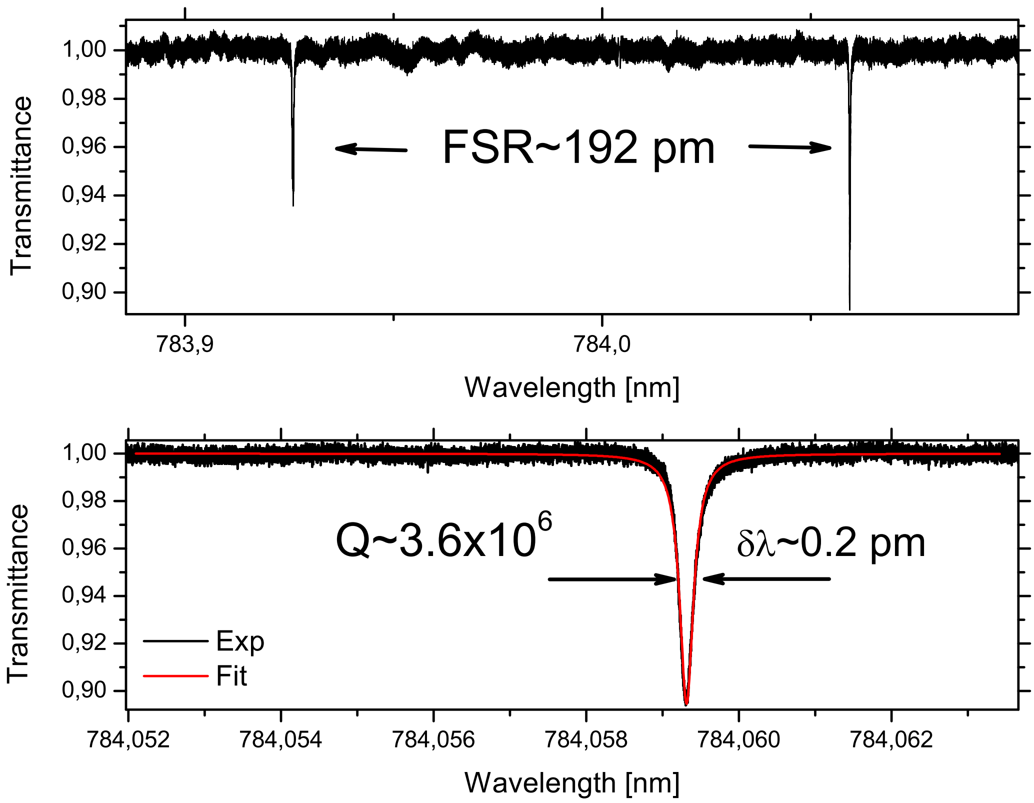

Figure 2.23: Normalized transmittance spectrum of a racetrack resonator with $R = 350$ μm and $l_w = 2.4$ μm in the NIR region. (top) the laser mode hopping makes the broad-band measurement of the sample difficult. In this case, at least two resonances may be identified, leading to a FSR of 192 pm. (bottom) the second resonance appears free from instrumental artifacts and is used to measure the Q-factor in the resonator. the total Q-factor obtained by fitting reaches the value of 3.6×10^6.

Dimensions		TEOS				PECVD			
R	l_w	Q_{tot}	Q_i	α_{tot}	T_{min}	Q_{tot}	Q_i	α_{tot}	T_{min}
[μm]	[nm]			[dB/cm]	[%]			[dB/cm]	[%]
75	950	3.4×10^4	5.5×10^4	11	6.8	5.6×10^4	7.4×10^4	8.3	26
100	950	1.6×10^5	2.1×10^5	2.8	26	1.7×10^5	2.1×10^4	2.9	40
100	1200	3.7×10^5	4.6×10^5	-	36	3.2×10^5	3.4×10^4	1.8	84
125	950	3.2×10^5	3.3×10^5	-	90	-	-	-	-
150	2400	3.6×10^5	4.1×10^5	1.8	56	-	-	-	-
250	2400	2.0×10^6	2.1×10^6	0.3	85	-	-	-	-
350	2400	3.6×10^6	3.7×10^6	0.2	89	-	-	-	-

Table 2.5: NIR measurements of the Q-factor of various resonators. Q_{tot} and Q_i represent the total and intrinsic Q-factors respectively. Together with the FSR, they permit to calculate the total loss coefficient α_{tot} inside the resonator. T_{min} represents the minimum transmission achieved on the resonance dip.

higher Q-factors with respect to the optimized ones. This reflects the fact that, forfeiting the single mode condition, enlarging the loading strip results in a much higher confinement under the strip, which in turn results in a higher Δ_{eff}. The propagation losses reported in the table are calculated using Eq. 2.7. Due to the instability of the NIR source, it has been sometimes impossible to asses the FSR accurately, and therefore two points are missing.

As it can be seen from the table, the Q-factors are steadily increasing as a function of the resonator radius, demonstrating that the losses are dominated by the bending contribution. Overall, the Q-factors of the resonators designed for NIR operation are one order of magnitude lower than the simulated ones, indicating that additional refinement is needed to obtain quantitative results.

IR Resonators measurements

In the IR case the laser source is much more stable and spans a wider range between 1490 nm and 1575 nm , allowing to obtain about 180 clean resonances per spectrum.

A sample spectrum, from a TEOS-loaded resonator with $l_w = 2400\ nm$ and $R = 350\ \mu$m is shown in Fig. 2.24. Panel a) shows the raw spectrum over the whole range. The spectrum is densely filled with deep resonances, which are near to critical coupling. The characterization of the spectra was made using the software routine that I developed during this thesis work. The software exploits the spurious FP background modulation, which is present due to the reflection at the waveguide facets, to normalize the resonances to the baseline, as shown in Fig. 2.24 b). Then, given the distance between the facets, the FP resonances FSR is estimated and used to measure the n_g of the bus waveguide, which has the same geometrical shape as the resonator. The FSR of the resonator is then estimated by using the bus waveguide group index and the known resonator perimeter. The resonance dips are then identified recursively by using the FSR to estimate the position of the next resonance. Finally, a Lorentzian fit that includes the FP background is performed on each resonance. It's worth note that while the total quality factor is well determined by the fit, it results from a combination of intrinsic and coupling terms that could not be easily distinguished. The identity of those two terms is determined by the general behavior (under- or over- coupler). In the present case, since all of the resonances are near the critical coupling, the two terms are almost equal.

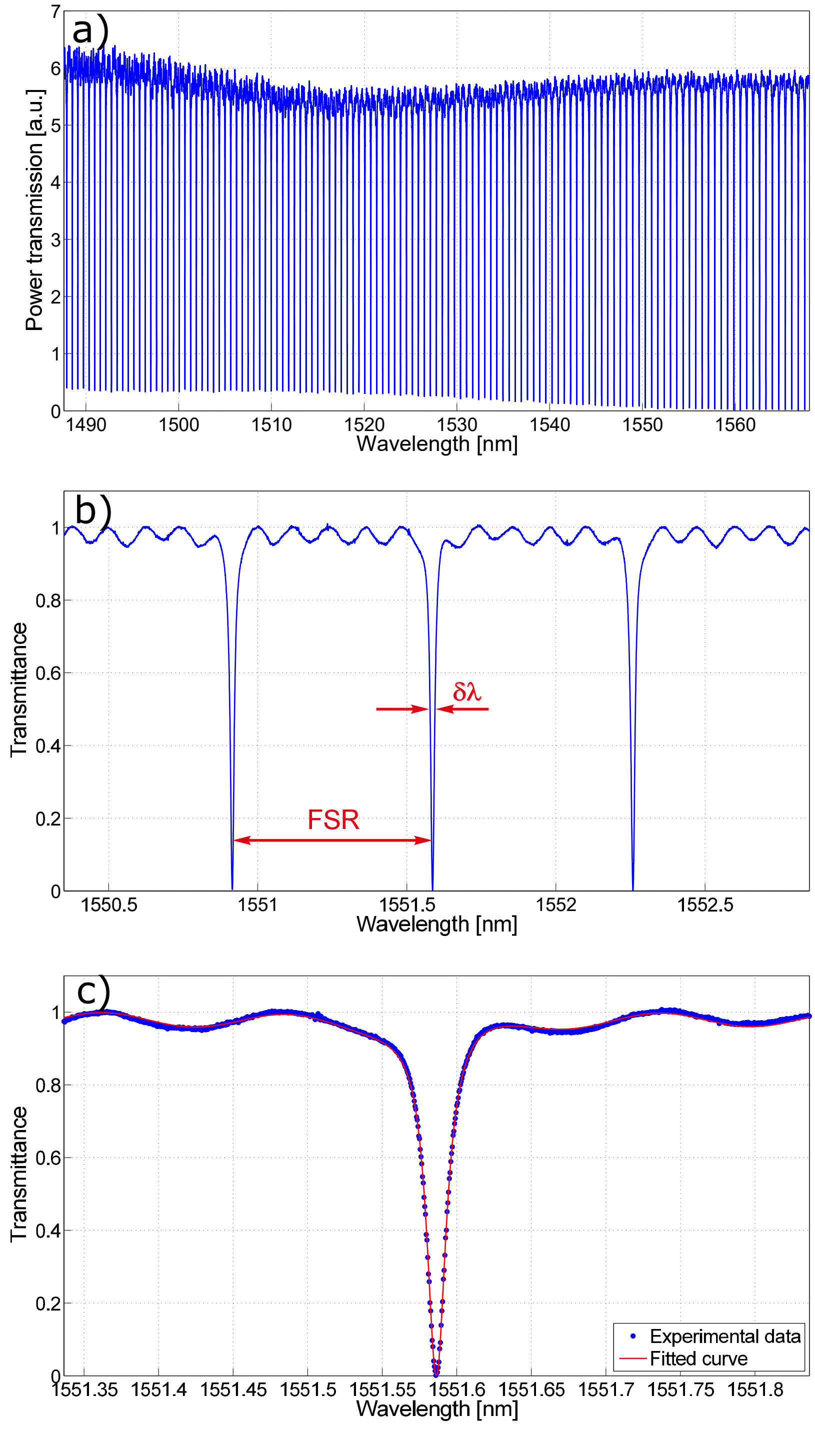

Figure 2.24: Transmission spectrum of a TEOS-loaded resonator with $l_w = 2400\ nm$ and $R = 350\ \mu$m using the IR source. a) the raw spectrum spans over 90 nm, permitting to collect data of over 150 resonances. b) using the routine that I developed during this thesis work, the spectrum is automatically normalized on the FP background, which is visible in the image as a small modulation. c) then, the transmission spectra of all resonances is fitted to a Lorentzian shape, by taking into account the FP modulation in the background.

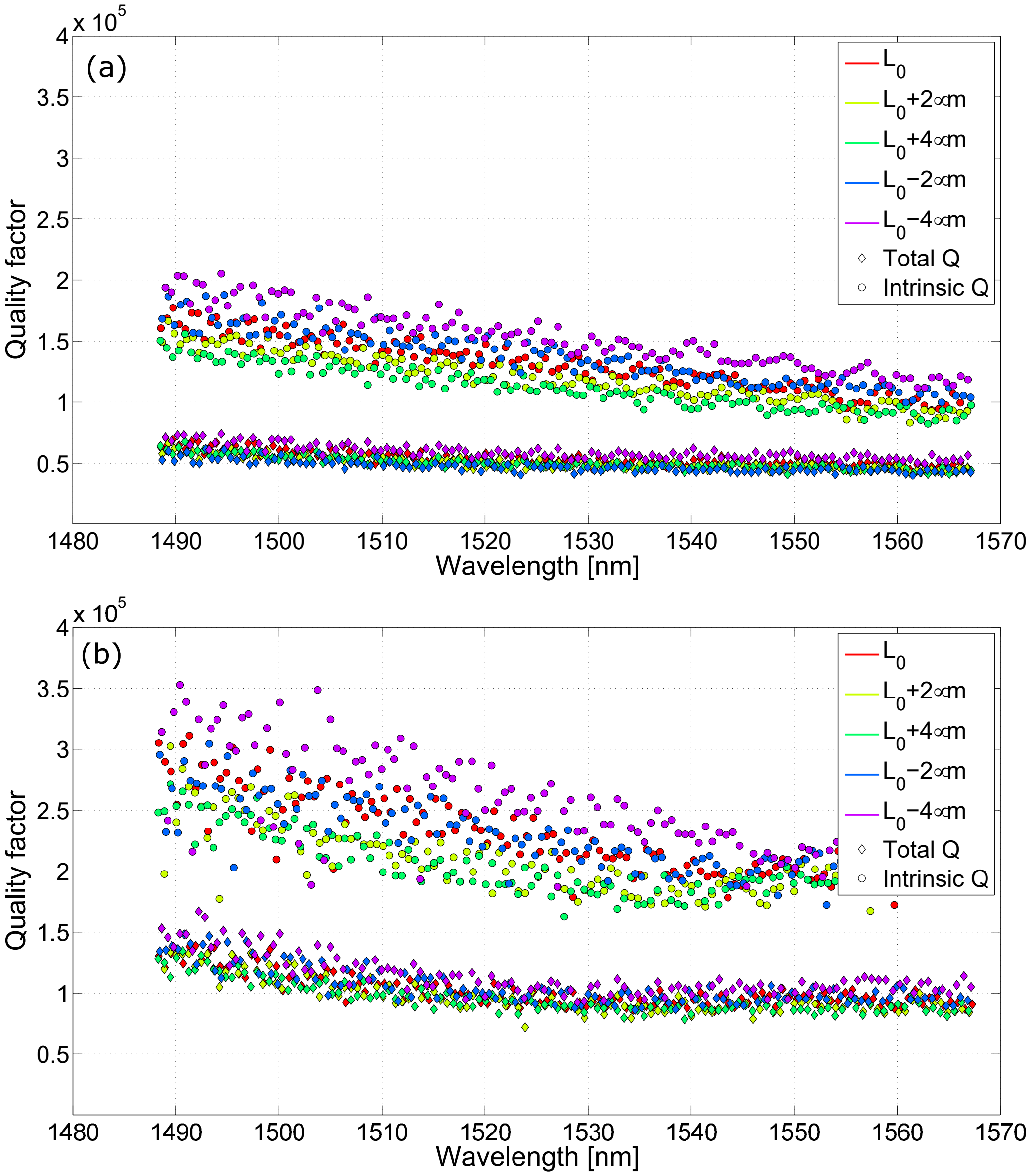

Figure 2.25: Quality factor estimations obtained by fitting the resonances of a (a) TEOS sample and a (b) PECVD sample. The measure refers to series of five racetrack resonators with $l_w = 2400\ nm$, $R = 350\ \mu$m and 2μm step variations around the designed critical coupling length designed for IR.

Figure 2.25 shows the resulting Q-factor estimations from the fits of the data acquired on (a) TEOS and (b) PECVD samples on the $l_w = 2400\ nm$, $R = 350\ \mu$m resonators. The results coming from the two different samples are represented on the same scale to facilitate the comparison. For each sample, the transmission measurements were realized over the five coupling length variations.

In the TEOS case (a), the total Q-factor remains stable around 5×10^5 over the whole spectrum, while the intrinsic quality factor steadily decreases from 1.7×10^5 at 1490 nm down to 1.0×10^5 at 1560 nm. In the PECVD case (b) the Q-factors are in general higher, reaching values around 3.5×10^5 near 1490 nm with the resonator with shorter coupler. The generally higher Q-factor of the PECVD may be explained by its large refractive index, compared to that of TEOS, that produces a larger effective refractive index contrast, as it was shown in the simulations reported in Fig. 2.18.

Thermal annealing

During the deposition of silicon oxide, especially via PECVD technique, hydrogen is trapped inside the deposited layer, forming Si-H and O-H bondings that may result in increased absorption losses. In order to reduce the hydrogen content, a couple of samples was annealed at 975°C for four hours in N_2 environment.

The resulting Q-factors measured on the annealed samples are reported in Fig. 2.28. The Q-factor of the TEOS samples experience a clear increase, bringing up the values over all of the range. An even more pronounced effect would be expected in PECVD, which usually has a higher content of hydrogen. However, the average Q-factors in the PECVD case are instead decreased. The effect may be explained by the rather large change in the bulk refractive index of PECVD after annealing.

Figure 2.27 shows the index dispersions of TEOS and PECVD oxide as deposited (as dep.) and after the annealing process. Both glasses tend to reach the thermally grown oxide dispersion after the annealing. The TEOS, being already deposited at 710°C, experiences a small positive refractive index change during the annealing process. In the case of PECVD oxide, instead, due to the low deposition temperature of 300°C, the refractive index dispersion change is much more prominent, with a net decrease of 0.012 RIU at 1550 nm. The net decrease in the refractive index of PECVD oxide after annealing is therefore the most plausible cause of the lowering of the quality factors.

Larger structures

From the previous measurements, it resulted that the best guiding structures are those with non-annealed PECVD oxide, that despite the losses induced by the higher hydrogen content obtains higher intrinsic Q-factor values, suggesting that the resonators are still in the bend-loss dominated regime. A further confirmation of this hypothesis comes from the measurement of the larger IR structures, realized with a l_w of 2.8μm. The Q-factors estimations for these structures are reported in Fig. 2.28, showing intrinsic Q-factor estimations approaching 9×10^5.

2.7 Conclusions

During this work I developed integrated strip-loaded waveguides for the NIR and third-telecom band region using etchless Si_3N_4 as the guiding material.
Making use of FEM simulations, I developed a model for optimized SL-waveguides introducing the concept of effective index contrast. I used the model to develop a

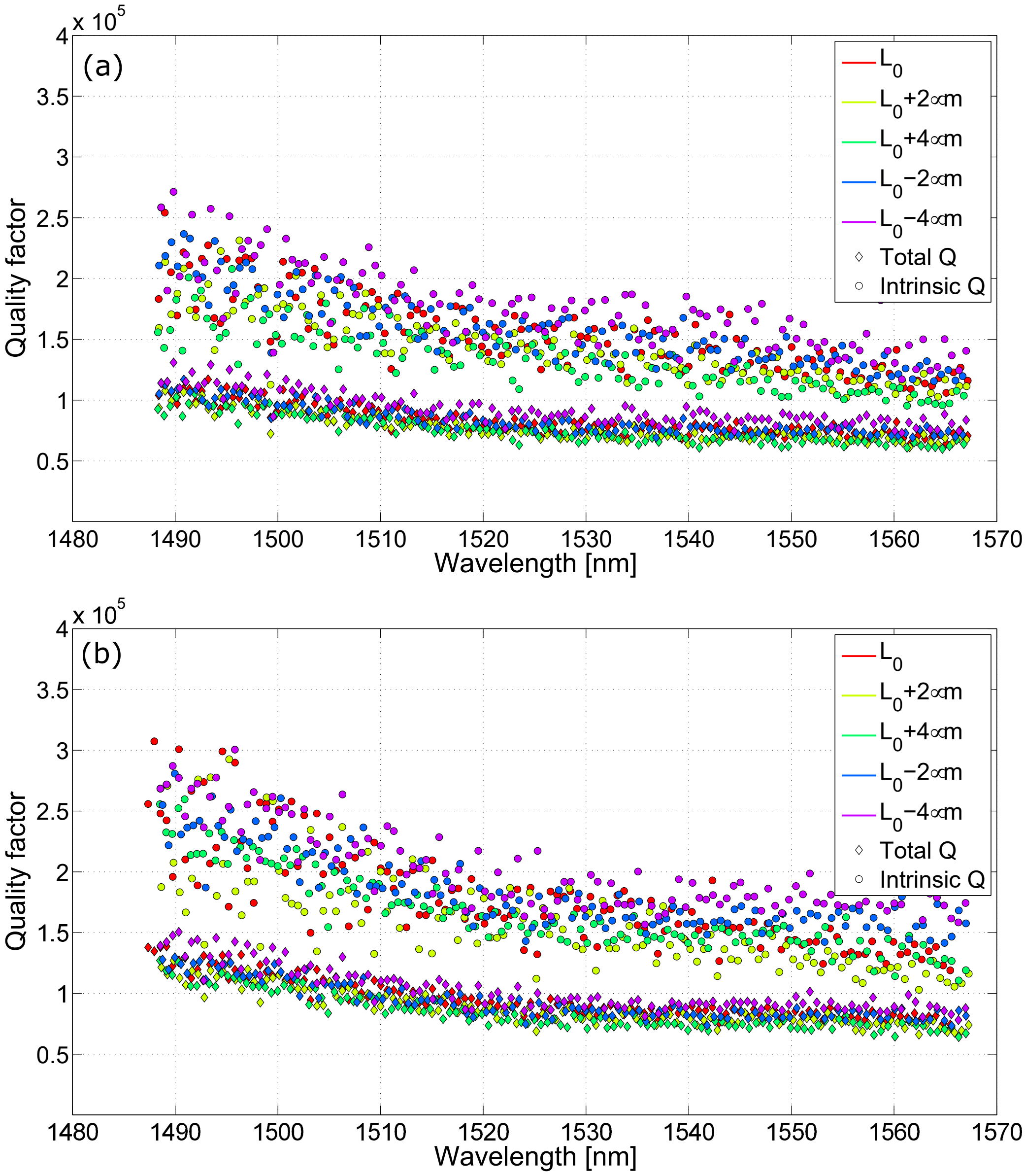

Figure 2.26: Quality factor estimations obtained by fitting the resonances of annealed (a) TEOS and (b) PECVD samples. The measure refers to series of five racetrack resonators with $l_w = 2400\ nm$, $R = 350\ \mu$m and 2μm step variations around the designed critical coupling length designed for IR.

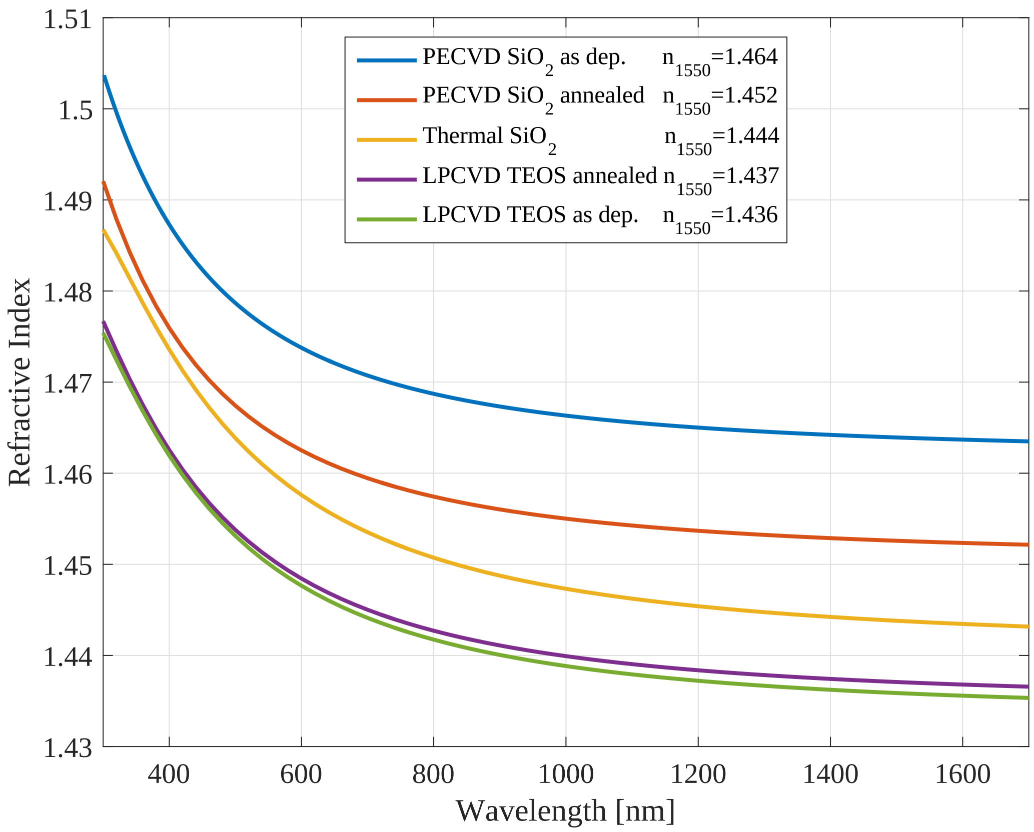

Figure 2.27: TEOS and PECVD oxide index dispersions before and after annealing, compared to that of thermally grown oxide.

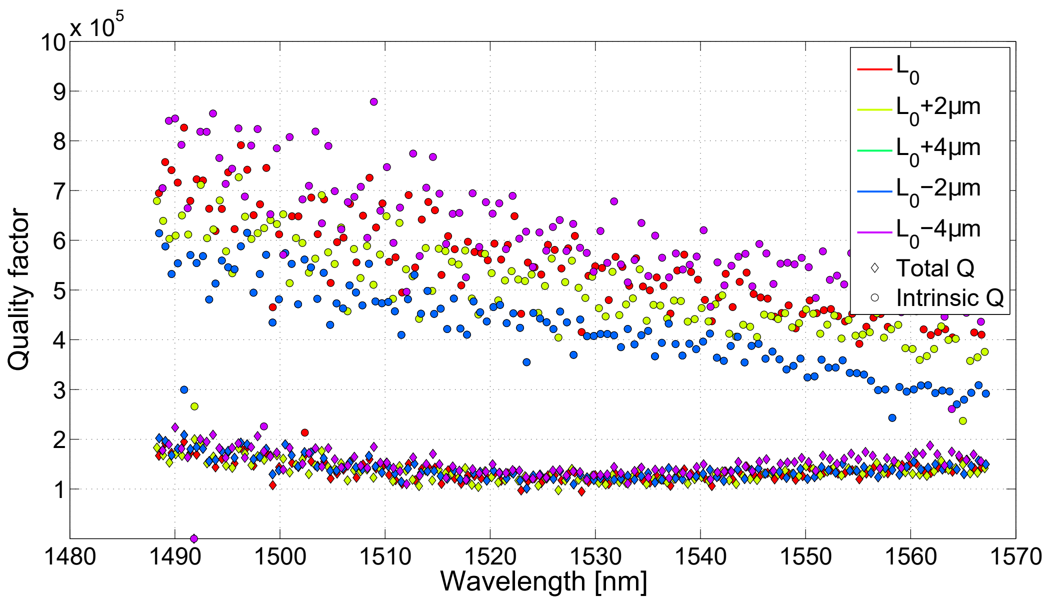

Figure 2.28: Q-factor estimations from the fit of the transmission measurement of large structures ($l_w = 2.8\ \mu$m) on a PECVD sample that was not annealed. The Q-factors of these structures exhibit the highest values in the IR range.

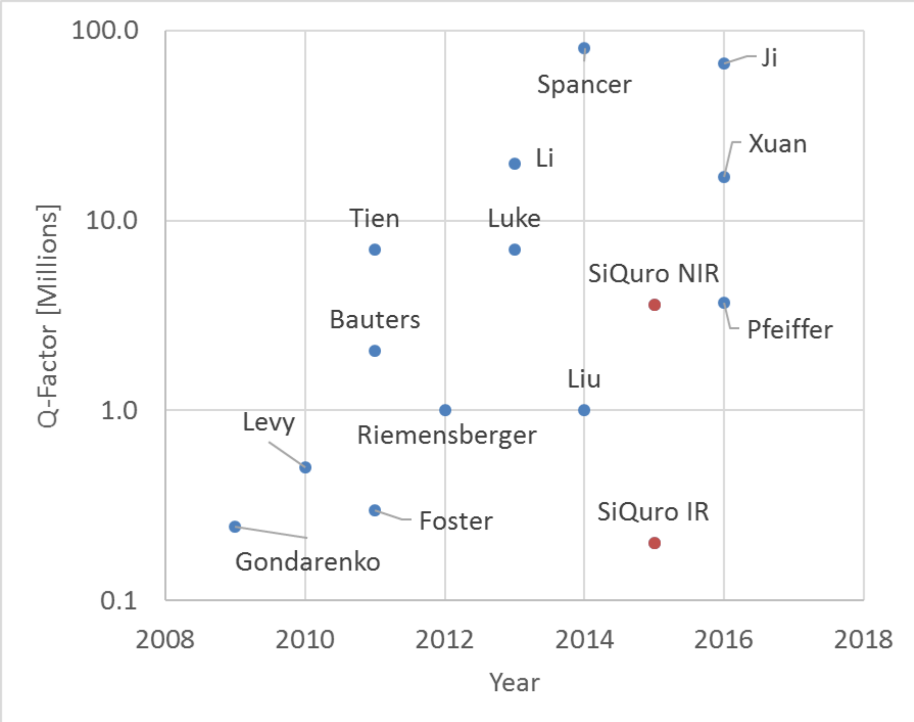

Figure 2.29: Quality factors of Si_3N_4 micro-resonators found in literature. The cited works are reported in Tab. 6.

fabrication process for SL-waveguides using a pre-existing layout optimizing the free parameters. Then, I fabricated the samples in the FBK fab facility and measured them in the NanoLab laboratories of the University of Trento. The optimized structures have been the object of the Laurea Magistrale thesis work of Lucio Stefan [88], which I supervised. Using the developed model, we designed optimized structures on dedicated layouts and fabricated the samples in the FBK fab facility. L.S. carried on the optical transmission measurements, which were then elaborated using the analysis routine I developed during this thesis work.

The realization of strip-loaded waveguide permitted to obtain UHQ-factors in both the NIR and third-telecom band region, obtaining values of the unloaded Q-factor as high as 3.7×10^6 and 0.9×10^6 respectively. The important improvement of these devices resides in the use of a thin Si_3N_4 film of only 80 nm and 115 nm for the two bands respectively. The realized resonators indeed achieved performances competing with devices obtained from 900 nm Si_3N_4 resonators which require special treatments to avoid film cracking [81]. A similar strategy, where the mode is strongly confined in the vertical direction, has been realized in channel waveguides with very high width-to-height aspect ratio in previous works [89, 90] obtaining comparable Q-factors. The most important limitation of this strategy lies in the high bend loss, which requires bend radii exceeding the millimeter to become comparable to the material losses. Figure 2.29, together with Tab. 6, give a picture of the state-of-the art in Si_3N_4 UHQ resonators, including the wg_w, wg_h and radius of curvature of the structures. The analysis of measurements of the optimized structures has been published as a paper [91].

The measurements of the larger structures suggested that the single-mode operation constraints are redundant, giving access to more favorable areas of the parameter configurations that could potentially lead to higher Q-factors. Furthermore, the variations induced by the use of different glasses as the loading strip suggest the exploration of other materials within the silicon platform.

Considering the high achieved Q-factors and the possibilities of improvement, further study of these structures could led to an on-chip platform of potential interest in many fields.

Chapter 3

Fano resonances in integrated disk resonators

3.1 Introduction

The study of the consequences of coupling a physical system to an environment constitutes the central problem in the theory of open systems [92]. On one hand, the coupling has dissipative components that allow the system to acquire and dissipate energy through decay channels. On the other hand, the reactive components of the coupling shift the energy levels and oscillation frequencies of the system.

In the past, the coupling between a system and the environment has been extensively studied in the form of atoms couped to the electromagnetic field. In this case, the dissipative and reactive components manifest as spontaneous emission of photons from an excited state [93, 94, 95] and the Lamb shift of transition frequencies [96, 97, 98], respectively.

In late 1970's, experimental studies [99] showed that destructive interference of different decay paths that lead to the same final continuum can suppress absorption by a multilevel atom via the so-called Coherent Population Trapping (CPT) [100] and Electromagnetically Induced Transparency (EIT) [101, 102] mechanisms. While originally these phenomena were discovered in the atomic physics context, a continuous interest has been devoted to analogous effects in solid-state systems [103], quantum billiards [104, 105, 106], photonic devices [107, 108, 109, 110, 111, 112, 113], and, very recently, opto-mechanical systems [114]. While in most experiments only the dissipative features are affected by the interference, the theory predicts that a similar phenomenon should also occur for the reactive components [92].

In photonics, a waveguide is often present in the vicinity of a resonator to provide with a mean of interaction. Indeed, the waveguide activates new radiative decay channels for the resonator modes via emission of light into the waveguide mode and vice-versa [115, 116, 117], which permits us to probe the resonator spectrum. Correspondingly, the waveguide alters the environment in which the resonator is embedded, causing also a reactive effect that results in a shift of the resonator mode frequencies.

Both the dissipative and the reactive coupling of the cavity modes to the waveguide turn out to be affected by interference phenomena between the said modes, which

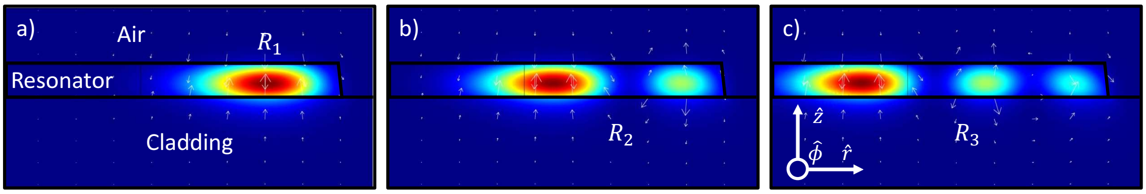

Figure 3.1: a) first, b) second and c) third radial modes electric field intensity distribution in an integrated microresonator. Red color corresponds to high value of field intensity, while deep blue corresponds to zero field. The white arrows represent the local direction of the electric field.

can be summarized as environment-induced inter-mode couplings.

In this chapter I report on a joint theoretical, experimental and computational study of a photonic device in which couples of spectrally overlapping modes are simultaneously coupled to the same waveguide. The presence of the waveguide near the resonator is demonstrated to contribute with both dissipative and reactive coupling components, which are affected by interference phenomena between the two modes. These couplings are modeled drawing an analogy with the atomic Coherent Population Trapping (CPT) for the dissipative component, and a photonic analogue of an off-diagonal Lamb-shift for the reactive part. Experimental observation of interference features in the transmission spectrum of the coupled waveguide permitted to verify the model on a discrete set of frequency-detuned resonance doublets, given by different azimuthal modes of the same resonator.

Then, in order to obtain a continuous sampling of the phenomenon, I extended the model to include all-optical non-linear interactions between the modes of the resonator. The non-linear interaction, mediated by the thermo-optic effect, is then exploited to achieve continuous detuning of the resonance doublets relative frequency, demonstrating mode crossing and complete disappearance of a resonance feature in the transmission spectrum.

3.2 Description of the system

The system under consideration is composed by an integrated microdisk Whispering Gallery Mode Resonator (WGMR) coupled to a waveguide (WG).

In general, the resonator possesses a number of modes, solutions of the Helmolt'z equation in radial coordinates, which depend on three quantum numbers: z,R,M for the axial, radial and azimuthal coordinate respectively. In the following, I will consider the microdisk resonator thin enough so that there exist only a single solution along the axial direction, that is $z = 1$. Furthermore, only a few of the radial solutions will be considered, and therefore it is useful to classify the modes with the same radial number i as the i^{th} Radial Mode Family (RMF) R_i. The first RMF, R_1, has a single lobe in the radial direction and travels near the interior border of the resonator, as shown in Fig. 3.1 a). Higher order RMF have more lobes, that progressively extend towards the inside of the resonator, (b,c).

The resonator is probed through a bus waveguide, which is placed near the resonator edge. When light is injected into the waveguide, the evanescent tails of the waveguide

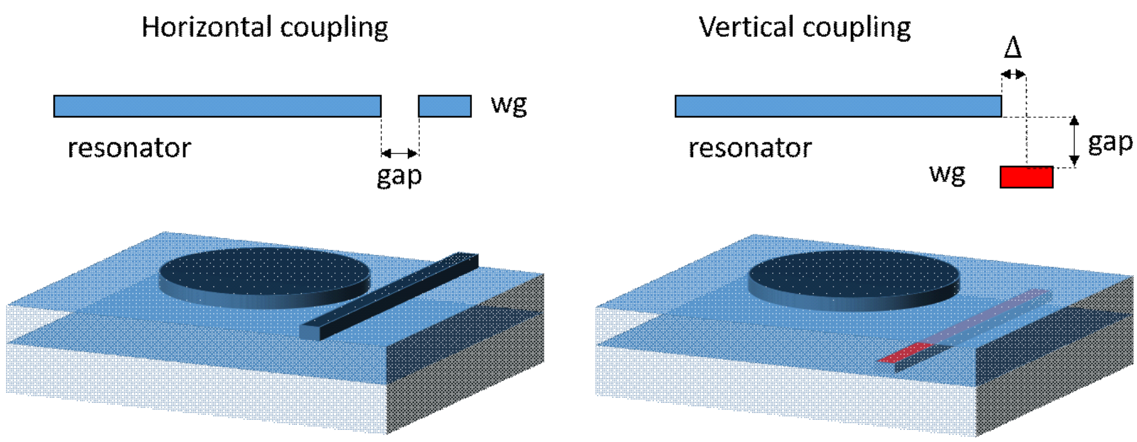

Figure 3.2: Typical (left) horizontal and (right) vertical coupling configurations for integrated microresonators. In the horizontal coupling the waveguide and the resonator are fabricated in the same material and the only parameter of the coupling is the gap amon the two. In the vertical coupling configuration, both a vertical gap and a lateral shift, Δ, are present.

modes overlap with those of the resonator, permitting to couple energy inside the resonator.

In integrated systems, the waveguide and the resonator are usually realized in the same layer, and are coupled through the in-plane evanescent tails of their respective modes. While this configuration offers the big advantage of requiring a single device layer, which is particularly relevant when using SOI wafers, the horizontal coupling offers limited degrees of freedom. Indeed, with a horizontally coupled microdisk resonator, the only coupling degree of freedom is the gap between the waveguide and the resonator. In this case, because of the RMFs field distribution along the radial direction, the first RMF, R_1, always has an larger coupling with the waveguide with respect to the higher order RMF modes, that being more confined within the inner region of the disk, are progressively less coupled.

In the present study, the integrated microdisk is vertically coupled with an integrated single-mode waveguide, which is located below the disk, as shown in Fig. 3.2. This vertical coupling configuration offers the possibility to place the waveguide under the resonator, allowing to access the evanescent tails of the inner modes in a preferential way. Using this technique, it is indeed possible to control the relative coupling among different radial families, as shown in Fig. 3.3. By tuning the relative coupling of modes, it becomes possible to achieve near-critical coupling condition for different RMFs at the same time.

The remarkable tunability of the waveguide-resonator coupling in the vertical coupling configuration may be explored by *ab initio* numerical simulations employing Final Elements Method (FEM), which I realized using a 3D full-wave commercial software. During this study I focused on the interactions between the first (R_1) and second (R_2) Radial Mode Families, that is emphasized by the simultaneous achievement or near-critical couping condition in the two RMF. The FEM simulations map the eigenmodes of the electromagnetic wave equation on a full 3D model of a waveguide-resonator system. Figure 3.3 shows an extract of the simulations near the coupling zone, where the waveguide approaches the edge of the resonator, progressively shifting the coupling from the R_1 modes to the inner R_2 modes. In Fig. 3.4 the coupling

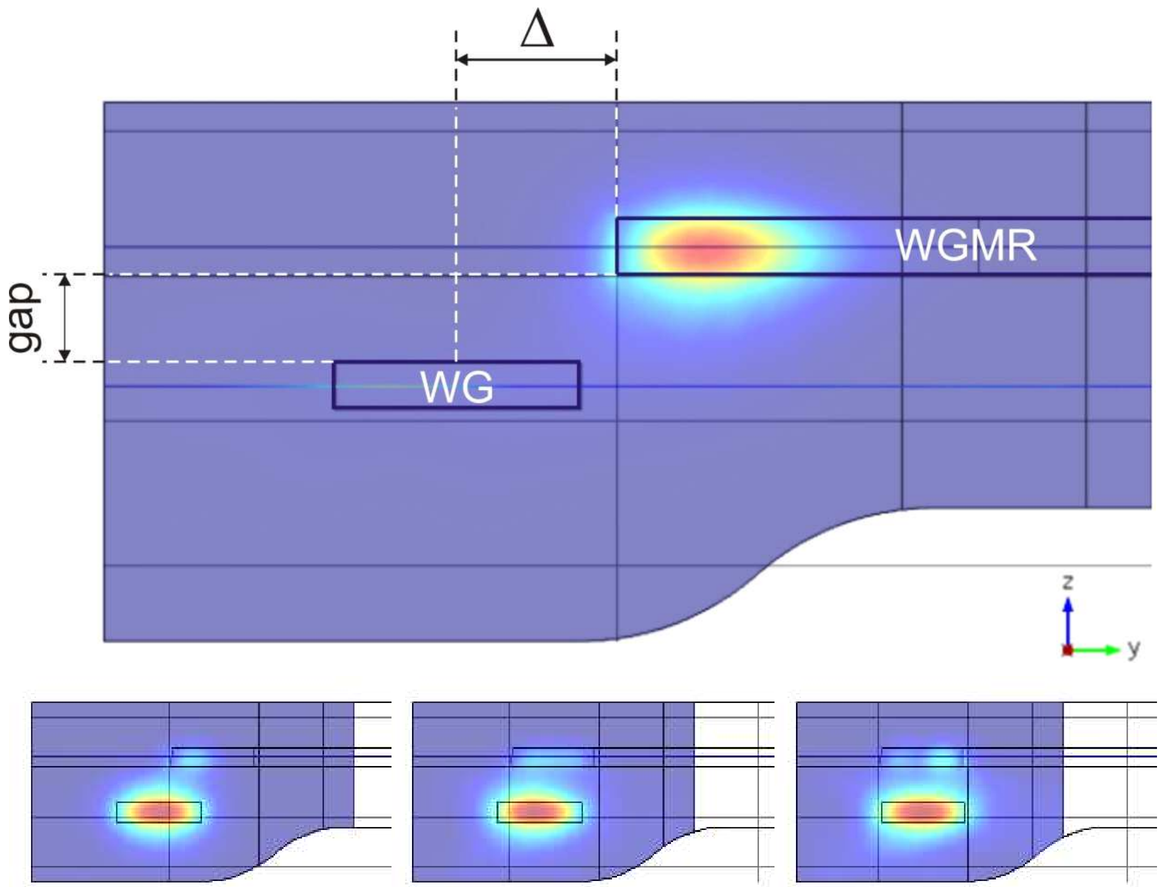

Figure 3.3: Simulation of the waveguide-resonator coupling using a full 3D model. (top) the waveguide is separated from the resonator through two parameters: the vertical gap and the horizontal shift Δ. (bottom panels) The relative coupling between the first and the second RMF changes as the waveguide is pushed further under the resonator, with an increasing fraction being coupled to the R_2 RMF.

ratio between the second and the first RMS in a disk resonator is reported. The coupling ratio is largest when the lateral position of the waveguide matches the main lobe of the second RMF. Indeed, the coupling ratio changes widely with the radial waveguide position, and the overall change spans over two orders of magnitude.

At the same time, the presence of the waveguides enables a reactive component which acts on each of the separated modes frequencies. The frequency shifts Δ_{11} and Δ_{22}, defined with respect to the eigenfrequencies ω_i^0 of the bare resonator, are generally positive when a high index object, the waveguide, is approached, resulting in a red shift of all modes of the resonator [115]. The effect becomes particularly interesting when the interacting modes overlap spectrally, which is possible in a microdisks supporting more than one radial mode family. In this case, in addition to the interaction between each of the separated modes and the waveguide, cross terms representing the exchange of photons from one mode to the other bridging through the waveguide appear, as sketched in Fig. 3.5.

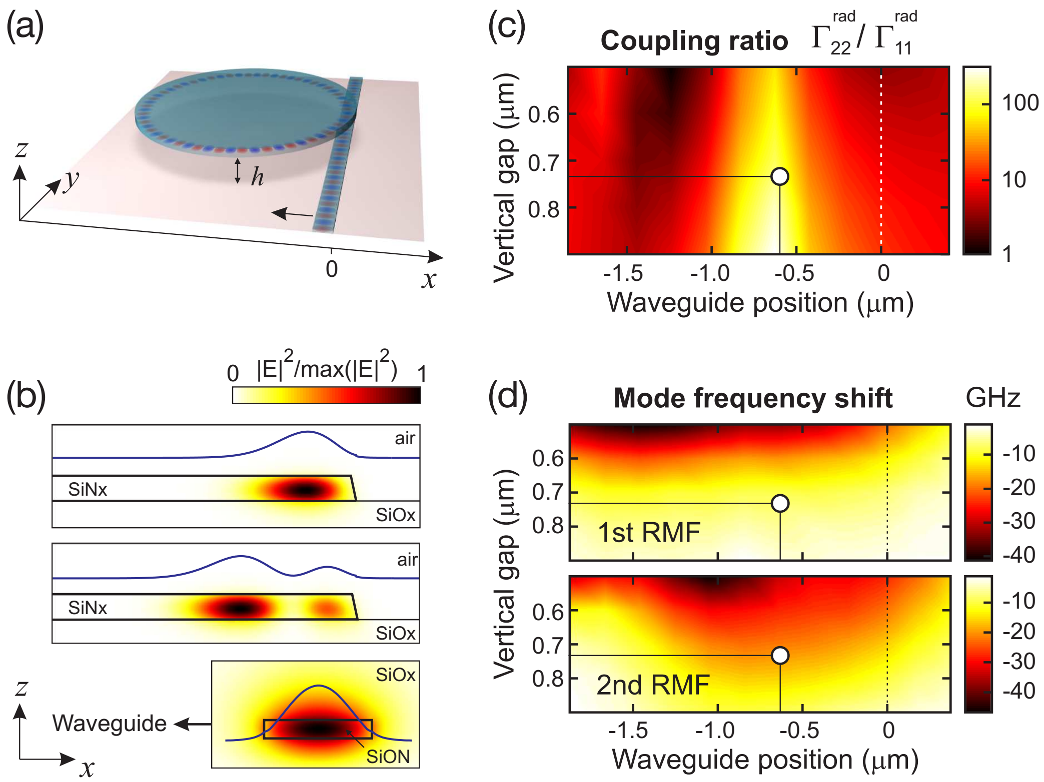

Figure 3.4: (a) the vertical coupling technique adds another degree of freedom in the waveguide-resonator coupling. In particular (b), the electric field profiles of the radial modes are different along the radial direction. The coupling ratio (c) between the waveguide and the R_2 and R_1 RMFs was simulated with 3D full-vector FEM simulations of the system, exploring the configuration space of the vertical coupling. The coupling ratio spans two orders of magnitude, with the strongest variations along the horizontal axis. The white dot refers to the coupling condition of the used resonators, that exhibit a stronger coupling for the R_2 family with respect to R_1. Furthermore (d), the presence of the waveguide detunes the resonant frequencies of the resonator by a value of the order of tens of GHz. Image taken from [118].

3.3 Analytical Theory

The general transmission spectra of a waveguide-resonator system has already been described in Sec. 0.2.3. In this case, however, the formalism of the dynamic equations of the mode amplitudes inside the resonator is more suitable to describe the system [119], as it can easily be extended to include the relevant quantities in the two-mode case. In this formalism the two mode amplitudes $\alpha_{i=1,2}$ are calculated by solving

$$\mathcal{L}_i(t) \equiv \mathrm{i}\frac{d\alpha_i}{dt} = \left[\omega_i^o + \Delta_{ii} - \mathrm{i}\frac{\gamma_i^{\mathrm{nr}} + \Gamma_{ii}^{\mathrm{rad}}}{2}\right]\alpha_i + \bar{f}_i E_{\mathrm{inc}}(t). \tag{3.1}$$

In Eq.3.1, when the modes are spectrally separated, ω_i^0 represents the (isolated-) mode bare frequency in the absence of the waveguide, while the term Δ_{ii}, as mentioned above, represents a frequency shift due to the self-interaction of the modes through the waveguide. The loss channels of the modes, represented inf Fig. 3.5, are the sum of the intrinsic non-radiative decay rates, γ_i^{rn}, and Γ_{ii}, which account for the mode losses through coupling with the waveguide. The last term $\bar{f}_i E_{\mathrm{inc}}(t)$ is the coupling

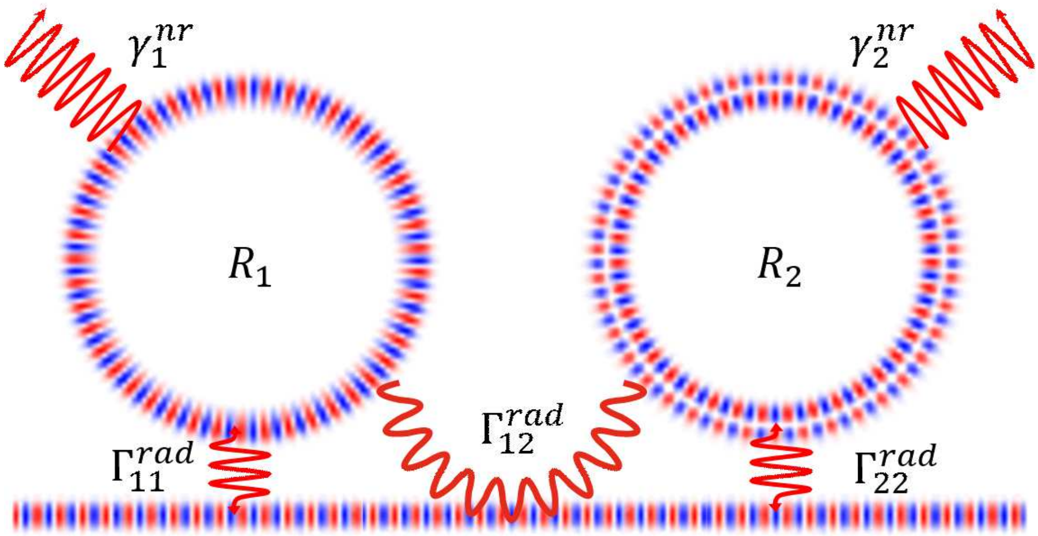

Figure 3.5: Representation of the various coupling terms of the resonator. Each RMF is coupled to the waveguide through the term $\Gamma_{ii}^{\mathrm{rad}}$ and to the environment with γ_i^{nr}. Furthermore, R_1 and R_2 are coupled together through the waveguide by the term Γ_{12}^{rmrad}. The two RMFs are actually inside the same resonator in partial spatial overlap.

amplitude that is gained from the waveguide, with the incident field that will be supposed monochromatic in the form $E_{\mathrm{inc}}(t) = E_{\mathrm{inc}} e^{-\mathrm{i}\omega_{inc} t}$.

When the modes lie in the same spectral region, further coupling terms Δ_{12} and Γ_{12} appear, taking into account for the coupling effect of the waveguide on the two mode oscillations:

$$\mathcal{D}_i(t) = \mathrm{i}\frac{d\alpha_j}{dt} = \mathcal{L}_i(t) + \left(\Delta_{12} - \mathrm{i}\frac{\Gamma_{12}^{\mathrm{rad}}}{2}\right)\alpha_{3-i}. \tag{3.2}$$

Formal application of the open-system theory provides with a general expression for the Hermitian matrices Δ and Γ^{rad}

$$\Delta_{ij} + \mathrm{i}\frac{\Gamma_{ij}^{\mathrm{rad}}}{2} = \int \frac{dK}{2\pi} \sum_{\beta} \frac{f_{\beta,i}^{*}(K)\, f_{\beta,j}(K)}{\omega_{\mathrm{inc}} - \Omega_{\beta}(K) - \mathrm{i}0^{+}}, \tag{3.3}$$

in terms of the coupling amplitudes $_{\beta,i}(K)$ of the i, j modes of the resonator with the waveguide mode of longitudinal wavevector K, propagation constant β and frequency $\Omega_\beta(K)$.

A quantitative estimation of the integral in Eq.3.3 is not generally possible, as it involves a summation over all of both guided and non-guided waveguide modes. Nevertheless, we may make some general considerations on the Γ^{rad} and Δ matrices under the hypothesis that the waveguide is single-moded. The $\Gamma_{12}^{\mathrm{rad}}$ coefficient,that represents the decay channel of a mode of the resonator into the other through the waveguide, is related to the radiative linewidths by $\Gamma_{12}^{\mathrm{rad}} = \sqrt{\Gamma_{11}^{\mathrm{rad}}\Gamma_{22}^{\mathrm{rad}}} = \Gamma_{21}^{\mathrm{rad}}$. Thanks to this relation, the Γ^{rad} matrix can then be written in the form $\Gamma_{ij}^{\mathrm{rad}} = \bar{\Gamma}\eta_i\eta j$ where the $\eta_{i,j}$ terms represent (real) weights of the relative coupling of the modes to the waveguide, normalized such that $\eta_1^2 + \eta_2^2 = 1$. A similar consideration may be done for the Δ matrix, where it is useful to isolate the contribution of the single waveguide propagating mode Δ^{rad} from all of the others as $\Delta = \Delta^{\mathrm{rad}} + \Delta^{\mathrm{other}}$. From our experimental evidence, there is no measurable contribution from the non-diagonal terms $\Delta^{\mathrm{other}}_{ij} = 0$ with $i \neq j$, while the diagonal terms $\Delta^{\mathrm{other}}_{11,22}$ are practically reabsorbed into the bare frequency as $\omega^b_i = \omega^0_i + \Delta^{\mathrm{other}}_{ii}$.

The remaining Δ^{rad} matrix may now be written as a constant multiplied by the weights matrix η, in analogy to Γ^{rad}. In compact matrix notation we have:

$$\eta_{ij} = \eta_i \eta_j, \tag{3.4a}$$
$$\Gamma^{\mathrm{rad}} = \bar{\Gamma}^{\mathrm{rad}} \eta, \tag{3.4b}$$
$$\Delta^{\mathrm{rad}} = \bar{\Delta}^{\mathrm{rad}} \eta. \tag{3.4c}$$

In Sec.0.2.3 I described the conditions for the critical-coupling between the resonator and the waveguide modes. In this case, coupling constant of each single RMF is represented by $\Gamma^{\mathrm{rad}}_{ii}$ that reaches under-,critical- or over-coupling regimes depending whether it is lower than, equal to, or larger than the intrinsic loss, that is translated into γ^{nr}_i in this formalism. The spectral features of the resonator modes are the most visible in the transmission spectrum near the critical-coupling condition, while the depth of the resonance features asymptotically vanishes for both under- and over- coupling conditions (cnf. Fig. 14). When two RMF families are present near critical condition, i.e. they both interact strongly with the same waveguide, the transmission spectra becomes much richer. As shown in Fig. 3.6, the application of Eq. 3.2 to resonances near the critical-coupling condition offer very different scenarios depending on the ratios of Γ^{rad} and Δ with respect to the intrinsic loss γ^{nr}_j.

In the figure the two resonances are considered to have very different non-radiative loss ($\gamma^{\mathrm{nr}}_1 = 0.1\gamma^{\mathrm{nr}}_2$) as it will be the case in our resonator for the first and second RMFs. In Fig. 3.6 a) both resonances are slightly under-coupled, i.e. $\Gamma^{\mathrm{rad}}_{jj} \lesssim \gamma^{\mathrm{nr}}_j$, and the non-diagonal reactive terms are vanishing $\Delta_{12} = 0$. The two modes manifest each as a dip in the transmission spectra, centered at frequency $\omega_j = \omega^0_j + \Delta_j j$. The modes are plotted for different values of the relative detuning $\delta = \omega_2 - \omega_1$, therefore with the broad R_2 resonance crossing the shallow R_1 mode, in the center. In this case, the modes interact weakly and the transmission spectra result simple superposition of the two dips for all values of the detuning. It's worth to note that proper inclusion of the non-diagonal dissipative components $\Gamma^{\mathrm{rad}}_{12}$ and $\Gamma^{\mathrm{rad}}_{21}$ is still necessary to avoid the appearance of non-physical features in the calculations, such as $T(\omega) > 1$. In Fig. 3.6 b), on the other hand, both resonances are slightly over-coupled $\Gamma^{\mathrm{rad}}_{jj} \lesssim \gamma^{\mathrm{nr}}_j$ while still keeping $\Delta_{12} = 0$. By increasing the coupling, the non-diagonal terms $\Gamma^{\mathrm{rad}}_{12}$ become more important and the mode amplitudes interfere when the modes overlap spectrally, giving complex features in the transmission. In particular, the narrow R_1 dip, visible in at the center of the spectra of the first and seventh row, is replaced by a complex Fano-like line shape [120, 121, 122] for moderate detuning (third and fifth rows), and even reverses it sign into a transmitting EIT-like feature for small values of the detuning (fourth row). Experimental observation of similar physics has been recently reported in [109, 111, 110]. Finally, in Fig. 3.6 c) the off-diagonal reactive coupling Δ_{12} is switched on to $\Delta_{12} = 0.6\gamma^{\mathrm{nr}}_2$, in a condition where the two resonances R_1 and R_2 are under- ($\Gamma^{\mathrm{rad}}_{11}/\gamma^{\mathrm{nr}}_1 = 0.125$) and over-coupled ($\Gamma^{\mathrm{rad}}_{22}/\gamma^{\mathrm{nr}}_1 = 2$) respectively. The most visible spectral feature that is introduced is that the spectra are no longer symmetric under the change of sign of the detuning δ. With respect to the case of panel b), the Fano feature has a reversed sign for moderate detuning (third and fifth rows) due to the opposite coupling regimes. Furthermore, the narrow

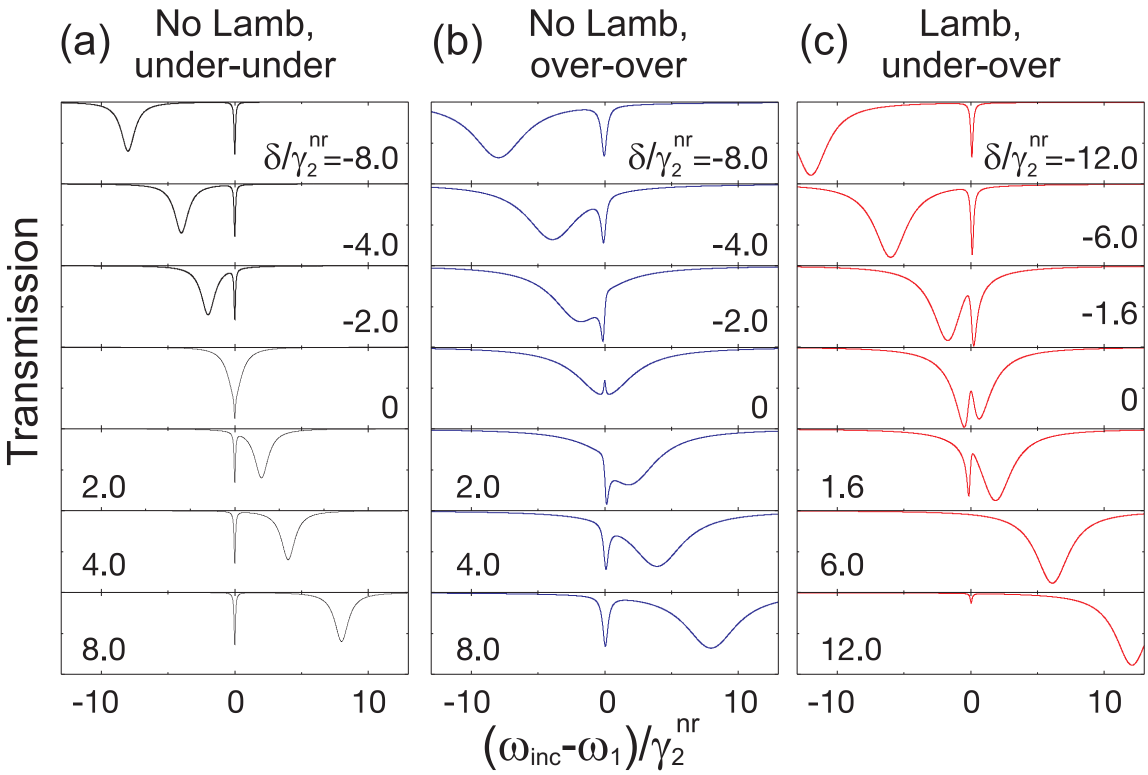

Figure 3.6: Transmission spectra calculated in different regimes at different values of the detuning $\delta = \omega_2 - \omega_1$. Each graph is plotted in normalized units $(\omega_{\rm inc} - \omega_1)/\gamma_2^{\rm nr}$. Considering no off-diagonal Lamb-like interaction ($\Delta_{12} = 0$) and similar losses ($\gamma_1^{\rm nr}/\gamma_2^{\rm nr} = 0.1$), when both modes are in (a) under-coupled ($\Gamma^{\rm rad}_{11,22}/\gamma^{\rm nr}_{1,2} = 0.25$) or (b) over-coupled ($\Gamma^{\rm rad}_{11,22}/\gamma^{\rm nr}_{1,2} = 4$) regime their interaction is symmetric with respect to δ. (c) when the $\Delta_{12}/\gamma_2^{\rm nr} = 0.6$ term is introduced and the coupling regimes differ ($\Gamma^{\rm rad}_{11}/\gamma_1^{\rm nr} = 0.125, \gamma_1^{\rm nr}/\gamma_2^{\rm nr} = 0.16$ ($\Gamma^{\rm rad}_{22}/\gamma_2^{\rm nr} = 2$), the spectrum is no more symmetric. Image from [118]

R_1 feature leaves a deep mark in the transmission spectra, which is unexpected given its under-coupled regime, having an amplified feature for positive detuning (second row) while reaching a region of complete feature suppression for some negative values (sixth row). This strange behaviour is explained in terms of destructive interference between the direct excitation of the R_1 resonance and the cross-coupled excitation from the R_2 mode mediated by the waveguide through the off-diagonal terms of Δ and $\Gamma^{\rm rad}$. Indeed, the two coupling paths almost cancel out around $\delta \approx \Delta_{12}\sqrt{\Gamma^{\rm rad}_{22}/\Gamma^{\rm rad}_{11}}$.

3.3.1 Transmission spectra

The steady state condition for the interacting modes may be written in a compact matrix notation making use of the auxiliary quantities

$$\delta_1 = \omega_{\rm inc} - \omega_1^{\rm b} + \frac{\rm i}{2}(\gamma_1^{\rm nr} + \Gamma^{\rm rad}_{11}) - \Delta^{\rm rad}_{11}, \tag{3.5a}$$

$$\delta_2 = \omega_{\rm inc} - \omega_2^{\rm b} + \frac{\rm i}{2}(\gamma_2^{\rm nr} + \Gamma^{\rm rad}_{22}) - \Delta^{\rm rad}_{22}, \tag{3.5b}$$

that represent the single-resonance couplings with the waveguide, and

$$a = \mathrm{i}\frac{\Gamma_{12}^{\mathrm{rad}}}{2} - \Delta_{12}^{\mathrm{rad}}, \tag{3.6}$$

that represents the waveguide-mediated coupling between the modes. Using these quantities, the interaction matrix $\mathbf{M}$ may be written as

$$\mathbf{M} = \begin{pmatrix} \delta_1 & a \\ a & \delta_2 \end{pmatrix} \tag{3.7}$$

and, finally, the steady state equation of the system becomes

$$\mathbf{M}\begin{pmatrix} \bar{\alpha}_1 \\ \bar{\alpha}_2 \end{pmatrix} = \begin{pmatrix} \eta_1 \\ \eta_2 \end{pmatrix} E_{\mathrm{inc}}. \tag{3.8}$$

Equation 3.8 may be inverted to find the steady state normalized mode amplitudes $\bar{\alpha}_i$

$$\bar{\alpha}_1 = \frac{\delta_2\eta_1 - a\eta_2}{a^2 - \delta_1\delta_2}, \tag{3.9a}$$

$$\bar{\alpha}_2 = \frac{\delta_1\eta_2 - a\eta_1}{a^2 - \delta_1\delta_2}. \tag{3.9b}$$

The amplitudes $\bar{\alpha}_i$ can be inserted in the transmission amplitude

$$t(\omega_{\mathrm{inc}}) = 1 - \mathrm{i}\bar{\Gamma}^{\mathrm{rad}}(\eta_1\bar{\alpha}_1 + \eta_2\bar{\alpha}_2), \tag{3.10}$$

obtaining the final expression

Fano interference and Lamb shifts

$$t(\omega_{\mathrm{inc}}) = 1 + \mathrm{i}\Gamma\left(\frac{\delta_2\eta_1^2}{a^2 - \delta_1\delta_2} + \frac{-2a\eta_1\eta_2}{a^2 - \delta_1\delta_2} + \frac{\delta_1\eta_2^2}{a^2 - \delta_1\delta_2}\right). \tag{3.11}$$

In the limiting case where one of the two resonances is not present, i.e. $\eta_i = 0$, the coupling term a which depends on the product $\eta_i\eta_j$ vanishes, recalling the usual expression for the remaining (single) resonance case

Single resonance limit

$$t_{\mathrm{single}}(\omega_{\mathrm{inc}}) = 1 - \mathrm{i}\bar{\Gamma}^{\mathrm{rad}}\left(\frac{\eta_j^2}{\delta_j}\right) = 1 - \mathrm{i}\frac{\Gamma_{jj}^{\mathrm{rad}}}{\omega_{\mathrm{inc}} - \omega_j^{\mathrm{b}} + \frac{\mathrm{i}}{2}(\gamma_j^{\mathrm{nr}} + \Gamma_{jj}^{\mathrm{rad}}) - \Delta_{jj}^{\mathrm{rad}}}. \tag{3.12}$$

On resonance, i.e. with the single-resonance mode frequency $\omega_{\mathrm{inc}} = \omega_j^{\mathrm{b}} + \bar{\Delta}^{\mathrm{rad}}$, the transmission amplitude is

$$t_{\mathrm{res}} = \frac{\gamma_j^{\mathrm{nr}} - \bar{\Gamma}^{\mathrm{rad}}}{\gamma_j^{\mathrm{nr}} + \bar{\Gamma}^{\mathrm{rad}}}. \tag{3.13}$$

For $\bar{\Gamma}^{\mathrm{rad}} < \gamma_j^{\mathrm{nr}}$ ($\bar{\Gamma}^{\mathrm{rad}} > \gamma_j^{\mathrm{nr}}$) one has the under- (over-) coupling regime and the transmission dip is partial, while it is complete for critical coupling $\bar{\Gamma}^{\mathrm{rad}} = \gamma_j^{\mathrm{nr}}$. In our case, the R_2 resonance is near to the critical coupling, leaving a deep feature in the transmission spectrum.

Fano interaction as perturbation

To introduce the effect of the second resonance, it may be useful to separate the effects of the two resonances, isolating the term that describes R_2 in Equation 3.11

$$t(\omega_{\text{inc}}) = 1 - \mathrm{i}\frac{\bar{\Gamma}^{\text{rad}}\,\eta_2^2}{\delta_2} - \mathrm{i}\frac{\bar{\Gamma}^{\text{rad}}\,\eta_1^2}{\delta_1 - a^2/\delta_2}\left(1 - \frac{a}{\delta_2}\frac{\eta_2}{\eta_1}\right)^2. \tag{3.14}$$

In this form, the first and the second term represent clearly the single resonance spectrum of Eq. 3.12: the second term, proportional to δ_2^2, describes the broad transmission dip due to the broader mode R_2, while the third term describes the Fano features with R_1. In our case, when the two peaks are spectrally close, the term $a^2\delta_2$ seems not to play a relevant role in the modulation of the transmission spectrum. The modulation of the R_1 feature is dominated by the square of the slowly varying factor

$$F_1 = 1 - \frac{a}{\delta_2}\frac{\eta_2}{\eta_1} = \frac{\omega_{\text{inc}} - \omega_2^{\text{b}} + \frac{\mathrm{i}}{2}\gamma_2^{\text{nr}}}{\omega_{\text{inc}} - (\omega_2^{\text{b}} + \eta_2^2\bar{\Delta}_{\text{rad}}) + \frac{\mathrm{i}}{2}(\gamma_2^{\text{nr}} + \eta_2^2\bar{\Gamma}_{\text{rad}})}, \tag{3.15}$$

that multiplies the R_1 amplitude in Eq. 3.14.

Focusing on the experimental case, let's now consider the situation when $\gamma_1^{\text{nr}} \ll \gamma_2^{\text{nr}}$ and $\eta_1 \ll \eta_2$. The broad resonance R_2 is close to the critical coupling, meaning that $\gamma_2^{\text{nr}} \approx \Gamma_{22}$, while R_1 is in under-coupled regime i.e. $\gamma_1^{\text{nr}} > \Gamma_{11}$.

For a very large off-diagonal coupling $\bar{\Delta}_{\text{rad}} \gg \gamma_2^{\text{nr}}, \bar{\Delta}_{\text{rad}} \gg \bar{\Gamma}_{\text{rad}}$, in an extended neighborhood of the R_2 peak (that is for $\omega_{\text{inc}} \approx \omega_2^{\text{b}} + \eta_2^2\bar{\Delta}_{\text{rad}}$), the F_1 factor can be much larger than one in modulus,

$$F_1 \approx \frac{\eta_2^2\bar{\Delta}_{\text{rad}} + \frac{\mathrm{i}}{2}\gamma_2^{\text{nr}}}{\frac{\mathrm{i}}{2}(\gamma_2^{\text{nr}} + \eta_2^2\bar{\Gamma}_{\text{rad}})} \simeq \frac{\bar{\Delta}_{\text{rad}}}{\mathrm{i}\bar{\Gamma}_{\text{rad}}}, \tag{3.16}$$

amplifying the R_1 feature even if this last is in under-coupled regime, as in Fig. 3.6, panel c), second and third rows. On the other hand, in the vicinity of the R_2 bare frequency $\omega_{\text{inc}} \simeq \omega_2^{\text{b}}$, F_1 may become very small,

$$F_1 \approx \frac{\gamma_2^{\text{nr}}}{\gamma_2^{\text{nr}} + \eta_2^2\bar{\Gamma}_{\text{rad}} + 2\mathrm{i}\eta_2^2\bar{\Delta}_{\text{rad}}} \simeq \frac{\gamma_2^{\text{nr}}}{2\mathrm{i}\bar{\Delta}_{\text{rad}}}. \tag{3.17}$$

suppressing the R_1 mode feature, as shown in Fig. 3.6, panel c), sixth and seventh rows. This peculiar suppression of the R_1 peak predicted by the theory is observed in the experiments for specific values of relative detuning of the two modes.

3.3.2 Experimental Results

Sample preparation

The samples has been fabricated in the FBK-CMM facility generally following the techniques described in Sec.0.3.1 for a two device layer fabrication. A $3\mu m$ thick silicon dioxide cladding was grown on top of a silicon wafer, followed by PECVD deposition of 300 nm silicon oxynitride SiO_xN_y that constitutes the first device layer (bus waveguides). The waveguide structures were lithographically patterned and transferred to the device layer using RIE. In order to fabricate flat resonators, planarization is necessary before the second device layer (resonators) is deposited. For this purpose, borophosphosilicate glass is deposited and re-flowed again at 1050°C forming a planar cladding above the waveguides. The second device layer is 400 nm thick, realized in silicon nitride SiN_x. The resonators patterning is realized analogously with a combination of lithographic and dry etching steps.

The transmission measurements were taken using an experimental setup similar to that described in Sec. 0.3.2. A tunable laser in the near-infrared region was coupled to the input facet of the waveguide with a lensed taper fiber. The transmission signal is collected with a similar lensed taper fiber at the output facet and fed to an InGaAs photodiode detector. Polarization controls were placed in both the input and output stages. The position of the waveguide with respect to the 40 μm radius resonator in the sample under investigation is reported in Fig. 3.4 with a white dot. The resulting spectrum features a number of resonances, as shown in Fig.3.7. Measurements

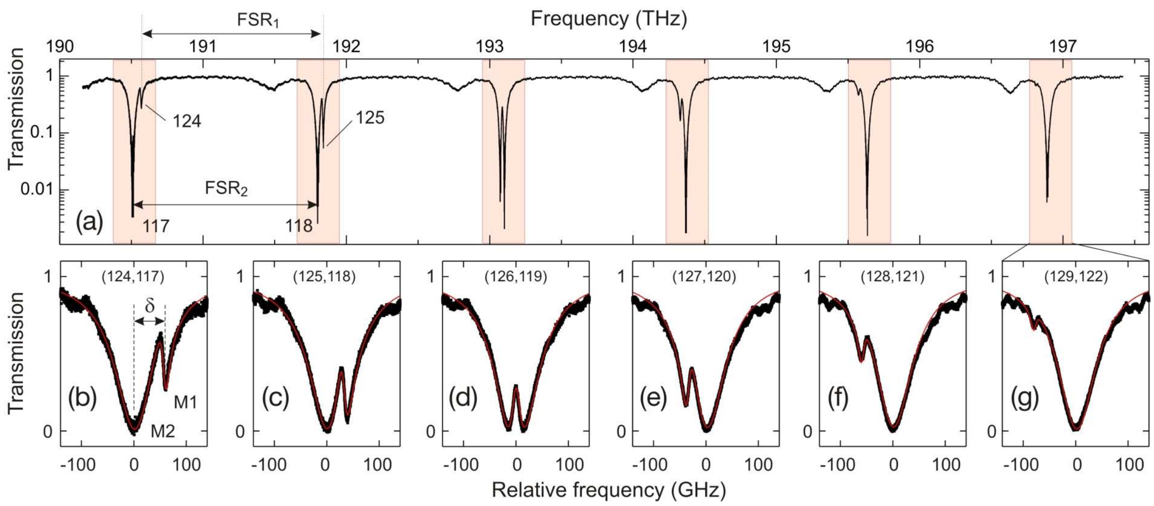

Figure 3.7: (a) measured normalized transmission spectrum as a function of the incident frequency, where six doublets are present. The spacing between the doublets is approximately 1.2THz, with $FSR_1 \approx 1.236$ THz and $FSR_2 \approx 1.256$ THz. (b-g) show the highlighted peaks (black) experimental data with (red) the analytical model fit, reported as a function of the relative frequency measured from ω_2 The azimuthal mode numbers M_1 and M_2 of the R_1 and R_2 RMFs are reported both in (a) and in (b-g). Image from [118].

In the spectrum, three combs of resonances are present, corresponding to the R_1, R_2 and R_3 radial mode families. The resonances of the R_1 and R_2 families are spectrally very close in the investigated region, forming doublets of resonances, composed by two azimuthal modes M and N of the R_1 RMF and of the R_2 RMF, respectively. The R_3 RMF is far enough from the R_1-R_2 doublet to be considered as not interacting, and thus is neglected in the discussion. Due to the difference in the effective refractive index of the R_1 and R_2 RMFs, the Free Spectral Range of their resonances is also different. Therefore, the resonances of the two intertwining combs slide spectrally one against the other, in a similar fashion to a Vernier scale [123], by varying the azimuthal mode numbers M and N by the same (integer) quantity l. Eventually, the resonances pass near a crossing point were doublets are formed. The relative detuning $\delta\omega^{12}$ of two modes in the couple is thus

$$\delta\omega_l^{12} = \omega_{M+l}^1 - \omega_{N+l}^2 \simeq \delta\omega_0^{12} + l \cdot \Delta\mathrm{FSR}_{12}, \tag{3.18}$$

where $\delta\omega_0^{12} = \omega_M^1 - \omega_N^2$ is the relative detuning of the (M, N) resonance doublet and $\Delta\mathrm{FSR}_{12} = \mathrm{FSR}_1 - \mathrm{FSR}_2$. Figure 3.7 shows the spectra of peak doublets with $M = 117$ and $N = 124$ with $l = 0, 1, .., 5$. The exact determination of the azimuthal number is a difficult task, and has been performed through numerical simulations of the device.

Thanks to the Verier effect, a set of spectra of similar resonances from the two RMFs but with a different detuning $\delta\omega_l^{12}$ are available to verify our model for the transmission, described by the squared modulus of Eq. 3.11. Therefore, all of the spectra of Fig. 3.7 b-g) are fitted with the two-coupled-resonances model separately. The fit line (red) is in perfect agreement with the experimental data. A higher perspective picture of the phenomenon may be constructed building a 2D map of peaks spectra against the detuning due to the different FSRs. Figure 3.8 shows the experimental spectra-detuning maps together with the analytical prediction. It's worth to note that the experimental spectra may only be acquired at discrete steps $\delta\omega_l^{12}$, so that the experimental map is an interpolation over the discrete azimuthal modes.

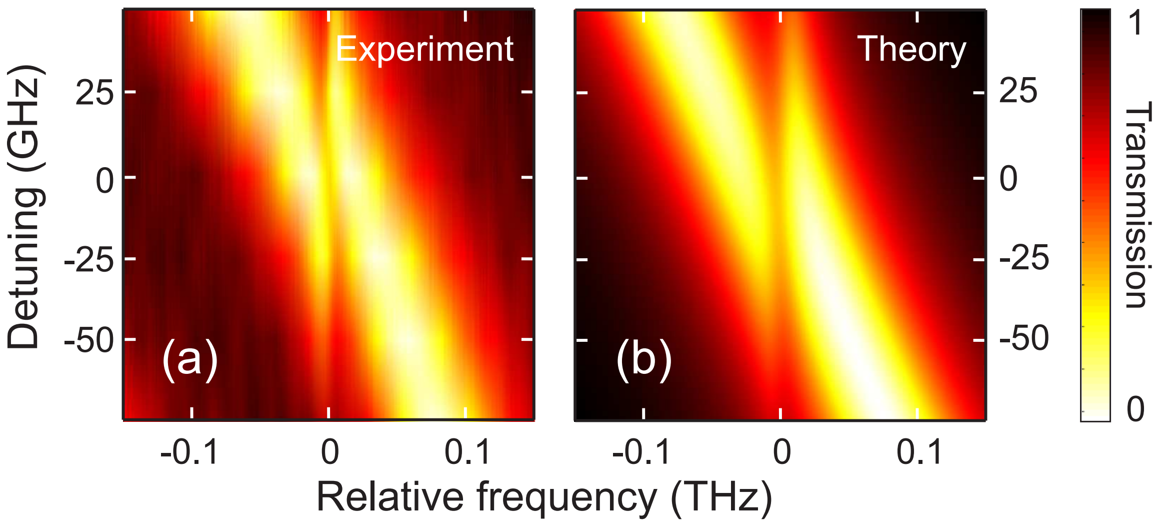

Figure 3.8: Color-map (a) of the doublets spectra against the detuning δ. In the image is realized by interpolation of six spectra taken at different azimuthal number and centered around the position of the R_1 peak. Color-map (b) of the analytical prediction for the same spectra.

The experiment was repeated on a different resonator on the same sample, with a larger radius $r = 50\mu m$. In this case the interference occurs between the R_1 and R_3 RMFs, with the R_2 spectrally well separated.

3.4 Thermo-optic control of Fano-Lamb interaction

As described previously, the relative detuning of the resonances changes with a discrete step of ΔFSR. This fact makes unlikely to observe the vanishing of the R_1 peak feature in the experimental spectrum. A mean of tuning the relative frequency of the two RMFs in a continuous way is desirable to capture all of the features predicted by the model. The problem of precise control of the PICs operational wavelengths is well known [124]. In practical applications, in order to select desired wavelengths, a spectral tunability of the resonant features is often achieved via thermo-optic effect. The thermo-optic effect is achieved by heating the sample, often through electrical micro-heaters made of a thin metal layer, that act as a resistor. The heating is exploited to modify the refractive index of the device acting on the optical path [125, 126, 127]. Due to it's simple mechanism, low cost and applicability to the majority of CMOS processes on virtually all of the optical range, electrical heaters are used in many devices. A huge drawback of the electro-heaters, however, is the poor spatial selectivity of the effect. Due to the metallic nature of the heaters they need to be spatially well-separated from the optical circuitry to avoid spurious losses. Having the heat-source far from the actual device means that the heat diffuses in a rather wide portion of the environment. This means that a whole region of the device is subject to the same thermal change, leading to a global frequency-shift of the modes that travel through the heated region. Other mechanisms have been demonstrated to alter the transmission of a single resonance, as inverse Raman scattering in Si devices [128, 129] with high selectivity to the operational frequency.

In this section I demonstrate an all-optical non-linear interaction, mediated by the thermo-optic effect, as a mean to achieve relative detuning of the resonator RMF resonances, i.e. a continuous tuning of δ_{12}. The selectivity is achieved by exploiting the mode-selective properties of a localized thermo-optic effect generated directly inside the resonator. In fact, the thermo-optic effect is modeled as an interaction through an optical pump and an optical probe, which are both spatially-localized modes of the resonator, extending the coupling model of Sec. 3.3 with including non-linear terms. The relative tunability and the model predictions are validated by pump-and-probe experiments, and are reproduced by numerical simulations. Finally, the relative tunability is used in the devices of the previous Sec.3.3.2 to achieve the condition of complete disappearance from the spectrum of one of the peaks, as well as a complete crossing of the resonances.

3.4.1 Analytical Theory

The refractive index of a material is a function of the material temperature. The thermo-optic coefficient dn/dT is defined, for small variation in temperature, as the first Taylor expansion of the refractive index as a function of the temperature. For a small, homogeneous variation of temperature by ΔT the refractive index of a material may be expanded as

$$n(\Delta T) = n_0 + \frac{dn}{dT}\Delta T, \tag{3.19}$$

where n_0 is the refractive index at the temperature around which the expansion is considered, in this case room temperature.

This reasoning can be extended to the effective refractive indices n_{eff}^R of a resonator's radial modes of order R, as

Thermal changes of n

$$n^R_{eff}(\Delta T) = n^R_{eff,\ 0} + \frac{dn^R_{eff}}{dT}\Delta T. \qquad (3.20)$$

where the coefficient $\frac{dn^R_{eff}}{dT}$ is an average of the bulk thermo-optic coefficients of the materials over which the modes extend, weighted by the mode profile. When the RMFs share a similar confinement factor, as it is the case for well-confined modes, $\frac{dn^R_{eff}}{dT} \approx \frac{dn_{eff}}{dT} \forall R$ as the weighted average is similar for all RMFs.

Thermal changes of ω

Including this expansion in Eq. 0.10 the resonant frequencies of the resonator may be approximated as

$$\omega_M \approx \frac{2\pi c M}{L n_{eff}}\left(1 - \frac{dn_{eff}}{dT}\frac{\Delta T}{n_{eff}}\right) = \omega^0_M + \delta\omega, \qquad (3.21)$$

where the "heated" resonances have a frequency of ω_M which is the "cold" cavity mode frequency ω^0_M plus a small spectral shift term $\delta\omega$, that depends weakly on ω because of the dispersion. Therefore, neglecting the weak dispersion effects on $\delta\omega$, all of the resonances shift together.

Local thermal field

In general, the action of a thermal field $\mathcal{T}(r)$ on a (probe, 's') mode with spatial distribution function $\mathcal{E}^s(r)$ results in a frequency shift

$$\delta\omega^s \propto -\int |\mathcal{E}^s(r)|^2 \frac{dn(r)}{dT}\frac{\mathcal{T}(r)}{n(r)}\, dr. \qquad (3.22)$$

from which it becomes apparent the importance of the spatial dependence of $\mathcal{T}(r)$.

Indeed, thermal fields $\mathcal{T}(r)$ with the appropriate spatial distribution matching that of the modes are obtainable by the optical modes themselves through the material absorption. By applying a strong optical pump to a resonance with spatial distribution function $\mathcal{E}^p(r)$ and amplitude α^p, heat will be generated at the position of the optical mode, producing thermal fields $\mathcal{T}(r)$ as shown in Fig. 3.9.

The thermal field generation may be modeled by a kernel functional $\chi(r, r')$ that takes into account for the absorption and the thermal diffusion in the host materials. Using the $\chi(r, r')$ formalism the thermal field may be written as

$$\mathcal{T}(r) = \int \chi(r, r')|\alpha^p \mathcal{E}^p(r')|^2 dr' = |\alpha^p|^2 \int \chi(r, r')|\mathcal{E}^p(r')|^2 dr'. \qquad (3.23)$$

Inserting the resonance-generated thermal field inside Eq. 3.22 we finally obtain

$$\delta\omega^s = -|\alpha^p|^2 \int \frac{|\mathcal{E}^s(r)|^2}{n(r)}\frac{dn(r)}{dT} \int \chi(r, r')|\mathcal{E}^p(r')|^2\, dr'\, dr\ , \quad (3.24)$$

where $\delta\omega^s$ explicitly depends on the overlap between $\mathcal{E}^s(r)$ and $|\alpha^p|^2\mathcal{E}^p(r)$ through the thermal diffusion kernel $\chi(r, r')$.

In a much more compact notation, the non-linear interaction will be summarized by the non-linear coefficient

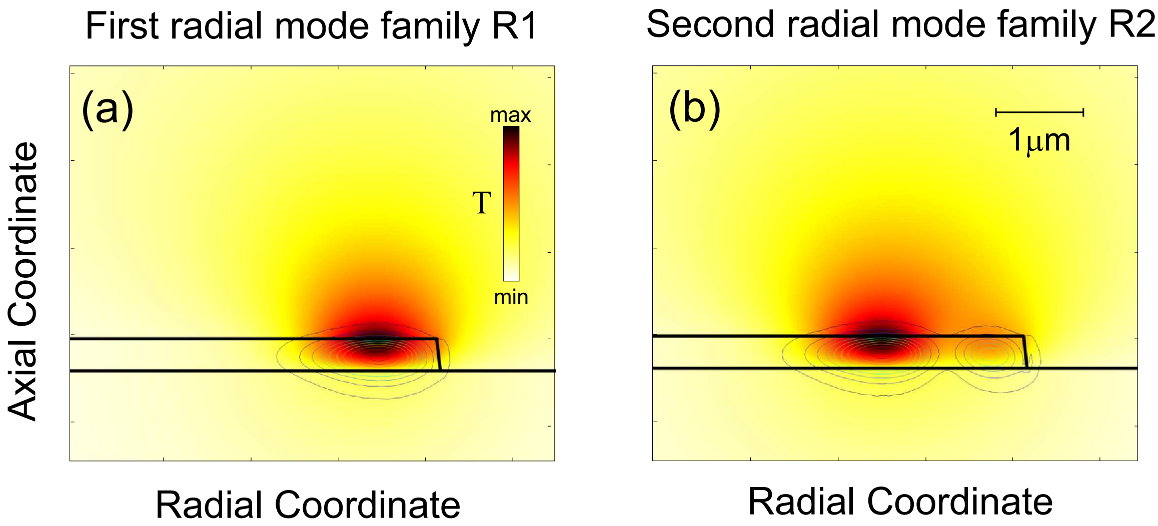

Figure 3.9: FEM simulations of the thermal fields $\mathcal{T}(r)$ generated by (a) the first and (b) the second optical radial family modes. The contour lines show the electric field profiles of the respective optical mode, which are considered the source of heating within the resonator and the cladding materials. The color-map represents the temperature variation induced by the modes with respect to the room temperature.

$$g_{ji} \equiv -\int \frac{|\mathcal{E}_i^s(r)|^2}{n(r)} \frac{dn(r)}{dT} \int \chi(r,r')|\mathcal{E}_j^p(r')|^2 \, dr' \, dr, \tag{3.25}$$

so that the frequency shift of the probe mode i due to the action the strongly pumped mode j is simply

Thermo-optic non-linear coefficient

$$\delta\omega_i^s = |\alpha_j^p|^2 g_{ji}. \tag{3.26}$$

Written in this form, the thermo-optical effect acts as a medium for a non-local optical non-linearity among the modes of the resonator. For a typical positive thermo optic coefficient, g_{ij} has a negative sign, as the resonances are red-shifted when the temperature increases.

Single Family tuning

It is useful at this point to analyze the effects of the thermo-optic mediated non-linearity on the simple case of a single RMF inside the resonator. The equation of motion $\mathcal{L}_i(t)$ for the single resonance i without the non-linear interaction was described in Eq.3.1. The thermo-optic nonlinearity acts as a frequency shift on the resonance, and therefore the non-linear dynamic equation for a single resonance becomes

$$\mathrm{i}\frac{d\alpha_i}{dt} = \mathcal{L}_i(t) + |\alpha_i|^2 g_{ii}\alpha_i. \tag{3.27}$$

Consider now to pump this resonance with a strong tunable laser-line, slowly moving the pump laser frequency from short to long wavelength around the resonance. Initially, no field is coupled inside the resonator, which remains unperturbed. Approaching the resonance from the blue side, some of the power flowing in the waveguide will

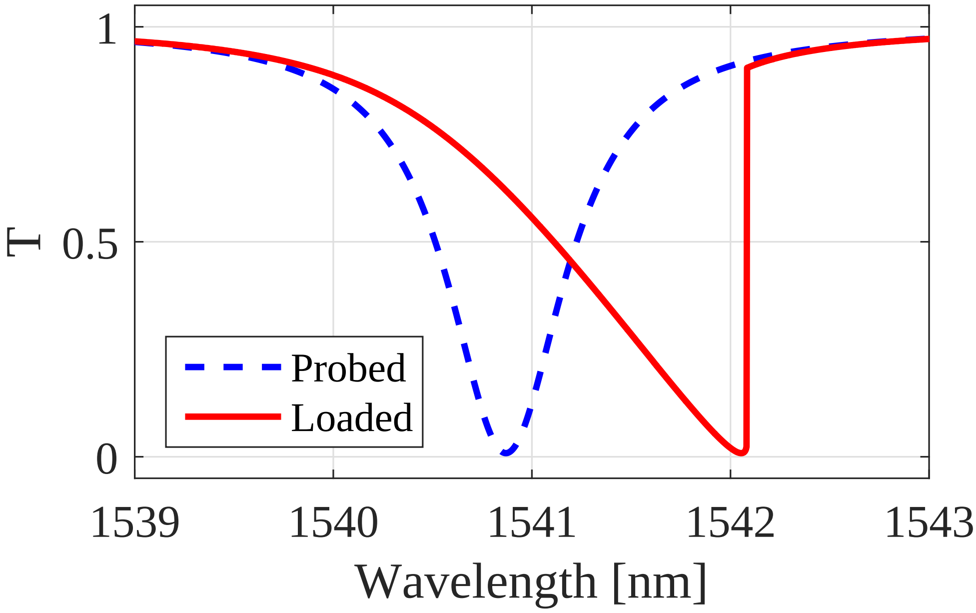

Figure 3.10: Resonant lineshape modification under a sweeping pump in the presence of optical non-linearity. The cold cavity spectrum (dashed line) is obtained with a weak probe. When sweeping the spectrum using a high power laser (solid line), the resonance shifts progressively due to the increasing non-linear effect, resulting in a spectrum with an apparent discontinuity, where the cavity mode de-locks from the pump laser.

be coupled to the resonator, that will begin to heat in the region of the optical mode. The heating will shift the resonance slightly to the red side, thus escaping the pump excitation frequency. As the pump frequency is swept further toward the red, inside the resonance dip, the resonance will escape further. The time-evolution of the intensity transmitted by the coupled waveguide results in an asymmetric triangular shape reported in Fig. 3.10. Depending on the pump strength, the frequency shift of the resonance can keep up with the pump sweep only up to a certain point. As soon as the peak is surpassed, indeed, the non-linear term decreases letting the resonance shift back to it's original frequency in a sudden de-lock [127].

Consider now the i-resonance as a part of a RMF, where only the ith resonance is strongly pumped (p),while the other resonances could be probed (s) with a white probe signal, weak enough to give negligible non-linear effect. The equations of motion for each of the j^{th} resonance become

$$\mathrm{i}\frac{d\alpha_j^s}{dt} = \mathcal{L}_j(t) + |\alpha_i^p|^2 g_{ij}\alpha_j^s, \tag{3.28}$$

where each resonance is coupled to the pumped ith through the g_{ij} non-linear coefficient.

The dynamic equations of the system 3.28 may be easily generalized to the case of multiple pumped resonances as a series of non-linear equations coupled by a g_{ji} matrix

$$\mathrm{i}\frac{d\alpha_i}{dt} = \mathcal{L}_i(t) + \sum_j |\alpha_j|^2 g_{ji}\alpha_i. \tag{3.29}$$

where i and j assume any value of the azimuthal number.

Since the resonances under consideration all belong to the same RMF, their electric field distribution function in the cross section of the resonator will be very similar, especially for large ($\gtrsim 100$) azimuthal numbers. In fact, for large azimuthal numbers the wavelength change of adjacent modes is small compared to the wavelength itself ($\mathrm{FSR}(\lambda)/\lambda \ll \lambda$) implying small changes in the cross-sectional features.

Last, within a range of azimuthal mode values, using $\mathcal{E}_j^p(r) \approx \mathcal{E}_i^s(r)$ in Eq.3.25, the single-RMF g_{ij} coefficients may be approximated all to the same $g_{ii} = g_R$ labeled with the R^{th} RMF.

Doublets tuning

Considering two different radial families R_1 and R_2, Eq.3.29 is still valid, with the i and j indices running over all of the modes of both families. In our particular case, where the resonances encounter regions of spectral overlap, the term $\mathcal{L}_i$ in Eq. 3.29 should be substituted by $\mathcal{D}_i$ of Eq. 3.2 that includes the off-diagonal coupling terms. As stated above, in a small range of azimuthal numbers, it is reasonable to assume that the g_{ij} elements coupling modes belonging to the same RMF are all the same g_{11} or g_{22}, coupling modes among R_1 and among R_2 respectively. In this particular case, a further term $g_{12} = g_{21}$ coupling modes of R_1 to modes of R_2 is identifiable with similar reasoning.

I will now consider the system within a proper pump (p) and probe (s) approach, where the dynamical evolution of a weakly probed doublet will be analyzed while a different pump doublet is strongly exited by a tunable laser. The equation for the pumped doublet reads

$$\mathrm{i}\frac{d\alpha_j^p}{dt} = \mathcal{D}_j^p + \left(g_{jj}|\alpha_j^p|^2 + g_{12}|\alpha_{3-j}^p|^2\right)\alpha_j^p, \tag{3.30}$$

where $j = 1, 2 (= R)$ runs over the two pumped peaks belonging to the two different RMFs. The equation of motion for (each of) the couple of probed peaks (s) are

$$\mathrm{i}\frac{d\alpha_j^s}{dt} = \mathcal{D}_j^s(t) + \left(g_{jj}|\alpha_j^p|^2 + g_{12}|\alpha_{3-j}^p|^2\right)\alpha_j^s. \tag{3.31}$$

where $j = 1, 2(=R)$ runs over the two probed peaks belonging to the two different RMFs.

The above set of equations provide a general description of the system during a pump and probe experiment. It's important to notice that only Eqs. 3.30 are actually non-linear, while Eqs. 3.31 are linear with respect to the α^s, since the α^p are threated as parameters that need to be obtained by explicit solution of Eqs. 3.30. Furthermore, it's worth tp note that because of the non-diagonal terms of Γ^{rad}, using $\mathcal{D}_i$ instead of $\mathcal{L}_i$ adds an important energy exchange channel between the two resonances, other than the frequency shift induced by the non-linear terms.

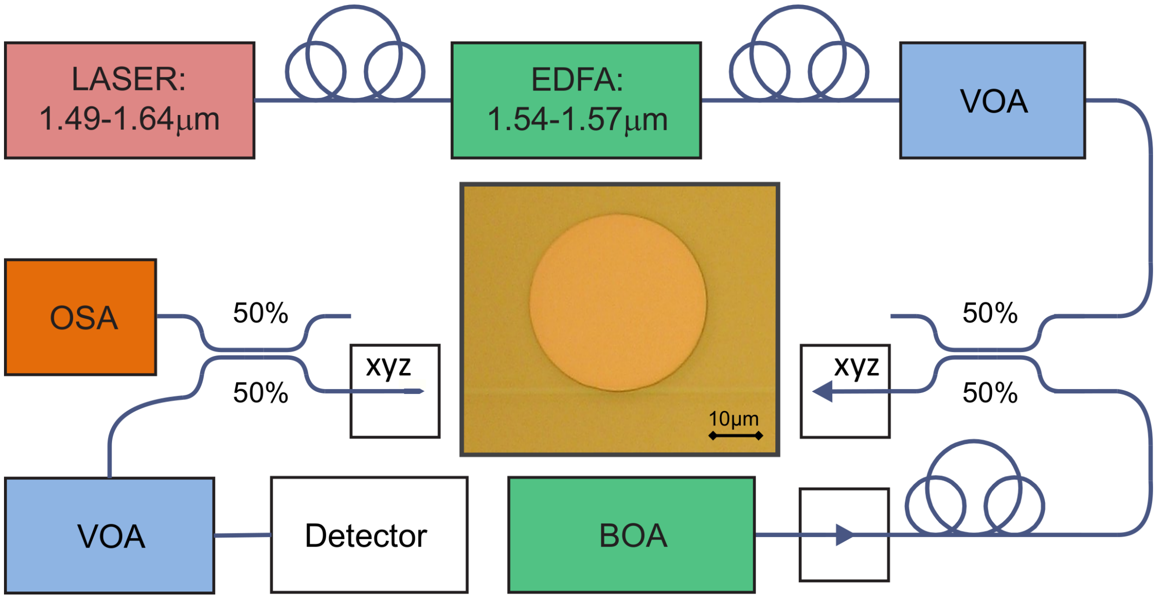

Figure 3.11: Experimental setup for the non-linear experiment. A Tunable laser, amplified with an Erbium Doped fiber Amplifier (EDFA), is mixed with the broadband signal of a Boosted Optical Amplifier (BOA) and shined into the sample with a taper fiber. The output is also collected with a taper fiber, split and fed to an Optical Spectrum Analyzer (OSA) and a broadband germanium detector to measure the probe and the pump spectra respectively.

3.4.2 Experimental results

The sample is the same as described in Sec.3.3.2 while the experimental setup, being quite different from that of Sec.0.3.2, is sketched in Fig. 3.11. The strong pump is provided by a mid-infrared tunable laser, fiber-coupled to an Erbium Doped Fiber Amplifier (EDFA) through a polarization control stage. The amplified light passes through another polarization stage and a Variable Optical Attenuator (VOA) and enters a 3 dB fiber coupler. On the other input of the fiber coupler, the broadband emission of a Booster Optical Amplifier (BOA), protected from back-reflections by an optical circulator, enters a polarization stage prior of merging with the pump line. The mixed signals are coupled to the sample with a lensed taper fiber actuated by a 3-axis piezoelectric stage. On the other side, the transmission signal is collected with an analogous lensed fiber and split in equal parts between an Optical Signal Analyzer (OSA) and a germanium detector, protected by another VOA.

The purpose of the OSA is to detect the transmission spectrum of the probe resonances, exited by the BOA. The germanium detector, on the other hand, integrates all the signal. However, since the total emission of the BOA in the detector's spectral range is negligible with respect of the high power emission of the EDFA, the signal on the detector well represents the transmission spectra of the strongly pumped resonance doublet.

Peak suppression

In order to maximize the differential non-linear effect on the frequency detuning δ in the probe doublet, it would be advisable to strongly excite a single resonance in order to maximize the differential non-linear effect between the two families. In

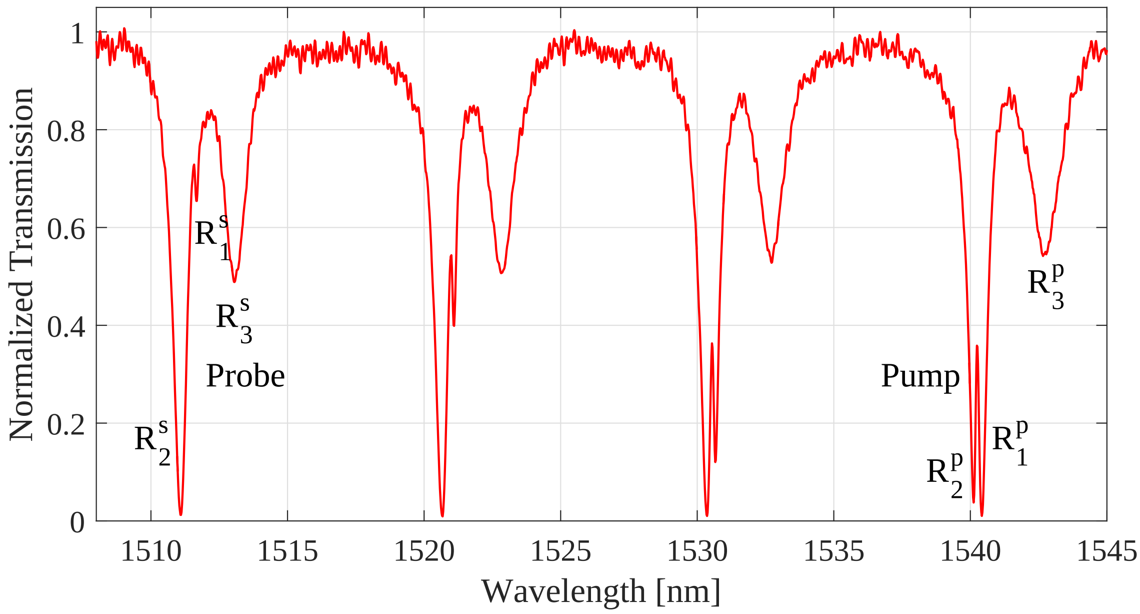

Figure 3.12: Cold cavity transmission spectrum of the peak-suppression pump and probe experiment, showing the whole spectral range between the pump and the probe. In this experiment, the pumped doublet is near 1540 nm, while the probe doublet at 1511 nm.

the accessible experimental range, limited by both the pump laser and the BOA emission, the two coupled peaks slide slowly on each other, never gaining enough spectral distance to achieve the favorable single-resonance excitation condition.

Nevertheless, it was possible to select two doublets of peaks that permitted the demonstration of the complete suppression of the R_1 feature of Eq. 3.14 by using the two-mode excitation described by Eqs. 3.30 on the pump and probe peaks shown in Fig. 3.12. The measurement on these two peak doublets produced a pump-probe mode mapping rich of features, reported in Fig. 3.13.

Figure 3.13 (a) reports the cold cavity spectrum (dashed lines) and the hot cavity (apparent) spectrum of the pump, when exited with a total power at the EDFA output of 2.0W. Figure 3.13 b) shows the evolution of the probe spectra as a function of the pump excitation. By confronting the two graphs, it is possible to reconstruct the dynamic evolution of the system.

Initially, the pump resonances are depleted and the probe is in a cold cavity condition, as shown by section A of 3.13 (c). As the pump moves toward the red (longer wavelength), it enters the R_2^p resonance, enabling the non-linearity. The probe spectrum moves accordingly, with the R_2^s resonance detuning towards the red slightly faster than the R_1^s. In this case, the difference in detuning is small because of the broad R_2^p spatial distribution inside the resonator, as it is shown in section B of panel c). When the pump enters more inside the R_2^p resonance the non-linear effect is augmented by the higher intensity inside the cavity. This may be seen from the probe resonances shifting towards the red at an increasing pace. Here the detuning is already appreciable, with the R_2^s resonance slowly moving closer to the R_1^s. Near the de-locking point of R_2^p, the R_1^s resonance finally reaches the vanishing point, as it is highlighted in cross section C of panel c) where the feature of the r_1^s resonance is not visible. Surprisingly, the de-locking of the R_2^p resonance is not instantaneous, as it is expected by analogy to the single-resonance case. The smooth de-locking is due

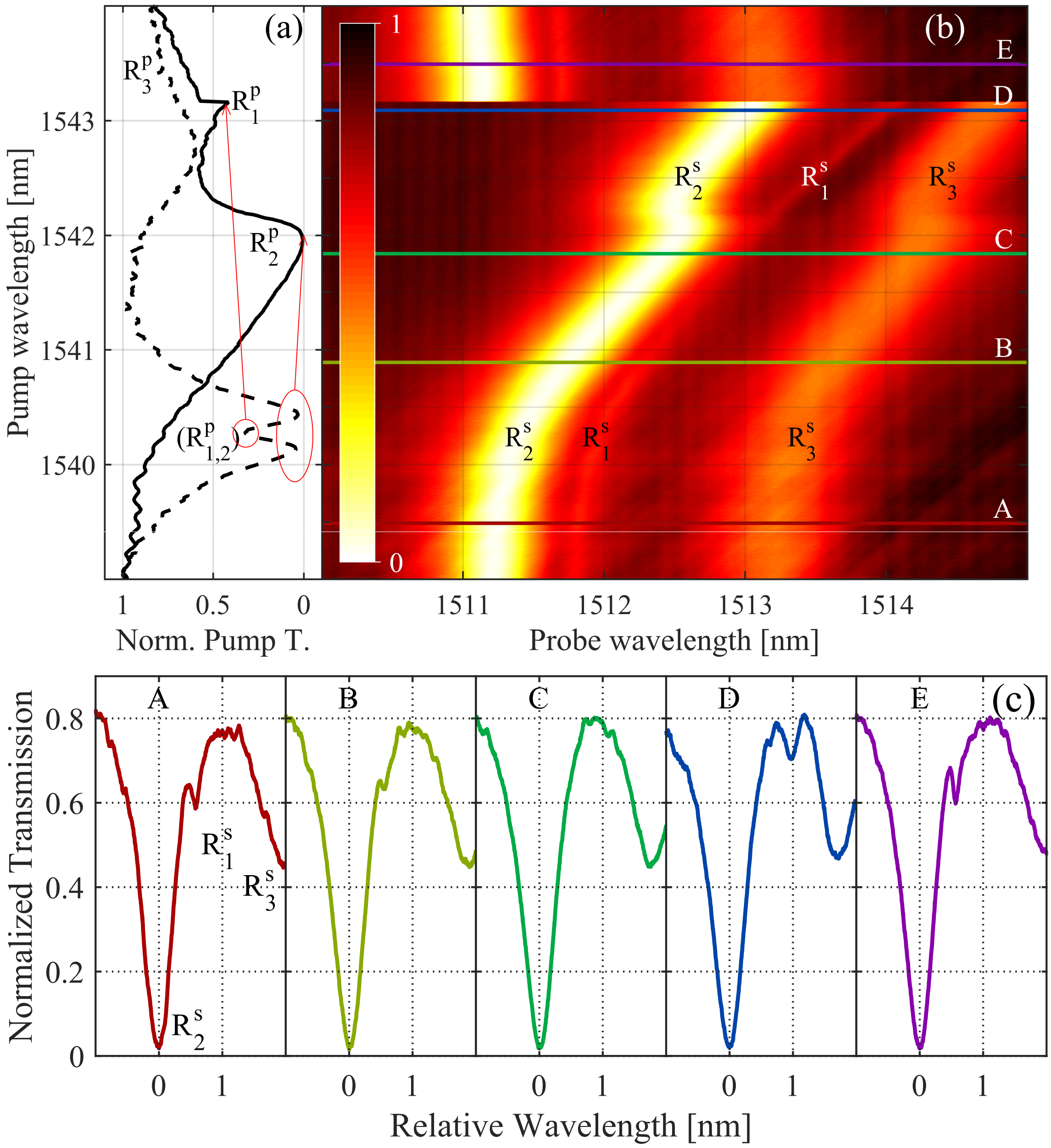

Figure 3.13: Results of the pump and probe experiment. Panel (a) shows the cold (dashed) and hot (solid) cavity transmission spectra of the device around the strongly pumped resonance doublet. The thermo-optic non-linearity, induced by the pumped doublet, affects also the other resonances (b), allowing for a relative detuning of the peaks as shown by the transmission color map. (c) Selected transmission spectra. Section A shows the transmission spectrum of the probe in weak pumping regime. When the pump enters the R_2^p resonance, the corresponding R_2^s peak is pushed towards the red, faster than R_1^2 (section B). Further increasing the detuning brings the two probe resonances even closer, eventually reaching the critical point, where a complete disappearance of the R_1^s peak feature takes place (section C). When the pump frequency surpasses the R_2^p resonance, locking instead on R_1^p, the corresponding R_1^s is rapidly shifted towards the red, while the effect on R_2^s is diminished, suddenly bringing δ to la large v alue (section D). Finally, when the pump has surpassed both resonances, the system returns to the cold cavity condition (section E).

to the fact that the non-diagonal term links together the intensities of R_1^p and R_2^p, giving a smooth transition. With the gradual decrease of the coupled power and its transition to the R_1^p resonance, the thermal field becomes more localized in the R_1^s

region, reducing its effect on the R_2^s resonance, that falls back towards the blue. The R_1^s resonance, instead, continues its detuning. Finally, also the R_1^p peaks de-locks, and since now the R_2^p is on its blue side, the de-locking is instantaneous. This is clearly visible by the sudden return of all of the probe resonances to their cold-cavity position.

This second, fast de-locking demonstrates how the smooth transition between R_2^p and R_1^p cannot be due to a slow thermal process, that would be present also here. It's worth to note that a R_3 RMF is also present both in the pump and probe analyzed spectra. In the pump spectra, the third family broad mode partially obscures the sudden de-locking of the R_1^p RMF with its intrinsically low transmission due to its slightly over-coupled regime. However, the very presence of this peak right after the R_1^p de-lock demonstrates how the spectrum is already returned near its cold cavity position, as shown with the dashed line. Indeed, the R_3^p still shows some non-linear effect, but due to its broad spectral and spatial profile the effect is much smaller than for the R_1 and R_2 resonances, as it is may be seen by the weak detuning of the R_2^s and R_1^s peaks in the top of the color-map. On the probe side, the R_3^s family may further demonstrate the spatial selectivity of the process: being even spatially broader than the R_2^s mode, it is overall less affected by the heating of both R_2^p and R_1^p. Along the whole experiment, the R_3^s peak follows the behavior of R_2^s but with a diminished effect and smoother transitions due to its lower spatial selectivity.

Other information may be extracted from the background signals: the FP crests generated by the waveguide facets are well visible in the background, and remain substantially unaffected by the pump evolution, demonstrating that the waveguide maintains a stable condition during the experiment. Finally, some weak shades that cut diagonally the probe spectrum are visible in the region at pump values around 1540 nm (for example near the label of section A). These features have exactly a slope of 1, meaning that they always move together with the pump. It is therefore believed that these features are not physical, but they are an artifact due to the pump stray light in the OSA.

Peaks crossing

In the previous case the R_1^s resonance is initially on the red side of the doublet. As we have seen, the initial faster detuning of R_2^s is rather small, while once the R_1^p is strongly excited, the non-linear effect is strong on R_1^s. If the initial condition is inverted, i.e. if the R_1^s peak feature is on the blue side of the doublet at cold cavity, it may be possible to find a condition where the two peaks cross. The experiment was then repeated with the pump and probe peaks configuration shown in Fig. 3.14, where the probe doublet, near 1560 nm wavelength, has the R_1^s on the correct side.

Figure 3.15 reports pump-and-probe experiments by using the same pump doublet near 1540 nm as in Fig.3.13, but looking at the new probe doublet near 1560 nm. The different panels expose the same experiment repeated at different pump power. In Fig. 3.15 a) to c) the input power is 0.5W, 1.0W and 2.0W respectively. In each case the initial heating of R_2^p produces an almost global shift towards the red, as expected from the results of the previous experiment. In a) the power is not enough to excite strongly the R_1^p resonance. In panel b), at an input power of 1.0W, the non-linearity is already strong enough to lock also the R_1^p resonance. Indeed, at around 1541.5 nm,

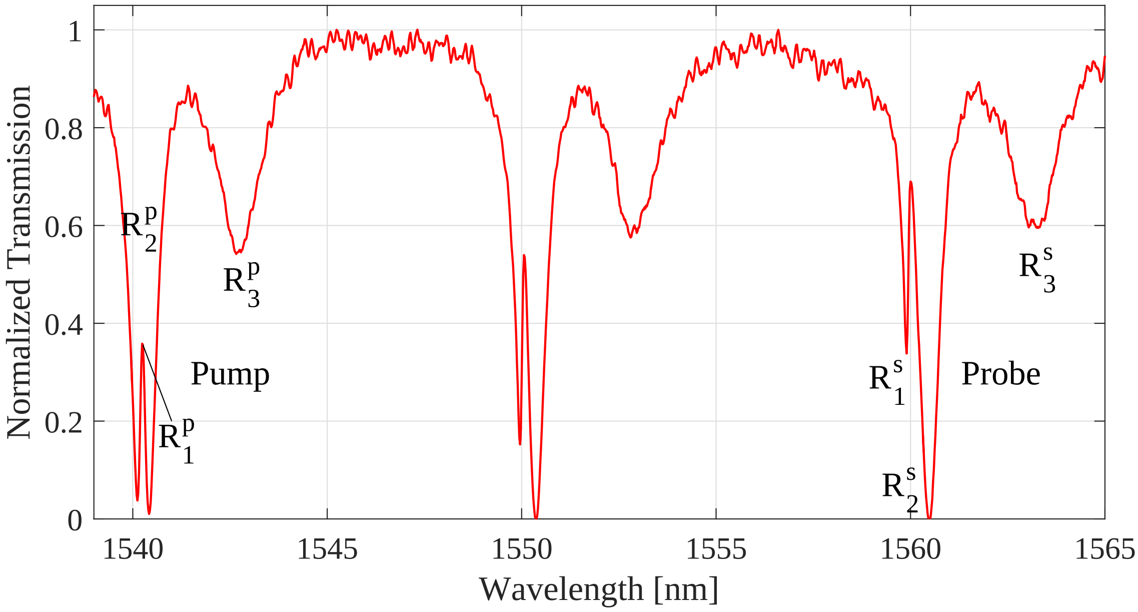

Figure 3.14: Cold cavity transmission spectrum of the peaks-crossing pump and probe experiment, showing the whole spectral range between the pump and the probe. In this experiment, the pumped doublet is near 1540 nm, while the probe doublet at 1560 nm.

the pump excitation transits from R_2^p to R_1^p. The effect is clearly visible in the probe spectrum as R_2^s is pushed back, while R_1^s accelerates until the two peaks cross. Then, the R_1^p family de-locks, bringing the system again in cold cavity. In this case, the presence of the R_3^p family is visible in the spectrum by the slight bending of both R_2^s and R_1^s resonances at pump wavelength between 1542.5 nm and 1544 nm. The effect is accentuated in panel c), where the pump power is further increased. Cross sections A,B, and C are reported in panel d) to highlight the crossing. In cross section A, the R_1^s feature is on the blue side of the doublet, making a dip in the R_2^s peak. Cross section B, right after the pump switching from R_2^p to R_1^p, shows the condition where the two resonances lay at the same central frequency. In section C, the pump is pushing R_1^p further in the red, bringing R_1^s on the red side of the probe doublet.

3.4.3 Numerical Simulations

In Secs. 3.4.2 and 3.4.2 I exposed the qualitative agreement between the non-linear interaction model developed in Sec. 3.4.1 and the experimental results. I will now establish a quantitative link by comparing the experimental results to numerical solutions of the system governed by equations Eqs. 3.30 and 3.31, making a concrete example with the experiment exposed in Fig. 3.15 b). First, in order to solve the pump equations Eqs. 3.30, the resonances parameters are extracted by fitting the cold cavity spectrum, while the (normalized) non-linear coefficients g_{ij} are instead estimated from the FEM simulations of Fig. 3.9. The values resulting from the fit are reported in Table 3.1.

Then, equations 3.30 were solved numerically to estimate the pump resonances amplitude evolution. During this study, the R_3 resonance has been always omitted, as it is believed to do not contribute to the interaction. Figure 3.16 a) shows that the experimental transmission spectrum (black line) of the pump and the simulated transmission (red dashed line) are in good agreement.

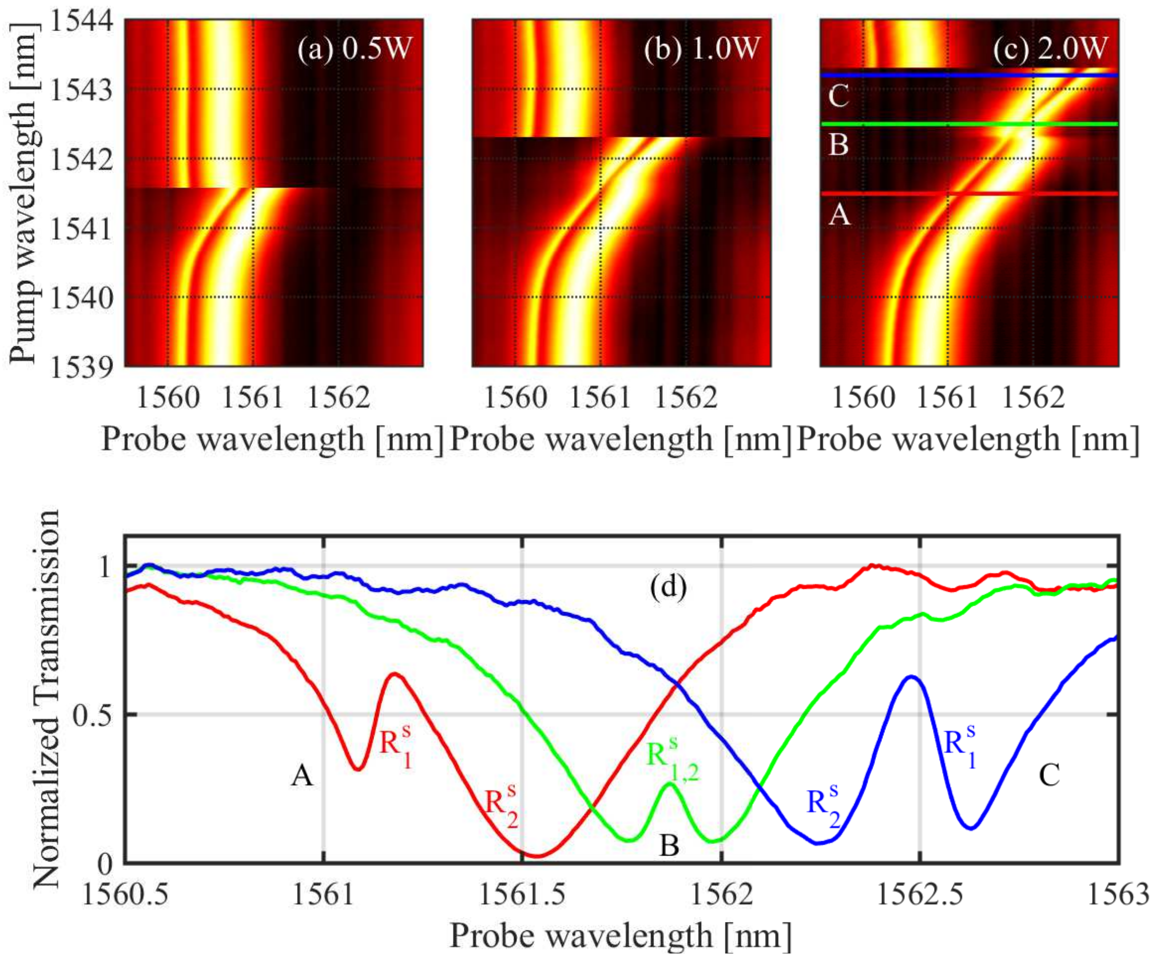

Figure 3.15: Pump and probe experiments demonstrating the complete crossing of the probe modes. Panels (a),(b) and (c) represent the same experiment repeated with different input power conditions of 0.5 W, 1 W and 2 W, respectively. (d) The selected cross-section spectra, under 2 W pump, demonstrate three cases of the relative detuning, which changes from positive (A) to negative (C) passing through the $\delta\omega_0^{12} \approx 0$ condition (B).

The experimental spectrum, shown in b), may now be reproduced by inserting the mode amplitudes of the pump modes as parameters in Eq. 3.31. Again, the other parameters were estimated from the cold-cavity spectrum, reported in Tab. 3.1, with the exception of η_1 and η_2. Indeed, Eqs. 3.30 and 3.31 do not explicitly consider thermal-induced variations of the η coupling weights. However, the coupling with the waveguide is affected by the local refractive index variations in the region of the coupling through the thermal field. Since this effect is not present in the model, I fit the η_1 parameter from the experimental spectra using a cold cavity model centered around the doublet. The resulting evolution of the η_1 parameter is reported in Fig. 3.16 c). η_2 can easily be obtained from η_1 as $\sqrt{1-\eta_1^2}$ due to the weights normalization property. Finally, Eqs. 3.31 are (linearly) solved to obtain the spectra of Fig. 3.16 d), which are in agreement with the experimental data.

As a further comment, while the transmission measurement measures a weighted superposition of the coupled mode amplitudes, the numerical simulation permits compute separately the mode amplitudes $\bar{\alpha}_i$ of Eq. 3.9b. Figure 3.17 reports the numerical simulation of the pump evolution (green) over the experimental data (black), together with the evolution of the mode amplitudes of R_1 (blue) and R_2 (red) in the

		R_1^p	R_2^p	R_1^s	R_2^s
η_i		0.0723	0.9974	0.0976*	0.9952*
γ_j^{nr}	[GHz]	4.400	20.581	5.558	28.01
ω_j^o	[THz]	194.532	194.374	192.15	191.92
g_{ii}		1.00	0.92	1.00	0.92
$\bar{\Delta}$	[GHz]	186.33		193.44	
$\bar{\Gamma}$	[GHz]	24.749		18.567	
g_{12}		0.90		0.90	

Table 3.1: Fit parameters of the cold cavity spectra of both pump and probe resonances, used in the simulations. In the probe case, the reported starred (*) values of η_i are the initial cold cavity values, but their evolution under the effect of the thermal field, reported in Fig. 3.16 (c), was used in the simulation.

hot- (solid) and cold-cavity (light colors) regimes. The simulation refers to the pump spectrum of Fig. 3.16. The numerical solution shows how both modes are initially dragged during the initial phase, where R_2^p is exited. In particular, the induced shift delays the R_1^p resonance strong excitation by about 0.5 nm. The R_1^p excitation indeed takes place as soon as the R_2^p resonance begins to loose mode energy, that is soon transferred to the R_1^p resonance, near the pump wavelength 1541.5 nm. R_1^p, having lower intrinsic loss, accumulates energy at a higher pace and with and up to a higher value than R_2^p, resulting in the stronger detuning witnessed in the experiments during the R_2^p locking.

3.5 Conclusions

The object of this study has been the modelization of the interaction between quasi-degenerate resonances in an integrated microdisk resonator. They system features doublets of modes with a variable degree of spectral overlap, i.e. frequency detuning of the two involved resonances. The transmission spectra of a bus waveguide coupled to such resonator exhibits non-Lorentzian lineshapes due to interference terms in the two resonances decay channels. While Fano-like resonances have been observed in the past in similar structures, our experiment showed features that couldn't be explained by means of a dissipative interaction only. Indeed, other than the typical Fano shape of the spectrally overlapping resonances, another peculiar behaviour have been observed experimentally: the features of one of the modes are strongly enhanced or suppressed depending on the sign of the relative frequency detuning of the two interacting resonances. The peculiar asymmetric feature, experimentally measured over a set of azimuthal resonances, has been reproduced by modeling the interaction between the resonance doublets and the bus waveguides in both dissipative and reactive components. Other than the excellent agreement with the experimental data, the model predicts the existence of a region with a strong suppression of one of the mode's feature in the transmission spectra.

Therefore, in the second part of this work, I developed a non-linear tuning of the resonance doublets relative frequency to provide experimental evidence of the prediction. The non-linear tuning is achieved in an all-optical pump and probe experiment, where the non-linearity is mediated by the resonator host material through the thermo-optic

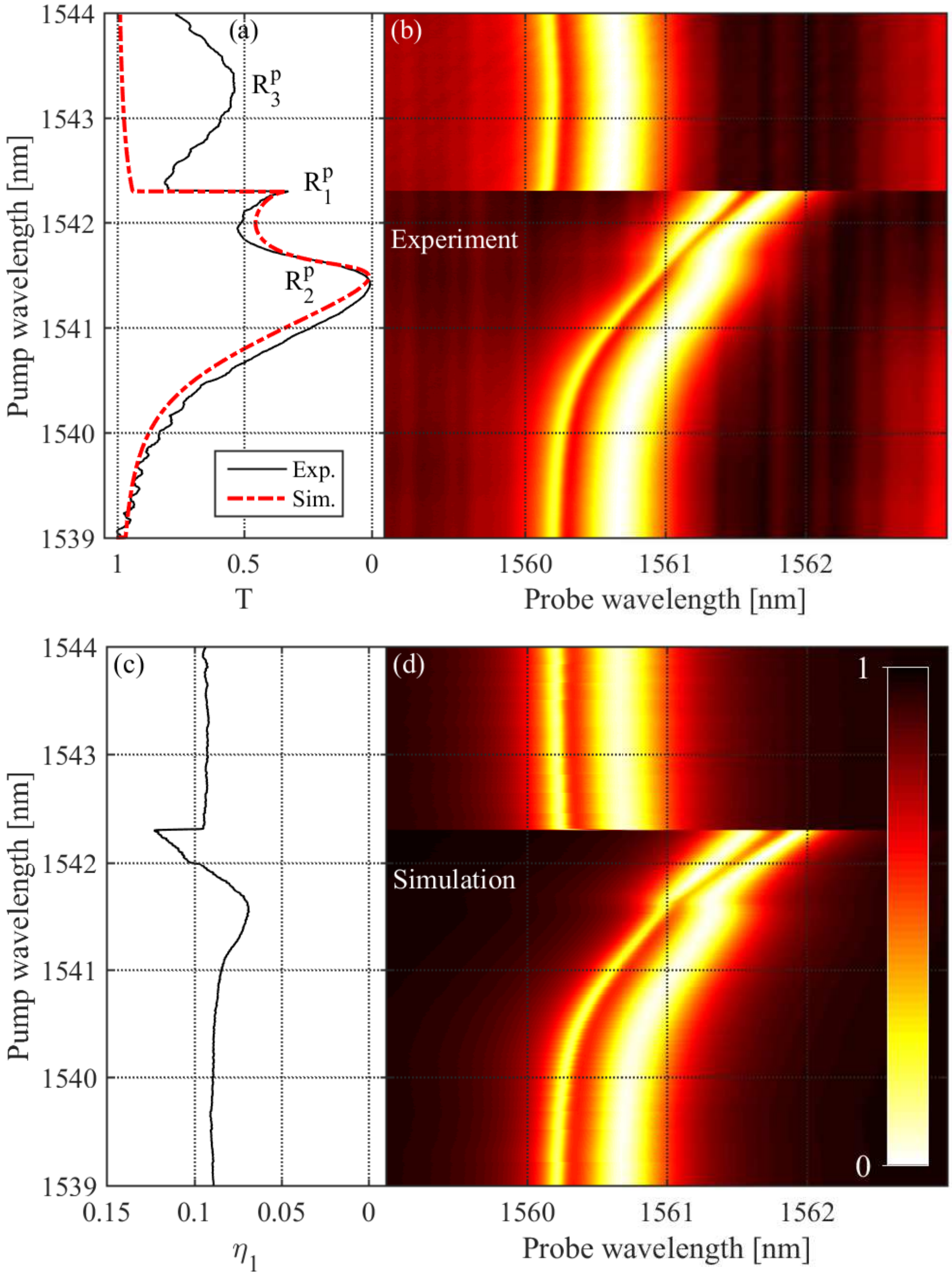

Figure 3.16: Experimental and simulated data of the pump and probe experiment. (a) the experimental pump transmission spectrum of the loaded cavity (black line) is simulated (dashed red) by inserting the cold cavity fit parameters into Eq. 3.30. In (b) the experimental transmission map of the transmitted intensity as a function of both pump and probe wavelength is shown. In (c) is reported the relative coupling η_1 among the two radial family modes to the waveguide, extracted from evolution reported in panel (b). Successively, η_1 is used to compute the evolution of the Γ and Δ matrices of Eq. 3.1 to take into account for the changes in the coupling induced by the thermally-induced $\delta n(r)$. Panel (d) shows the transmission map as a function of both pump and probe wavelength using the simulated pump excitation (a) for Eq. 3.31.

effect. After extending the reactive coupling model to the non-linear case, I performed pump and probe experiments to verify its resonance-tuning capabilities. With non-linear tuning experiments I demonstrated both the resonance feature disappearance and even complete mode crossing of resonances on the same chip. The agreement

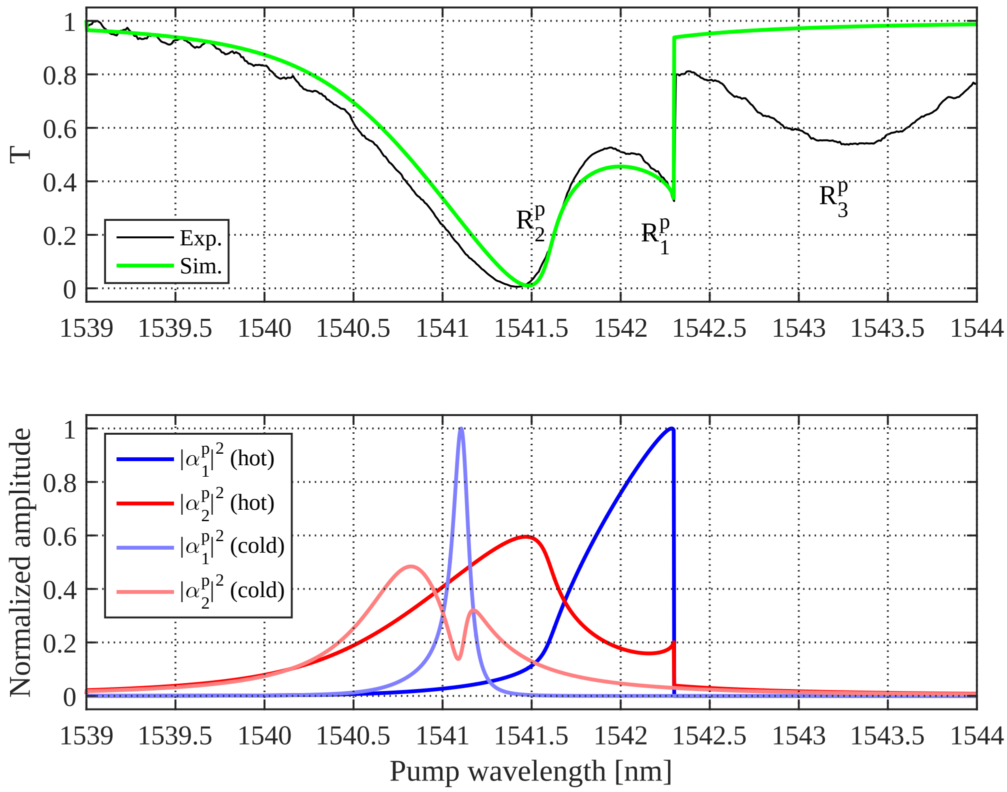

Figure 3.17: (top) the experimental and simulated transmission spectra are plotted with (bottom) the simulated hot-cavity (bright colours) and cold-cavity (light colours) normalized mode amplitudes inside the resonator for input power 1.0W. In the cold cavity condition the (red) R_2 peak amplitude has a dip in correspondence to the (blue) R_1 resonance due to the non-diagonal coupling. In the hot-cavity condition, spanning from short to long wavelength, the coupling allows for a smooth de-lock of R_2^p. Indeed, instead of the sudden de-locking expected from Fig. 3.10 the energy is gradually transferred to R_1^p that keeps the resonator heated. The instantaneous de-lock of the resonance is still present in R_1^p.

between the experimental results and the theory have then been validated through numerical simulations.

From the developed generalized theory of the interaction, further considerations emerged, that couldn't be addressed at the time of the experiments.

In the investigated samples, the R_1 and R_2 RMFs had spectral overlap along all of the accessible spectral range. Due to both the spectral overlap and the effect of Γ^{rad}, both pump modes are excited, reducing the differential action. It's worth to note, however, that in the case of non-interacting resonances the differential shift should be much more effective. Indeed, in the presence of a spectral region where the resonances are well separated in frequency, the pump could be applied to the R_1 resonance only, maximizing the relative shift.

In the presented study, the focal point that allowed the differential shift for the two RMF was the local heating of the resonator due to the fact that the profile of the heat source coincides with the optical modes. While thermal diffusion poses limitations to the possibilities of this technique, the theory developed in Sec. 3.4.1 is general and could be exploited in other geometries. For example, the effect could be exploited even within an uniform thermal field by proper engineering of the modal shapes by using materials with a very different (possibly opposite) thermo-optic coefficient.

As a further improvement of the physical description of the system, the effect of the thermal field on the waveguide coupling may be fully included in dynamic equations. This effect of the thermal field on the coupling with the waveguide should be furthermore included also in Eqs. 3.30, where the dynamic variations of η have been neglected in the present work.

Overall, the study was carried on in collaboration with Iacopo Carusotto, Fernando Ramiro Manzano and Mher Ghulinyan. Regarding the modeling of the Fano-Lamb-like interaction, up to Sec. 3.3.2 I collaborated to the data collection, analysis and interpretation as well as to the development of the model that describes the reactive coupling. I carried on the numerical simulations that mapped the mode waveguide coupling of the modes, both in the degenerate and in the frequency-separated cases, as well as their analysis. I also collaborated to the transmittivity simulations with F.Ramiro-Manzano. Finally I collaborated to the writing of the resulting article [118]. Regarding the second part, I've been the principal investigator of the non-linear studies of Sec. 3.4. I carried on the passive and pump-and-probe experiments in collaboration with F.Ramiro-Manzano, and developed the non-linear model with the collaboration of I. Carusotto. Finally, I performed the numerical simulations, data fitting and analysis of Sec. 3.4.3. The results of Sec. 3.4 have also been reported in [130].

Chapter 4

$\chi^{(2)}$ non-linearities in silicon

4.1 Introduction

One of the key objectives of the project SiQuro is the generation, manipulation and interferometry of correlated photon pairs within a single chip.

Nowadays, non-linear generation schemes for photon pairs exploit often $\chi^{(2)}$ nonlinearities of bulky crystals, typically $LiNbO_3$ and BaB_2O_4 [29].

The use of $\chi^{(2)}$ non-linearity enables a number of phenomena: Second Harmonic Generation (SHG), Sum Frequency Generation (SFG), Difference Frequency Generation (DFG), Spontaneous Parametric Down Conversion (SPDC), [131, 132, 2, 133] , and electro-optic modulation (Pokels effect). The electro-optic modulation is of great interest for the growing field of the Silicon Photonics especially concerning the realization of ultrafast modulators [134], which otherwise rely on the free carrier dispersion modulation within the waveguide [135, 136, 137, 138]

The project SiQuro aims at the implementation of $\chi^{(2)}$ non-linearities within Silicon-On-Insulator waveguides, opening the road for the implementation of new functionalities on the integrated silicon platform. This goal constitutes an important step towards the development of an All-On-a-Chip (AOC) standard in which an increasingly high number of functionalities is realized within the same material platform-silicon, and through the same fabrication standard-CMOS.

Silicon, due to the inversion symmetry of its crystalline structure, does not naturally possess a $\chi^{(2)}$ tensor. It was proven, however, that stressed silicon exhibits second order non-linear behaviour that was attributed to $\chi^{(2)}$ non-linearity in the form of Pockels effect [139, 140] or SHG [141, 142].

At the time the SiQuro project started in 2013, the exact relation between the strain and the $\chi^{(2)}$ was not clear, and effective values of the strain-induced $\chi^{(2)}$ spanning a range from 15 pm/V [139] to 339 pm/V [143] were reported. During the project $\chi^{(2)}$ and $\chi^{(3)}$ non-linearities in strained SOI waveguides and Silicon Nano-Cristals (SiNC) have been investigated in order to obtain quantitative relations that could be used to design and implement the SPDC and SFG functionalities required by the project.

The experimental studies realized within SiQuro [144, 145, 146] demonstrated that the strain-induced $\chi^{(2)}$ is much smaller than what previously believed, attributing

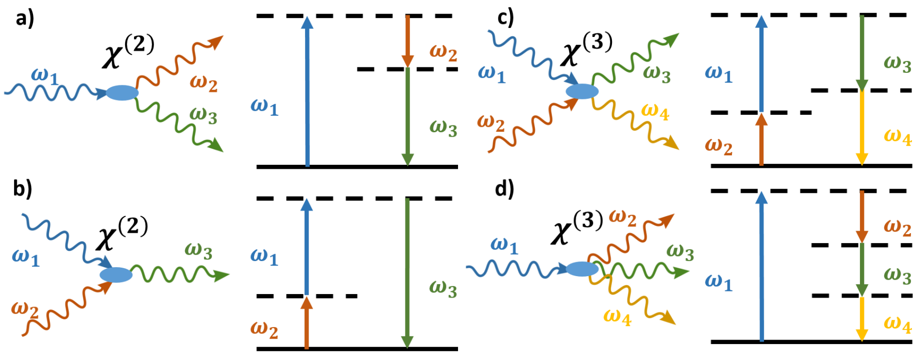

Figure 4.1: Feynman diagrams and virtual-level representations of some multi-photon processes. a) Spontaneous Parametric Down Conversion (SPDC) and b) Sum Frequency Generation (SFG) are $\chi^{(2)}$ processes while c) and d) represent Four Waveg Mixing (FWM) through $\chi^{(3)}$ optical non-linearity.

the high measured values to carrier dispersion effects [147, 148, 149]. These results supported the evolution of the theoretical analysis on the exact relation between the second order non-linearity and the stress [150, 151], from which the $\chi^{(2)}$ tensor in silicon resulted as linearly dependent on the strain gradient tensor.

In my thesis work, I collaborated to the design, fabricated, and performed the passive optical characterization of Si_3N_4-stressed silicon structures, which have then been used by Massimo Borghi and Mattia Mancinelli to measure the non-linear effects in strained silicon.

4.2 Nonlinear susceptibility

The macroscopic polarization of a material may be expanded in Taylor series with respect to the incident field(s) E as

$$P(E) = \epsilon_0 \chi_{\mathrm{TOT}}(E) E \approx \epsilon_0 \left(\chi^{(1)} \cdot E + \chi^{(2)} \cdot E^2 + \chi^{(3)} \cdot E^3 + \dots\right) \tag{4.1}$$

where the $\chi^{(n)}$ tensor coefficients are called n^{th}-order susceptibility tensors [152, 138]. The first coefficient, $\chi^{(1)}$, is the linear response of the polarizability. Its real part represents the usual material polarizability, while it's imaginary part reflects the material absorption. The $\chi^{(2)}$ and $\chi^{(3)}$ represent in general multi-photon interactions, with three and four photons on the Feynman-diagram interaction node as shown in Fig. 4.1. In this picture, the photons interact with each other through the polarizability of the material, exchanging energy.

The diagrams shown in Fig. 4.1 a) and b) are of particular interest in the case of project SiQuro. Diagram a) describes Spontaneous Parametric Down Conversion (SPDC) where a couple of photons is created from a single photon through $\chi^{(2)}$ interaction. Energy conservation imposes that $\omega_1 = \omega_2 + \omega_3$, so that both generated photons will have a lower energy with respect to the first. In the particular case when $\omega_2 = \omega_3$ the two created photons have the same energy and, since they are inherently created simultaneously, they may be used to realize coincidence experiments. In the case of SiQuro, the III-V laser, with a wavelength $\sim$ 1490 nm would be used to

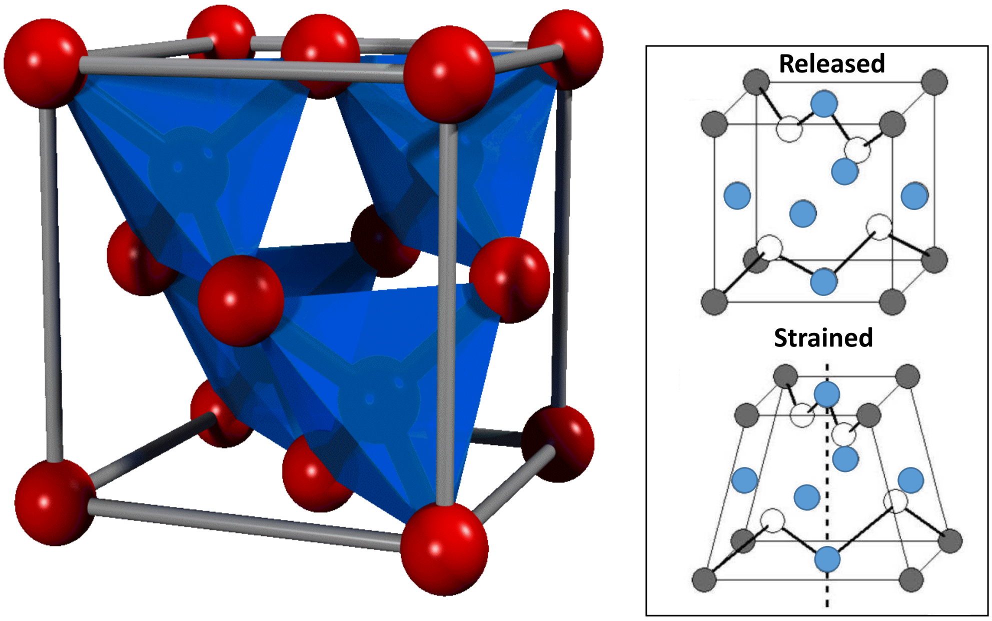

Figure 4.2: a) Face Centered Cubic crystalline structure of silicon. The orange tetrahedra highlight the symmetric environment in which each atom is immersed. b) by applying an inhomogeneous strain on the lattice it is possible to break the inversion symmetry.

generate couples of photons with a wavelength of $\sim$ 2980 nm through SPDC, that are then manipulated in the PIC.

After the manipulation, the photons are up-converted to the NIR band using another $\chi^{(2)}$ process: Sum Frequency Generation. In this case, following the diagram shown in Fig. 4.1 b), two photons are mixed together to form a photon of higher energy. In the SiQuro case, one of the MIR photons with a wavelength $\sim$ 2980 nm is mixed with the laser pump at 1490 nm, creating a photon around 933 nm according to $\omega_1 + \omega_2 = \omega_3$. The up-converted photons lie at the edge of the detection band of the Single-Photon Avalanche Diode (SPAD) which is used as a detector.

Crystalline Silicon has a diamond structure, which is centrosymmetric. The point situated at the center of the unit cell of the crystal is called inversion point. The centrosymmetric property implies that any point located at position r with respect to the inversion point is equivalent to the one located at $-r$. Such a system is said to posses an inversion symmetry. The same property holds for the crystal polarization, leading to the equation

$$P(E) = -P(-E). \tag{4.2}$$

For Eqs. 4.1 and 4.2 to be valid at the same time it follows that the second order susceptibility tensor $\chi^{(2)} = 0$ (as for all even orders, $\chi^{(2n)} = 0$), meaning that native crystalline silicon has no second order non-linearity.

However, a non-zero $\chi^{(2)}$ tensor may be obtained by breaking the inversion symmetry of the crystalline structure. The symmetry may be broken by straining the silicon layer. This way, the fundamental cell results distorted, as it is shown in Fig. 4.2, resulting in symmetry breaking [139, 141, 142, 153, 154, 143, 155].

The possibility to obtain non-zero $\chi^{(2)}$ directly in silicon obtained a huge impact on silicon photonics due to the possibility of using the Pockels effect to realize ultrafast modulators [140] as opposed to modulators exploiting other effects [29, 134, 137, 136, 135] .

4.2.1 Design

Many approaches have been pursued in the attempt to quantify precisely the value of $\chi^{(2)}$ in various configurations of strained silicon. In the case of SiQuro, the structures are realized within a 250 nm thick SOI device layer. The choice of a thinner layer with respect to the 500 nm thick SOI of WP1 is due to two main reasons: (i) to better exploit the strain gradient, which is concentrated near the surface of the waveguide, and (ii) to obtain small effective mode areas, necessary for the all-optical fields SFG and SPDC experiments.

For the purpose of measuring the $\chi^{(2)}$ value, Mach-Zehnder Interferometers (MZI) exploiting the Pockels effect have been used [139, 140, 153, 143]. As explained in Sec. 1.6 the output of a MZI is sensible to the optical length difference between its two arms. In this case, one of the arms is immersed into a static or low-frequency electric field by applying a voltage to electrodes above or near the arm of the interferometer. If a $\chi^{(2)} \neq 0$ tensor is present in the waveguide immersed in the low-frequency electric field, the optical mode traveling inside should be subject to an index variation induced by the Pockels effect, which results into a modulation of the MZI interference.

The measurements obtained from the MZI experiments resulted in a wide range of effective $\chi^{(2)}$ values that ranged from 15 pm/V [139] to 339 pm/V [143] in structures expected to have similar strain conditions. In these experiments, a MZI is realized by using silicon waveguides that are then strained by a stressing layer, typically silicon nitride Si_3N_4, which is deposited on top of the waveguides. The stressing layer locally induces a deformation in the Si fundamental cell, breaking the inversion symmetry and thus enabling a $\chi^{(2)} \neq 0$ non-linearity.

The $\chi^{(2)}$ change is probed through the measure of the refractive index variation, Δn, that is produced by an externally applied low-frequency (LF) electric field on one of the arms of the interferometer. The MZI is sensible to the refractive index variations, as the modulation of the refractive index inside a single arm contributes to the total difference in optical path between the two arms. At the output of the MZI the interference pattern is indeed proportional to $cos(\varphi_0 + \Delta\varphi(\Delta n))$ where φ_0 is the phase due to the unbalanced arms when no external electric field is applied and $\Delta\varphi(\Delta n(E_{\text{LF}}))$ is the contribution due to the electric field modulation. The index modulation at the optical frequency ω_{opt} is expected to be linear, as from Eq. 4.1 the second-order term takes the form

$$P_{\text{LF}}(\omega_{\text{opt}}) = \epsilon_0 \chi^{(2)} E_{\text{LF}} \cdot E(\omega_{\text{opt}}) \tag{4.3}$$

where the term $\chi^{(2)} E_{\text{LF}}$ plays the role of a linear polarization, parametrized by the low-frequency field intensity. Indeed, the total polarization for the optical field may be written as

$$P(\omega_{\text{opt}}) = P^{(1)} + P_{\text{LF}}(\omega_{\text{opt}}) = \epsilon_0 \left(\chi^{(1)} + \chi^{(2)} E_{\text{LF}}\right) E(\omega_{\text{opt}}) \tag{4.4}$$

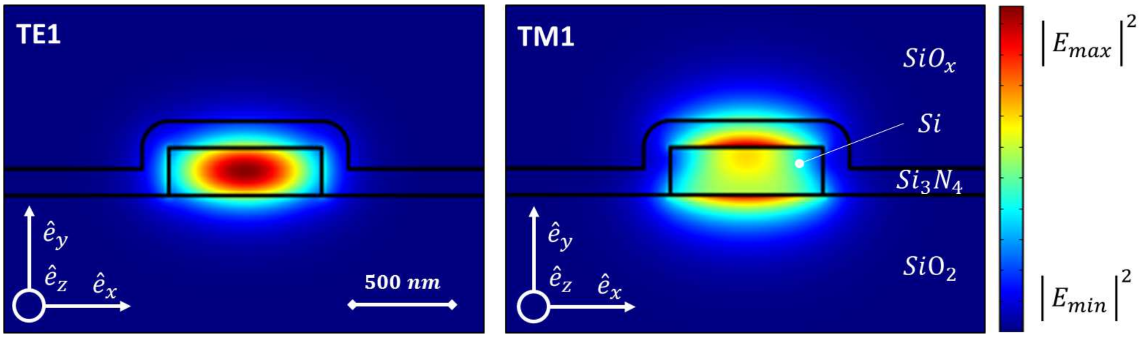

Figure 4.3: Simulated TE1 and TM1 modes optical field intensity inside a SOI waveguide covered by a conformal layer of Si_3N_4 (CAP configuration).

which leads to a total displacement field

$$D = \epsilon_0 E(\omega_{\rm opt}) + P(\omega_{\rm opt}) = \epsilon_0 \epsilon_r^{\rm eff} E(\omega_{\rm opt}) \tag{4.5}$$

with $\epsilon_r^{\rm eff} = 1 + \chi^{(1)} + \chi^{(2)} E_{\rm LF}$. The refractive index may be expanded making use of the relation $n = \sqrt{\epsilon_r^{\rm eff} \mu_r}$ with $\mu_r = 1$. Taking $n_0 = \sqrt{1+\chi^{(1)}}$, the effective index in the absence of non-linearity, the total refractive index may be expanded for small values of $\chi^{(2)} E_{\rm LF}$ as

$$\begin{aligned} n &= \sqrt{1+\chi^{(1)}+\chi^{(2)}E_{\rm LF}} = \sqrt{1+\chi^{(1)}}\sqrt{1+\frac{\chi^{(2)}E_{\rm LF}}{1+\chi^{(1)}}} \\ &\approx n_0\left(1+\frac{\chi^{(2)}E_{\rm LF}}{2n_0^2}\right) \approx n_0 + \Delta n. \end{aligned} \tag{4.6}$$

Equation 4.6 permits us to establish a linear relation between Δn and $\chi^{(2)} E_{\rm LF}$, allowing to obtain an estimation of $\chi^{(2)}$ once the value of Δn is measured as a function of $E_{\rm LF}$, which is determined by the tension V applied on the electrodes.

As it was stated above, in Eq. 4.1 the non-linear susceptibilities $\chi^{(2)}$ and $\chi^{(3)}$ are described by tensors, as in general both the polarization P and the incident fields E are vectorial quantities. The $\chi^{(2)}$ tensor depends on three indices ijk, running over the spatial directions $\hat{e}_x$ $\hat{e}_y$ $\hat{e}_z$. In our case of electro-optic interaction the ijk indices represent the direction of the polarization, the optical field, and the static electric field, respectively.

In the following, we will consider the optical field propagating along the $\hat{e}_z$ direction in a rectangular waveguide , with the TE and TM polarizations defined along $\hat{e}_x$ and $\hat{e}_y$ respectively, as shown in Fig. 4.3. The optical field has a weak component along the direction of propagation $\hat{e}_z$, which is excluded from the future considerations.

As it is shown in Fig. 4.4, it is possible to arrange aluminum electrodes above the waveguide a) in a triplet, so that the field is directed along $\hat{e}_y$ as a low-frequency TM mode, or in a doublet b) with the electric field directed along $\hat{e}_x$ mimicking a low-frequency TE mode.

Using the Δn measurement that was described above, the optical field acts as both the excitation and the probe of the induced effect, therefore limiting the measurable

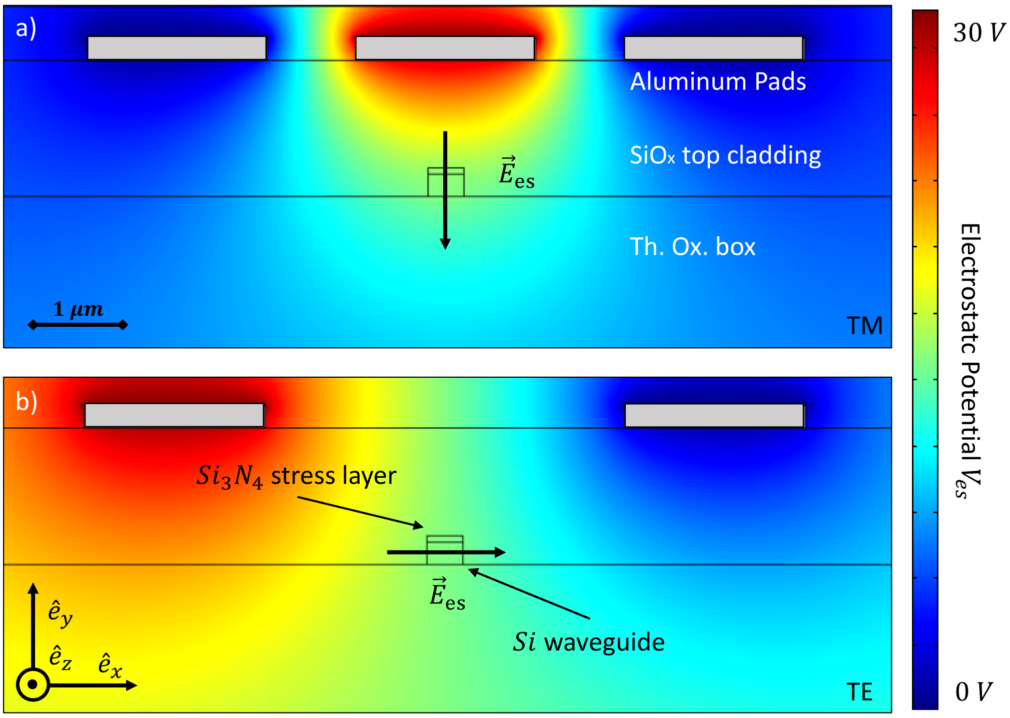

Figure 4.4: Simulation of the electric potential distribution (colormap) near aluminum pads electrodes. The electrodes are realized above a Si waveguide embedded in a thick silica cladding, necessary to insulate the optical mode from the metallic stripes. a) using a triplet of electrodes it is possible to obtain a vertical field distribution in the region of the waveguide, which acts as a low-frequency TM mode. b) Using two electrodes the electric field is instead directed along the $\hat{e}_x$ axis, miming an low-frequency TE mode. In this simulation the exact conformation of the top cladding has been approximated as flat and the silicon as an ideal dielectric.

polarization to the same direction of the optical field, i.e. fixing $i = j$. In principle, it is possible to overcome this difficulty by propagating at the same time both TE and TM fields inside the waveguide, and probe the cross-interaction for $i \neq j$, but this approach presents many practical difficulties due to the different design parameters required for the two polarizations. The $\chi^{(2)}$ components that is possible to map directly are, therefore, restricted to $\chi^{(2)}_{xxx}$, $\chi^{(2)}_{xxy}$, $\chi^{(2)}_{yyx}$, $\chi^{(2)}_{yyy}$.

To overcome this limitation, it is possible to realize structures at different orientations by making use of the relation

$$\chi^{(2)}_{abc} = \sum_{ijk} R_{ai} R_{bj} R_{ck} \chi^{(2)}_{ijk} \tag{4.7}$$

where R_{ai}, R_{bj} and R_{ck} are rotation matrices. However, it has to be taken into account that the strain is mainly expressed along the transverse direction of the waveguide, whichever the orientation.

The shift Δn induced by the $\chi^{(2)}$ non-linearity was expected to be rather small. Assuming values of the order $\chi^{(2)} \approx 100pm/V$ and $E \approx 10^6$ V/m as from [140] the refractive index shift, calculated using Eq. 4.6, is of the order $\Delta n \approx 10^{-4}$ RIU. In order to appreciate such small refractive index variations, very long MZI are used, of the order of 1-2cm [140].

The dimension of the sensing structure may be fairly reduced, and the resolution increased, by making use of a micro-resonator structure instead [156, 157, 37]. A racetrack resonator spectrum is characterized by a comb of dips in the transmission that correspond to resonances. The resonance dips in the spectrum of a resonator are used to measure small refractive index changes in two ways:
(i) if the refractive index variation is big enough, that is, it is at least comparable to the FWHM of the resonance, the drift of the resonance may be directly measured;
(ii) if $\Delta n \ll$ FWHM it is possible to measure the transmission signal variations around the half-height of the resonance, where the lineshape derivative is maximum. In this case the signal is proportional to the derivative of the resonance, and is hence amplified by the Q-factor of the resonator.

The resonance shift associated to a $\Delta n \approx 10^{-4} RIU$ estimated before is $\Delta\lambda = \lambda_0(\Delta n/n_g) \approx 40$pm near the third telecom band. In order to apply the method (i) to measure a significant spectral shift, the resonance FWHM should then be of the same order of the shift, which imposes a reasonable Q-factor of the resonances in the order of 4×10^4. The design of the racetrack resonators was carried out by Massimo Borghi (UniTn) and is detailed in [145].

Strain layer

As mentioned before, strain is required to break the inversion symmetry of the crystal and generate a non-zero $\chi^{(2)}$ in silicon. The strain is applied to the waveguides by depositing at a high temperature a layer of material that has a different thermal expansion coefficient with respect to silicon. When the structures are brought back to room temperature after the deposition, the difference in the thermal expansion coefficients of Si and the deposited material induces a stress near the interface of the materials, resulting in a strain. The most used CMOS compatible material to strain silicon is silicon nitride (Si_3N_4), which is deposited on the wafer at a temperature of 770°C.

In order to obtain different configurations of the strain and strain gradient inside the waveguide, the arms of the racetrack resonator have been realized as waveguides

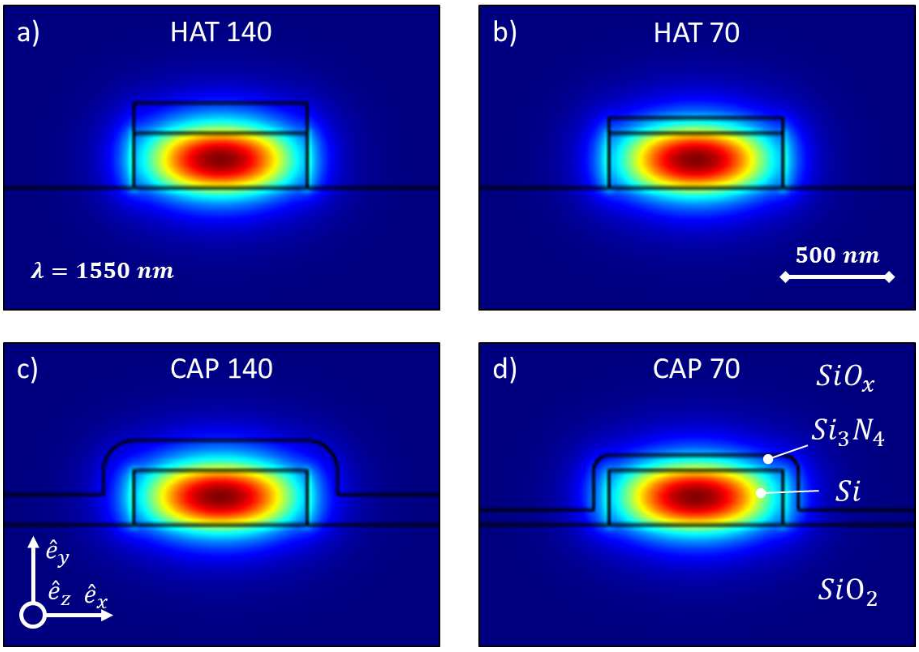

Figure 4.5: Color-map of the TE1 mode field distribution in the four stressing-layer configurations. Red color represents higher intensity. The waveguides were realized using two deposition schemes: conformal (c-d, CAP) and non-conformal (a-b, HAT). Both configurations have been realized with two layer thicknesses of 70 nm (b,d) and 140 nm (a,c).

of different width, spanning from 400 nm to 4 μm in steps of 400 nm, which are then tapered down to 400 nm over 40 μm near the bends to preserve single-mode operation of the resonators. Furthermore, the Si_3N_4 straining layer has been realized in four different configurations. The four configurations are given by the combination of two thicknesses for the stressing layer, 70 nm or 140 nm, and two deposition configurations, conformal (CAP) or non-conformal (HAT) as shown in Fig. 4.5.

In order to apply the low-frequency electric field, aluminum electrodes were realized near the straight arms of the racetrack in two configurations to realize both TE and TM polarized fields in the region of the waveguide. In order to insulate the silicon waveguides from the metallic electrodes, a 900 nm PECVD oxide cladding is deposited above the waveguides prior the metal layer's deposition. By making use of FEM simulations the electric field inside of the waveguides was estimated to be in the order of 10^4 V/m for an applied tension of 1V on the electrodes. Figure. 4.6 shows two examples of the simulations in (a) TE and (b) TM electrostatic modes. The simulation refers to waveguides in HAT configuration with 70 nm of Si_3N_4 stressing layer and an applied tension of 30V. During the design procedure, the FEM simulations were realized without considering free charges effects in silicon and, therefore, the electric field inside the waveguide has a linear behavior with respect to the tension applied on the aluminum pads.

Finally, for each TE/TM configuration and resonator arm width the resonators have been realized at five different angles of 0°, 30°, 45°, 60°, 90°, realizing a total of $N = 2\times10 = 100$ different device realizations on the layout, which is shown in Fig. 4.7 (top). The red level in the layout is the silicon device layer. The bus waveguides are well visible while the resonators are partially covered by the aluminum tracks and electrodes (green). The bottom image is an optical picture of one of the realized devices. The yellowish color of the silicon structures is due to the combined effect

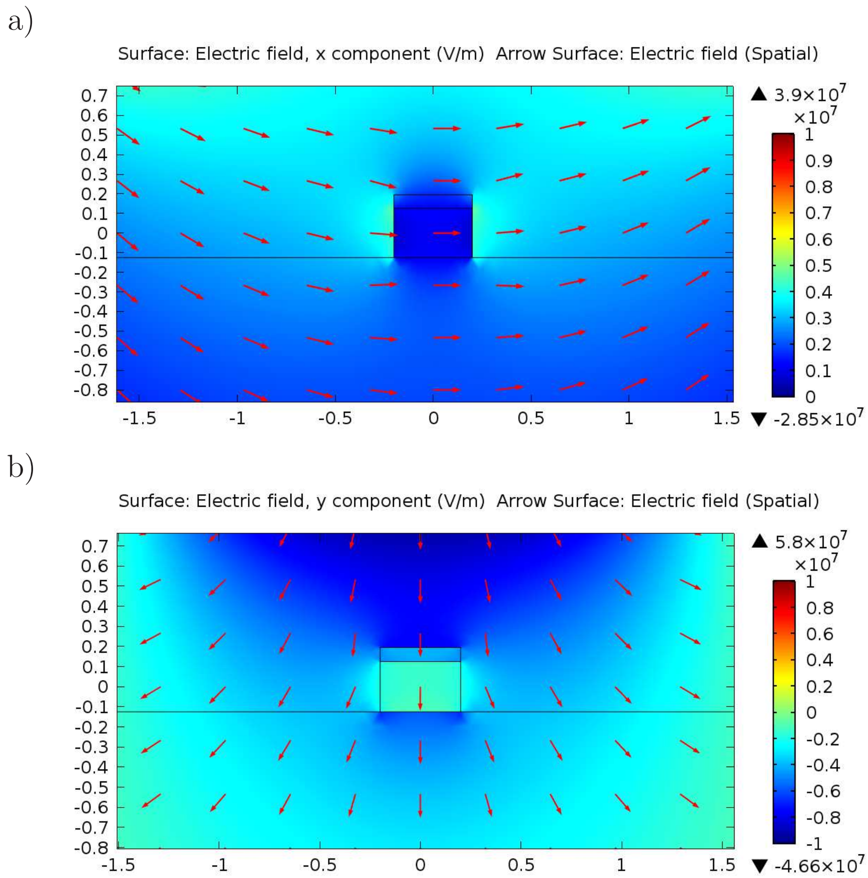

Figure 4.6: Electric field intensity and direction for the (a) TE and (b) TM configurations of the low-frequency electric field with an applied tension on the pads of 30V.

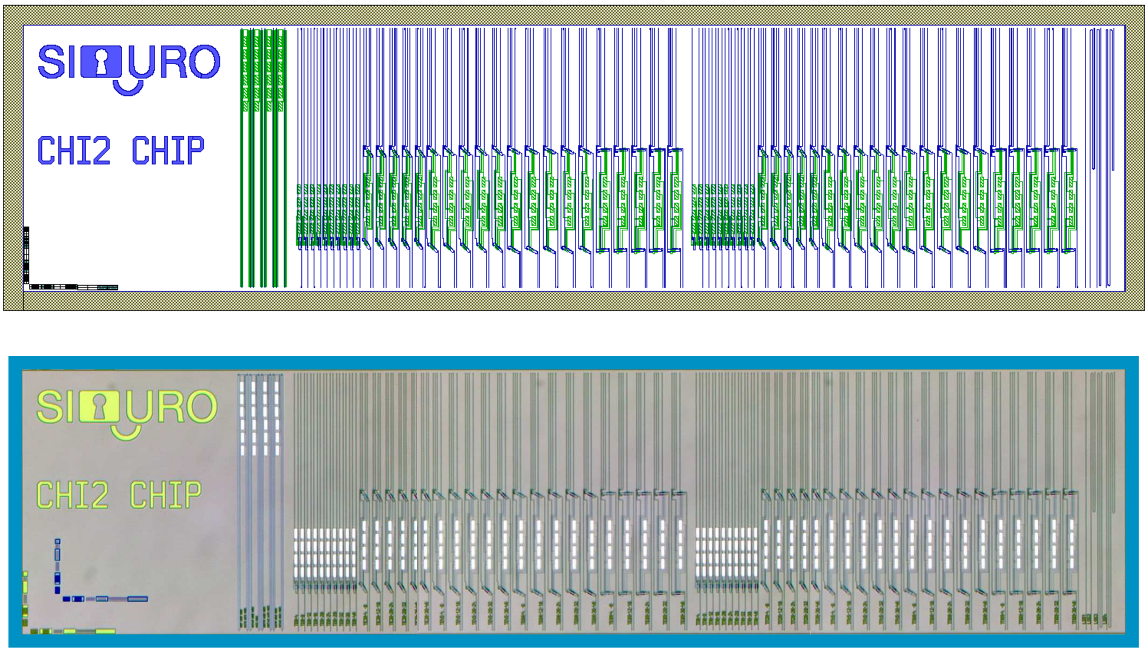

Figure 4.7: (top) image of the layout, compared to (bottom) a composed-optical image of the realized device. In the layout, the silicon device layer is represented in red, while in the optical image is yellowish. In green(gray) the aluminum pads realized for the contact-tip are well visible.

	Layer thickness	
	140 nm	70 nm
HAT	ki2A	ki2B / ki2B*
CAP	ki2C	ki2D

Table 4.1: Stress layer configurations for the processed wafers.

of the Si_3N_4 and Si layers. The aluminum pads for the contact-tip used to drive the electrodes are well visible as white rectangles between the resonator rows.

4.2.2 Fabrication

The devices were fabricated in the FBK-CMM facility in four configurations using four different SOI wafers. The stress layer configurations designed for each wafer are reported in table 4. Furthermore, an additional configuration, where the Si_3N_4 is removed, has been realized to obtain reference samples.

The device layout is transferred to the SOI layer by using stepper lithography. However, since the LPCVD deposition of Si_3N_4 is naturally conformal, the HAT and the CAP configurations have to be processed separately. In the HAT configuration, indeed, the Si_3N_4 is present only on the top surface of the waveguide. Therefore, on wafers ki2A and ki2B Si_3N_4 layers of 140 nm and 70 nm, respectively, were deposited at the temperature of 770°C directly on the unpatterned SOI wafers. Then, the Si_3N_4 layer on top of the wafer is coated with photoresist, which is patterned using lithography. The layout pattern is then transferred from the photoresist to the Si_3N_4 and then to the SOI by using RIE.

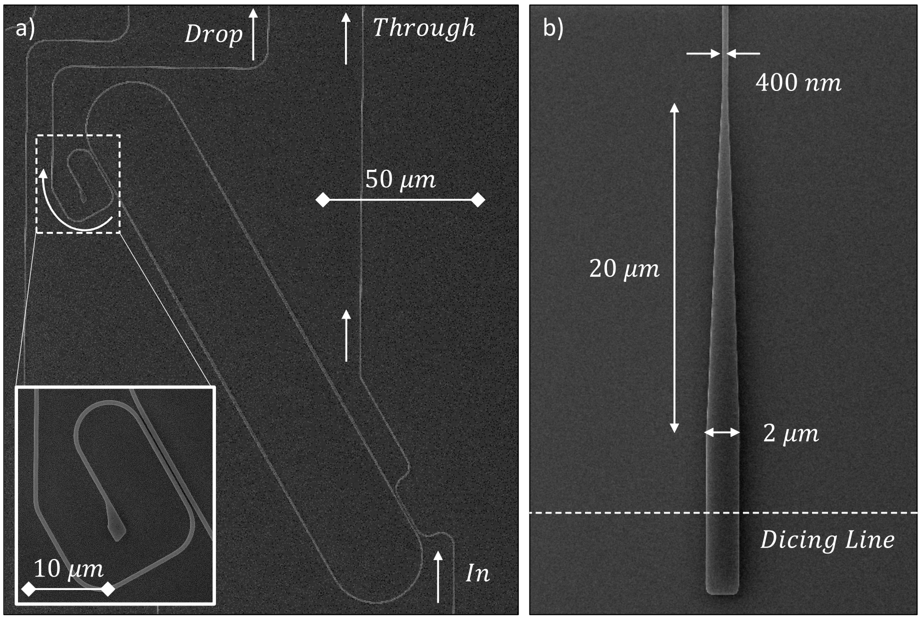

Figure 4.8: SEM image of a) a racetrack resonator and b) a waveguide end-taper at the SOI waveguide level. a) the white arrows indicate the In-Through and the Drop bus waveguides. The inset shows the directional coupler which couples the racetrack to the Drop waveguide. To avoid the formation of FP resonances in the Drop waveguide the unused side of the waveguide is terminated with a wide structure designed to suppress spurious reflection. b) the tapered waveguide ends with a 2 μm wide straight termination, which is partially etched away during the DRIE facet definition process.

A portion of the ki2B wafer, ki2B*, was dedicated to control devices where the stressing Si_3N_4 layer is then removed completely. To preserve the surface properties of the waveguides, the Si_3N_4 removal is performed by wet-etching in H_3PO_4 solution diluted with H_2O at 85%. To perform the nitride etching in H_3PO_4 a Hard Mask is necessary, and therefore a 70 nm thick layer of TEOS was deposited on the wafer to form a protection layer. After the VASE thickness control on the Si_3N_4 and TEOS thicknesses, half of the ki2B wafer was covered with photoresist, leaving the ki2B* region unprotected. After development, the unprotected ki2B* region was undergone selective wet-oxide etching in BHF solution to remove the stop layer followed by oxygen plasma to remove the residual photoresist. Then, the wafer was undergone wet nitride-etch to remove the stressing layer in the ki2B*, while the other half is protected by he TEOS etch-stop layer. Finally, the TEOS was removed also on the remaining portion of the wafer via BHF, resulting in a wafer half covered by the 70 nm Si_3N_4 layer.

At this point the ki2B(+ki2B*) and ki2A wafers are ready for the device layer etching.

In the conformal (CAP) configuration the silicon must be etched before the deposition of Si_3N_4. To obtain vertical sidewalls, a 70 nm TEOS hard mask was realized on top of the ki2C and ki2D wafers. After this, all four wafers were covered with photoresist, that was then patterned with lithography (cf. Sec.0.3.1). The photoresist pattern is transferred to the TEOS layer first, by using RIE. On the ki2A and ki2B, the silicon nitride layer was also defined at this stage using RIE. Finally, the pattern is transferred to the silicon, always using RIE, after which the residual photoresist is removed along with the TEOS hard mask. Figure 4.8 shows a SEM image of the defined structures. Panel a) shows an image of a racetrack resonator with a tilt of

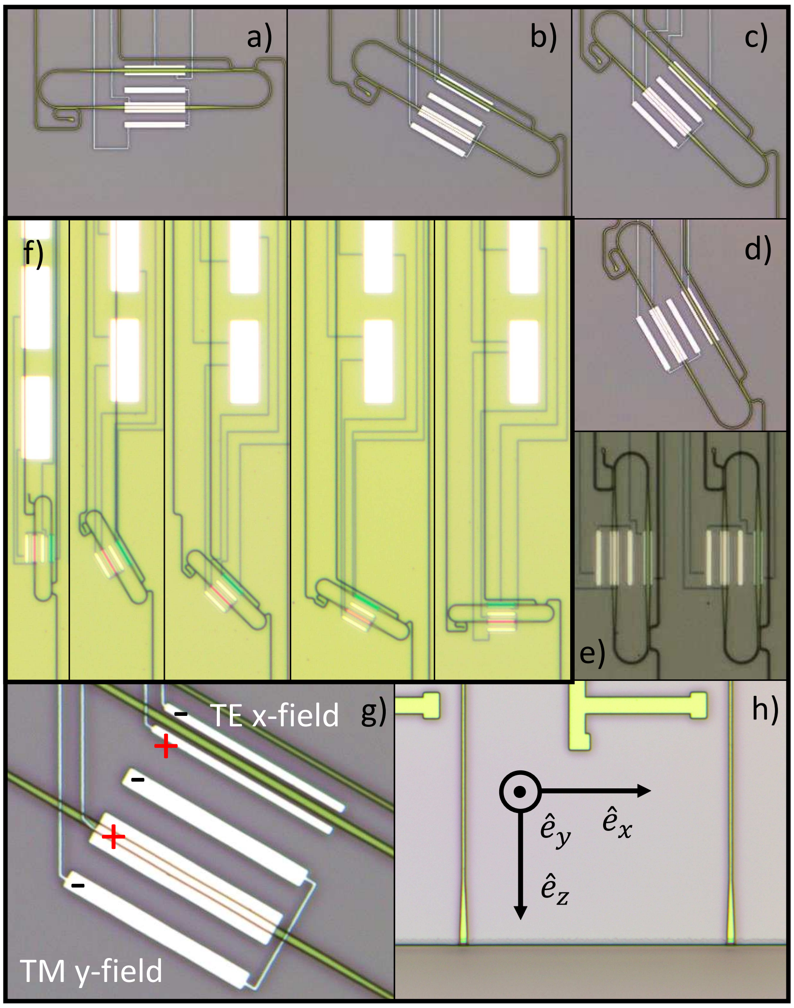

Figure 4.9: Optical images of the (green) realized resonators with the (white) metallic electrodes. a-e) The resonators are realized with different orientations with respect to the crystalline direction of the wafer, at an angle of 90°, 60°, 45°, 30°and 0°respectively. The resonators are polarized by applying a tension to the large pads visible on top of panel f), which are connected to the two sets of electrodes g) for TE and TM polarization of the low-frequency electric field, which are polarized as shown by the +/- symbols. h) the facets of the tapered waveguides are defined by a combination of RIE and DRIE, that leave the waveguides cut as it was sketched in Fig. 4.8

30°. This resonator keeps a waveguide width of 400 nm over it's whole length, and therefore no tapering is present. The white arrows mark the input-output and drop waveguides, that are coupled with the resonator through Directional Couplers (DC), shown in the inset. Panel b) shows a waveguide termination with the 20 μm long taper that terminates with a waveguide width of 2 μm.

On the ki2C and ki2D wafers, the conformal Si_3N_4 CAP layers are added at this point, depositing 140 nm and 70 nm of material, respectively. After the differentiated definition of the waveguide geometry, the wafers were covered with a 900 nm thick PECVD silicon oxide cladding to insulate the optical modes from the metallic aluminum layer used to realize the electrodes. The 250 nm thick aluminum layer is deposited with sputtering technique at room temperature, and then patterned with lithography and finally etched using RIE.

Figure 4.9 shows optical images of some of the final devices. Panels a)-e) show (green) silicon racetrack resonators, tilted at different angles of 90°, 60°, 45°, 30°and 0°respectively. Each resonator has both sets of electrodes for TE and TM polarization of the low-frequency electric field, which are polarized as shown by the +/- symbols in panel g) using the large pads visible on the top of panel f).

The input-output waveguides are terminated at the end of the chip with tapers that widen the waveguide up to 2 μm over 20 μm. The waveguide facets are defined by patterning the wafers with a dedicated mask, that leaves the termination of the tapers unprotected, as marked by the dashed line in Fig. 4.8 b). RIE is used to define the chip border through the PECVD oxide cladding, the Si_3N_4 and SOI device layers and the thermal oxide box. Finally, the chip border is defined using DRIE, to permit the dicing of the chip without damaging the defined facets as shown in Fig. 4.9 h).

4.2.3 Passive Characterization

After the dicing, I performed passive characterization on some of the structures. The measurements have been realized using the setup described in Sec. 0.3.2, by measuring the transmission of the through and drop ports of a series of resonators with varying arms width guiding TM polarization. The measurements were then analyzed with the routine I developed during this thesis work to obtain a measure of the Q-factors on a large number of resonances within the ~50 nm spectral range.

Figure 4.10 a) shows the transmission spectra of the ten measured resonators normalized to the background in the spectral range 1520 nm-1566 nm. Since the FSR of the resonator is $\sim 1.35\ nm$ there are about 32 resonances per spectrum. Figure 4.10 b) reports the fitted normalized spectrum of a resonance with a Q-factor of 48950 which corresponds to a FWHM of 33 pm. Each resonance of panel a) is fitted in analogous way to the resonance reported in panel b), obtaining the Q-factor estimations reported in panel c). The total Q-factor, which is relevant for the measure of Δn averages around 5×10^4, in good agreement with the target design value.

From the fit of the resonances of Fig. 4.10 it is also possible to calculate the FSR, which is reported in Fig. 4.11 a). The free spectral range increases slightly with increasing the resonator's arm width, indicating a change in the group index. On the other side, the FSR of the Fabry-Perot resonances that form between the facets of the bus waveguide remains unvaried, as the bus waveguide is kept of the same width for all resonators. The waveguide FSR is shown in Fig. 4.11 b) using the same color code of panel a). The thick lines represent a quadratic fit of the data.

Both the FSRs of the waveguide and of the resonators are used to estimate the group index, as reported in Fig. 4.11 c). In the case of the waveguides (thick lines) the group index is calculated from the fit of panel b), giving an $n_g \approx 4.17$ at 1550 nm for 400 nm×250 nm SOI waveguides buried in PECVD oxide. In the case of the resonators the estimation of n_g through the FSR corresponds to a weighted average over the resonator's length that contains regions fixed at $wg_w = 400\ nm$ to maintain single-mode operation along the bends, and larger regions to test different strains. The average group index of the resonators, reported with starred dots, is calculated point by point using the FSR reported in panel a).

4.3 Stress measurements

As it was mentioned before, Si_3N_4 layers are usually realized to strain the silicon waveguide.

The stress exerted by the deposited layers is quantifiable by measuring the curvature of test silicon wafers before and after the deposition of the material by using Stoney's formula [158]:

$$\sigma_{\text{layer}} = \frac{Y_{\text{Si}} d_w^2}{r(6d_m(1 - \nu_{\text{Si}}))} \tag{4.8}$$

where Y_{Si} is the Young modulus of c-Si, d_w^2 is the width of the substrate wafer, r is the radius of curvature of the wafer, d_m is the thickness of the deposited film and ν_{Si} is the Poisson's ration for c-Si.

We measured the radius of curvature of the five layer configurations on couples of twin wafers. The analyzed materials were

- Si_3N_4, deposited with LPCVD technique with a film thickness of 135 nm;
- PECVD SiO_x, 860 nm;
- LPCVD TEOS, 910 nm;

furthermore, the composed effect of Si_3N_4 and silica was also measured with

- 860 nm of PECVD SiO_x, above 135 nm of LPCVD Si_3N_4 (the configuration realized on the devices);
- 910 nm of LPCVD TEOS, above 135 nm of LPCVD Si_3N_4.

Each configuration was measured on both twin wafers. Then, one of the twin wafers for each configuration was annealed at 950°C for 2 hours in N_2 environment. Figure 4.13 shows the results of the measurements. LPCVD Si_3N_4 produces a strong tensile stress, which was measured to be as high as 1.4GPa, with good accordance between the measurements on the two twin wafers. The stress exerted by Si_3N_4 increases further with the annealing, reaching the value of 1.6 GPa. On the other hand, the two oxides produce a compressive stress, which resulted -417 MPa for PECVD SiO_x and only -26 MPa for TEOS. Annealing the oxides produces opposite effects: the PECVD oxide stress increases up to -319 MPa while the value for the TEOS layer decreases down to -133 MPa.

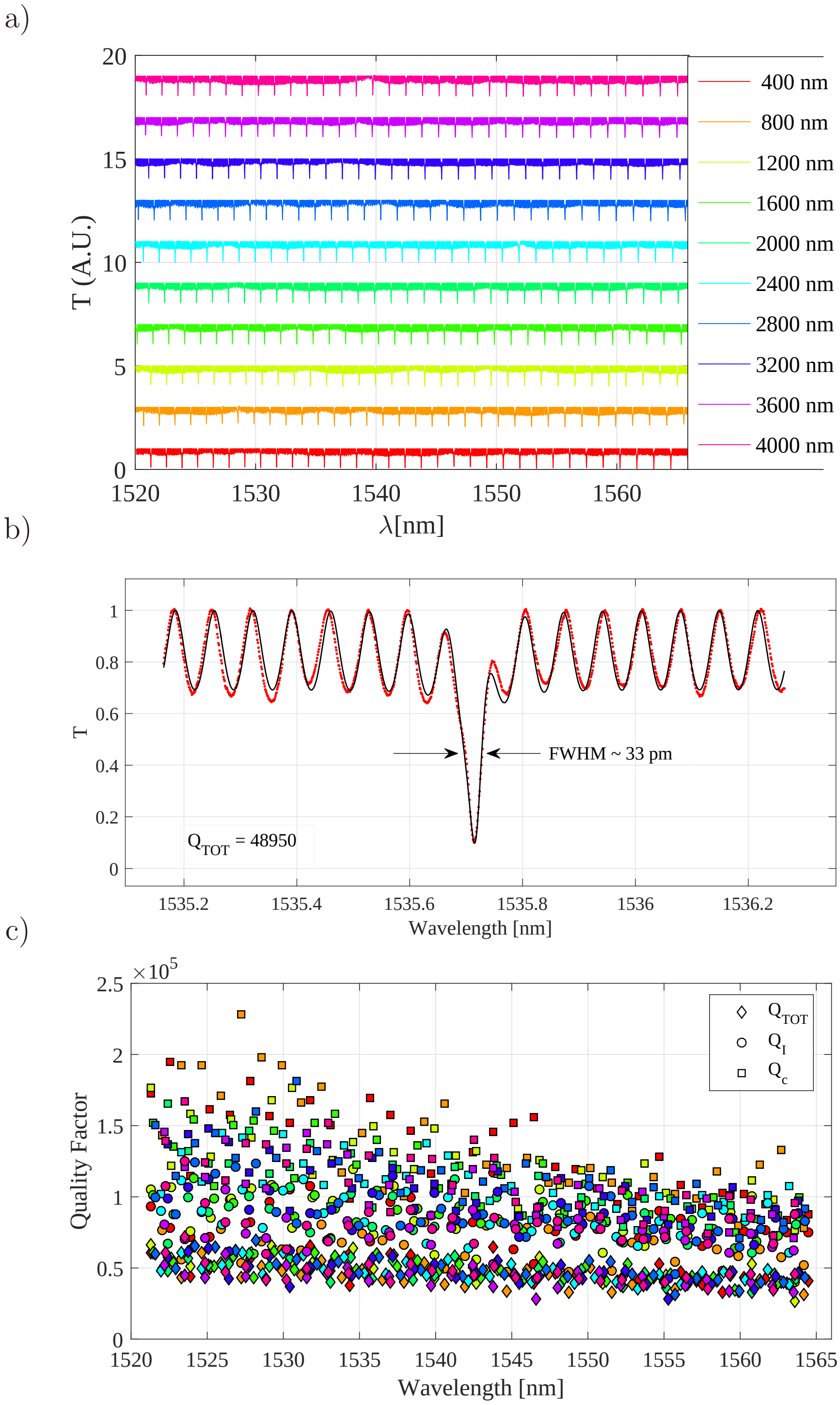

Figure 4.10: a) Normalized transmission spectra of ten resonators, with varying arm width. Using the routine that I developed during this thesis, the spectra are normalized on the baseline and the resonances are identified. b) each resonance is then fitted to accurately measure the Q-factor and the central position. c) the Q-factors of each resonance are reported using the same color convention as in a).

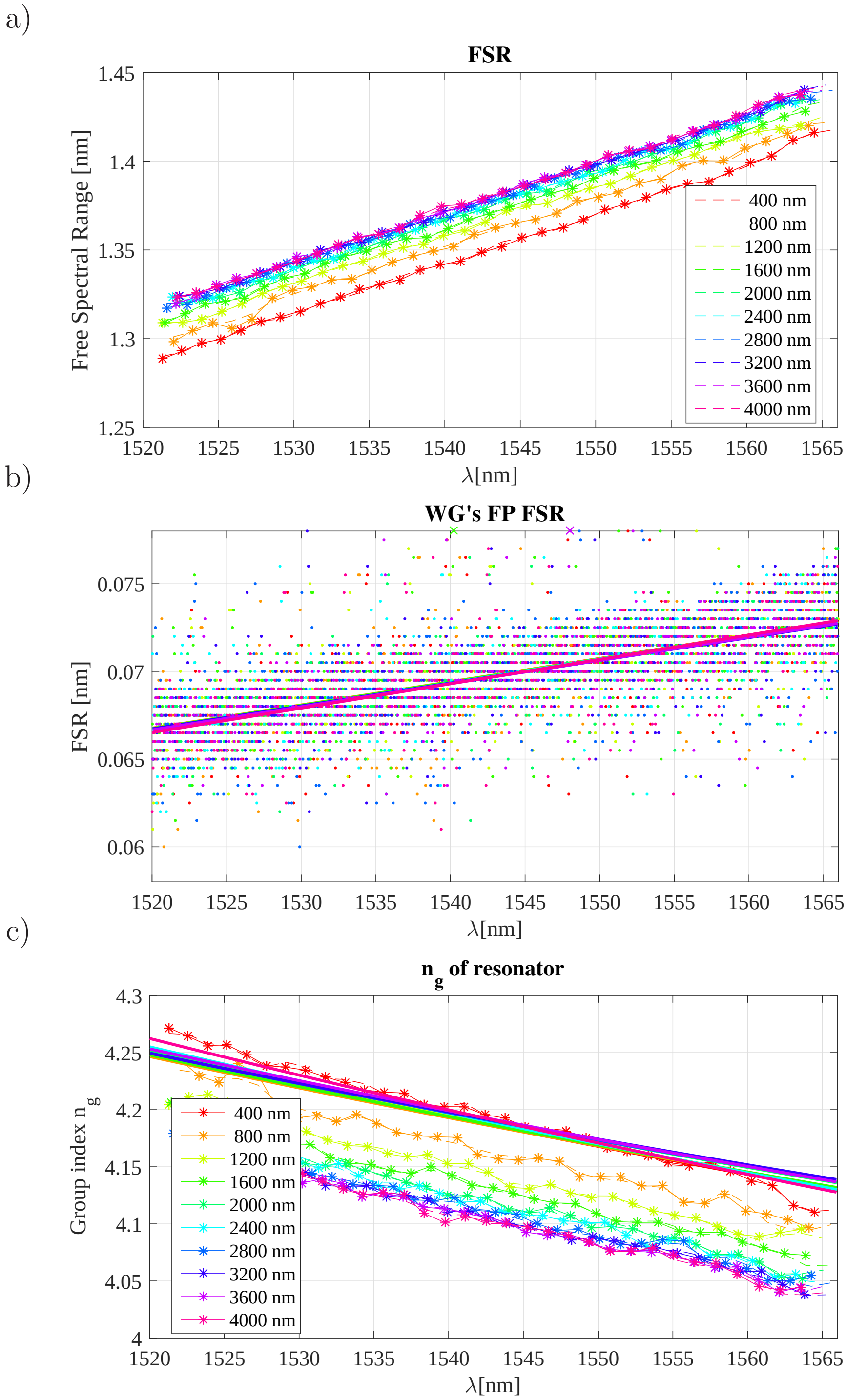

Figure 4.11: a) using the central positions of the resonances calculated in Fig. 4.10 it is possible to estimate the FSR of the resonators. The FSR of the racetrack resonators is affected by the arm width variation, increasing for larger widths. b) the FSR of the Fabry-Perot resonances that are formed between the facets of the bus waveguide, on the other hand, remains constant as expected, as it does not resent of the resonator's arm changes. The solid lines represent polynomial fits of the points, that follow the same code color as panels a) and c). c) From the FSRs it is possible to estimate the group index n_g of both the WGs (solid lines) and of the resonators (starred points).

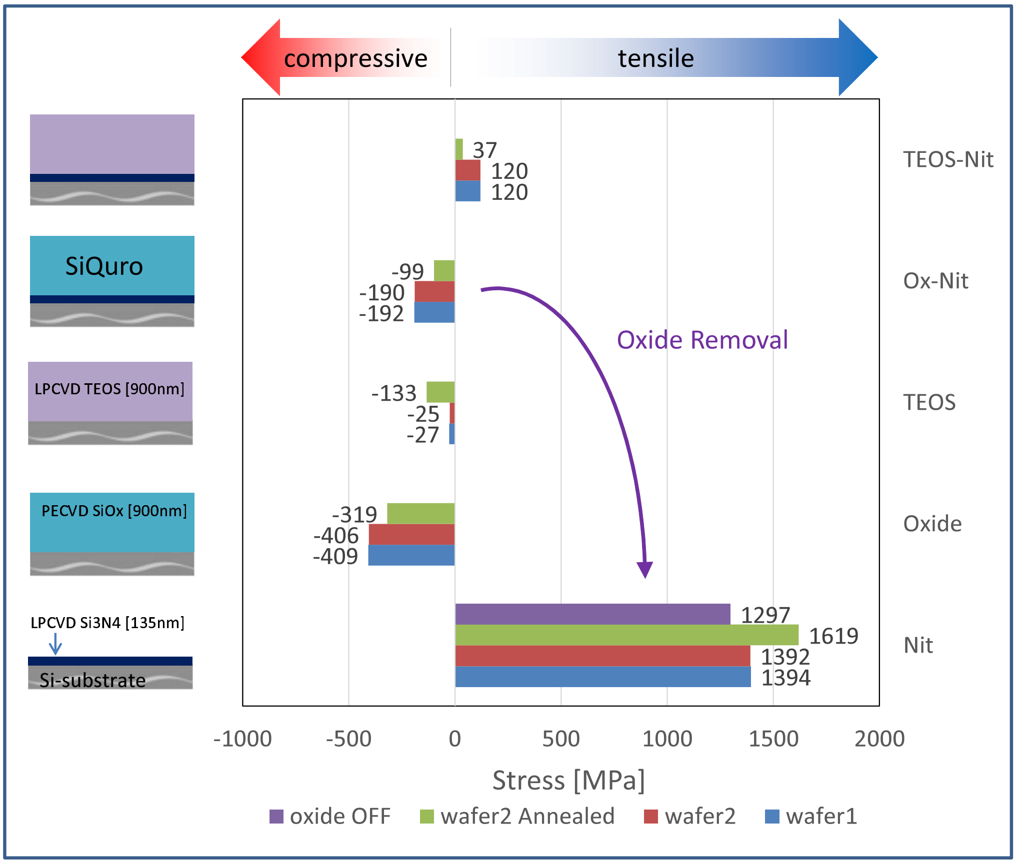

Figure 4.12: Stress measurements of various layers, measured with the wafer bow technique. The stress values have been measured on layers of LPCVD Si_3N_4 135 nm thick, PECVD silicon oxide 900 nm thick, TEOS oxide 900 nm thick and combinations of the Si_3N_4 with the two oxides. As expected, the Si_3N_4 layer exhibits a strong tensile stress. When combined with the thick oxide layer, however, the stress is reduced, even becoming compressive.

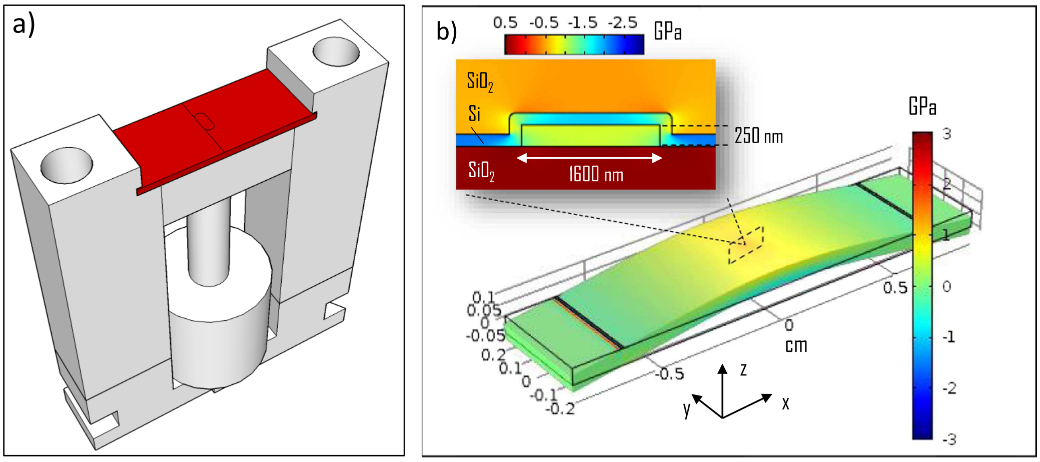

Figure 4.13: a) 3D model of the stressing sample holder. While two small indentations keep the sample borders in place, the cylinder in the middle acts on a screw that pushes against the center of the sample (red) stressing the resonator, sketched above the sample. b) FEM simulations of the stress distribution directed along the x direction inside the sample for a CAP waveguide near the half-course of the screw.

The measurements on the composed layers reveal how the combination of compressive stress and large value of thickness of the oxide cladding annihilates the tensile stress of Si_3N_4, inverting the sign in the case of silica, that has a larger compressive stress. The total stress values are indeed reduced to 120 MPa in the TEOS-Si_3N_4 configuration, down to the -191 MPa of the PECVD oxide-Si_3N_4 wafers, which represent the cladding of the realized devices. Annealing of these wafers brings even worse results, with the TEOS-Si_3N_4 reaching a total stress of 37 MPa.

A further test was then realized measuring the total bow of the remaining wafer of PECVD oxide-Si_3N_4 after etching the oxide in BHF, where the total stress returned comparable to the original Si_3N_4-only wafer.

Therefore, a series of devices without the top oxide cladding was realized by etching the silica away. Furthermore, a stressing device was realized to permit the measurement of different levels of stress in the exact same resonator. The device, sketched in Fig. 4.13 a), consists in a sample holder where a manually operated screw pushes the sample against the two small indentations present near the borders, straining the sample. The amount of stress induced in the resonators is estimated through numerical simulations, as shown in panel b). After some tests to determine the screw range over with the elastic regime of the samples is preserved, the device was operated exerting a displacement of 125 μm, corresponding to a an average stress inside the waveguide of about -0.48 GPa.

4.4 $\chi^{(2)}$ measurements

The non-linear optical measurements have been carried out in the NL-laboratories of the University of Trento. As it turned out already during the passive characterization measurements, thermal fluctuations in the room temperature of the order of 0.5°C are enough to shift the resonant position by its FWHM. It was therefore decided to perform locked-in-phase measurements near the maximum of the lineshape derivative of the resonance dip feature to obtain the maximum transmission modulation. I participated in the discussion and first stages of the experiments, where the anomalous behaviour of the modulation was discovered. Then, I collaborated in the setup of the lock-in experiment, that I will describe briefly, while the final measurements were carried out by Massimo Borghi and Mattia Mancinelli (UniTn). The results of the lock-in measurements, together with the high frequency modulation study of the same samples [144], demonstrated that most of the electro-optic effect inside of the silicon waveguides was due to free carrier dispersion.

The Δn fluctuations, described in Eq. 4.6, are valid only in the region where the electrodes exert their strong electric field on the waveguide, that is over a region L_{arm}, shorter than the total perimeter L of the resonator [159]. The total shift of a resonance with a central wavelength λ_l^0 then reads as

$$\Delta\lambda_l = \lambda_l^0 \frac{\Delta n_{\text{eff}}}{n_g} \frac{L_{\text{arm}}}{L} \tag{4.9}$$

where Δn_{eff} is the effective shift produced by the overlap of the optical mode and the strain-induced $\chi^{(2)}$ non-linearity.

Indeed, being due to the gradient of the strain, the $\chi^{(2)}$ non-linearity has a spatial distribution inside the waveguide resulting in a tensor $\chi^{(2)}_{WG,ijk}(r_\perp)$ that depends on the transverse spatial coordinates $r_\perp = (x, y)$ following the strain gradient. As the strain is generated inside the waveguide, the optical mode profile distribution $\mathcal{E}_m(r_\perp)$ will overlap with the $\chi^{(2)}_{WG,ijk}(r_\perp)$, generating an effective $\chi^{(2)}_{\text{eff,m}}$ for the mode, defined through the usual overlap integral. Dropping the ijk versor indices (by assuming that both the optical and the electrical fields are TE polarized and the strain is mainly directed along $\hat{e}_x$ direction, for simplicity), the $\chi^{(2)}_{\text{eff,m}}$ effective tensor may be written as

$$\chi^{(2)}_{\text{eff,m}} = \frac{\int_{\text{core}} \chi^{(2)}_{WG,ijk}(r_\perp) n^2(r_\perp) |\mathcal{E}_m(r_\perp)|^2 \, dr_\perp}{\int n^2(r_\perp) |\mathcal{E}_m(r_\perp)|^2 \, dr_\perp}. \tag{4.10}$$

The effective index shift Δn_{eff} may then be calculated as

$$\Delta n_{\text{eff}} = \frac{\chi^{(2)}_{\text{eff,m}} E_{\text{LF}} n_g}{2 n_0^2}, \tag{4.11}$$

where the E_{LF} is approximated to be homogeneously distributed inside the waveguide. By considering a linear dependence of the field inside the waveguide with respect to the potential V applied on the electrodes $E_{\text{LF}} = \frac{dE_{\text{LF}}}{dV} V$, the position of the resonance λ_l may be expressed as a function of the applied potential as

$$\lambda_l(V) = \lambda_l^0 \left(1 + \frac{\chi^{(2)}_{\text{eff,m}} E_{\text{LF}} n_g L_{\text{arm}}}{2 n_0^2 L} \frac{dE_{\text{LF}}}{dV} V \right). \tag{4.12}$$

Considering now the transmission signal of a resonance

$$S(V(t), \lambda) = 1 - A_l \left(\frac{\gamma^2}{\gamma^2 + (\lambda - \lambda_l(V(t)))^2} \right) \tag{4.13}$$

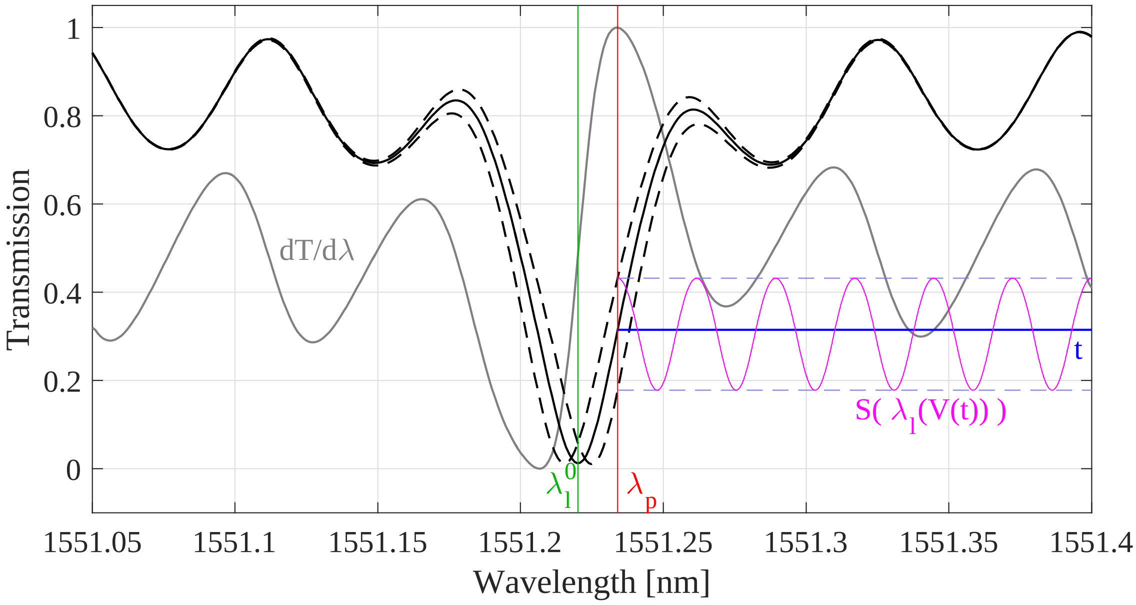

Figure 4.14: Simulated transmission modulation of a measured resonance with its Fabry-Perot background. The (solid black) transmission spectrum at V=0 with the dip in (green) λ_l^0 is modulated (dashed black lines) by the applied tension V(t). By positioning at the (red) maximum of (gray) $dT/d\lambda$, λ_p, where the modulation is maximum, the lambda shift $\Delta\lambda(V(t))$ is transduced into the transmitted intensity $S(\lambda_l(V(t)), \lambda_p)$ following Eq. 4.13

and by knowing the dependence of $\lambda_l(V)$ with respect to the applied potential, it is finally possible to compute the time dynamic evolution of the transmission signal as

$$\frac{dS(t)}{dt} = \left(\frac{\partial S}{\partial \lambda_l}\frac{\partial \lambda_l}{\partial V}\right)\frac{dV}{dt}. \tag{4.14}$$

Considering now a small modulation of the tension $V(t) = V_0 cos(\omega_k t)$ and by expanding the $\frac{\partial \lambda_l}{\partial V}$ in Taylor series around the mean value $V = 0$, the dynamic equation of the transmission signal may be written as

$$\frac{dS(t)}{dt} = \sum_n \frac{-V_0\omega_k sin(\omega_k t)}{n!}\left[\frac{\partial S}{\partial \lambda_l}\frac{\partial^n \lambda_l}{\partial V^n}\left(\frac{\partial \lambda_l}{\partial V}\right)_{V=0}(V_0 cos(\omega_k t))^n\right], \tag{4.15}$$

which is an expansion over the modulation harmonics due to the product $sin(\omega_k t)cos(\omega_k t)^n$.

The output signal may then be rewritten for the first and second harmonics, keeping the Taylor expansion terms up to the third order, as

$$S(\omega_k) = \frac{\partial S}{\partial \lambda_l}\left[\left(\frac{\partial \lambda_l}{\partial V}\right)_{V=0} V_0 + \frac{1}{4}\left(\frac{\partial^3 \lambda_l}{\partial V^3}\right)_{V=0} V_0^3\right], \tag{4.16}$$

$$S(2\omega_k) = \frac{\partial S}{\partial \lambda_l}\left[\frac{1}{2}\left(\frac{\partial^2 \lambda_l}{\partial V^2}\right)_{V=0} V_0^2 + \frac{1}{24}\left(\frac{\partial^4 \lambda_l}{\partial V^4}\right)_{V=0} V_0^4\right]. \tag{4.17}$$

As it can be seen from Eq. 4.16 the first harmonic component of the signal depends only on odd powers of the applied voltage amplitude, while from Eq. 4.17 only the even powers contribute to the second harmonic. By plugging the expression for λ_l of Eq. 4.12, which is linear in V, into Eqs. 4.16 and 4.17 the signal amplitudes result

$$S(\omega_k) = \frac{\partial S}{\partial \lambda_l}\left(\frac{\lambda_l^0 \chi^{(2)}_{\mathrm{eff,m}} L_{\mathrm{arm}}}{2n_0^2 L}\frac{dE_{\mathrm{LF}}}{dV} V_0\right), \tag{4.18a}$$

$$S(2\omega_k) = 0, \tag{4.18b}$$

where only the linear relation between the applied voltage and the first harmonic amplitude $S(\omega_k)$ survived, as is expected in the case of pure electro-optic modulation.

The experimental setup used to measure the $S(\omega_k)$ and $S(2\omega_k)$ components is sketched in Fig. 4.15 a). A fiber-coupled tunable laser connected to a function generator provides with a signal that is modulated at the frequency $\omega_\lambda = 1.2\ KHz$. The light, after a polarization control stage, is injected into the sample with a tapered fiber. The tension on the electrodes that generate the low-frequency electric field in the resonator's arm is modulated at a frequency $\omega_k = 1.6\ KHz$ by a second function generator. The light is collected ad the other end of the sample through a second tapered fiber and measured by a detector. The signal of the detector is fed to two lock-in amplifiers. The first lock in is synchronized with the modulation of the laser wavelength to measure the local derivative of the transmission $\frac{\partial S}{\partial \lambda_l}$, while the second lock-in is locked on the modulation of the low-frequency electric field.

During the experiments, however, anomalous behaviors of $S(\omega_k)$ with varying V_0 were encountered, together with non-zero values of the $S(2\omega_k)$ component. Indeed, in some samples the behaviour of of the first harmonic component seemed to have a cubic trend, while the behaviour of the second harmonic was cubic, as shown if Fig. 4.15. The fact was explained by extending the signal amplitude expression of Eq. 4.13, including variations in the resonance transmission amplitude

$$S(V(t),\lambda) = 1 - A_l(V(t))\left(\frac{\gamma^2}{\gamma^2 + (\lambda - \lambda_l(V(t)))^2}\right), \tag{4.19}$$

which bring additional terms into the dynamic equation that now reads as

$$\frac{dS(t)}{dt} = \left(\frac{\partial S}{\partial \lambda_l}\frac{\partial \lambda_l}{\partial V} + \frac{\partial S}{\partial A_l}\frac{\partial A_l}{\partial V}\right)\frac{dV}{dt}. \tag{4.20}$$

The resulting mode amplitudes for the first and second harmonics up to fourth order terms in $\frac{\partial \lambda_l}{\partial V}$ therefore result as

$$\begin{aligned} S(\omega_k) =& \frac{\partial S}{\partial \lambda_l}\left[\left(\frac{\partial \lambda_l}{\partial V}\right)_{V=0} V_0 + \frac{1}{4}\left(\frac{\partial^3 \lambda_l}{\partial V^3}\right)_{V=0} V_0^3\right] \\ &+ \frac{\partial S}{\partial A_l}\left[\left(\frac{\partial A_l}{\partial V}\right)_{V=0} V_0 + \frac{1}{4}\left(\frac{\partial^3 A_l}{\partial V^3}\right)_{V=0} V_0^3\right], \end{aligned} \tag{4.21}$$

$$\begin{aligned} S(2\omega_k) =& \frac{\partial S}{\partial \lambda_l}\left[\frac{1}{2}\left(\frac{\partial^2 \lambda_l}{\partial V^2}\right)_{V=0} V_0^2 + \frac{1}{24}\left(\frac{\partial^4 \lambda_l}{\partial V^4}\right)_{V=0} V_0^4\right] \\ &+ \frac{\partial S}{\partial A_l}\left[\frac{1}{2}\left(\frac{\partial^2 A_l}{\partial V^2}\right)_{V=0} V_0^2 + \frac{1}{24}\left(\frac{\partial^4 A_l}{\partial V^4}\right)_{V=0} V_0^4\right]. \end{aligned} \tag{4.22}$$

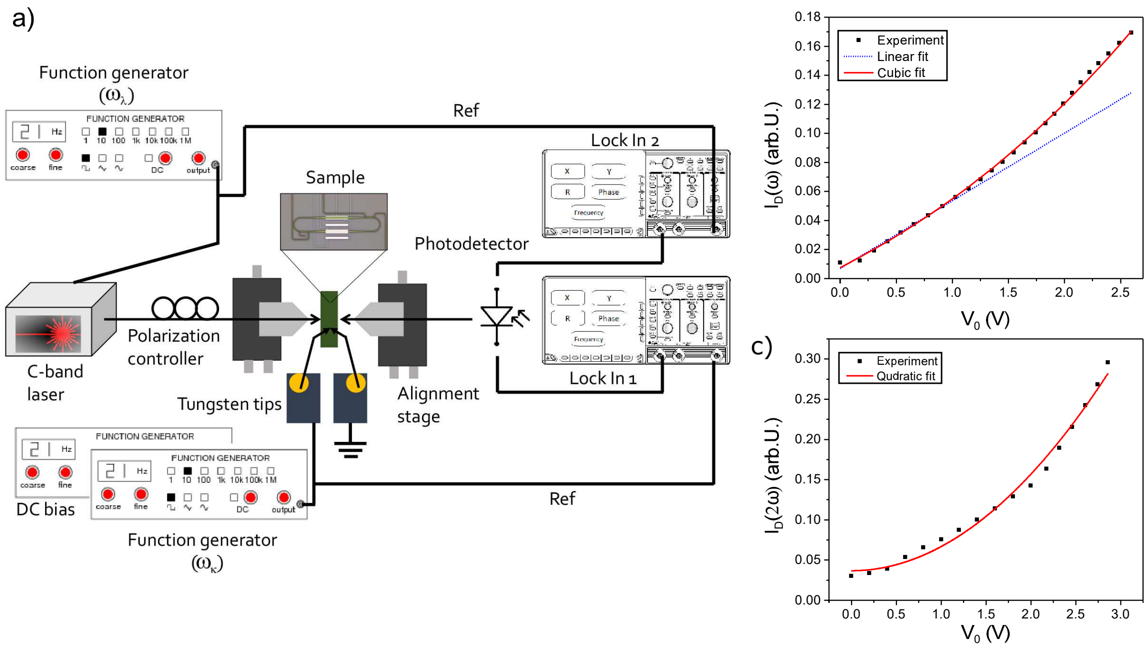

Figure 4.15: a) schematic of the lock-in experiment setup. The light of a modulated IR laser is injected into the sample with a tapered fiber. The electric field in the sample is modulated at a frequency ω_k through the electrodes above the resonator, which are connected to a second function generator. At the output, the light is collected with another tapered fiber and the intensity is measured by a detector which provides the signal for the two lock-in amplifiers synchronized with the laser and the electrodes respectively. b)(black squares) the anomalous behaviour of the collected data in the first harmonic $S(\omega_k)$ cannot be explained by a slope fit (blue), but rather with a polynomial $S(\omega_k) = a_0 + a_1 V_0 + a_2 V_0$ (red). c)(black squares) the measured second second harmonic component $S(2\omega_k)$, which should be identically null, exhibits instead a measurable quadratic trend $S(2\omega_k) = c_0 + c_1 V^2$. The data of both b) and c) were collected on an untilted resonator with $wg_w = 1.2$ μm.

which now contain terms in both even and odd functions due to the fact that $\frac{\partial S}{\partial \lambda_l}$ and $\frac{\partial S}{\partial \lambda_l}$ have opposed parity.

By fitting the lock-in experimental measurements using this model for the signal amplitudes, the strange behavior of the signal first harmonic component with no defined parity was explained in terms of amplitude modulation of the resonance. The resulting resonance shift and amplitude were explained by including carrier dispersion effects as an additional shift $\Delta n_c(V)$ into Eq. 4.11 and by the effect of the carrier absorption $\Delta\alpha_c(V)$ losses on the resonance amplitude. A complete description of the experiment is detailed in [160].

4.5 Conclusions

$\chi^{(2)}$ non-linearities are of paramount relevance for project SiQuro, as SPDC and SFG are expected to play a central role in the generation and measurement of correlated photons.

While silicon naturally exhibits zero $\chi^{(2)}$ non-linearity due to the inversion symmetry of the crystalline structure, an effective non-linearity may be obtained breaking the symmetry by applying a strain gradient. In order to design integrated devices that may show SPDC and SFG effects, a realistic measure of the induced $\chi^{(2)}_{\text{eff,m}}$, which affects the optical modes inside waveguide structures is required.

During the thesis work I collaborated on the design and simulation of SOI racetrack resonator structures with different shapes and orientations to map the various components of the $\chi^{(2)}$ tensor, that were expected to be of the order of 100 pm/V. Then, I fabricated the devices in the FBK clean room facility, designing a process to obtain four different Si_3N_4 stressing configurations on the waveguides. I performed systematic passive optical characterization on the structures, demonstrating Q-factors in the order of 5×10^4 in accordance with the designed quantities obtained through FEM simulations. Furthermore, I characterized the actual stress exerted on the waveguides by bow measurements on dedicated test wafers.

Then, the samples were tested with applying an external electric field on the resonators arm to probe the stress-induced non-linearity. The measurements were performed in the NL laboratories aiming at mapping the $\chi^{(2)}$ tensor in silicon by using the various geometrical configurations. However, high frequency measurements demonstrated that the electro-optic effect measured with an external electric field vanishes for frequencies above the inverse of the carrier lifetime in the waveguides (1GHz), which was measured by a time-resolved pump and probe experiment [144]. By measuring at frequencies higher than the inverse carrier lifetime, an upper limit of the $\chi^{(2)}_{\text{eff,m}}$ was estimated to be 8 ± 3pm/V, which corresponds to the minimum detectable signal of the experiment.

As a further proof of the responsibility of free carrier dispersion in causing the electro-optic modulation in the Si_3N_4-stressed resonators, locked-in-phase experiments were realized. In these experiments, the anomalous behavior of the resonance transmission modulation is explained by introducing the effect of free carriers through an effective index shift and absorption following Soref's equations [161, 138] . The channels through which the carriers are introduced in the waveguide are still not certain, and may vary upon the fabrication techniques used to realize the samples. This model demonstrated that the carrier induced effective electro-optic non-linearity reached 600pm/V in our samples with a modulation frequency of 1.2KHz, possibly explaining the wide range of values reported in literature.

While the measurements demonstrated an upper limit for the $\chi^{(2)}_{\mathrm{eff,m}}$ which is one order of magnitude lower than what previously reported in literature, this does not exclude the presence of $\chi^{(2)}$ phenomena in silicon. Indeed, SHG was demonstrated in strained silicon [162, 141], an effect that is not explainable by free carriers alone. It is however possible that the SHG measurement in these works, where the estimated $\chi^{(2)}$ was of the order of 40 pm/V, results from a combination of an electro-static field generated by the charges trapped at the Si-Si_3N_4 interface that interact through the $\chi^{(3)}$ non-linearity, giving a second-order non-linearity contribution. This "dressed" $\chi^{(3)}$, known as Electric Field Induced Second Harmonic (EFISH), could be responsible for the $\chi^{(2)}$ estimations being higher than the measured lower limit [163].

As a further consideration, the $\chi^{(2)}$ susceptibility is in general dispersive, and the value at optical frequencies may be substantially different from the low-frequency values obtained by the homodyne experiments [150, 151].

In either case, it is apparent that the stress induced $\chi^{(2)}$ non-linearity in silicon waveguides is lower than expected, and further investigations, or other effects, are required to obtain correlated photons within project SiQuro

Within the framework of SiQuro, pure $\chi^{(3)}$ phenomena have been considered as a possible source of correlated photon pairs both in silicon and in silicon nano-crystals [164, 146]. Very recently it was suggested that EFISH could be exploited to obtain an effective $\chi^{(2)}$ in silicon in the order of 40 pm/V [165]. In this case, a periodic p-i-n junction provides a large electric field inside the waveguide, permitting to exploit the $\chi^{(3)}$ non-linearity as an effective $\chi^{(2)}$, proportional to the reverse bias applied on the junction.

Chapter 5

Edge profile engineering for photonic applications

5.1 Introduction

In the previous chapters, most of the etching processes on produced samples have been performed using dry anisotropic Reactive Ion Etching (RIE) Chemical wet etching, where the materials are dissolved into an etching solution, is however an important part of the IC technology [166] The wet-etching exhibits isotropic properties and a high SiO_2/Si selectivity, that may reach 1000:1 using BHF solutions [167]. These two properties make wet-etching ideal for the elimination of buried sacrificial layers, often used in the Micro-ElectroMechanical Systems (MEMS) technology to realize suspended structures [168, 169, 170]. In the PIC case, the wet chemical-etching is appreciated for the resulting high quality surfaces, as it is the case for the application exposed in Sec. 1.3.

The wet etching may also be used to transfer a pattern through lithography in a similar fashion to the RIE process described in Sec. 0.3.1. Due to its isotropic behavior however, the use of wet-etching for pattern definition has a major drawback in the sidewall profile formation. A purely isotropic etching, indeed, forms sidewalls with a circular profile. However i is known from literature that in real applications the etching profile may differ from the circular shape. In some processes, during prolonged etching, the photoresist gradually peels off from the device, gradually exposing the material to the etchant. In this cases, the final etch profile results in angled sidewalls, called "wedge" [171, 80], or even more complex features [172, 173].

In this work, the interaction between the photoresist, standard BHF etching solution, and frequently used PIC materials has been investigated [132, 174, 175]. In particular, a thorough analysis on thermally grown silicon oxide (Th.Ox.), TEOS, PECVD silicon oxide, PECVD silicon nitride (SiN_x) and PECVD silicon oxynitride (SiO_xN_y) has been realized. The formation of the various etching profiles is mathematically formalized, making an analogy with supersonic waves propagation. Then, the model is used to fit the profile formed on specifically realized samples. The adhesion factor of the photoresist on the primed materials is investigated through the adhesion work and the immersion tension values for each of the materials. The values of these quantities are measured by contact angle technique and correlated with the etching

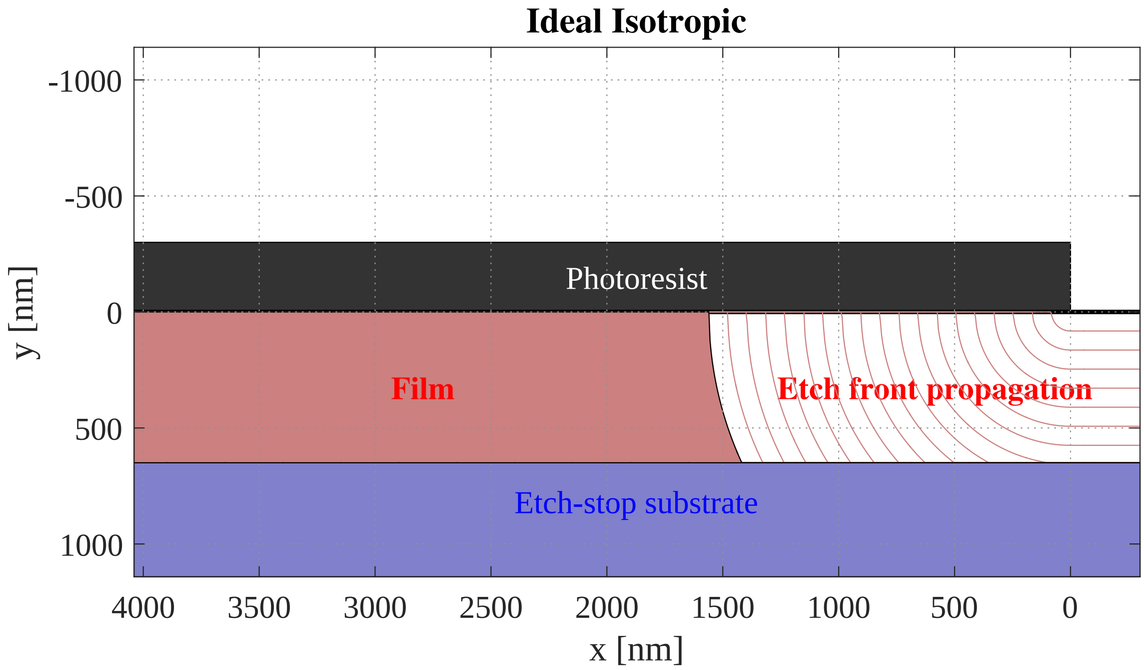

Figure 5.1: Isotropic etching profiles. The etched material (solid red) is covered by (solid black) patterned photoresist. When the etching begins, a circular etching front (red lines) propagates under the photoresist etch, while a flat front is created in the unprotected region. If the etching continues after reaching the (solid blue) etch-stop underneath material under the unprotected region, the circular front continues to expand between the photoresist and the etch-stopping material.

behaviors. Finally, I propose some practical applications that exploit the developed model to match the 500 nm thick rib waveguides that constitutes the PIC of the laser in WP1 with the 250 nm thick SOI structures WP2.

5.2 Mathematical description of etching profiles

The isotropic etching produces circular profiles originating from the interface between the photoresist and the material at the photoresist edge.
Looking at Fig. 5.1, let us consider to have a layer of material (red) with thickness h, for which the isotropic wet-etching rate is u_i, deposited over substrate (solid blue) that is not etched in the solution, and therefore acts as an etch-stopper. Consider now a patterned photoresist (solid black) layer which covers the film in the region with $x < 0$. In the case of ideal isotropic etching, the profile (x,y(x,t)) (red lines) initially evolves in circular shapes obeying:

Isotropic profile

$$y(x,t) = \begin{cases} u_i t & x < 0 \\ \sqrt{u_i^2 t^2 - x^2} & 0 \leq x \leq u_i t \\ 0 & x > u_i t \end{cases} \tag{5.1}$$

for $0 \leq t \leq t_h = h_i/u_i$, i.e. until the etching reaches the substrate. After t_h the etching may still continue, even if the end of the material is reached. In this case, the circular fronts are constrained between the underneath material that is hypothesized to act as an etch stop, and the photoresist, as shown by the etching fronts reported in Fig. 5.1.

Wedge profile

Often, a gradual peeling of the photoresist mask occurs during the wet-etching. If the wet-etchant somehow insinuates between the photoresist and the material layer, the photoresist edges lift gradually, leaving the underneath material unprotected. As the photoresist-material contact edge-point moves, the virtual origin of the isotropic circular etching moves accordingly as shown in Fig.5.2.

From a mathematical point of view, the effect is similar to the Mach angle formation in aerodynamics. In the aerodynamics case, the isotropic fronts are sound waves generated from a point. When an object travels at a velocity u_o, greater than the speed of sound u_s, the spherical pressure waves generated along its trajectory form an angled front, called shock wave. The shock wave front forms at an angle $\theta_a = \mathrm{arcsin(u_s/u_o)}$ with respect to the trajectory [177]. In the etching case, the isotropic fronts propagate at a speed u_i. When the photoresist peels, new isotropic fronts are generated at the detaching point that moves at a speed $u_m > u_i$, constant in first approximation, as shown in Fig. 5.2. The superposition of isotropic fronts generated along the photoresist detachment trajectory form an angled profile with $\theta_m = \mathrm{arcsn(u_i/u_m)}$, that is called "wedge". The generated profile (x,y(x,t)) is

$$y(x,t) = \begin{cases} u_i t & x < 0 \\ \sqrt{u_i^2 t^2 - x^2} & 0 \leq x \leq (u_i^2/u_m)t \\ tan(\theta_m)(u_m t - x) & (u_i^2/u_m)t < x \leq u_m t \\ 0 & x > u_m t \end{cases} \tag{5.2}$$

for $0 \leq t \leq t_h$, as shown in Fig. 5.3 (red lines).

The bottom part of the etching profile, under the photoresist edge, has a residual circular profile that extends for $0 \leq x \leq (u_i^2/u_m)t$. This smooth transition between the flat front of the unprotected material and the wedge can be removed by over-etching, as it is shown in Fig 5.3. The peeling of the photoresist is not always immediate. Considering $t = 0$ the beginning of the etching bath, the peeling may start at a time $t_0 > 0$. Up to time $t = t_0$, the etching is isotropic and it is described by Eq. 5.1. Then, at time t_0, a new front will be formed at the photoresist-material interface, as described by Eq. 5.2. Figure 5.4 shows the profiles (red lines) resulting from the combination of isotropic and wedge etching.

Knee formation profile

Since the new front originates after a certain time t_0, its origin point will not be on a flat surface, but rather at a point where the remaining flat surface meets the circular shape of the isotropic etching forming a 90°angle. When the wedge front propagates, this angle remains, forming a knee feature on the sidewall of the waveguide. The knee coordinates will propagate following (see Figs. 5.2)

$$\begin{aligned} x_k(t) =& \frac{u_i}{u_m^2}\sqrt{t_0(2(t-t_0)u_m + t_0(u_i+u_m))(u_m-u_i)^2(u_i+u_m)} + \\ &+ \left(\frac{u_i}{u_m}\right)^2 (t_0 u_i + (t-t_0)u_m)\,, \\ y_k(t) =& tan(\theta_m)\left(u_m(t-t_0) - (x_k(t) - u_i t_0)\right). \end{aligned} \tag{5.3}$$

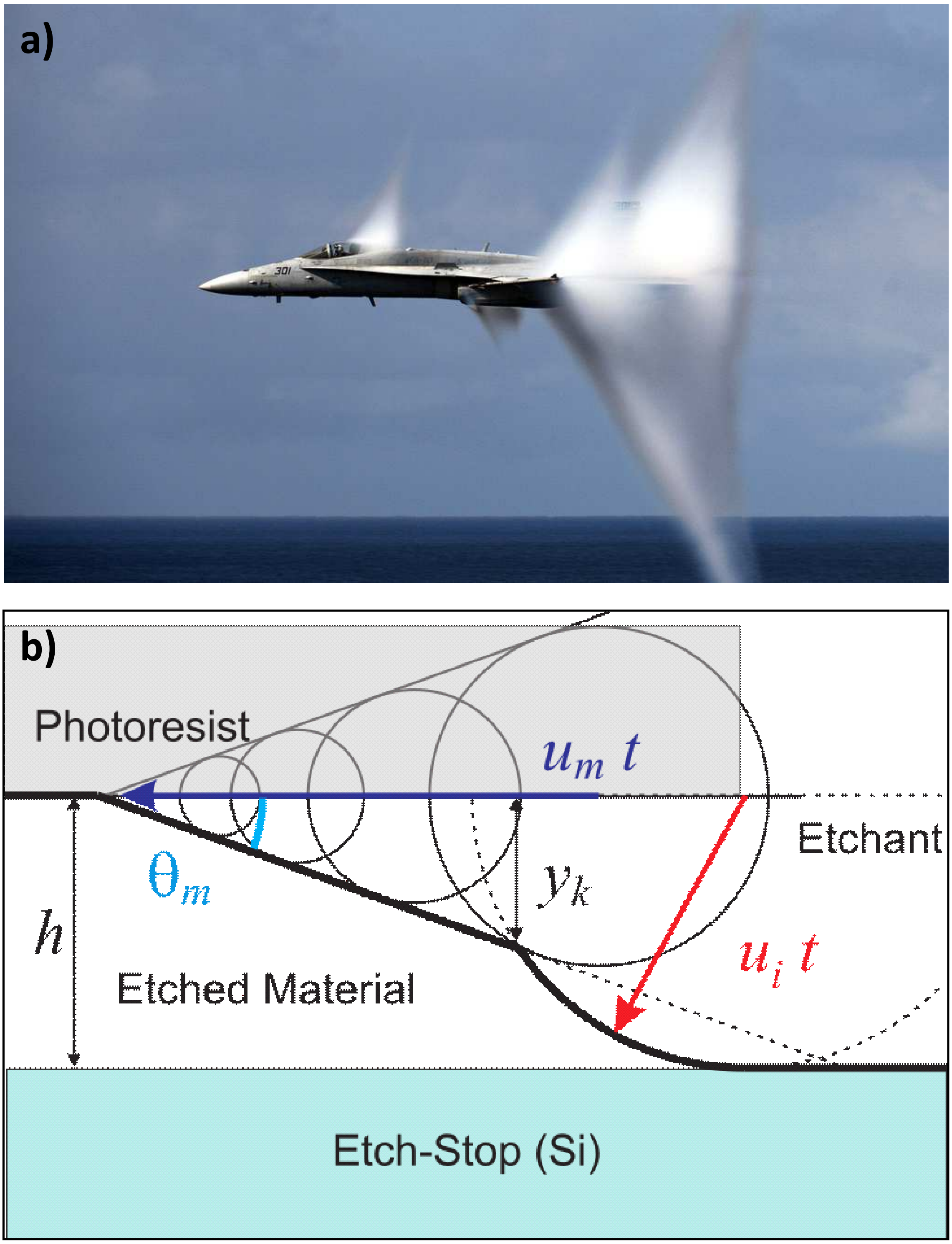

Figure 5.2: a) An F/A-18C Hornet breaks the sound barrier, forming a wavefront with the characteristic Mach angle [176]. b) Sketch of the Mach-angle profile formation in the general case when the etching begins isotropically with u_i and has a wedge asymptote. The relevant quantities u_i, u_m, θ_m are highlighted in colors.

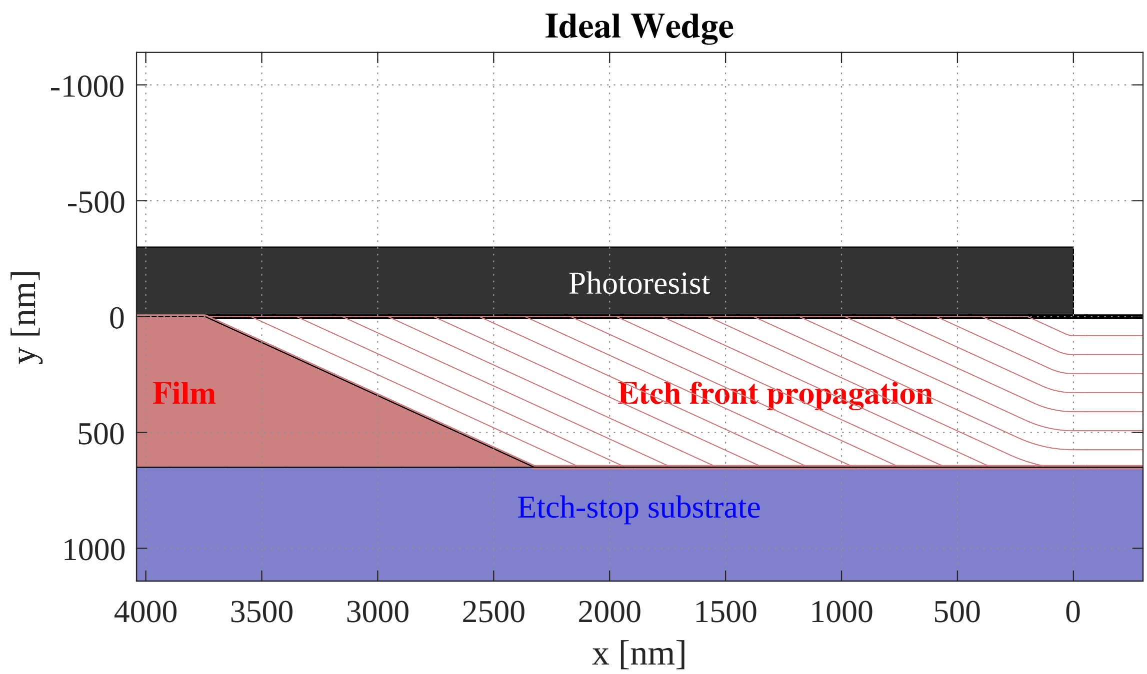

Figure 5.3: Wedge etching profiles. The etched material (solid red) is covered by (solid black) patterned photoresist. When the etching begins, a series of circular etching fronts propagates under the photoresist etch, generating (red lines) angled fronts while flat fronts are created in the unprotected region. If the etching continues after reaching the (solid blue) etch-stop underneath material under the unprotected region, the angled front continues to expand between the photoresist and the etch-stopping material at speed $u_m = 2u_i$ in the picture. It's worth note that the etching time is the same as Fig. 5.1, but due to the fast moving etching front, a much bigger area is etched.

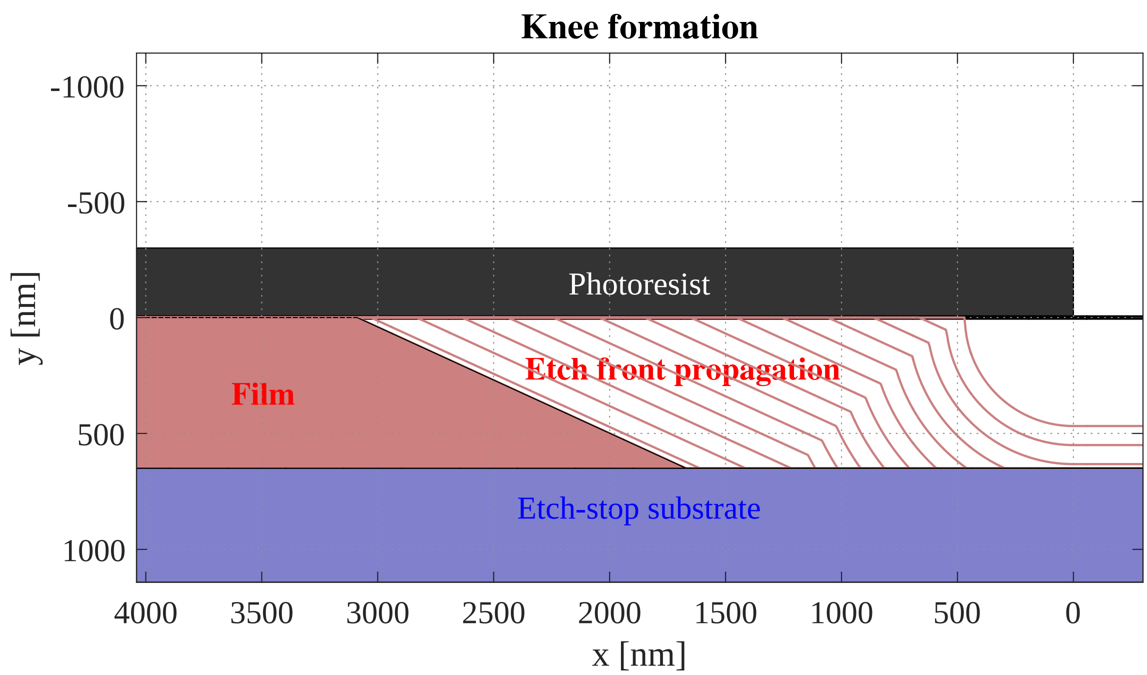

Figure 5.4: Formation of knees during the etching. The initial conditions are the same as in Fig. 5.1. At time $t = t_0$ the photoresist commences detaching and a series of circular etching fronts propagates under the photoresist etch, generating angled fronts similar to Fig. 5.3. The retarded photoresist detachment produces a knee that propagates during the etching following Eq. 5.3. In this case, over-etching is advisable to get rid of the knee.

The sidewall profile will therefore be described for $t_0 \leq t \leq t_h$ as

$$y(x,t) = \begin{cases} u_i t & x < 0 \\ \sqrt{u_i^2 t^2 - x^2} & 0 \leq x \leq x_k(t) \\ tan(\theta_m)(u_m(t-t_0) - x + u_i t_0) & x_k(t) \leq x \leq (u_m(t-t_0) + u_i t_0) \\ 0 & x > (u_m(t-t_0) + u_i t_0), \end{cases} \tag{5.4}$$

as shown by the red lines in Fig. 5.4. The knee is often not desirable if the wet-etching is used to define a photonic device, because it will augment the scattering [78]. The knee feature grows in size as the etching advances inside the material up to $t = t_h$, where the unprotected material is etched completely. The knee may be eliminated by continuing the etching for $t > t_h$ (over-etching). In this case Eq. 5.4 still holds under the condition that the new over-etched profile stops at the etch-stop material, namely $y_{\text{over}}(x,t) = min(h, y(x,t)) \forall x, t$. Asymptotically, the profile will be the same as Eq. 5.2, with a time shift of t_0.

Summarizing, the etch profiles may be categorized into three cases:

- **Circular** profile, obtained with perfect photoresist adhesion. The etched profile will obey Eq. 5.1, which is equivalent to Eq. 5.4 in the $t_0 \to \infty$ limit.
- **Wedge** profile, which occurs in the case of very poor photoresist adhesion. The photoresist peeling starts almost immediately with the etching. If the peeling is faster than the etching rate, the etching front results angled forming the wedge profile, as described by Eq. 5.2 which is equivalent to Eq. 5.4 in the $t_0 \to 0$ limit.
- **Knee** profile is obtained in the intermediate case, when the resist adhesion is not perfect and starts peeling at a time $t_0 > 0$. The profile begins with a circular shape, and then an angled front is formed at time $t_0 > 0$. The knee feature is formed at the change of etching regime, and evolves following Eq. 5.3. The profile is described by Eq. 5.4.

5.2.1 Experimental data

Samples of various materials were realized to verify the mathematical model for the profile. The samples were realized depositing the materials directly on silicon wafers using the procedure described in Sec.0.3.1, patterning the surface with standard lithography, and dicing the wafer. The samples are realized using common PIC materials:

- SiO_2 films grown via wet-thermal oxidation (Th.Ox.);
- SiO_x films grown from tetraethylorthosilicate (TEOS) precursor in a low-pressure chemical vapor deposition (LPCVD) chamber;
- TEOS as above, plus thermal annealing at 1050°C for 90 min in N_2 environment.
- SiO_x films grown in a plasma-enhanced chemical vapor deposition (PECVD) chamber;
- PECVD SiO_x as above, plus thermal annealing at 1050°C for 90 min in N_2 environment.

- silicon nitride (SiN_x) films grown via PECVD;
- silicon oxynitride (SiO_xN_y) films grown via PECVD.

Each wafer was patterned with standard lithography and etched with standard buffered hydrofluoric acid (:1 BHF) solution, for which the silicon substrate acts as an ideal etch-stop. The used materials composition, their growth and deposition conditions are

1. Thermal oxide – H_2O vapor-assisted growth in an LPCVD chamber at 1050 °C for 10.5 h, for a thickness of 1877 nm;
2. TEOS oxide – LPCVD deposition from tetraethylorthosilicate $Si(OC_2H_5)_4$ at 710 °C for 138 min, thickness of 1010 nm;
3. SiO_x – PECVD deposition at 300 °C from a mixture of nitrous oxide (N_2O, 3200 sccm) and silane (SiH_4, 10 sccm) gases using low frequency (380 kHz) plasma, 2032 nm;
4. SiN_x – PECVD deposition at 300 °C from a mixture of nitrogen (N_2, 3200 sccm), silane (SiH_4, 40 sccm) and ammonia (NH_3, 40 sccm) gases using an alternation between the high and low plasma frequencies (duty cycle of 13.56 MHz for 50 s and 308 kHz for 10 s), 437 nm;
5. $SiON_x$ –PECVD deposition at 300 °C from a mixture of nitrous oxide (N_2O, 100 sccm), nitrogen (N_2, 17150 sccm), silane (SiH_4, 50 sccm) and ammonia (NH_3, 65 sccm) gases using low frequency (380 kHz) plasma, 478 nm.

Each wafer was realized together with a test twin wafer, that was used to measure the bulk isotropic etching rate of the material in BHF solution. The wafers were patterned using the standard lithography procedure described in Sec. 0.3.1 using positive OIR^{TM}674 photoresist from Fujifilm Electronic Materials and hexamethyldisilizane (HDMS) photoresist adhesion promoter, which plays an important role for the photoresist adhesion. Then, the wafers were cleaved to obtain a number of samples.

For each wafer, a number of dices (at least eight) was time-etched in BHF solution, each with a different etching time, to reconstruct the profile evolution. Using different dices instead of performing multiple successive etch operations on the same dice is important in order to avoid artifacts from the washing/drying operations that may functionalize the surface and to obtain reliable etching times. After the timed-etching samples were immediately rinsed in distilled water to stop the etching. In preparation for the SEM imaging, the photoresist is removed using and oxygen plasma and cleaved again, exposing the etching profile.

SEM characterization, together with the interferometric measures of etching depth, permitted to reconstruct the etching profile evolution of the samples. Figure 5.5 reports a selection of SEM profiles, together with the theoretical prediction, that span over all of the three cases for possible profiles. Figure 5.5 (a) reports the profile of TEOS, which exhibits purely isotropic etching. The thermal oxide, reported in panel (b), exhibits a mixed behaviour characterized by the presence of the knee. In panels (c) and (d) the purely wedge etch profiles of SiON and SiN substrates (without annealing) are reported.

The profiles of Th.Ox, and SiON and SiN without annealing were further character-

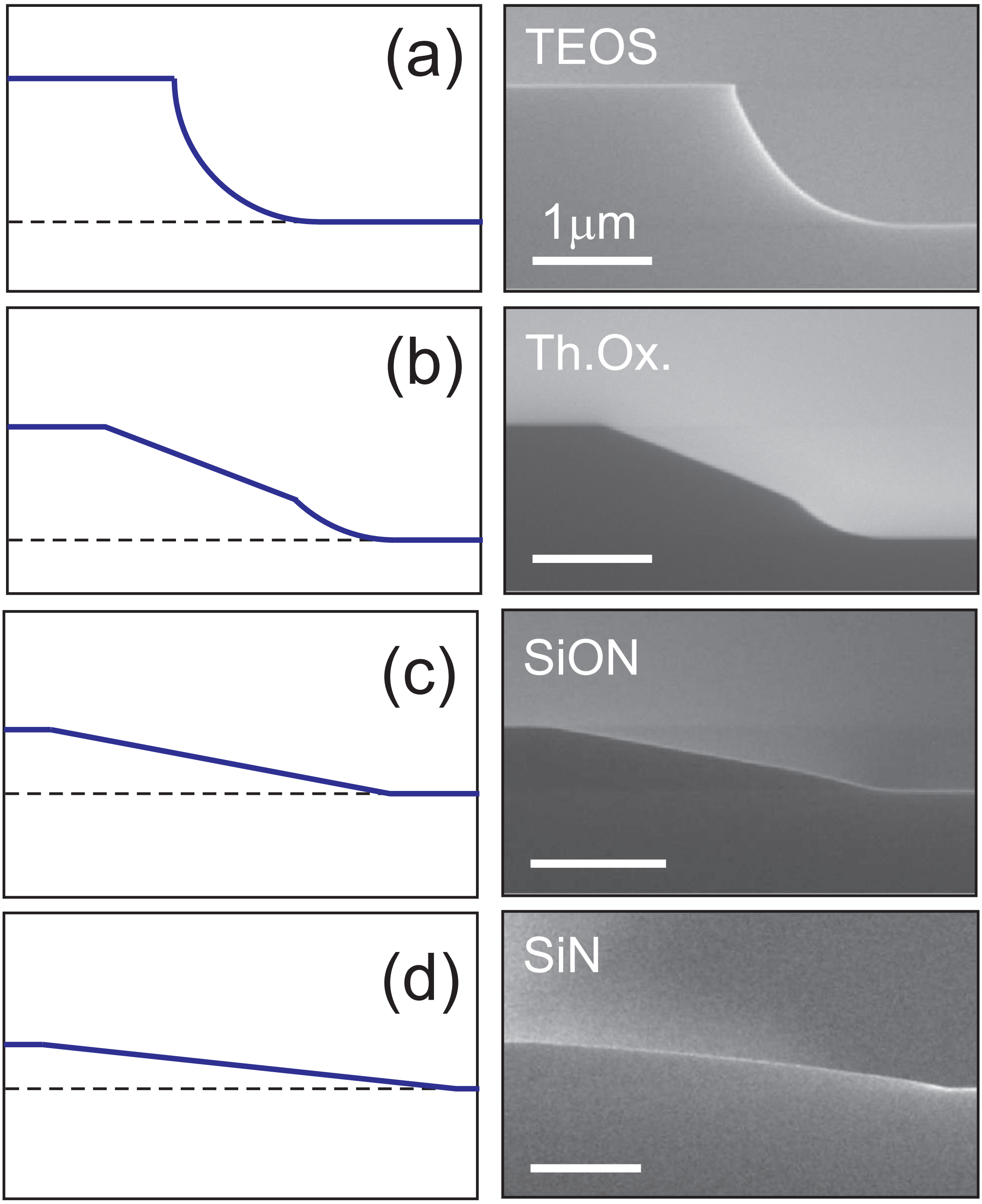

Figure 5.5: Selected SEM images of the etched profiles of various materials with the corresponding theoretical profiles for (a) TEOS, (b) Thermal Oxide, (c) PECVD silicon oxynitride and (d) PECVD silicon nitride.

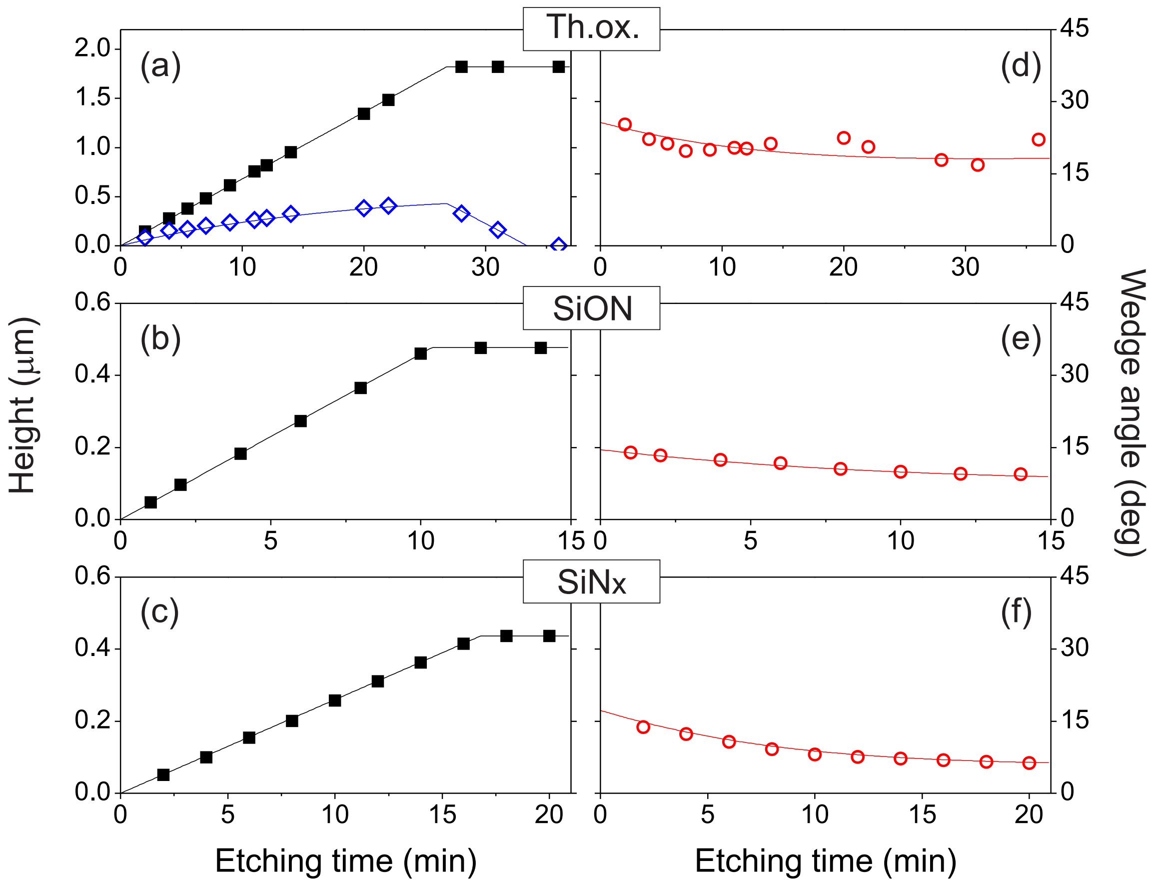

Figure 5.6: (black squares) height and (red circles) angle of the wedge profiles as a function of the etching time for the realized samples, measured with interferometry and SEM analysis respectively. Each dot corresponds to a different sample that has been etched continuously for the reported time. The black and red lines correspond to the fit of height and angle respectively plugging the logistic function of Eq.5.5 into Eqs.5.2 and 5.4 to describe the photoresist detachment rate. In the case of Th.Ox, the evolution of the knee height has also been measured (blue diamonds) and fitted using Eq.5.3. The errorbars are omitted due to insignificant values. Image from [178].

Material	Treatment	Etch rate (nm/min)	Profile type	Wedge angle (deg)
LPCVD TEOS	As deposited	228	Circular	–
LPCVD TEOS	Annealed	82	Wedge	$15°40' \pm 10'$
Th. Oxide	As grown	68	Circular + Wedge	$16°32' \pm 3'$
PECVD SiO_x	Annealed	70	Circular + Wedge	$29°32' \pm 11'$
PECVD SiON	As deposited	46	Wedge	$9°30' \pm 3'$
PECVD SiN_x	As deposited	26	Wedge	$7°18' \pm 14'$

Table 5.1: Etch parameters and asymptotic profile characteristics of the investigated materials.

ized to verify the model. The etch depths as a function of time, which are reported in Fig. 5.6 (a-c) (full squares), exhibit a stable isotropic etch rate u_i up to $t = t_h$ where the etch-stop is met. The values of u_i for the different materials are obtained by linear fitting of the experimental points with the law $d(t) = u_i t$ for $t < t_h$. For $t > t_h$, the thickness $d(t > t_h) = h$ remains constant, thanks to the etch-stop capability of Si. In Fig. 5.6 (d-f) the measured wedge angles θ_m for the wedge regions are reported in red circles. The wedge angle varies slightly during the etch process, with the angle decreasing in time in all cases. This feature may be easily included in the model by considering a peeling rate that varies with time $u_m(t)$ rather than being constant. In this case, the time evolution of u_m has been modeled for $t > 0$ considering a saturation of the peeling rate with a logistic function of the kind

$$u_m(t) = u_i \left(1 + \frac{b}{1 + e^{-a(t-t_0)}}\right). \tag{5.5}$$

The experimental data is therefore fitted with $\theta_m(t) = \arcsin(\mathrm{u_i}/\mathrm{u_m}(\mathrm{t}))$ obtaining good agreement with the experimental values as shown by the red lines in Fig. 5.6 panels (d-f). In the SiON and SiN cases, the photoresist detaching begins as soon as the wafer is immersed in the etching bath at $t_0 = 0$, and a wedge profile is formed since the beginning of etching. In the Th.Ox. case, the knee is present. The evolution of the height of the knee $y_k(t)$, reported with empty diamonds symbols in panel (a), produced a fit value of $t_0 \approx 2$min. The resulting isotropic etch rates and asymptotic angles of the wedge are reported in Tab. 5.1.

5.2.2 Surface energy estimation

The etching profiles exposed in Fig. 5.5 are very diverse. Fitting the experimental data for the etched depth and wedge angle (Fig. 5.6) with the developed model permitted the estimation of very different etch velocities at the interface between the photoresist and the material, as shown in Fig. 5.7 b). This is an indication that the reasons behind the origin of the different behaviors of profile formation lies in the interaction between photoresist, adhesion promoter, BHF etching solution, and the studied materials. Therefore, a detailed characterization of the thermodynamical properties of these materials and their interfaces with the photoresist was performed.

Contact angle measurements

The total surface free energy (SFE) was estimated for both polar and dispersive components via contact angle measurements [179]. The contact angle θ_L, the total SFE γ_L, the dispersive(polar) components γ_S^d (γ_S^p) and γ_L^d (γ_L^p) for the surface and the liquid, respectively, are linked together by:

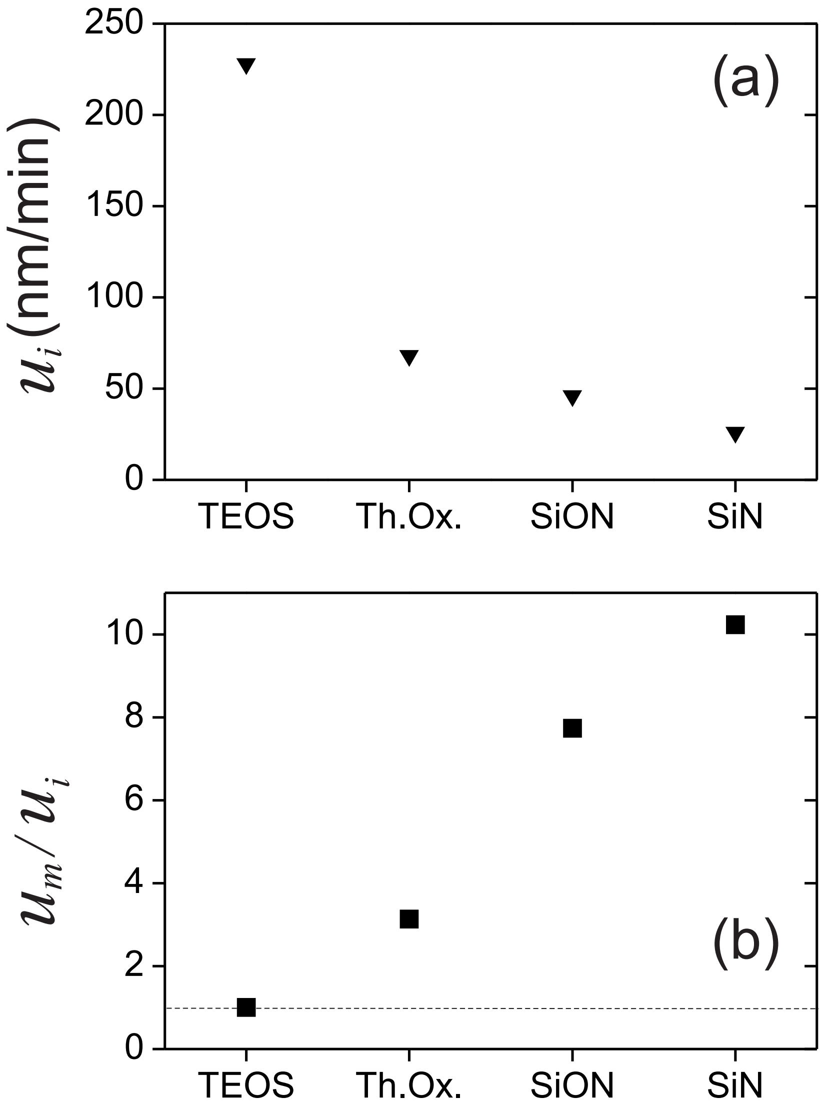

Figure 5.7: (a) Isotropic etch rates u_i and (b) u_m/u_i ratios (Mach number) for the materials of Fig. 5.5, resulting from the fits of the data reported in Fig. 5.6. The TEOS has the highest isotropic etching rate and exhibits circular profile. The u_m/u_i should lie on the dashed line of (b) or below. The other materials report u_i values below 100 nm/min, with asymptotically wedge behavior as shown by the high u_m/u_i that reaches 10 in the case of SiN. Image from [178].

	Bare surface			With adhesion promoter		
Material	γ^d	γ^p	$\theta_{L/P(F)}$	γ^d	γ^p	$\theta_{L/P(F)}$
Photoresist	40.0 ± 1.5	5.0 ± 1.0	92.0 ± 2.0	-	-	-
LPCVD TEOS	41.0 ± 1.6	30.6 ± 0.6	51.0 ± 2.0	38.5 ± 1.3	22.0 ± 0.8	79.0 ± 2.0
LPCVD SiO_2	38.3 ± 1.5	26.2 ± 0.7	67.8 ± 1.7	36.7 ± 1.6	11.2 ± 1.0	85.5 ± 2.0
PECVD SiON	40.0 ± 1.6	27.0 ± 0.5	50.3 ± 1.7	32.5 ± 1.5	19.1 ± 1.0	72.3 ± 1.7
PECVD SiN_x	37.0 ± 2.0	28.6 ± 0.5	62.3 ± 2.0	34.2 ± 1.4	17.2 ± 1.2	70.1 ± 1.9

Table 5.2: Experimentally determined dispersive and polar components of SFE, in units of mJ/m^2, of the photoresist and the dielectric films. Contact angles of BHF droplets with the considered surfaces are also reported. Error bars correspond to standard deviations for eight independent measurements.

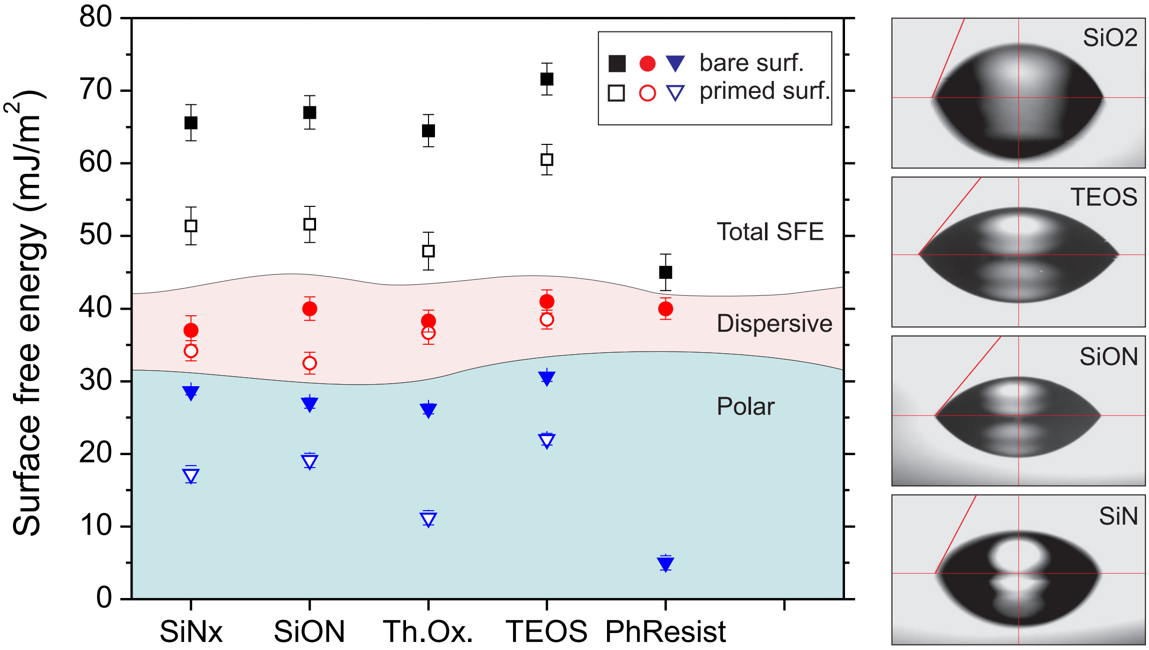

Figure 5.8: (left) Measured values of the total SFE and its dispersive and polar components for the different films and the photoresist. In the case of dielectric materials the measurements were performed both for bare and primed surfaces. (right) Examples of photograms of BHF droplets on dielectric films. Image from [178].

$$\gamma_L \cos\theta_L = 2\sqrt{\gamma_S^d \gamma_L^d} + 2\sqrt{\gamma_S^p \gamma_L^p}. \tag{5.6}$$

The SFE is calculated by measuring the static contact angle of known probing liquids (water and diiodomethane)[180] using a home-made system equipped with a high-resolution dispenser. BHF solution was also used as a probing liquid, to estimate the BHF contact angle with respect to each surface. For each measurement, 2 μl droplets were placed on the films, images were acquired with a camera and were analyzed by Drop-Analysis method [181]. In the BHF case, special care was taken to make a fast measurement to avoid artifacts due to the droplet sinking in the materials due to the etching. The SFE was measured for both the photoresist and the dielectric materials. For these last, both for bare and adhesion promoter-coated surfaces were measured. The results of the measurements are reported in Tab. 5.2 and summarized in Fig. 5.8

As it can be seen from Fig. 5.8, the application of a thin (sub-nanometer) adhesion promoter film reduces slightly (~ 5 %) the dispersive component of SFE, γ_S^d, while

	Bare surface	With adhesion promoter
Material	f_w	f_w^*
LPCVD TEOS	0.48 ± 0.04	0.51 ± 0.04
LPCVD SiO_2	0.29 ± 0.04	0.32 ± 0.04
PECVD SiON	0.37 ± 0.04	0.4 ± 0.04
PECVD SiN_x	0.5 ± 0.04	0.56 ± 0.04

Table 5.3: The calculated wet adhesion factor for bare (f_w) and primed (f_w^*) surfaces.

it suppresses significantly ($\sim$ 40 % to 70 %) the polar one, γ_S^p, confirming that the HDMS is effective as an adhesion promoter for the used materials. The balance between the two competing forces present in a system where the photoresist (P) and the film (F) form an adhesive interface, while the liquid etchant (L) tends to penetrate the P/S interface may be estimated through the adhesion factor f_w defined as [182]: Adhesion Factor

$$f_w = \frac{\gamma_L(\cos\theta_{L/F} + \cos\theta_{L/P})}{2\sqrt{\gamma_F^d\gamma_L^d} + 2\sqrt{\gamma_F^p\gamma_L^p}}, \tag{5.7}$$

where γ_L is the surface tension of the etchant, $\theta_{L/F}$ and $\theta_{L/P}$ are the wetting angles on the film and the photoresist. The adhesion factor gives an indication of the capability of the etchant to win the photoresist-dielectric adhesion and insinuate in between. For values $f_w < 1$ the photoresist adhesion to the substrate should be sufficient to prevent the etchant penetration into the P/F interface. Instead, peeling will occur easily when $f_w > 1$. Clearly, the absolute value of f_w is only indicative, and an eventual failure of adhesion may depend on the duration of etching, especially in cases when $f_w \lesssim 1$. The resulting adhesion factor values, reported in Tab. 5.3, are between 0.32 and 0.56, indicating that the photoresist should adhere to all of the materials. However, the absence of a clear trend of f values does not bring to a reasonable conclusion neither about the diversity of etch profiles nor about the difference in the observed wedge angle values from one to another material.

A further consideration may be made. The photoresist is acting as a hard-mask material in this process, and the photoresist peeling generates the $u_m > u_i$ etch-front velocity which is necessary to the wedge angle formation. An analogous effect could be obtained by realizing a thick hard mask of a material with an etching rate $u_f > u_i$. In this case, the HM material would be etched faster than the underneath layer, leaving progressively uncovered the top surface of the material and thus forming a wedge front. This fact could allow proper engineering of the wedge etching process by choosing an appropriate sacrificial-hard-mask layer.

In our case, it is possible that the adhesion promoter plays the role of a sacrificial hard mask. In fact, the material that exhibits an isotropic, circular profile is also the material with the highest etch-rate, which is possibly much higher than the adhesion promoter, while the materials that result in wedge profiles have the lowest etching rates, possibly lower than the adhesion promoter.

5.3 Possible Applications

The device layers of Chapt. 1 and Chapt. 4 make use of SOI wafers with different silicon layer thicknesses of 500 nm and 250 nm respectively. The integration of the

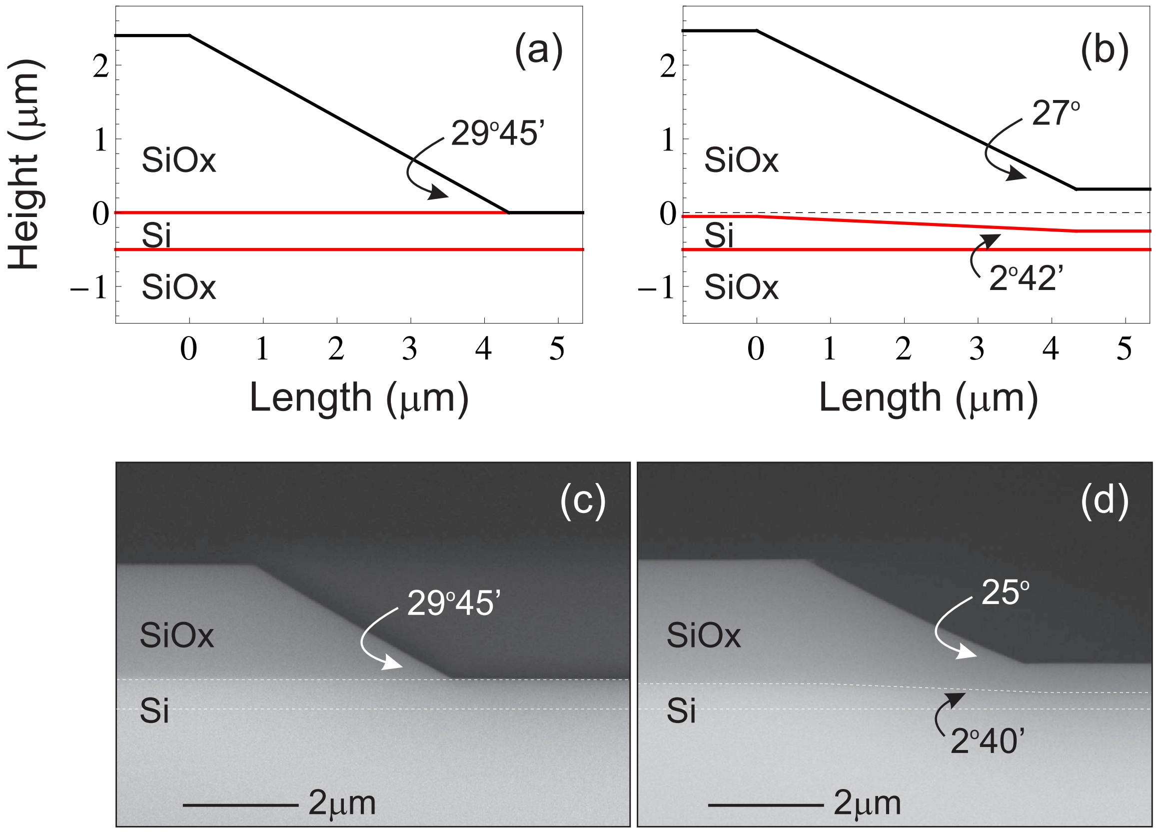

Figure 5.9: (a) the simulation of the formed wedge profile in a 2.4 μm-thick annealed PECVD SiO_x layer after 42 min of etching in BHF, and (b) the simulated tapered-profile transfer to underlaying c-Si layer after a growth of 550 nm of thermal SiO_2 in the oxide-free area. Panels (c) and (d) show the SEM cross-sectional images for the realized samples in the (a) and (b) cases respectively. A smooth tapering at an angle of $2°40'$ over a 4 μm length is formed in excellent agreement with the model prediction. Image from [178].

different functionalities within a single chip -and therefore within a single process- is one of the aims of project SiQuro. The efficient coupling of the light beams between various components constitutes one of the main and challenging problems in integrated optics and photonics technology. Adiabatic tapering is considered as an efficient mean for both inserting light from an optical fiber into an integrated waveguide [183, 184, 185], as well as for a low-loss transfer of optical modes between waveguides of different geometries within the same chip [186, 187, 188, 189, 190, 191]. In most situations, the input-output coupling of a PIC is realized by designing a horizontal taper, as described in Sec. 1.4. In some cases, as it is for project SiQuro, waveguides of different vertical dimension are present, as it is the case for the 500 nm height RIB waveguides of WP1 that need to be coupled to the 250 nm channel waveguides of WP2. In this case, a three-dimensional (vertical) tapering is required.

Several technological approaches for the realization of dielectric vertical tapers have been developed in the past. Typically, these include a combination of (i) either a shadow mask [188] or gray-tone [189, 190, 191, 192] lithography to realize a variable-height photoresist mask and (ii) a dry ion plasma etching step to transfer the pattern to the waveguide material.

The losses of such realized tapers can vary from 2.3 dB [188] down to 0.7 dB [191] and are mainly due to contributions from the geometrical-optical design part (modes back-reflection) and the mode scattering at the taper-environment interface. While

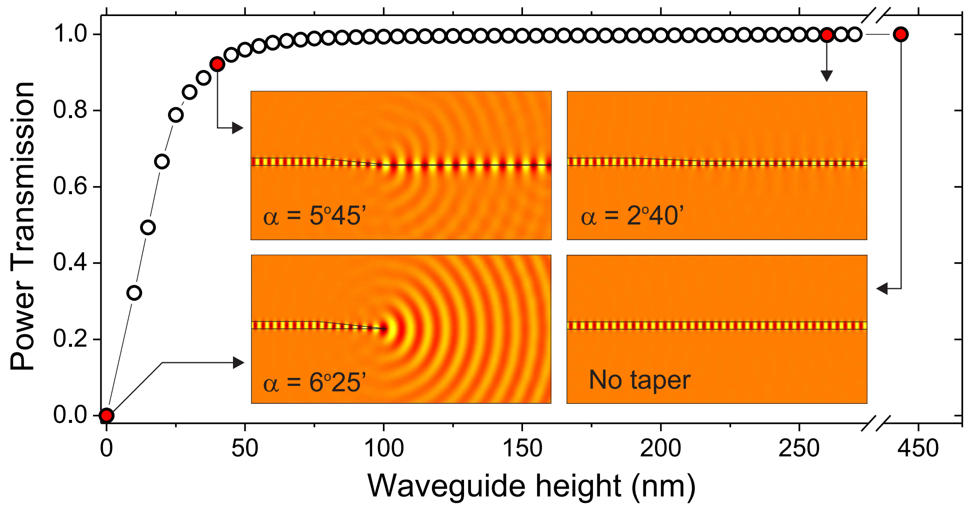

Figure 5.10: FEM simulations of a silicon vertical taper waveguide coupler. The input waveguide height of 448 nm is progressively reduced by a 4 μm-long taper down to a final height that is varied from 448 nm (straight waveguide) to 0 nm (complete inverse taper). The dots show the transmission of the taper as a function of the output height for a TE polarized wave at $\lambda = 1.55$ μm. The taper loss for the 260 nm tall waveguide, ($\alpha = 2°40'$) is 0.001 dB. The various insets show the electric field distribution for selected values of the tapering angle. Image from [178].

the geometry-dependent loss can be minimized by using an optimized design, the scattering loss reduction is limited to the roughness induced by the plasma etching techniques. In case of conventional plasma-etched Si, this last can be of the order of $\sigma = 4 \div 15$ nm's [193] and even reduced down to below 2 nm by applying the oxidation smoothing technique [194] used in Sec.1.3. Since the scattering loss is proportional to σ^2, a reduction of the roughness down to levels of $\sigma = 0.15$ nm of a polished Si wafer may reduce the scattering loss by two orders of magnitude.

The mastery over the formation of wedge profiles could provide an efficient tool for designing 3D structures, such as vertical tapers, on crystalline silicon. The proposed method makes use of thermal-oxidation to transfer the wedge profile from a SiO_2 sacrificial layer to the underneath SOI layer. The SiO_2 wedge profile acts as a graded diffusion barrier for the oxidization process of the underneath silicon, permitting the realization of a smooth transition from the 500 nm device layer to the 250 nm one. The possible roughness at the Si/SiO_2 interface is expected to be inferior to $\sigma = 0.45$ nm, which corresponds to a wedge profile roughness in a BHF-etched thermally grown SiO_2 [78].

Starting from a SOI substrate with a thickness of 500 nm, we first deposit a 2.4 μm-thick PECVD SiO_2 layer and anneal it in an N_2 ambient for 90 min at a temperature of 1050°C. After a lithographic definition of the step pattern in photoresist, a 42 min BHF etching is performed in order to realize a $\theta_m \approx 30°$smooth wedge profile on top of the Si layer as shown in Fig. 5.9 (a) and (c).

Then, a wet thermal oxidation of Si is performed at a temperature of 925°C for 300 min. The oxidization process of silicon produces a larger volume of SiO_2 than the consumed Si, with a ratio of 2.2, that grows on the surface as shown in Fig. 5.9 (b) and (d). Therefore, during thermal oxidation, a layer of 500 nm of oxide grows over the unprotected silicon, out of the 252 nm of Si that is oxidized, reducing the SOI layer thickness to 248 nm. In the meantime, only an additional 113 nm of SiO_2 is grown below the 2.4 μ-thick oxide-protected part of the wafer. Here, the original device layer height is reduced down to only 448 nm. Consequently, the thickness of the Si device layer below the oxide taper is smoothly varying from 448 nm down to 248 nm. As a result, a thermally grown Si taper of 4 μm length and an angle of only $2°40'$ is realized on the SOI platform. Finally, if needed, the oxide layer on top of the Si can be removed selectively in the same BHF solution.

The realized structure is also studied via FEM simulations in a 2D model for fundamental TE-polarized mode at a wavelength of 1.55μm, as shown in the insets of Fig. 5.10. The transmission coefficient is measured between an input (left) waveguide with height of 448 nm and and output (right) waveguide with variable height assuming linear vertical tapering along 4μm. The output thickness is varied from 448 nm (straight waveguide) down to 0 nm (complete inverse taper). The insets show the transverse electric field distribution and the formed angles for particular heights of 448 nm, 260 nm, 40 nm and 0 nm, linked by arrows to corresponding red dots in the transmission graph. The simulated losses around 260 nm are of only 0.001 dB, which are negligible with respect to the propagation losses in most devices, making it an effective vertical coupler. Another challenge in the SiQuro project is the integration of the Single Photon Avalanche Diode (SPAD) detectors. A solution is to bond the SPAD on top of the PIC. This solution requires a vertical coupler, such as a grating, to send couple the light out of the device plane into the detector. Unfortunately, grating couplers are not available in silicon within our lithography resolution. Here I propose to exploit the wedge surfaces to produce vertical couplers realizing angled mirrors on the wedge sidewall of a sacrificial layer in front of the termination of a waveguide, as sketched in Fig. 5.11 a).

Figure 5.11 b) shows a FEM simulation of the coupler in the input configuration. The light beam, shined from the top, is reflected by the wedge sidewall of a thick oxide layer into the device layer. A full-tapered waveguide, fabricated with the wedge-masked oxidation described above, collects the light that is therefore coupled to the PIC. The same configuration may be used also in reverse configuration in order to deviate the light from the waveguide to the top, as shown in Fig. 5.11 c). While the shape of the upward beam is irregular, in the case of a large ($> 20\mu$m) detector bonded over the chip only the total upward power flux is important, as the exact profile of the field does not matter.

Figure 5.12 reports the preliminary results on the characterization of a realized proof of concept device for the coupling from the chip towards the vertical direction. The samples consist of silicon oxynitride waveguides (SiO_xN_y, or SiON for brevity) deposited on a thermal oxide substrate and buried in a thick layer of BPSG glass and PECVD silicon oxide. The waveguides, defined through RIE, are realized with the output faced buried inside the chip. Deep trenches are then etched using the process described above in correspondence of the waveguides termination, exposing the waveguide faced and realizing a dielectric mirror in front of the waveguide, as sketched in Fig. 5.12 a). Pane b) shows an optical image of the realized samples, where both the buried waveguides and the trenches are visible. The samples have then been diced and the characterized using a VCSEL operating at a 850 nm wavelength. In this

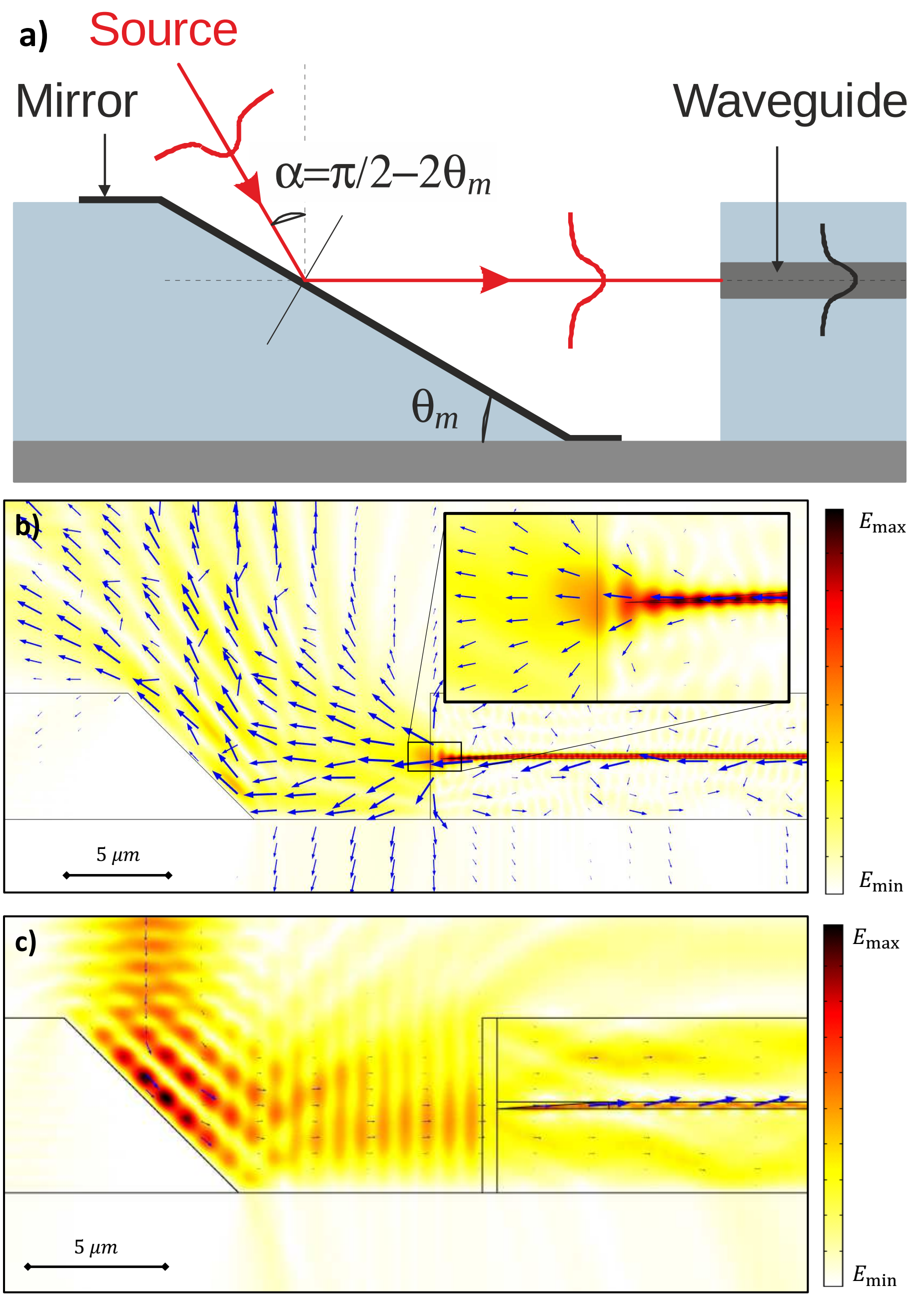

Figure 5.11: a) sketch of the vertical coupler configuration. The wedge wall of a dielectric sacrificial layer, possibly covered by a thin metal layer, is used as a mirror to couple the light between the device layer and an external source/detector. b) FEM simulations of an external coupler exploiting the wedge technology to build an integrated tilted dielectric mirror. An external beam is shined on the wedge surface of a thick oxide layer. The light is mostly reflected to the buried SOI waveguide on the left. c) the structure works also in reverse configuration, as a coupler from an external beam to the device layer. The blue arrows show the direction of the power flux.

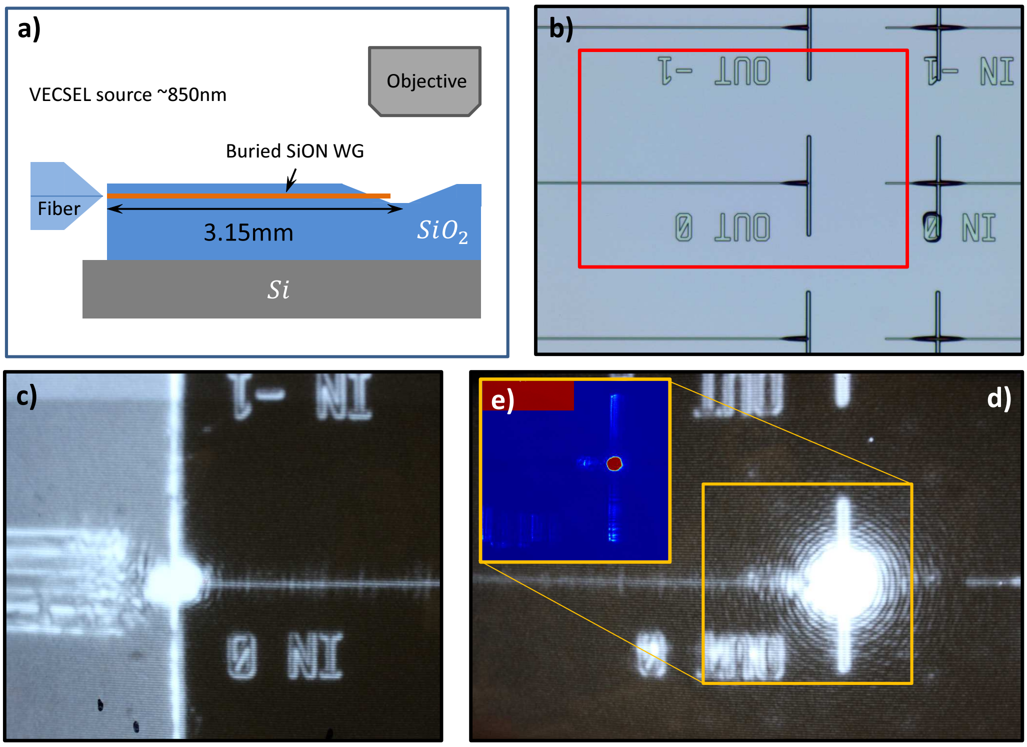

Figure 5.12

case, the light is coupled to the input of the sample through a tapered fiber (c) and the signal is collected by measuring the upward scattered light in the trench region (d). The inset e) shows the light profile collected from a CCD camera placed in proximity of the sample, showing that, qualitatively, a consistent portion of the light is scattered directly upward.

5.4 Conclusions

In this work the etching profiles of various materials that are common in silicon technology have been investigated. I developed a model for the etching profile formation that describes and reproduces the wedge and knee features that have been observed experimentally. Furthermore, the model permits engeenering of the wedge profile, and provides the condition to avoid and/or remove the knee feature in the structures. The model has been validated through experimental measurements of dedicated samples that have been realized in the FBK fab. Finally, the model has been used to develop working devices.

The first developed device exploits high-temperature wet-oxidation of silicon to transfer the wedge profile of a SiO_2 layer to SOI. Numerical simulations have been used to simulate both a vertical coupler between in a SOI layer with different heights and complete vertical inverse tapering. The vertical taper has also been experimentally demonstrated on a test wafer with the correct dimensions to match different components of the SiQuro project.

Another device that has been realized thanks to the developed wedge technology is an input-output coupler that exploits the wedge wall of a SiO_2 layer as a mirror to couple the light from the PIC plane to the top of the wafer and viceversa. In particular, while FEM simulations show that the vertical beam has an irregular shape, the total power flux that is directed upward is promising for the purpose of coupling to a wide bound detector. Indeed, a proof-of-concept device featuring silicon oxynitride waveguides embedded in a silicon oxide cladding, where the mirror is carved, has been fabricated. The measurement of the upward coupled intensity from this prototype show promising results for further development.

Conclusions

This thesis work has been largely carried out within the framework of the project SiQuro. Due to the large variety and multiplicity of topics covered by the project, during the thesis I had the opportunity to explore the whole life-cycle of a variety of photonic integrated circuits development. From the design and numerical simulations of the structures, to the development of customized fabrication processes, the measurement of the devices characteristics and the analysis of the data I had the opportunity to explore different aspects of silicon photonics. In some cases, for the final production of a photonic chip, the whole process has been repeated with iterative optimization steps. Due to the continuous optimization steps, together with the intrinsic fabrication-time requirements, most of the results presented in this work have been carried out in parallel and, therefore, did not follow a clear timeline. An advantage that was made possible from this approach is that while different materials and waveguide geometries have been used in the various chapters, the technological advancements developed during each work provided with collateral solutions that could be applied to different material and technological platforms.

Chapter 1 discussed the advancement in the realization of a heterogeneously integrated mode-locked laser on SOI platform. Although the realization of similar devices has been reported in literature, the realization of an integrated laser is a complex process which requires a number of tasks, only a portion of which have been covered in this work. The first task that was addressed is the design of the silicon PIC that constitutes part of the complex (hybrid) cavity of the laser. Here, I worked on the design of the waveguide geometry performing numerical simulations to individuate the best configuration and fabrication strategy which is feasible within the limits of UV lithography. The design of the structures was carried on in collaboration with III-V Lab (France), and made use of FEM simulations to predict the behavior of the realized structures under the effect of conformational variations due to the fabrication tolerances, enabling the possibility to perform fine adjustments on-line, during the fabrication process. Together with the design of the structures, a dedicated fabrication process was also specifically developed to achieve propagation loss below the threshold of 2 dB/cm, set by the lasing condition. The obtained propagation losses of only 1.7 dB/cm, achieved through a smoothing process using the RCA cleaning procedure, are in line with the state of the art, which is impressive considering the use 365 nm UV lithography instead of Deep-UV or e-beam lithography. The result has been obtained through multiple iterative processes, during which different technological improvements were developed, such as an anti-reflection HM and the inverse-taper terminations of the waveguides. In particular, the technological improvement provided by the anti-reflection HM, is now being used in the FBK fab to realize the next generations of SOI chips for the SiQuro project. The passive characterization of the fabricated structures demonstrated the transmission spectra in accordance with the design expectations. In parallel with the design and fabrication, adhesive wafer bonding technology using BCB polymer was developed within the FBK facility. Wafer bonding is indeed necessary to integrate the III-V active material structures on the silicon photonic circuit. At the end of this work, structured III-V wafers have been bonded on the fabricated SOI photonic circuit, and are ready for the processing of the III-V material, that will be carried on by III-V Lab. In the meanwhile, further development of the bonding process is being carried on to increase the yield of the bonding process.

In Chapter 2 low-loss integrated structures have been addressed, using a different guiding material: Si_3N_4. Silicon nitride is a silicon-compatible material that offers an intermediate refractive index between those of silicon and silica. The high transparency over a large bandwidth and the lower index with respect to silicon permit to realize low-loss structures that operate from the infrared region down to the visible. UHQ resonators based on thick Si_3N_4 layers have already been demonstrated. However, the devices reported in literature were realized in 900 nm thick Si_3N_4 resonators, that require special treatments to avoid film cracking. In this chapter Si_3N_4 resonators with quality factors comparable to those known from the literature have been reported, realizing structures that feature a Si_3N_4 film as thin as 115 nm. The structures have been realized exploiting a strip-loaded (SL) configuration, which is conceptually similar to the rib geometry used to achieve low-loss SOI waveguides in Chapter 1. Although pioneering studies on the SL geometry date back to the seventies, the field seems still rather unexplored. During this work the SL configuration has been studied and optimized for two particular operating wavelengths, requiring *a priori* single mode operation. During the experiments it was demonstrated that the single mode operation condition imposed during the simulation stage could be relaxed, obtaining resonant structures with much higher performances. The UHQ-factors obtained within such structures, together with the relaxed fabrication requirements suggest that the strip-loaded configuration should be considered as a legitimate silicon-compatible integrated platform for the development of high-performance PIC. The modeling and simulations of the structures developed during this work indeed suggest that there is still space for further improvement, especially considering development in terms of used materials and optimization of the geometry.

Relaxing the single-mode operation condition in a micro-resonator could crowd the spectrum with multiple families of resonances. The interaction between resonances belonging to different radial families in amorphous SiN_x microdisk resonators mediated by the interaction with the bus waveguide is the subject of Chapter 3. In this chapter the interaction of an integrated microdisk resonator and a vertically coupled waveguide was studied with the formalism of open-system physics. The coupling of the modes of the resonator with the bus waveguide was described in terms of both dissipative and reactive components, drawing formal analogies with the physics of an atom immersed in a bath of electromagnetic modes. The model for the dynamic equations of the cavity resonances that result from this analogy has been investigated computationally and verified experimentally on doublets of coupled resonances belonging to different radial families of the resonator. The major novelty in the developed model resides in the introduction of off-diagonal reactive terms in the coupling of the resonator modes with the waveguide. The inclusion of such terms introduces strongly asymmetric features in the transmission spectrum of the system, where the spectral features of one of the resonances results strongly enhanced or suppressed depending on the sign of the relative central frequency detuning. Due to the difference in the Free Spectral Range of the two radial families, experimental observation of interacting modes with different relative detuning has been possible, albeit on a discrete grid of the relative detuning of doublet peaks. Because of the limited experimental spectral range and the discrete nature of the sampling over different azimuthal modes, it was not possible to directly observe the mode feature suppression in the transmission spectrum predicted by the developed model. In order to obtain experimental data on the resonator's transmission over a broader range of configurations a pump-and-probe optical experiment has been designed to detune the relative frequency of the resonances exploiting the thermo-optic effect. The model has therefore been extended to include non-linear detuning of the resonance doublets induced by a localized thermo-optic effect. The atypical localization of the thermal field has been achieved through a pump-and-probe approach, where a doublet of resonances is strongly pumped to generate a localized thermal field precisely in the region where the optical modes extend. The system is probed through resonances with a different azimuthal mode that travel in the same region of the resonator, thus maximizing the interaction with the generated thermal field through the thermo-optic effect. The extended model has been experimentally validated, demonstrating continuous detuning of the modes relative frequency in the investigated doublets and permitting the experimental verification of the resonance feature suppression predicted by the model. Furthermore, by using the thermo-optic mediated non-linear tuning, complete crossing of the doublet resonances has also been demonstrated. To conclude the study, the non-linear dynamic equations of the system have been solved numerically, confirming the agreement with the experimental observations.

Chapter 4 dealt with the challenge of measuring strain-induced $\chi^{(2)}$ optical non-linearity in silicon. Indeed, being a centrosymmetric crystal, silicon does not posses a $\chi^{(2)} \neq 0$ non-linearity by itself. However, the possibility to induce such effect directly on silicon would enable a series of non-linear optical effects, among which operations on photons, such as SFG and SPDC, which are of interest for project SiQuro. In the past, all-optical and electro-optical experiments reported the presence of a $\chi^{(2)} \neq 0$ non-linearity in strained silicon, where the crystal lattice is strained and the inversion symmetry is broken. Most of those experiments relied on the measurement of the electro-optical Pockels effect in MZI structures strained by a Si_3N_4 layer. In those experiments, a static electric field was applied to electrodes in proximity of the MZI arms, producing a strong electric field in the region of the waveguide which in turn induced an electro-optical modulation of the refractive index inside the waveguide. This chapter reports a different experimental approach, where the MZI is replaced by a racetrack resonator, which offers a much higher sensitivity. Instead of the static measurement of the interference fringes shifts induced by the applied electrostatic field, a homodyne detection of the transmission signal modulation along the slope of a cavity resonance has been used. This approach permitted to reveal that the modulation included higher harmonics of the low-frequency electrical modulation, which should not be present if the refractive index variation is caused purely by the Pockels effect. Further investigations permitted to discover that the anomalous behaviour of the signal corresponding to the first and second harmonics of the modulation, as a function of the modulation intensity, is compatible with refractive index and absorption modulation induced by free carriers in the waveguide. The comparison of measurements on the vast set of samples, realized in different strain and geometrical configurations, led to the development of a model for the carrier injection inside the waveguide, which varied largely from sample to sample. The identification of carrier dispersion as the cause of the measured electro-optic modulation was further confirmed by high-frequency modulation experiments, where it was shown that the carrier lifetime in the waveguide determines the upper limit of the modulation frequency response. This experiment posed an upper limit of 8 ± 3 pm/V to the effective $\chi^{(2)}$ in the waveguide, a value which is more than an order of magnitude smaller than what reported in literature. This result leaves an open issue, since SHG, an effect that could not be due to the bare presence of free carriers, has been reported in strained silicon. Further investigations on the nature of the non-linear optical generation are being now investigated, considering in particular the hypothesis of EFISH effects due to the combination of $\chi^{(3)}$ non-linearity and static electric field in the waveguide due to trapped charges. The measured upper limit on the strain-induced $\chi^{(2)}$, much lower than expected, suggests that other routes than SFG and SPDC should be undertaken to generate correlated photons within the integrated structure, for example by the use of $\chi^{(3)}$ effects, that were already considered as a valid alternative in the original outline of SiQuro. In either case, the photonic circuit for non-linear generation of correlated photons is expected to be realized within the 250 nm SOI platform, which offers the possibility to realize waveguides with a low effective mode area. The need of a matching device between the 500 nm SOI of the laser in WP1, and the 250 nm thick SOI structures of WP2 has been addressed in the last chapter.

In Chapter 5, the formation of edges with different shape -circular, angled (wedge) and combinations- during the edge definition through wet chemical etching of various silicon based materials has been modeled drawing a formal analogy with the Mach wavefront formation from aerodynamics. The model describes different regimes of edge shape formation depending on the ratio of the isotropic etching speed of the chemical bath and the rate at which the protecting layer, typically made of photoresist, is removed. Dedicated samples have been realized in five common CMOS materials: three types of silicon oxide (TEOS, thermally grown and PECVD), PECVD SiO_{xNy} and PECVD SiN_x that exhibited all three types of profile formation. The measurements of sample profiles, realized with VASE and SEM images, provided experimental demonstration of the developed model. From the mastery over the wedge angle formation, two technological applications have been developed. The first application features a vertical coupler in silicon, which is realized by transferring the wedge profile of a thick SiOx layer through wet-oxidization of silicon. The knowledge of the wedge formation permits to engineer the oxide layer shape, that acts as a graded diffusion barrier for the underneath silicon. The result is the realization of an etch-less vertical taper, which has been experimentally demonstrated on a blank silicon proof-of-concept device. FEM simulations of the structure showed that the inverse taper, when used to match a 448 nm thick layer with a 248 nm one, produces negligible losses.

The second application features the realization of an input-output vertical coupler. This application could be used in WP3 to couple the PIC with an external detector bonded to the chip, until simultaneous integration of both the photonic circuit and the detector is realized. In this case an oxide wedge surface is used to realize an integrated angled mirror, which could be used to re-direct the light from a waveguide to the vertical direction and vice-versa. A proof-of-concept device, studied through FEM simulations, has also been realized and demonstrated through qualitative imaging measurements. Given the promising preliminary results, the implementation of further improvements, such as a metalized wedge surface and an inverse tapering of the waveguide (by using the first developed application) are expected to provide with a performant device, at least in the case where the exact shape of the output beam is not relevant. This solution offers a practical alternative to grating couplers, that are often impossible to realize within UV lithography due to the stringent requirements in terms of lithography resolution.

In conclusion, this thesis constitutes a step forward in the realization of All-On-Chip silicon photonics. During this thesis work a number of technological improvements have been accomplished, both realizing devices comparable to the state of the art and developing new technologies which have been made possible by the development of physical models of the involved phenomena.

Acknowledgments

Nos esse quasi nanos gigantum humeris insidentes
Bernard of Chartres

By working on the whole development chain of PICs I collaborated with a lot of people working in different groups, and draw knowledge from many sources that I acknowledge in the Bibliography. The experience of a Ph.D. program, however, goes beyond the scholar formation and research. Here I would like to thank the rather large lot of people that created the favorable environment that made this work possible.

First of all, I want to thank my supervisor, Mher Ghulinyan. Working daily with him side-by-side has been a very funny, instructive and enjoyable experience. *Eh, ciao Mher!*. Together with Mher, I'd like to thank the head of the FMPS unit, Georg Pucker, and the head of the NanoLab group, Lorenzo Pavesi, for their advices and mentoring during these three years.

I also wish to thank all my colleagues of the FMPS unit, in particular Ruben Bartali, Alina Samusenko and Lucio Stefan, together with Costanza Manganelli, with which I shared ideas, helpful advices and, most importantly, cheerful jokes. I would like to acknowledge the staff of the MicroTechnologies Laboratory of the CMM for providing their technological support and experience during the design of the processes and the fabrication of the devices.

A special thanks goes to the colleagues of the NanoLab laboratory of the University of Trento, where most of the optical measurements have been performed. In particular I would like to thank Massimo Borghi, Mattia Mancinelli and Fernando Ramiro-Manzano for teaching me different aspects of the lab-life, and Fabio Turri, Alessandro Trenti and Santanu Manna for patiently helping me with the experimental setups more than once.

During the experience in the IPSP Scientific Committee and as the Ph.D. students representative I peeked a look behind the curtains of the administrative staff, whose work goes often unseen. I'd like to thank in particular Tanya Yatskevich, Lucia Dorna, Laura Martuscelli, Micaela Paoli for their continuous support.

Another important and formative experience has been that of teaching assistant for "Physics Laboratory I", a first year course. I really enjoyed going again through the fundamentals of experimental physics from a rather different perspective. I wish to thank Giovanni Andrea Prodi, Mauro Hueller and Mariano Dimauro for their helpful and friendly insights.

I wish to express my gratitude to the group FisiciTn, in particular to Lorenzo Contessi, Michele Valentini, Fabrizio Larcher and Simone Normani for their support as friends, useful discussions as colleagues, and most importantly for sharing their enthusiasm with me.

I thank my family for their everyday love, encouragement and support.
I thank Marina, for her patient love and enthusiastic starry nights.

Thank you all,
Martino

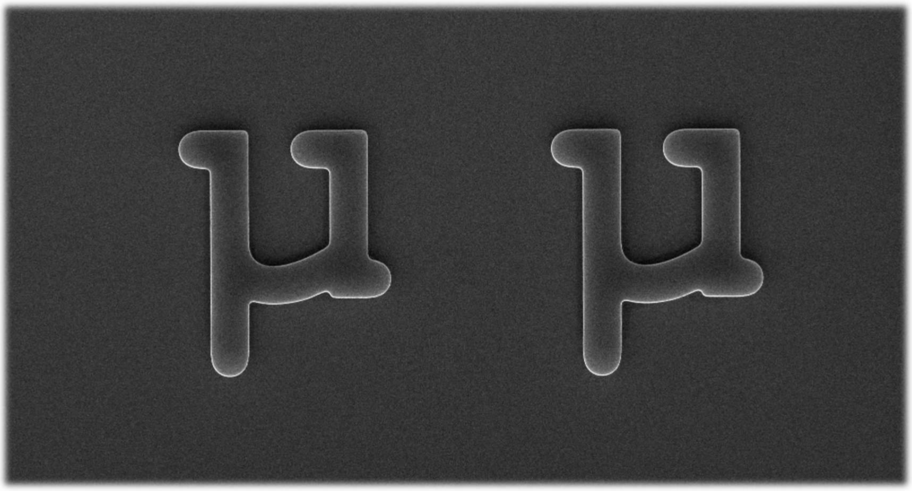

Dissemination activity

Peer-reviewed papers

Ghulinyan, Mher, Fernando Ramiro Manzano, Nikola Prtljaga, Martino Bernard, Lorenzo Pavesi, Georg Pucker, e Iacopo Carusotto. *Intermode Reactive Coupling Induced by Waveguide-Resonator Interaction.* Physical Review A 90, n. 5 (5 novembre 2014). doi:10.1103/PhysRevA.90.053811.

Stefan, L., M. Bernard, R. Guider, G. Pucker, L. Pavesi, e M. Ghulinyan. *Ultra-High-Q Thin-Silicon Nitride Strip-Loaded Ring Resonators.* Optics Letters 40, n. 14 (15 luglio 2015): 3316. doi:10.1364/OL.40.003316.

Borghi, M., M. Mancinelli, F. Merget, J. Witzens, M. Bernard, M. Ghulinyan, G. Pucker, e L. Pavesi. *High-Frequency Electro-Optic Measurement of Strained Silicon Racetrack Resonators.* Optics Letters 40, n. 22 (15 novembre 2015): 5287. doi:10.1364/OL.40.005287.

Ghulinyan, M., M. Bernard, R. Bartali, e G. Pucker. *Formation of Mach Angle Profiles during Wet Etching of Silica and Silicon Nitride Materials.* Applied Surface Science 359 (dicembre 2015): 67986. doi:10.1016/j.apsusc.2015.10.114.

Bisadi, Z., M. Mancinelli, S. Manna, S. Tondini, M. Bernard, A. Samusenko, M. Ghulinyan, et al. *Silicon Nanocrystals for Nonlinear Optics and Secure Communications: Silicon Nanocrystals for Nonlinear Optics and Secure Communications.* Physica Status Solidi (a) 212, n. 12 (dicembre 2015): 265971. doi:10.1002/pssa.201532528.

Manna, Santanu, Martino Bernard, Stefano Biasi, Fernando Ramiro Manzano, Mattia Mancinelli, Mher Ghulinyan, George Pucker, e Lorenzo Pavesi. *Stimulated Degenerate Four-Wave Mixing in Si Nanocrystal Waveguides.* Journal of Optics 18, n. 7 (2016): 075801. doi:10.1088/2040-8978/18/7/075801.

Borghi, Massimo, Mattia Mancinelli, Martino Bernard, Mher Ghulinyan, Georg Pucker, e Lorenzo Pavesi. *Homodyne Detection of Free Carrier Induced Electro-Optic Modulation in Strained Silicon Resonators.* Journal of Lightwave Technology 34, n. 24 (15 dicembre 2016): 565768. doi:10.1109/JLT.2016.2628183.

Bernard, Martino, Fernando Ramiro Manzano, Lorenzo Pavesi, Georg Pucker, Iacopo Carusotto, e Mher Ghulinyan. *Complete Crossing of Fano Resonances in an Optical Microcavity via Nonlinear Tuning.* Photonics Research 5, n. 3 (1 giugno 2017): 168. doi:10.1364/PRJ.5.000168

Proceedings

Franchi, Matteo, Davide Gandolfi, Luca Matteo Martini & al. *Proceedings of the event Industrial Problem Solving with Physics 2014.* Trento, 2014.
http://events.unitn.it/en/ipsp2014

Bernard, M., N. Prtljaga, G. Pucker, L. Pavesi, I. Carusotto, e M. Ghulinyan. *Off-diagonal photonic Lamb shift in reactively coupled waveguide-resonator system*, 952006, 2015. doi:10.1117/12.2178984.

Bernard, Martino, Stefano Tondini, Giuliano Zendri & al. *Proceedings of the event Industrial Problem Solving with Physics 2015.* Trento, 2015.
http://events.unitn.it/en/ipsp2015

Schools, Workshops and Conferences

On Light, Electrons, and Metamaterials, school, 3-5 December 2013, Trento (Italy).

Frontiers of Opto- and Electro-mechanics workshop, workshop, 27-30 January 2014, Fai della Paganella (Italy).

Training Course Comsol MultiPhysics Analisi elettromagnetiche in alta frequenza con Comsol Multiphysics, course, 10 February 2014, Sesto Fiorentino (Italy).

SiQuro Course on Silicon photonics, course within the SiQuro project 3-5 March 2014, Trento (Italy).

Industrial Problem Solving with Physics 2014, workshop, 21-26 July 2014, Trento (Italy)

SiQuro course on Microfabrication Techniques for Silicon Photonics, course within the project SiQuro, 9-10 September 2014, Trento (Italy).

NanotechItaly2014, conference, 28 November 2014, Venice (Italy).

Strongly correlated fluids of light and matter, school, 12-23 January 2015, Trento (Italy).

SPIE Micro technologies, conference, 3-6 May 2015, Barcelona, (Spain).

SiQuro Course on Quantum optics, course within the project SiQuro, 19-20 May 2015, Trento (Italy).

Industrial Problem Solving with Physics 2015, workshop, 20-25 July 2015, Trento (Italy). Organizer, member of the Scientific Committee, and editor of the proceedings.

SiQuro Course on Silicon Detectors, course within the project SiQuro, 16-17 September 2015, Trento (Italy).

SiQuro Course on Experimental Quantum Optics, course within the project SiQuro, 10-11 March 2016, Zurich (Swiss).

SiQuro course on Cryptography, course within the project SiQuro, 1-2 September 2016, Trento (Italy).

Appendices

Appendix A

process	Wafer				
	ki2A	ki2B	ki2B*	ki2C	ki2D
LPCVD Si_3N_4 140 nm	x				
LPCVD Si_3N_4 70 nm		x			
PECVD TEOS 70 nm,		x		x	x
Half wafer lithography		x	x		
Opt.Insp.		x	x		
Resist Hard Bake		x			
BHF oxide-etch			x		
Oxygen plasma			x		
Nitride etch			x		
BHF oxide-etch		x			
CHI2-Si stepper lithography	x	x	x	x	x
Opt.Insp.	x	x	x	x	x
Oxygen plasma "flash"	x	x	x	x	x
Resist Hard Bake	x	x	x	x	x
Tegal903 Etch TEOS				x	x
Tegal903 Etch Si_3N_4	x	x	x		
Tegal6510 Etch Si	x	x	x	x	x
Oxygen Plasma	x	x	x	x	x
BHF TEOS removal				x	x
LPCVD Si_3N_4 140 nm				x	
LPCVD Si_3N_4 70 nm					x
PECVD oxide 900 nm,	x	x	x	x	x
Sputter ALU 250 nm,	x	x	x	x	x
CHI2-Metal stepper lithography	x	x	x	x	x
Opt.Insp.	x	x	x	x	x
Resist Hard Bake	x	x	x	x	x
Oxygen plasma "flash"	x	x	x	x	x
Tegal6510 Al Etch	x	x	x	x	x
Oxygen Plasma	x	x	x	x	x
Opt.Insp	x	x	x	x	x

Table 4: Fabrication process followed for the realization of the Si_3N_4-stressed SOI racetrack resonators used to measure the $\chi^{(2)}$ in strained silicon The process is described in Sec. 4.2.2.

Appendix B

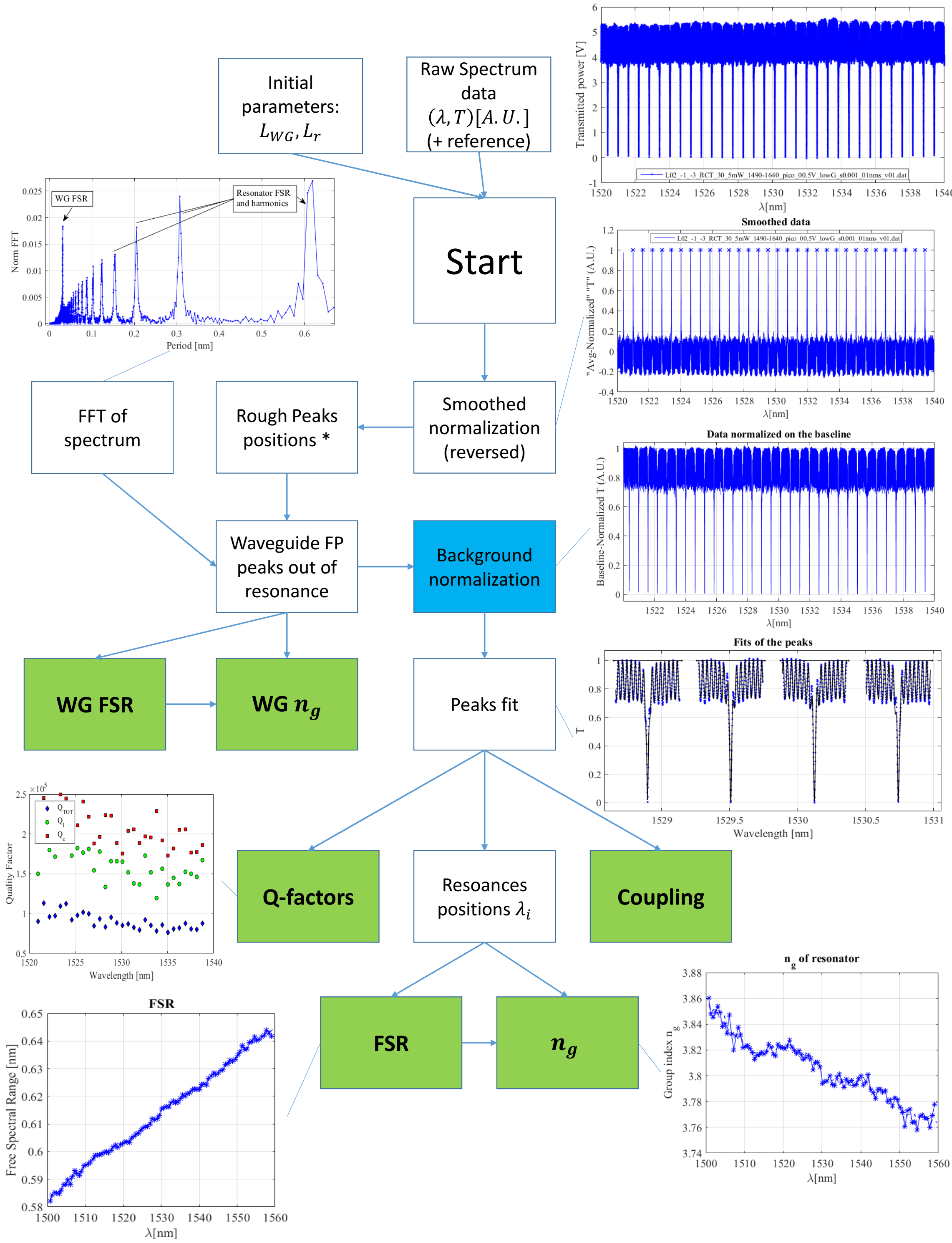

Figure 13: Flowchart of the "TrovaPicchi" resonator transmission analysis routine that was developed during this thesis work. This routine, with slight variations, has been used in Chapters 1, 2 and 4 to analyze the response of single-mode ring resonators.

Appendix C

Author	Year	Ref.	Tech	WG type	wg_w [nm]	wg_h [nm]	wg_e [nm]	Loss [dB/cm]
Lee	2001	[194]	UV 436 nm	strip	500	200	-	32
Lardenois**	2003	[195]	N.A.	rib	1000	380	70	0.4
Lardenois**	2003	[195]	N.A.	rib	1000	200	30	0.5
Vlasov	2004	[196]	e-beam	strip	445	220	-	3.4
Dumon	2004	[197]	DUV 248 nm	strip	500	220	-	2.4
Tsuchizawa	2005	[198]	e-beam	strip	400	200	-	2.8
Tsuchizawa	2006	[199]	e-beam	strip	480	200	-	2
Kuan	2009	[63]	e-beam	rib	1000	2500	1800	1.35
Kuan	2009	[63]	UV 365 nm	rib	1000	2500	1800	13.5
Cardenas*	2009	[58]	e-beam	"hill"	1500	80	-	0.3
Dong	2010	[200]	DUV	rib	2000	250	50	0.3
Bogaerts	2011	[62]	DUV 193 nm	strip	460	220	-	1.36
Bogaerts	2011	[62]	DUV 193 nm	rib	700	220	70	0.27
Bolten	2013	[201]	e-beam	rib	350	220	175	2.4
Lee	2015	[61]	UV 436 nm	strip	5000	340	-	0.9
Hagan**	2016	[202]	DUV 193 nm	strip	530	220	-	3.3
Hagan**	2016	[202]	DUV 193 nm	rib	560	220	170	1.9
SiQuro	2016	-	UV 365 nm	strip	400	240	-	5
SiQuro	2016	-	UV 365 nm	rib	550	500	200	1.7

Table 5: Propagation losses in SOI structures in the c-band, as reported in Fig. 1.23.
* The waveguide has no definite shape.
** Not in the c-band.

Author	Year	Ref.	wg_w [nm]	wg_h [nm]	Curv. Rad. [μm]	Q-factor Millions
Gondarenko	2009	[79]	900	644	20	0.24
Levy	2010	[203]	900	711	58	0.5
Bauters	2011	[89]	2800	80	4000	2.1
Foster	2011	[204]	1500	750	112	0.3
Tien	2011	[90]	2800	80	2000	7.0
Riemensberger	2012	[205]	1700	750	50	1.0
Li	2013	[206]	8000	400	240	20.0
Luke	2013	[81]	1800	910	115	7.0
Liu	2014	[207]	2000	550	100	1.0
Spancer	2014	[208]	11000	40	9650	81.0
Stefan (SiQuro NIR)	2015	[91]	2400	115	350	3.6
Stefan (SiQuro IR)	2015	[91]	2400	115	350	0.2
Xuan	2016	[209]	3000	600	100	17.0
Pfeiffer	2016	[210]	1500	1350	238	3.7
Ji	2016	[211]	10000	730	115	67.0

Table 6: Q-factor of Si_3N_4 resonators during the years. The values are also reported inf Fig. 2.29

Symbols and abbreviations

α	Propagation losses
β	Propagation constant
b_h	Slab height
$\chi^{(2)}$	Second-order electric susceptibility tensor
$\chi^{(3)}$	Third-order electric susceptibility tensor
c	Speed of light in vacuum
κ	Coupling coefficient
λ	Wavelength
L	Length of the cavity
l_h	Strip-load height
l_w	Strip-load width
M	Azimuthal mode number
n_{eff}	Effective refractive index
n_g	Group index
Q	Quality factor, figure of merit
t	Transmittance coefficient
T	Transmission coefficient
wg_h	Waveguide height
wg_r	Rib waveguide slab height
wg_w	Waveguide width

Table 5.7: Frequent symbols used in the thesis work.

AD	Add Drop filter
AOC	All-On-a-Chip
AP	All-Pass filter
BCB	Benzocyclobutene (bonding adhesive)
BHF	Buffered HydroFluoric acid
BOA	Booster Optical Amplifier
CMOS	Complementary Metal Oxide Semiconductor
CMP	Chemical Mechanical Polished
DC	Directional Coupler
DI	DeIonized
DRIE	Deep Reactive Ion Etching
DUV	Deep Ultra Violet (light)
EDFA	Erbium Doped Fiber Amplifier
ER	Etching Rate
FE	Field Enhancement factor
FP	Fabry-Perot
GVD	Group Velocity Dispersion
HM	Hard Mask
IC	Integrated Circuit
IPA	IsoPropyl Alcohol (Propan-2-ol)
LOC	Lab On a Chip
LPCVD	Low Pressure Chemical Vapour Deposition
MEMS	Micro-ElectroMechanical Systems
MQW	Multilayer Quantum Well
MZI	Mach Zehnder Interferometer
NIR	Near InfraRed
OSA	Optical Signal Analyzer
PECVD	Plasma Enhanced Chemical Vapour Deposition
PIC	Photonic Integrated Circuit
PML	Perfect Matched Layer
QRNG	Quantum Random Number Generator
RCA	Standard cleaning process for Silicon
RIE	Reactive Ion Etching
RIU	Refractive Index Unit
RMF	Radial Mode Family
SEM	Scanning Electron Microscope
SiNC	Silicon Nano-Crystals
SL	Strip-Loaded
SLM	Sagnac Loop Mirror
SOI	Silicon On Insulator
SPAD	Single Photon Avalanche Diode
TEOS	TetraEthyl OrthoSilicate (glass)
VASE	Variable Angle Spectroscopic Ellipsometer
VLSI	Very Large Scale Integration
VOA	Variable Optical Attenuator
WG	Waveguide
WGMR	Whispering Gallery Mode Resonator

Table 5.8: Acronyms and abbreviations used in the thesis work.

Bibliography

[1] http://events.unitn.it/en/siquro.

[2] Lorenzo Pavesi and G. Guillot, editors. *Optical interconnects: the silicon approach.* Number 119 in Springer series in optical sciences. Springer, Berlin ; New York, 2006.

[3] Ren-Jean Essiambre and Robert W. Tkach. Capacity Trends and Limits of Optical Communication Networks. *Proceedings of the IEEE*, 100(5):1035–1055, May 2012.

[4] Christoforos Kachris, Konstantinos Kanonakis, and Ioannis Tomkos. Optical interconnection networks in data centers: Recent trends and future challenges. *IEEE Communications Magazine*, 51(9):39–45, 2013.

[5] Christoforos Kachris, Keren Bergman, and Ioannis Tomkos, editors. *Optical Interconnects for Future Data Center Networks.* Optical Networks. Springer New York, New York, NY, 2013.

[6] Cisco global cloud index: Forecast and methodology 2012-2017. *White Paper*, 2013.

[7] Jiajia Chen, Yu Gong, Matteo Fiorani, and Slavisa Aleksic. Optical interconnects at the top of the rack for energy-efficient data centers. *IEEE Communications Magazine*, 53(8):140–148, 2015.

[8] The zettabyte era – trends and analysis. *CISCO White Paper*, 2016.

[9] Y.; Hosaka T.; Miyashita T. Miya, T.; Terunuma. Ultimate low-loss single-mode fibre at 1.55 m. *Electronics Letters*, 15, 1979.

[10] G. P. Agrawal. *Nonlinear fiber optics.* Elsevier/Academic Press, Amsterdam, fifth edition edition, 2013.

[11] Jean Louis Malinge. A view on the Silicon Photonics trends and Market prospective, July 2014.

[12] Ahmed Khaled. Adapted from `http://spectrum.ieee.org/image/MTk1MTMzOA`.

[13] http://www.cringely.com/wp-content/uploads/2013/10/642px-Moores_law_1970-2011.png.

[14] III Reliability Counts. Gordon E. Moore, Life Fellow, IEEE. *Readings in Computer Architecture*, page 56, 2000.

[15] Peter D. Griffin James D. Plummer, Michael Deal. *Silicon VLSI technology: fundamentals, practice, and modeling.* Prentice Hall, us ed edition, 2000.

[16] `http://www.itrs2.net/`.

[17] David AB Miller. Optical interconnects to electronic chips. *Applied Optics*, 49(25):F59–F70, 2010.

[18] Hazelwood Kim. http://www.cs.virginia.edu/kim/courses/cs3330/lec/cs3330-chap1-power.pdf, 2010.

[19] Zhaohui Li, Ivan Shubin, and Xiang Zhou. Optical interconnects: recent advances and future challenges. *Optics Express*, 23(3):3717, February 2015.

[20] Daoxin Dai and John E. Bowers. Silicon-based on-chip multiplexing technologies and devices for Peta-bit optical interconnects. *Nanophotonics*, 3(4-5), jan 2014.

[21] J.K. Doylend and A.P. Knights. The evolution of silicon photonics as an enabling technology for optical interconnection. *Laser & Photonics Reviews*, 6(4):504–525, July 2012.

[22] J.P. Soref, R.A.; Lorenzo. Single-crystal silicon: a new material for 1.3 and 1.6 m integrated-optical components. *Electronics Letters*, 21(21), 1985.

[23] A.; Schppert B.; Petermann K.; Burbach G. Schmidtchen, J.; Splett. Low loss singlemode optical waveguides with large cross-section in silicon-on-insulator. *Electronics Letters*, 27(16), 1991.

[24] B. N. Kurdi and D. G. Hall. Optical waveguides in oxygen-implanted buried-oxide silicon-on-insulator structures. *Optics letters*, 13(2):175–177, 1988.

[25] Winnie N. Ye and Yule Xiong. Review of silicon photonics: history and recent advances. *Journal of Modern Optics*, 60(16):1299–1320, September 2013.

[26] Gerhard Abstreiter. Engineering the future of electronics. *Physics World*, 5(3):36, 1992.

[27] Richard A. Soref. Silicon-based optoelectronics. *Proceedings of the IEEE*, 81(12):1687–1706, 1993.

[28] Richard Soref. The Past, Present, and Future of Silicon Photonics. *IEEE Journal of Selected Topics in Quantum Electronics*, 12(6):1678–1687, November 2006.

[29] Ed L. Wooten, Karl M. Kissa, Alfredo Yi-Yan, Edmond J. Murphy, Donald A. Lafaw, Peter F. Hallemeier, David Maack, Daniel V. Attanasio, Daniel J. Fritz, Gregory J. McBrien, and others. A review of lithium niobate modulators for fiber-optic communications systems. *IEEE Journal of selected topics in Quantum Electronics*, 6(1):69–82, 2000.

[30] Wim Bogaerts, Martin Fiers, and Pieter Dumon. Design challenges in silicon photonics. *IEEE Journal of Selected Topics in Quantum Electronics*, 20(4):1–8, 2014.

[31] William S. C Chang. *Fundamentals of guided-wave optoelectronic devices.* Cambridge University Press, Cambridge, 2010.

[32] Lukas Chrostowski and Michael Hochberg. *Silicon Photonics Design: From Devices to Systems*. Cambridge University Press, 2015.

[33] Minhao Pu, Liu Liu, Haiyan Ou, Kresten Yvind, and Jrn M. Hvam. Ultra-low-loss inverted taper coupler for silicon-on-insulator ridge waveguide. *Optics Communications*, 283(19):3678–3682, October 2010.

[34] Guanghui Ren, Shaowu Chen, Yongpeng Cheng, and Yao Zhai. Study on inverse taper based mode transformer for low loss coupling between silicon wire waveguide and lensed fiber. *Optics Communications*, 284(19):4782–4788, September 2011.

[35] Alfred Driessen, Douwe H. Geuzebroek, HJWM Hoekstra, Henry Kelderman, Edwin J. Klein, Dion JW Klunder, Chris GH Roeloffzen, Freddy S. Tan, Evgueni Krioukov, Cees Otto, and others. Microresonators as building blocks for VLSI photonics. In *AIP Conference Proceedings*, volume 709, pages 1–18. IOP Institute of Physics publishing LTD, 2004.

[36] Zhen Sheng, Liu Liu, Sailing He, Dries Van Thourhout, and Roel Baets. Silicon-on-insulator microring resonator for ultra dense WDM applications. In *Proceedings of IEEE Conference on Group IV Photonics (IEEE, 2009)*, pages 122–124, 2009.

[37] Wim Bogaerts, Peter De Heyn, Thomas Van Vaerenbergh, Katrien De Vos, Shankar Kumar Selvaraja, Tom Claes, Pieter Dumon, Peter Bienstman, Dries Van Thourhout, and Roel Baets. Silicon microring resonators. *Laser & Photonics Reviews*, 6(1):47–73, 2012.

[38] Amnon Yariv. Critical coupling and its control in optical waveguide-ring resonator systems. *IEEE Photonics Technology Letters*, 14(4):483–485, 2002.

[39] D. G. Rabus. *Integrated ring resonators: the compendium*. Number 127 in Springer series in optical sciences. Springer, Berlin, 2007.

[40] H.G. Tompkins and W.A. McGahan. *Spectroscopic Ellipsometry and Reflectometry: A User's Guide*. Wiley, 1999.

[41] Yenista Tunics T100S. https://yenista.com/IMG/pdf/TUNICS-T100S_DS_201204-2.pdf.

[42] Rodolfo E. Camacho-Aguilera, Yan Cai, Neil Patel, Jonathan T. Bessette, Marco Romagnoli, Lionel C. Kimerling, and Jurgen Michel. An electrically pumped germanium laser. *Optics express*, 20(10):11316–11320, 2012.

[43] Jifeng Liu, Xiaochen Sun, Rodolfo Camacho-Aguilera, Lionel C. Kimerling, and Jurgen Michel. Ge-on-Si laser operating at room temperature. *Optics letters*, 35(5):679–681, 2010.

[44] Alexander W. Fang, Hyundai Park, Ying-hao Kuo, Richard Jones, Oded Cohen, Di Liang, Omri Raday, Matthew N. Sysak, Mario J. Paniccia, and John E. Bowers. Hybrid silicon evanescent devices. *Materials today*, 10(7):28–35, 2007.

[45] Gnther Roelkens, Joris Van Campenhout, Joost Brouckaert, Dries Van Thourhout, Roel Baets, P. Rojo Romeo, P. Regreny, A. Kazmierczak, C. Seassal, X. Letartre, and others. III-V/Si photonics by die-to-wafer bonding. *Materials Today*, 10(7):36–43, 2007.

[46] Damien Bordel, Maxime Argoud, Emmanuel Augendre, Julie Harduin, Paul Philippe, Nicolas Olivier, Sonia Messaoudne, Karen Gilbert, Philippe Grosse, Badhise Ben Bakir, and Jean-Marc Fedeli. Direct and Polymer Bonding of III-V to Processed Silicon-On-Insulator for Hybrid Silicon Evanescent Lasers Fabrication. pages 403–410, 2010.

[47] Hyundai Park, Matthew N. Sysak, Hui-Wen Chen, Alexander W. Fang, Di Liang, Ling Liao, Brian R. Koch, Jock Bovington, Yongbo Tang, Kristi Wong, Matt Jacob-Mitos, Richard Jones, and John E. Bowers. Device and Integration Technology for Silicon Photonic Transmitters. *IEEE Journal of Selected Topics in Quantum Electronics*, 17(3):671–688, May 2011.

[48] S. Keyvaninia, S. Verstuyft, L. Van Landschoot, F. Lelarge, G.-H. Duan, S. Messaoudene, J. M. Fedeli, T. De Vries, B. Smalbrugge, E. J. Geluk, J. Bolk, M. Smit, G. Morthier, D. Van Thourhout, and G. Roelkens. Heterogeneously integrated III-V/silicon distributed feedback lasers. *Optics Letters*, 38(24):5434, December 2013.

[49] Guang-Hua Duan, Christophe Jany, Alban Le Liepvre, Alain Accard, Marco Lamponi, Dalila Make, Peter Kaspar, Guillaume Levaufre, Nils Girard, Francois Lelarge, Jean-Marc Fedeli, Antoine Descos, Badhise Ben Bakir, Sonia Messaoudene, Damien Bordel, Sylvie Menezo, Guilhem de Valicourt, Shahram Keyvaninia, Gunter Roelkens, Dries Van Thourhout, David J. Thomson, Frederic Y. Gardes, and Graham T. Reed. Hybrid III–V on Silicon Lasers for Photonic Integrated Circuits on Silicon. *IEEE Journal of Selected Topics in Quantum Electronics*, 20(4):158–170, July 2014.

[50] Soren Dhoore, Lianyan Li, Amin Abbasi, Gunther Roelkens, and Geert Morthier. Demonstration of a Discretely Tunable III-V-on-Silicon Sampled Grating DFB Laser. *IEEE Photonics Technology Letters*, 28(21):2343–2346, November 2016.

[51] J.-M. Fedeli, B. Ben Bakir, N. Olivier, Ph. Grosse, L. Grenouillet, E. Augendre, P. Phillippe, K. Gilbert, D. Bordel, and J. Harduin. InP on SOI devices for optical communication and optical network on chip. page 79420O, February 2011.

[52] Gnther Roelkens, Dries Van Thourhout, Roel Baets, R. Ntzel, and Meint Smit. Laser emission and photodetection in an InP/InGaAsP layer integrated on and coupled to a Silicon-on-Insulator waveguide circuit. *Optics express*, 14(18):8154–8159, 2006.

[53] M. Lamponi, S. Keyvaninia, C. Jany, F. Poingt, F. Lelarge, G. de Valicourt, G. Roelkens, D. Van Thourhout, S. Messaoudene, J.-M. Fedeli, and G. H. Duan. Low-Threshold Heterogeneously Integrated InP/SOI Lasers With a Double Adiabatic Taper Coupler. *IEEE Photonics Technology Letters*, 24(1):76–78, January 2012.

[54] III-V lab. `http://www.3-5lab.fr/`.

[55] Yunan Zheng, Doris Keh-Ting Ng, Yongqiang Wei, Wang Yadong, Yingyan Huang, Yongming Tu, Chee-Wei Lee, Boyang Liu, and Seng-Tiong Ho. Electrically pumped heterogeneously integrated Si/III-V evanescent lasers with micro-loop mirror reflector. *Applied Physics Letters*, 99(1):011103, 2011.

[56] Yi Zhang, Shuyu Yang, Hang Guan, Andy Eu-Jin Lim, Guo-Qiang Lo, Peter Magill, Tom Baehr-Jones, and Michael Hochberg. Sagnac loop mirror and micro-ring based laser cavity for silicon-on-insulator. *Optics Express*, 22(15):17872, July 2014.

[57] COMSOL. `https://www.comsol.it/`.

[58] Jaime Cardenas, Carl B. Poitras, Jacob T. Robinson, Kyle Preston, Long Chen, and Michal Lipson. Low loss etchless silicon photonic waveguides. *Optics express*, 17(6):4752–4757, 2009.

[59] D.K. Sparacin, S.J. Spector, and L.C. Kimerling. Silicon waveguide sidewall smoothing by wet chemical oxidation. *Journal of Lightwave Technology*, 23(8):2455–2461, August 2005.

[60] Werner Kern. The evolution of silicon wafer cleaning technology. *Journal of the Electrochemical Society*, 137(6):1887–1892, 1990.

[61] Dong Ho Lee, Sung Joong Choo, Uiseok Jung, Kyung Woon Lee, Kwang Woong Kim, and Jung Ho Park. Low-loss silicon waveguides with sidewall roughness reduction using a SiO_2 hard mask and fluorine-based dry etching. *Journal of Micromechanics and Microengineering*, 25(1):015003, January 2015.

[62] W Bogaerts and S K Selvaraja. Compact Single-Mode Silicon Hybrid Rib/Strip Waveguide With Adiabatic Bends. *IEEE Photonics Journal*, 3(3):422–432, June 2011.

[63] Kuan Pei Yap, A. Delage, J. Lapointe, B. Lamontagne, J.H. Schmid, P. Waldron, B.A. Syrett, and S. Janz. Correlation of Scattering Loss, Sidewall Roughness and Waveguide Width in Silicon-on-Insulator (SOI) Ridge Waveguides. *Journal of Lightwave Technology*, 27(18):3999–4008, September 2009.

[64] Gnther Roelkens, B. Bataillou, Joost Brouckaert, Frederik Van Laere, Dries Van Thourhout, and Roel Baets. Adhesive bonding of III-V dies to processed SOI using BCB for photonic applications. In *210th ECS Meeting*, volume 3, pages 321–326, 2006.

[65] Marco Lamponi. *Hybrid III-V on silicon lasers for telecommunication applications*. Theses, Universit Paris Sud - Paris XI, March 2012.

[66] Kerry J. Vahala. Optical microcavities. *Nature*, 424(6950):839–846, 2003.

[67] V.B. Braginsky; M.L. Gorodetsky; V.S. Ilchenko. Quality-factor and nonlinear properties of optical whispering-gallery modes. *Physics Letters A*, 137, 1989.

[68] A. A.; Ilchenko V. S. Gorodetsky, M. L.; Savchenkov. Ultimate Q of optical microsphere resonators. *Optics Letters*, 21(7), 1996.

[69] T. J.; Spillane S. M.; Vahala K. J. Armani, D. K.; Kippenberg. Ultra-high-Q toroid microcavity on a chip. *Nature*, 421(6926), 2003.

[70] M. J. Thorpe. Broadband Cavity Ringdown Spectroscopy for Sensitive and Rapid Molecular Detection. *Science*, 311(5767), 2006.

[71] Jiangang Zhu, Sahin Kaya Ozdemir, Yun-Feng Xiao, Lin Li, Lina He, Da-Ren Chen, and Lan Yang. On-chip single nanoparticle detection and sizing by

mode splitting in an ultrahigh-Q microresonator. *Nature Photonics*, 4(1):46–49, January 2010.

[72] T. J. Kippenberg, R. Holzwarth, and S. A. Diddams. Microresonator-Based Optical Frequency Combs. *Science*, 332(6029):555–559, April 2011.

[73] Alessia Pasquazi, Lucia Caspani, Marco Peccianti, Matteo Clerici, Marcello Ferrera, Luca Razzari, David Duchesne, Brent E. Little, Sai T. Chu, David J. Moss, and Roberto Morandotti. Self-locked optical parametric oscillation in a CMOS compatible microring resonator: a route to robust optical frequency comb generation on a chip. *Optics Express*, 21(11):13333, June 2013.

[74] Carlos A.; Panepucci Roberto R.; Lipson Michal Almeida, Vilson R.; Barrios. All-optical control of light on a silicon chip. *Nature*, 431(7012), 2004.

[75] Lian-Wee Luo, Noam Ophir, Christine P. Chen, Lucas H. Gabrielli, Carl B. Poitras, Keren Bergmen, and Michal Lipson. WDM-compatible mode-division multiplexing on a silicon chip. *Nature Communications*, 5, January 2014.

[76] H. Rokhsari and K. J. Vahala. Ultralow Loss, High Q , Four Port Resonant Couplers for Quantum Optics and Photonics. *Physical Review Letters*, 92(25), June 2004.

[77] Davide Grassani, Stefano Azzini, Marco Liscidini, Matteo Galli, Michael J. Strain, Marc Sorel, J. E. Sipe, and Daniele Bajoni. Micrometer-scale integrated silicon source of time-energy entangled photons. *Optica*, 2(2):88, February 2015.

[78] Hansuek Lee, Tong Chen, Jiang Li, Ki Youl Yang, Seokmin Jeon, Oskar Painter, and Kerry J. Vahala. Chemically etched ultrahigh-Q wedge-resonator on a silicon chip. *Nature Photonics*, 6(6):369–373, May 2012.

[79] Alexander Gondarenko, Jacob S. Levy, and Michal Lipson. High confinement micron-scale silicon nitride high Q ring resonator. *Optics express*, 17(14):11366–11370, 2009.

[80] Fernando Ramiro-Manzano, Nikola Prtljaga, Lorenzo Pavesi, Georg Pucker, and Mher Ghulinyan. A fully integrated high-Q whispering-gallery wedge resonator. *Optics express*, 20(20):22934–22942, 2012.

[81] Kevin Luke, Avik Dutt, Carl B. Poitras, and Michal Lipson. Overcoming Si_3n_4 film stress limitations for high quality factor ring resonators. *Optics Express*, 21(19):22829, September 2013.

[82] Gustavo S.; Cardenas Jaime; Poitras Carl; Lipson Michal Luo, Lian-Wee; Wiederhecker. High quality factor etchless silicon photonic ring resonators. *Optics Express*, 19(7), 2011.

[83] Austin Griffith, Jaime Cardenas, Carl B. Poitras, and Michal Lipson. High quality factor and high confinement silicon resonators using etchless process. *Optics express*, 20(19):21341–21345, 2012.

[84] V. Ramaswamy. Strip-Loaded Film Waveguide. *Bell System Technical Journal*, 53(4):697–704, 1974.

[85] F. P. Payne and J. P. R. Lacey. A theoretical analysis of scattering loss from planar optical waveguides. *Optical and Quantum Electronics*, 26(10):977–986, 1994.

[86] Davide Gandolfi. *On-chip photonic label-free biosensors*. phd, University of Trento, Trento, March 2015.

[87] E. A. J. Marcatili. Bends in Optical Dielectric Guides. *Bell System Technical Journal*, 48(7), 1969.

[88] Lucio Stefan. Ultra-high quality factor strip-loaded resonators. Master degree, Universit degli studi di Trento, Trento, 2014.

[89] Martijn J. R.; John Demis; Dai Daoxin; Tien Ming-Chun; Barton Jonathon S.; Leinse Arne; Heideman Ren G.; Blumenthal Daniel J.; Bowers John E. Bauters, Jared F.; Heck. Ultra-low-loss high-aspect-ratio Si_3n_4 waveguides. *Optics Express*, 19(4), 2011.

[90] Ming-Chun Tien, Jared F. Bauters, Martijn JR Heck, Daryl T. Spencer, Daniel J. Blumenthal, and John E. Bowers. Ultra-high quality factor planar Si 3 N 4 ring resonators on Si substrates. *Optics express*, 19(14):13551–13556, 2011.

[91] L. Stefan, M. Bernard, R. Guider, G. Pucker, L. Pavesi, and M. Ghulinyan. Ultra-high-Q thin-silicon nitride strip-loaded ring resonators. *Optics Letters*, 40(14):3316, July 2015.

[92] Francesco Petruccione Heinz-Peter Breuer. *The theory of open quantum systems*. Oxford University Press, 2002.

[93] Eric S.; Kleppner Daniel Hulet, Randall G.; Hilfer. Inhibited Spontaneous Emission by a Rydberg Atom. *Physical Review Letters*, 55(20), 1985.

[94] Eli Yablonovitch. Inhibited spontaneous emission in solid-state physics and electronics. *Physical review letters*, 58(20):2059, 1987.

[95] Peter Lodahl, A. Floris Van Driel, Ivan S. Nikolaev, Arie Irman, Karin Overgaag, Danil Vanmaekelbergh, and Willem L. Vos. Controlling the dynamics of spontaneous emission from quantum dots by photonic crystals. *Nature*, 430(7000):654–657, 2004.

[96] Willis E. Lamb Jr and Robert C. Retherford. Fine structure of the hydrogen atom by a microwave method. *Physical Review*, 72(3):241, 1947.

[97] I. S.; Schawlow A. L. Hnsch, T. W.; Shahin. Optical Resolution of the Lamb Shift in Atomic Hydrogen by Laser Saturation Spectroscopy. *Nature Physical Science*, 235(56), 1972.

[98] A. Lempicki, L. Andrews, S. J. Nettel, B. C. McCollum, and E. I. Solomon. Spectroscopy of Cr 3+ in Glasses: Fano Antiresonances and Vibronic" Lamb Shift". *Physical Review Letters*, 44(18):1234, 1980.

[99] GAML Alzetta, A. Gozzini, L. Moi, and G. Orriols. An experimental method for the observation of rf transitions and laser beat resonances in oriented Na vapour. *Il Nuovo Cimento B (1971-1996)*, 36(1):5–20, 1976.

[100] E. Arimondo. Coherent population trapping in laser spectroscopy. In E. Wolf, editor, *Progress in Optics*, volume 35, pages 257–354. Elsevier, Amsterdam, 1996.

[101] A.; Harris S. E. Boller, K.-J.; Imamolu. Observation of electromagnetically induced transparency. *Physical Review Letters*, 66(20), 1991.

[102] Michael Fleischhauer, Atac Imamoglu, and Jonathan P. Marangos. Electromagnetically induced transparency: Optics in coherent media. *Reviews of modern physics*, 77(2):633, 2005.

[103] D. Brunner, B. D. Gerardot, P. A. Dalgarno, G. Wust, K. Karrai, N. G. Stoltz, P. M. Petroff, and R. J. Warburton. A Coherent Single-Hole Spin in a Semiconductor. *Science*, 325(5936):70–72, July 2009.

[104] S. Rotter, F. Libisch, J. Burgdrfer, U. Kuhl, and H.-J. Stckmann. Tunable Fano resonances in transport through microwave billiards. *Physical Review E*, 69(4), April 2004.

[105] M. Mendoza and P. A. Schulz. Imaging and switching of Fano resonances in open quantum cavities. *Physical Review B*, 71(24), June 2005.

[106] Andrey E. Miroshnichenko, Sergej Flach, and Yuri S. Kivshar. Fano resonances in nanoscale structures. *Reviews of Modern Physics*, 82(3):2257–2298, August 2010.

[107] L. Maleki, A. B. Matsko, A. A. Savchenkov, and V. S. Ilchenko. Tunable delay line with interacting whispering-gallery-mode resonators. *Optics letters*, 29(6):626–628, 2004.

[108] Qianfan Xu, Sunil Sandhu, Michelle L. Povinelli, Jagat Shakya, Shanhui Fan, and Michal Lipson. Experimental Realization of an On-Chip All-Optical Analogue to Electromagnetically Induced Transparency. *Physical Review Letters*, 96(12), March 2006.

[109] Yun-Feng Xiao, Lina He, Jiangang Zhu, and Lan Yang. Electromagnetically induced transparency-like effect in a single polydimethylsiloxane-coated silica microtoroid. *Applied Physics Letters*, 94(23):231115, June 2009.

[110] Chun-Hua Dong, Chang-Ling Zou, Yun-Feng Xiao, Jin-Ming Cui, Zheng-Fu Han, and Guang-Can Guo. Modified transmission spectrum induced by two-mode interference in a single silica microsphere. *Journal of Physics B: Atomic, Molecular and Optical Physics*, 42(21):215401, November 2009.

[111] Bei-Bei Li, Yun-Feng Xiao, Chang-Ling Zou, Yong-Chun Liu, Xue-Feng Jiang, You-Ling Chen, Yan Li, and Qihuang Gong. Experimental observation of Fano resonance in a single whispering-gallery microresonator. *Applied Physics Letters*, 98(2):021116, January 2011.

[112] Jianqiang Gu, Ranjan Singh, Xiaojun Liu, Xueqian Zhang, Yingfang Ma, Shuang Zhang, Stefan A. Maier, Zhen Tian, Abul K. Azad, Hou-Tong Chen, Antoinette J. Taylor, Jiaguang Han, and Weili Zhang. Active control of electromagnetically induced transparency analogue in terahertz metamaterials. *Nature Communications*, 3:1151, October 2012.

[113] Qingzhong Huang, Zhan Shu, Ge Song, Juguang Chen, Jinsong Xia, and Jinzhong Yu. Electromagnetically induced transparency-like effect in a two-bus waveguides coupled microdisk resonator. *Optics Express*, 22(3):3219, February 2014.

[114] S. Weis, R. Riviere, S. Deleglise, E. Gavartin, O. Arcizet, A. Schliesser, and T. J. Kippenberg. Optomechanically Induced Transparency. *Science*, 330(6010):1520–1523, December 2010.

[115] Andrey B . Matsko. *Practical Applications of Microresonators in Optics and Photonics*. CRC Press 2009, 2009.

[116] D.L. Lee. *Electromagnetic Principles of Integrated Optics*. Wiley, 1986.

[117] Amnon Yariv. Universal relations for coupling of optical power between microresonators and dielectric waveguides. *Electronics letters*, 36(4):321–322, 2000.

[118] M. Ghulinyan, F. Ramiro Manzano, N. Prtljaga, M. Bernard, L. Pavesi, G. Pucker, and I. Carusotto. Intermode reactive coupling induced by waveguide-resonator interaction. *Phys. Rev. A*, 90:053811, 2014.

[119] D. F. Walls and G. J. Milburn. *Quantum Optics*. Springer, 1994.

[120] U. Fano. Effects of configuration interaction on intensities and phase shifts. *Phys. Rev.*, 124:1866–1878, Dec 1961.

[121] C.Cohen-Tannoudji, J.Dupont-Roc, and G.Grynberg. *Processus d'interaction entre photons et atomes*. InterEditions and Editions du CNRS, 1988.

[122] Andrey E. Miroshnichenko, Sergej Flach, and Yuri S. Kivshar. Fano resonances in nanoscale structures. *Reviews of Modern Physics*, 82(3):2257–2298, August 2010.

[123] Giora Griffel. Vernier effect in asymmetrical ring resonator arrays. *IEEE Photonics Technology Letters*, 12(12):1642–1644, 2000.

[124] Po Dong, Wei Qian, Hong Liang, Roshanak Shafiiha, Ning-Ning Feng, Dazeng Feng, Xuezhe Zheng, Ashok V Krishnamoorthy, and Mehdi Asghari. Low power and compact reconfigurable multiplexing devices based on silicon microring resonators. *Optics express*, 18(10):9852–9858, 2010.

[125] Tryggve Bk. Thermal coefficient of refractive index of optical glasses. *Journal of the Optical Society of America*, 59, 1969.

[126] Y. Henry Wen, Onur Kuzucu, Moti Fridman, Alexander L. Gaeta, Lian-Wee Luo, and Michal Lipson. All-Optical Control of an Individual Resonance in a Silicon Microresonator. *Physical Review Letters*, 108(22), June 2012.

[127] F. Ramiro-Manzano, N. Prtljaga, L. Pavesi, G. Pucker, and M. Ghulinyan. Thermo-optical bistability with Si nanocrystals in a whispering gallery mode resonator. *Optics Letters*, 38(18):3562, September 2013.

[128] Y. Henry Wen, Onur Kuzucu, Taige Hou, Michal Lipson, and Alexander L. Gaeta. All-optical switching of a single resonance in silicon ring resonators. *Optics letters*, 36(8):1413–1415, 2011.

[129] Y. Henry Wen, Onur Kuzucu, Moti Fridman, Alexander L. Gaeta, Lian-Wee Luo, and Michal Lipson. All-Optical Control of an Individual Resonance in a Silicon Microresonator. *Physical Review Letters*, 108(22), June 2012.

[130] Martino Bernard, Fernando Ramiro Manzano, Lorenzo Pavesi, George Pucker, Iacopo Carusotto, and Mher Ghulinyan. Complete crossing of Fano res-

onances in an optical microcavity via nonlinear tuning. *arXiv preprint arXiv:1701.06332*, 2017.

[131] Malvin Carl Teich Bahaa E. A. Saleh. *Fundamentals of photonics*. Wiley series in pure and applied optics. Wiley, 1st edition, 1991.

[132] Lorenzo Pavesi and David J. Lockwood, editors. *Silicon photonics I*. Number v. 94 in Topics in applied physics. Springer, Berlin ; New York, 2004.

[133] Boyd R.W. *Nonlinear Optics*. AP, 3ed. edition, 2008.

[134] G. T. Reed, G. Mashanovich, F. Y. Gardes, and D. J. Thomson. Silicon optical modulators. *Nature Photonics*, 4(8):518–526, August 2010.

[135] Richard; Liao Ling; Samara-Rubio Dean; Rubin Doron; Cohen Oded; Nicolaescu Remus; Paniccia Mario Liu, Ansheng; Jones. A high-speed silicon optical modulator based on a metaloxidesemiconductor capacitor. *Nature*, 427(6975), 2004.

[136] Qianfan Xu, Bradley Schmidt, Sameer Pradhan, and Michal Lipson. Micrometre-scale silicon electro-optic modulator. *Nature*, 435(7040):325–327, May 2005.

[137] Melissa Ziebell, Delphine Marris-Morini, Gilles Rasigade, Jean-Marc Fdli, Paul Crozat, Eric Cassan, David Bouville, and Laurent Vivien. 40 Gbit/s low-loss silicon optical modulator based on a pipin diode. *Optics express*, 20(10):10591–10596, 2012.

[138] J. Leuthold, C. Koos, and W. Freude. Nonlinear silicon photonics. *Nature Photonics*, 4(8):535–544, August 2010.

[139] Rune S. Jacobsen, Karin N. Andersen, Peter I. Borel, Jacob Fage-Pedersen, Lars H. Frandsen, Ole Hansen, Martin Kristensen, Andrei V. Lavrinenko, Gaid Moulin, Haiyan Ou, Christophe Peucheret, Beta Zsigri, and Anders Bjarklev. Strained silicon as a new electro-optic material. *Nature*, 441(7090):199–202, May 2006.

[140] Bartos Chmielak, Michael Waldow, Christopher Matheisen, Christian Ripperda, Jens Bolten, Thorsten Wahlbrink, Michael Nagel, Florian Merget, and Heinrich Kurz. Pockels effect based fully integrated, strained silicon electro-optic modulator. *Optics express*, 19(18):17212–17219, 2011.

[141] M. Cazzanelli, F. Bianco, E. Borga, G. Pucker, M. Ghulinyan, E. Degoli, E. Luppi, V. Vniard, S. Ossicini, D. Modotto, S. Wabnitz, R. Pierobon, and L. Pavesi. Second-harmonic generation in silicon waveguides strained by silicon nitride. *Nature Materials*, 11(2):148–154, December 2011.

[142] F Bianco, K Fedus, F Enrichi, R Pierobon, M Cazzanelli, M Ghulinyan, G Pucker, and L Pavesi. Two-dimensional micro-Raman mapping of stress and strain distributions in strained silicon waveguides. *Semiconductor Science and Technology*, 27(8):085009, August 2012.

[143] Pedro Damas, Xavier Le Roux, David Le Bourdais, Eric Cassan, Delphine Marris-Morini, Nicolas Izard, Thomas Maroutian, Philippe Lecoeur, and Laurent Vivien. Wavelength dependence of Pockels effect in strained silicon waveguides. *Optics Express*, 22(18):22095, September 2014.

[144] M. Borghi, M. Mancinelli, F. Merget, J. Witzens, M. Bernard, M. Ghulinyan, G. Pucker, and L. Pavesi. High-frequency electro-optic measurement of strained silicon racetrack resonators. *Optics Letters*, 40(22):5287, November 2015.

[145] Massimo Borghi. *Linear, nonlinear and quantum optics in Silicon Photonics*. phd, University of Trento, March 2016.

[146] Santanu Manna, Martino Bernard, Stefano Biasi, Fernando Ramiro Manzano, Mattia Mancinelli, Mher Ghulinyan, George Pucker, and Lorenzo Pavesi. Stimulated degenerate four-wave mixing in Si nanocrystal waveguides. *Journal of Optics*, 18(7):075801, 2016.

[147] S. Sharif Azadeh, F. Merget, M. P. Nezhad, and J. Witzens. On the measurement of the Pockels effect in strained silicon. *Optics Letters*, 40(8):1877, April 2015.

[148] Rajat Sharma, Matthew W. Puckett, Hung-Hsi Lin, Felipe Vallini, and Yeshaiahu Fainman. Characterizing the effects of free carriers in fully etched, dielectric-clad silicon waveguides. *Applied Physics Letters*, 106(24):241104, June 2015.

[149] Rajat Sharma, Matthew W. Puckett, Hung-Hsi Lin, Andrei Isichenko, Felipe Vallini, and Yeshaiahu Fainman. Effect of dielectric claddings on the electro-optic behavior of silicon waveguides. *Optics Letters*, 41(6):1185, March 2016.

[150] C. L. Manganelli, P. Pintus, and C. Bonati. Modeling of strain-induced Pockels effect in Silicon. *Optics Express*, 23(22):28649, November 2015.

[151] Pedro Damas, Delphine Marris-Morini, Eric Cassan, and Laurent Vivien. Bond orbital description of the strain-induced second-order optical susceptibility in silicon. *Physical Review B*, 93(16), April 2016.

[152] Richard A. Soref. Nonlinear refractive index of IVIV compound semiconductors. *Applied optics*, 31(23):4627–4629, 1992.

[153] Bartos Chmielak, Christopher Matheisen, Christian Ripperda, Jens Bolten, Thorsten Wahlbrink, Michael Waldow, and Heinrich Kurz. Investigation of local strain distribution and linear electro-optic effect in strained silicon waveguides. *Optics Express*, 21(21):25324, October 2013.

[154] Matthew W. Puckett, Joseph S. T. Smalley, Maxim Abashin, Andrew Grieco, and Yeshaiahu Fainman. Tensor of the second-order nonlinear susceptibility in asymmetrically strained silicon waveguides: analysis and experimental validation. *Optics Letters*, 39(6):1693, March 2014.

[155] Massimo Cazzanelli and Joerg Schilling. Second order optical nonlinearity in silicon by symmetry breaking. *Applied Physics Reviews*, 3(1):011104, March 2016.

[156] Graham T. Reed and Andrew P. Knights. *Silicon photonics: an introduction*. John Wiley, Chichester ; Hoboken, NJ, 2004.

[157] Marco Masi, Rgis Orobtchouk, Guofang Fan, Jean-Marc Fedeli, and Lorenzo Pavesi. Towards a Realistic Modelling of Ultra-Compact Racetrack Resonators. *Journal of Lightwave Technology*, November 2010.

[158] G. G. Stoney. The Tension of Metallic Films Deposited by Electrolysis. *Proceedings of the Royal Society A: Mathematical, Physical and Engineering Sciences*, 82(553):172–175, May 1909.

[159] Wouter J. Westerveld, Suzanne M. Leinders, Pim M. Muilwijk, Jose Pozo, Teun C. van den Dool, Martin D. Verweij, Mirvais Yousefi, and H. Paul Urbach. Characterization of Integrated Optical Strain Sensors Based on Silicon Waveguides. *IEEE Journal of Selected Topics in Quantum Electronics*, 20(4):101–110, July 2014.

[160] Massimo Borghi, Mattia Mancinelli, Martino Bernard, Mher Ghulinyan, Georg Pucker, and Lorenzo Pavesi. Homodyne Detection of Free Carrier Induced Electro-Optic Modulation in Strained Silicon Resonators. *Journal of Lightwave Technology*, 34(24):5657–5668, December 2016.

[161] Richard Soref and Brian Bennett. Electrooptical effects in silicon. *IEEE journal of quantum electronics*, 23(1):123–129, 1987.

[162] S. V. Govorkov, V. I. EmelYanov, N. I. Koroteev, G. I. Petrov, I. L. Shumay, and V. V. Yakovlev. Inhomogeneous deformation of silicon surface layers probed by second-harmonic generation in reflection. *JOSA B*, 6(6):1117–1124, 1989.

[163] Clemens Schriever, Federica Bianco, Massimo Cazzanelli, Mher Ghulinyan, Christian Eisenschmidt, Johannes de Boor, Alexander Schmid, Johannes Heitmann, Lorenzo Pavesi, and Jrg Schilling. Second-Order Optical Nonlinearity in Silicon Waveguides: Inhomogeneous Stress and Interfaces. *Advanced Optical Materials*, 3(1):129–136, January 2015.

[164] Z. Bisadi, M. Mancinelli, S. Manna, S. Tondini, M. Bernard, A. Samusenko, M. Ghulinyan, G. Fontana, P. Bettotti, F. Ramiro-Manzano, G. Pucker, and L. Pavesi. Silicon nanocrystals for nonlinear optics and secure communications: Silicon nanocrystals for nonlinear optics and secure communications. *physica status solidi (a)*, 212(12):2659–2671, December 2015.

[165] E. Timurdogan, C. V. Poulton, M. J. Byrd, and M. R. Watts. Electric field-induced second-order nonlinear optical effects in silicon waveguides. *Nature Photonics*, 11(3):200–206, February 2017.

[166] Richard N. Tauber Stanley Wolf. *Silicon Processing for the VLSI Era: Process Technology*, volume Vol. 1. Lattice Press, 2nd edition, 1999.

[167] T. Ohmi, editor. *Scientific Wet Process Technology for Innovative LSI/FPD Manufacturing*. CRC Press, 2006.

[168] A. Grosse, M. Grewe, and H. Fouckhardt. Deep wet etching of fused silica glass for hollow capillary optical leaky waveguides in microfluidic devices. *J. Micromech. Microeng.*, 11:257–262, 2001.

[169] D. J. Monk, D. S. Soane, and R. T. Howe. A review of the chemical reaction mechanism and kinetics for hydrofluoric acid etching of silicon dioxide for surface micromachining applications. *Thin Solid Films*, 232:1–12, 1993.

[170] J. Bhler, F.-P. Steiner, and H. Baltes. Silicon dioxide sacrificial layer etching in surface micromachining. *J. Micromech. Microeng.*, 7:R1–R13, 1997.

[171] T. J. Kippenberg, S. M. Spillane, D. K. Armani, and K. J. Vahala. Fabrication and coupling to planar high-Q silica disk microcavities. *Appl. Phys. Lett.*, 83:797–799, 2003.

[172] R. A. Haken, I. M. Baker, and J. D. E. Beynon. An investigation into the dependence of the chemically-etched edge profiles of silicon dioxide films on etchant concentration and temperature. *Thin Solid Films*, 18(1):S3–S6, 1973.

[173] Kirt R. Williams and Richard S. Muller. Etch rates for micromachining processing. *Journal of Microelectromechanical systems*, 5(4):256–269, 1996.

[174] M. Lipson. Guiding, Modulating, and Emitting Light on Silicon: Challenges and Opportunities. *J. Lightwave Technol.*, 23:4222–4238, 2005.

[175] B. Jalali and S. Fathpour. Silicon photonics. *IEEE J. Lightwave Technol.*, 24:4600–4615, 2006.

[176] U.s. department of defence photos. https://www.flickr.com/photos/39955793@N07/5811868587 .

[177] John D. Anderson and John D. Anderson. *Fundamentals of aerodynamics*. Anderson series. McGraw-Hill, New York, 5th ed edition, 2011.

[178] M. Ghulinyan, M. Bernard, R. Bartali, and G. Pucker. Formation of Mach angle profiles during wet etching of silica and silicon nitride materials. *Applied Surface Science*, 359:679–686, December 2015.

[179] D. K. Owens and R. C. Wendt. Estimation of the surface free energy of polymers. *J. Appl. Polym. Sci.*, 13:1741–1747, 1969.

[180] W. A. Zisman. Relation of the Equilibrium Contact Angle to Liquid and Solid Constitution. In F. M. Fowkes, editor, *Contact Angle, Wettability and Adhesion*, pages 1–51. American Chemical Society, Washington, DC, 1964.

[181] D. Kolacyak, J. Ihde, Ch Merten, A. Hartwig, and U. Lommatzsch. Fast functionalization of multi-walled carbon nanotubes by an atmospheric pressure plasma jet. *J. Colloid Interf. Sci.*, 359:311–317, 2011.

[182] H. Yanazawa. Adhesion model and experimental verification for polymerSiO system. *Colloids and Surfaces*, 9:133–145, 1984.

[183] T. Tsuchizawa, T. Watanabe, K. Yamada, and H. Morita. Low loss mode size converter from 0.3 m square Si wire waveguides to singlemode fibres. *Electron. Lett.*, 38:1669–1670, 2002.

[184] M. A. Foster, A. C. Turner, J. E. Sharping, B. S. Schmidt, M. Lipson, and A. L. Gaeta. Broad-band optical parametric gain on a silicon photonic chip. *Nature*, 441:960–963, 2006.

[185] T. Brenner and H. Melchior. Integrated Optical Modeshape Adapters in InGaAsP/InP for efficient Fiber-to-Waveguide Coupling. *IEEE Photon. Technol. Lett.*, 5:1053–1056, 1993.

[186] A. Mekis and J. D. Joannopoulos. Tapered Couplers for Efficient Interfacing Between Dielectric and Photonic Crystal Waveguides. *J. Lightwave Technol.*, 19:861–865, 2001.

[187] R. S. Fan and R. B. Hooker. Tapered polymer single-mode waveguides for mode transformation. *J. Lightwave Technol.*, 17:466–474, 1999.

[188] B. Jacobs, R. Zengerle, K. Faltin, and W. Weiershausen. Vertically tapered spot size transformers fabricated by a simple masking technique. *Electronics Letters*, 31:794–796, 1995.

[189] A. Sugita, A. Kaneko, K. Okamoto, M. Itoh, A. Himeno, and Y. Ohmori. Very low insertion loss arrayed-waveguide grating with vertically tapered waveguides. *IEEE Photon. Technol. Lett.*, 12:1180–1182, 2000.

[190] A. Sure, T. Dillon, J. Murakowski, Ch Lin, D. Pustai, and D. W. Prather. Fabrication and characterization of three-dimensional silicon tapers. *Opt. Express*, 11:3555–3561, 2003.

[191] B. Han, E. Rigo, R. Guider, S. Larcheri, G. Nunzi Conti, M. R. Vanacharla, A. Chiasera, M. Ferrari, L. Pavesi, G. Pucker, and M. Ghulinyan. Development and optical characterization of vertical tapers in SiON waveguides using gray-scale lithography. In *Integrated Photonics: Materials, Devices, and Applications*, pages 80690K1–80690K9. Proc. of SPIE, 2011.

[192] C. M. Waits, B. Morgan, M. Kastantin, and R. Ghodssi. Microfabrication of 3d silicon MEMS structures using gray-scale lithography and deep reactive ion etching. *Sensors and Actuators A: Physical*, 119:245–253, 2005.

[193] R. Ptri, P. Brault, O. Vatel, D. Henry, E. Andr, Ph Dumas, and F. Salvan. Silicon roughness induced by plasma etching. *J. Appl. Phys.*, 75:7498–7506, 1994.

[194] Kevin K. Lee, Desmond R. Lim, Lionel C. Kimerling, Jangho Shin, and Franco Cerrina. Fabrication of ultralow-loss Si/SiO 2 waveguides by roughness reduction. *Optics letters*, 26(23):1888–1890, 2001.

[195] S. Lardenois, D. Pascal, L. Vivien, E. Cassan, S. Laval, R. Orobtchouk, M. Heitzmann, N. Bouzaida, and L. Mollard. Low-loss submicrometer silicon-on-insulator rib waveguides and corner mirrors. *Optics letters*, 28(13):1150–1152, 2003.

[196] Yurii Vlasov and Sharee McNab. Losses in single-mode silicon-on-insulator strip waveguides and bends. *Optics express*, 12(8):1622–1631, 2004.

[197] P. Dumon, W. Bogaerts, V. Wiaux, J. Wouters, S. Beckx, J. Van Campenhout, D. Taillaert, B. Luyssaert, P. Bienstman, D. Van Thourhout, and R. Baets. Low-Loss SOI Photonic Wires and Ring Resonators Fabricated With Deep UV Lithography. *IEEE Photonics Technology Letters*, 16(5):1328–1330, May 2004.

[198] T. Tsuchizawa, K. Yamada, H. Fukuda, T. Watanabe, Jun-ichi Takahashi, M. Takahashi, T. Shoji, E. Tamechika, S. Itabashi, and H. Morita. Microphotonics devices based on silicon microfabrication technology. *IEEE Journal of Selected Topics in Quantum Electronics*, 11(1):232–240, January 2005.

[199] Tai Tsuchizawa, Koji Yamada, Hiroshi Fukuda, Toshifumi Watanabe, Shingo Uchiyama, and Seiichi Itabashi. Low-loss Si wire waveguides and their application to thermooptic switches. *Japanese journal of applied physics*, 45(8S):6658, 2006.

[200] Po Dong, Wei Qian, Shirong Liao, Hong Liang, Cheng-Chih Kung, Ning-Ning Feng, Roshanak Shafiiha, Joan Fong, Dazeng Feng, Ashok V. Krishnamoorthy, and others. Low loss shallow-ridge silicon waveguides. *Optics express*, 18(14):14474–14479, 2010.

[201] J. Bolten, C. Manecke, T. Wahlbrink, M. Waldow, and H. Kurz. Study on exposure strategy to minimize optical propagation losses in silicon waveguides fabricated by electron beam lithography. In *Lasers and Electro-Optics Europe (CLEO EUROPE/IQEC), 2013 Conference on and International Quantum Electronics Conference*, pages 1–1. IEEE, 2013.

[202] David E Hagan and Andrew P Knights. Mechanisms for optical loss in SOI waveguides for mid-infrared wavelengths around 2 m. *Journal of Optics*, 19(2):025801, February 2017.

[203] Jacob S. Levy, Alexander Gondarenko, Mark A. Foster, Amy C. Turner-Foster, Alexander L. Gaeta, and Michal Lipson. CMOS-compatible multiple-wavelength oscillator for on-chip optical interconnects. *Nature Photonics*, 4(1):37–40, January 2010.

[204] Mark A. Foster, Jacob S. Levy, Onur Kuzucu, Kasturi Saha, Michal Lipson, and Alexander L. Gaeta. Silicon-based monolithic optical frequency comb source. *Optics Express*, 19(15):14233–14239, 2011.

[205] Klaus; Herr Tobias; Brasch-Victor; Holzwarth Ronald; Kippenberg Tobias J. Riemensberger, Johann; Hartinger. Dispersion engineering of thick high-Q silicon nitride ring-resonators via atomic layer deposition. *Optics Express*, 20(25), 2012.

[206] Qing Li, Ali A. Eftekhar, Majid Sodagar, Zhixuan Xia, Amir H. Atabaki, and Ali Adibi. Vertical integration of high-Q silicon nitride microresonators into silicon-on-insulator platform. *Optics Express*, 21(15):18236, July 2013.

[207] Yang Liu, Yi Xuan, Xiaoxiao Xue, Pei-Hsun Wang, Steven Chen, Andrew J. Metcalf, Jian Wang, Daniel E. Leaird, Minghao Qi, and Andrew M. Weiner. Investigation of mode coupling in normal-dispersion silicon nitride microresonators for Kerr frequency comb generation. *Optica*, 1(3):137, September 2014.

[208] Daryl T. Spencer, Jared F. Bauters, Martijn J. R. Heck, and John E. Bowers. Integrated waveguide coupled Si_3n_4 resonators in the ultrahigh-Q regime. *Optica*, 1(3):153, September 2014.

[209] Yi Xuan, Yang Liu, Leo T. Varghese, Andrew J. Metcalf, Xiaoxiao Xue, Pei-Hsun Wang, Kyunghun Han, Jose A. Jaramillo-Villegas, Abdullah Al Noman, Cong Wang, Sangsik Kim, Min Teng, Yun Jo Lee, Ben Niu, Li Fan, Jian Wang, Daniel E. Leaird, Andrew M. Weiner, and Minghao Qi. High-Q silicon nitride microresonators exhibiting low-power frequency comb initiation. *Optica*, 3(11):1171, November 2016.

[210] Martin H. P. Pfeiffer, Arne Kordts, Victor Brasch, Michael Zervas, Michael Geiselmann, John D. Jost, and Tobias J. Kippenberg. Photonic Damascene process for integrated high-Q microresonator based nonlinear photonics. *Optica*, 3(1):20, January 2016.

[211] Xingchen Ji, Felippe A. S. Barbosa, Samantha P. Roberts, Avik Dutt, Jaime Cardenas, Yoshitomo Okawachi, Alex Bryant, Alexander L. Gaeta, and Michal Lipson. Breaking the Loss Limitation of On-chip High-confinement Resonators. *arXiv:1609.08699 [physics]*, September 2016. arXiv: 1609.08699.